Imaging laser-induced fragmentation of molecular beams, from positive to negative molecules

by

Benjamin Berry

B.S., Kansas State University, 2010

AN ABSTRACT OF A DISSERTATION

submitted in partial fulfillment of the
requirements for the degree

DOCTOR OF PHILOSOPHY

Department of Physics
College of Arts and Sciences

KANSAS STATE UNIVERSITY
Manhattan, Kansas

2018

Abstract

The use of ultrafast lasers allows one to study and even control quantum mechanical systems on their natural timescales. Our aim is to study the fragmentation of small molecules in strong laser fields as a means to gain understanding of molecular dynamics and light-matter interactions. Our research group has utilized fast, positively charged molecular ion beams as targets to study and control fragmentation by strong laser fields. This approach allows for detection of all molecular fragments including neutrals, and a coincidence three-dimensional momentum imaging technique is used to characterize the fragmentation. A natural extension of these types of studies is to expand the types of molecular systems that can be studied, from positively charged molecules to neutral and negatively charged molecules. To that end, the primary technical development of this dissertation involved the generation and use of fast, negatively charged molecular beams. Using fast molecular anion beams as targets allows for the study of fragmentation in which all fragments are neutral. As a demonstration, we employ this capability to study F_2^- dissociation and photodetachment. The dissociation pathways are identified and used to evaluate the initial vibrational population of the F_2^- beam. The role of dissociation in photodetachment is also explored, and we find that it competes with other dissociative (F+F) and non-dissociative (F_2) photodetachment mechanisms. Also highlighted are studies of fragmentation of LiO^-, in which the dissociation into $Li+O^-$ fragments provides information about the structure of LiO^-, including the bond dissociation energy, which was found to be larger than values based on theory. Studies of the autodetachment lifetimes of LiO^- were also performed using a pump-probe technique.

Additional experimental advancements have made successful pump-probe studies of the ionization of HD^+ and Ar_2^+ possible. Enhancement in the ionization of dissociating HD^+ and Ar_2^+ was observed at surprisingly large internuclear separation where the fragments

are expected to behave like separate atoms. The analysis methods used to quantify this enhancement are also described.

Finally, the production of excited Rydberg D* fragments from D_2 molecules was studied utilizing a state-selective detection method. The carrier-envelope phase dependence of D* formation was found to depend on the range of excited final states of the atomic fragments. We also measured the excited state population of the D* fragments.

Together, the studies presented in this work provide new information about fragmentation of positive, negative, and neutral molecules in strong laser fields, and the experimental developments serve as building blocks for future studies that will lead to a better understanding of molecular dynamics.

Imaging laser-induced fragmentation of molecular beams, from positive to negative molecules

by

Benjamin Berry

B.S., Kansas State University, 2010

A DISSERTATION

submitted in partial fulfillment of the
requirements for the degree

DOCTOR OF PHILOSOPHY

Department of Physics
College of Arts and Sciences

KANSAS STATE UNIVERSITY
Manhattan, Kansas

2018

Approved by:

Major Professor
Itzik Ben-Itzhak

Copyright

Abstract

The use of ultrafast lasers allows one to study and even control quantum mechanical systems on their natural timescales. Our aim is to study the fragmentation of small molecules in strong laser fields as a means to gain understanding of molecular dynamics and light-matter interactions. Our research group has utilized fast, positively charged molecular ion beams as targets to study and control fragmentation by strong laser fields. This approach allows for detection of all molecular fragments including neutrals, and a coincidence three-dimensional momentum imaging technique is used to characterize the fragmentation. A natural extension of these types of studies is to expand the types of molecular systems that can be studied, from positively charged molecules to neutral and negatively charged molecules. To that end, the primary technical development of this dissertation involved the generation and use of fast, negatively charged molecular beams. Using fast molecular anion beams as targets allows for the study of fragmentation in which all fragments are neutral. As a demonstration, we employ this capability to study F_2^- dissociation and photodetachment. The dissociation pathways are identified and used to evaluate the initial vibrational population of the F_2^- beam. The role of dissociation in photodetachment is also explored, and we find that it competes with other dissociative (F+F) and non-dissociative (F_2) photodetachment mechanisms. Also highlighted are studies of fragmentation of LiO^-, in which the dissociation into $Li+O^-$ fragments provides information about the structure of LiO^-, including the bond dissociation energy, which was found to be larger than values based on theory. Studies of the autodetachment lifetimes of LiO^- were also performed using a pump-probe technique.

Additional experimental advancements have made successful pump-probe studies of the ionization of HD^+ and Ar_2^+ possible. Enhancement in the ionization of dissociating HD^+ and Ar_2^+ was observed at surprisingly large internuclear separation where the fragments

are expected to behave like separate atoms. The analysis methods used to quantify this enhancement are also described.

Finally, the production of excited Rydberg D* fragments from D_2 molecules was studied utilizing a state-selective detection method. The carrier-envelope phase dependence of D* formation was found to depend on the range of excited final states of the atomic fragments. We also measured the excited state population of the D* fragments.

Together, the studies presented in this work provide new information about fragmentation of positive, negative, and neutral molecules in strong laser fields, and the experimental developments serve as building blocks for future studies that will lead to a better understanding of molecular dynamics.

Table of Contents

List of Figures

List of Tables

Acknowledgments

The work presented in this dissertation would not have been possible without the important contributions of several people. Furthermore, many more have had significant impacts on my education since I began working in the J.R. Macdonald Lab almost ten years ago. It would be impossible for me list them all here, let alone adequately express my gratitude for their wisdom, support, and encouragement. I will attempt to point out a few of these people here.

First and foremost, I would like to express my deepest gratitude to my adviser, Itzik Ben-Itzhak. The value of his teaching and mentorship cannot be overstated. Since I joined his group as a sophomore undergraduate student, he has been instrumental in my growth as a scientist, passing on his knowledge, excitement, and approach to quality research. I am grateful to him for taking me on as an undergraduate and as a graduate student, and I fully recognize the privilege of having an excellent teacher and scientist as an adviser. I also thank Kevin Carnes, from whom I have learned many technical skills, and I greatly appreciate his vision and attention to detail. Thanks to Brett Esry for holding the level of physics in my research to a high standard. Discussions with him and his group have had a considerable influence on my physics education, for which I am extremely grateful. I also thank the additional members of my Ph.D. committee, Artem Rudenko, Dan Higgens, and Liang-Wu Cai for their time and insight.

I feel incredibly lucky to have worked with many great students and postdocs in Itzik's group who have made the long hours in the lab so much more enjoyable. I am sincerely grateful for the time I have spent learning with and from you. Thanks to Bethany Jochim, Travis Severt, Peyman Feizollah, Mohammad Zohrabi, Raju Pandiri, Jyoti Rajput, Utuq Ablikim, Nora Kling, Kelsie Betch, Adam Summers, and Dustin Hayes. I am also grateful to previous group members Jarlath McKenna, Max Sayler, and Bishwanath Gaire, for their encouragement early in my career. Thanks to Nora Kling for putting up with me as a clueless

undergraduate my first year in the lab. And I am especially grateful to Bethany, Travis, Peyman, Mo, and Raju, for their significant contributions to the work in this dissertation, and for their friendship and companionship inside and outside of the lab.

A great deal of my understanding of AMO physics has come through discussions with Brett Esry's group. I thank Youliang Yu, Yujun Wang, Shuo Zeng, and Brandon Rigsbee for many fruitful discussions. I am thankful for the knowledge and insight of Eric Wells from Augustana University, and Jack Maseberg and Sam DeVore from Fort Hayes State University. I thank Thorsten Weber for the opportunity to contribute to beamtimes at the Advanced Light Source at Lawrence Berkeley National Laboratory. I am extremely grateful to Frank Chmara of Peabody Scientific for his extensive help with our ion sources.

The quality research done at the J.R. Macdonald Laboratory is facilitated by the outstanding support staff, and I am grateful to several members for their time and dedication to helping make my projects possible. Thanks to Charles Fehrenbach for his assistance with the lasers and ion sources. Thanks to Chris Aikens, Mike Wells, Al Rankin, and Justin Millette for spending significant time helping me solve countless technical problems. Thanks to Scott Chainey for his help with all electronics issues. Thanks to Vince Needham for helping with computer and LabView issues. Thanks to Bob Krause for interrupting his retirement to teach us how to safely operate our sputter source. I am lucky to have been a part of the Macdonald Lab and the Physics department at K-State, and I am grateful to all of the people who made working here so great.

I am thankful to my loving and supporting family: Jeff, Lisa, Josh, Michelle, Frank, Wanda, Cody, and Michelle. And most importantly, I thank my wife, Shanda, for sharing this experience with me, for being the steadying force through all the happiness and frustration, and for her sacrifices and support.

This Ph.D. work was supported by the Chemical Sciences, Geosciences, and Biosciences Division, Office of Basic Energy Sciences, Office of Science, U.S. Department of Energy under Award No. DE-FG02-86ER1

Chapter 1

Introduction

1.1 Overview

The development of ultrafast, intense lasers has had a dramatic impact on the study of light-matter interactions [1, 2]. Femtosecond pulses (10^{-15} seconds) have provided tools for probing molecular dynamics on their natural timescales. For example, laser pulses are used to initiate molecular dynamics and take "snapshots" as reactions, such as bond cleavage or bond rearrangement, are taking place. These types of studies of molecular reaction dynamics on ultrashort timescales fall under the area of science known as *femtochemistry*, and its pioneers were awarded the 1999 Nobel Prize in chemistry [3]. Moreover, with the intense, ultrashort laser pulses now available, highly nonlinear, multiphoton processes such as excitation, ionization, and other nonlinear phenomena can be driven in atoms and molecules. Strong field interactions with atoms and molecules coherently drive many processes that may interfere, which has inspired many studies utilizing the strong laser field to control atomic and molecular dynamics [4]. The mechanisms that steer the behavior of atoms and molecules in strong fields are still not fully understood, and building understanding of the basic processes that occur in atoms and molecules at a fundamental level is important to applying this knowledge to larger systems.

1.2 Our Approach

Our research group is interested in studying the fragmentation of molecules by intense, ultrashort laser pulses in order to understand and manipulate molecular dynamics. To that end, the fragmentation of fast molecular ion beams has been used as a tool to explore the nature of interactions between strong laser fields and molecules. The use of molecular ion beams has allowed studies of benchmark systems, such as the one-electron H_2^+ [5–10] and the simplest triatomic H_3^+ [11–14]. The knowledge gained from these studies has been extended to more complex systems including O_2^+, CO^{2+}, and others [15–19].

One of the main advantages of using a fast molecular ion beam as a target is the ability to measure neutral fragments that are otherwise difficult to detect. Neutral fragments retain the velocity of the ion beam, providing sufficient kinetic energy for detection by commonly used particle detectors. With this capability in mind, a natural extension of the molecular beam studies is to produce a fast beam of neutral molecules, which will allow the study of their fragmentation directly without the need for ionization by measuring all neutral fragments. The challenge of creating fast neutral beams can be accomplished in many ways. For example, positive molecular ions can be neutralized by electron capture, or negative molecular ions can be neutralized by photodetachment. We are pursuing both of these approaches, but chose to first focus on photodetachment of negative ions. A large step toward realizing this goal involves the development of the capability to generate and use negative molecular ion beams. While the ultimate goal is to produce fast beams of neutral molecules, molecular anions are interesting systems to study in their own right. For instance, the energy needed to detach an electron from a molecular anion is comparable to, or even lower than, the dissociation energy, allowing for competition between dissociation and electron detachment.

My primary contribution in this regard was to expand our capability to study molecular fragmentation to the case of fast molecular anion beams. This involved incorporating new ion sources and new sections of beamline into the existing apparatus, generating several different molecular anions, and adapting our imaging and analysis methods for negatively charged ions. This significant experimental development led to the studies of dissociation

of F_2^- and LiO^- as well as their photodetachment. Imaging the fragmentation provides information about the dissociation pathways and photodetachment mechanisms, and also allows us to determine properties of the molecular anions.

Furthermore, I have been involved in a variety of projects focusing on fragmentation of positively charged molecular ion beams as well as neutral molecules. A few examples of projets I led include studies of the ionization of molecular ions using a pump-probe technique, and also the development of an apparatus used to state-selectively detect Rydberg atomic fragments from molecules.

1.3 Document organization

The studies presented in this work were performed with the goal of understanding the laser-induced fragmentation of molecular anions, cations, and neutral molecules. As the development of molecular anion beams was the main technical development of this work, molecular anions are the focus of the first and largest part of this document. Building on the general introduction provided here, more specific background information regarding each project is given at the start of each section. The experimental developments leading to our first studies involving negative ions are presented in Chapter 2. This includes the generation of fast molecular anion beams, imaging their fragmentation, and some details of the laser system used to perform all of the studies presented in this work.

These experimental developments enabled the studies on the fragmentation of molecular anions presented in Chapter 3. Specifically, studies of dissociation and photodetachment of F_2^- are presented in Section 3.3, in which the dissociation and photodetachment pathways are explored for a variety of laser pulse parameters. Studies involving the dissociation of LiO^- are presented in Section 3.4. The results are used to provide new information about the dissociation energy of the ground state of LiO^-. In addition, preliminary results of time-resolved measurements of the autodetachment lifetime of LiO^- as well as highlights from a few preliminary measurements involving other diatomic and triatomic anions are presented.

In the second part of this dissertation, a few selected studies of the fragmentation of

positively charged molecular ion beams and neutral molecules are presented. The fragmentation of HD^+ and Ar_2^+ was studied using a pump-probe technique, and is described in Chapter 4. In these studies, dissociation of the molecular ion is initiated by a pump pulse, and a probe pulse ionizes the molecule during its dissociation after a controllable delay. Ionization is found to be enhanced at large pump-probe delays corresponding to surprisingly large internuclear distances.

Studies of the laser-induced formation of excited D* fragments from D_2 are presented in Chapter 5. A state-selective method of measuring the D* fragments is used to study the dependence of D* formation on the carrier-envelope phase of ultrashort (sub-5 fs) laser pulses. This method is also used to measure the excited state population of D* atoms.

Finally, a summary of the topics covered in this dissertation and possible future directions are presented in Chapter 6.

Chapter 2

Experimental Methods

2.1 Scope

A summary of the experimental methods used in this dissertation is given in this chapter. The primary technical development in this work, which involves the generation and use of negatively charged molecular ion beams, is presented in Section 2.2. These developments made the studies of the fragmentation of molecular anions presented in Chapter 3 possible. The coincidence 3D momentum imaging technique used in these experiments has been described in detail elsewhere [12, 20], so only the main points are described in section 2.3. However, imaging in negative ion experiments required some modifications that are described in more detail as they are new to this work. The laser system and some details of its application in all of the projects included in this dissertation are described in section 2.4. The experimental techniques specific to the work presented in Chapters 4 and 5, which involve pump-probe studies of HD^+ and Ar_2^+ fragmentation, and measurements of Rydberg atomic D* fragments from D_2, are described in the respective chapters.

2.2 Development of negatively charged molecular ion beams

The experimental studies involving molecular ion beams in this dissertation utilize the laser-induced molecular dissociation imaging (LIMDI) technique developed by Ben-Itzhak's group [5, 21]. Coincidence 3D momentum imaging (see Sec. 2.3) implemented in this crossed-beams setup is used to study the fragmentation of molecular ions by intense ultrashort laser pulses. The use of molecular ion beams in strong field studies of light-matter interactions provides some advantages over the more commonly used neutral targets, though it also has some disadvantages.

The application of molecular ion beams allows the study of benchmark molecules, like diatomic one-electron H_2^+ [22–25] and the simplest triatomic molecule, H_3^+ [11, 13–15, 26–28]. The key advantage to this approach is that the detection of neutral molecular fragments is made possible due to the kinetic energy of the neutral fragments (which carry a fraction of the keV energy of the ion beam). This allows for kinematically complete studies of dissociation as well as the study of fragmentation resulting in only neutral fragments. The main disadvantage of using molecular ion beams is their extremely low target density. For comparison, the typical density of an ion beam target is $\sim 10^5$ molecules/cm^3 while the density of a neutral gas jet target is $\sim 10^{11}$ molecules/cm^3 and is even higher in gas cells. Moreover, the ion beam target is 2-3 orders of magnitude less dense than the residual gas density in our ultra-high vacuum (UHV) system. Therefore, laser interactions with background atoms and molecules are more likely than with the ion beam target, and often experimental "tricks" must be used to limit the contributions of background ions in the ion-beam measurement. Typically, the speed of the ion beam is chosen to separate beam fragments from the background in time. The measurement of fragments in coincidence further separates the beam fragments from the background.

The use of negatively charged molecular ions, which have their own unique properties, creates the possibility to study dissociation of neutral molecules by detecting all neutral

fragments. Studies of molecular anions using ultrafast lasers are relatively scarce, though. To our knowledge, only a few other groups study strong field laser interactions with negatively charged molecules [29–32].

Most molecular anions are unstable or weakly bound [33], thus generating high-density beams is difficult. A major effort in this work went towards the generation and use of molecular anion beams. The following sections describe the implementation of anion beams using two different types of ion sources, a duoplasmatron that produces negative ions from gases and a sputter source that uses solid targets.

2.2.1 Duoplasmatron ion source

Duoplasmatron ion sources are commonly used to produce positively charged ion beams from gases; however, they can also be used to produce negatively charged ions which are the focus of our efforts. The duoplasmatron used in this work is a water-cooled Peabody Scientific PS-100 source [34].

The duoplasmatron is a filament ion source that consists of a cathode (filament), intermediate electrode, and anode, as shown in Fig. 2.1. Electrons are emitted from the cathode and accelerated toward the anode due to the voltage difference between cathode and anode. The intermediate electrode has a small aperture that focuses the electrons and guides them toward the anode. An axial magnetic field further constricts the electrons to a narrow beam. The plasma discharge is sustained at low pressure ($\sim$100 mTorr), which is important for maintaining low pressure throughout the vacuum system. Typical discharge voltage and current are 75 V and 1 A, and the discharge is adjusted to optimize the ion beam output. Gas introduced into the source interacts with the plasma, producing positive and negative ions. A small aperture in the anode allows for extraction of positive or negative ions as well as electrons.

The electron discharge is produced by thermionic emission from the filament. A current of 20-30 A heats the filament to 800-2000 °C depending on the filament type. Two types of filaments are commonly used, oxide-coated and thoriated. The oxide-coated filament is a

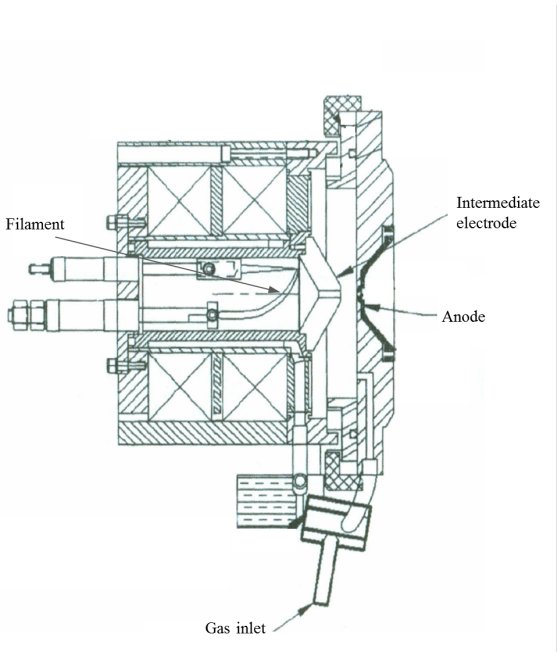

Figure 2.1: Diagram of the duoplasmatron adapted from [34]. Electrons are emitted from the filament and guided through the intermediate electrode toward the anode where they form a dense plasma. Gas introduced into the source interacts with the plasma, producing positive and negative ions, which are extracted through a hole in the anode.

fine platinum mesh coated with an alkaline-carbonate coating (typically a mixture of barium, strontium, and calcium). Heating the filament converts the carbonates to oxides, and this conditioning process is done slowly to maintain low pressure in the source. Thermionic emission from the oxides occurs at 800-1000 °C. An oxide coated filament can be operated for a couple hundred hours before recoating is needed.

Some gases (especially hydrocarbons) seem to interact with the oxide coating, causing instability and drastically reducing the lifetime of the filament. In these cases, a thoriated tungsten filament is used. The 1-mm thick tungsten filament (doped with 2% thorium) is heated to 2000 °C, which causes thorium atoms to move to the surface and emit electrons. The tungsten filaments have lifetimes of up to about 100 hours of operation. High current beams of positive ions have been produced from the source including H_2^+, H_3^+, Ar_2^+, and HeH^+. Beams of H_2^+ and H_3^+ are produced by introducing pure hydrogen gas into the source. The H_3^+ beam is dominant with hundreds of μA current measured about 2 m from the exit of the source after an inflection magnet. The H_2^+ current is lower by about a factor of 5, but

may be optimized by running the source at lower pressure or by mixing the hydrogen with a buffer gas (typically argon). An Ar_2^+ beam is generated from pure argon, and optimum source conditions include operating at very low source pressure and low magnet current. Several nA of Ar_2^+ have been achieved. Introducing a 3:1 H_2:He gas mixture to the source yields hundreds of nA of HeH^+.

In negative-ion operation, the intermediate electrode is moved off-axis, selecting the periphery of the plasma which contains more negative ions than the central part. This condition makes the production of negative ion beams less stable and more sensitive to source parameters, so more careful tuning of the source is needed for negative ions. The H^- beam is one of the easiest anion beams to tune, and a few μA of beam current is typically generated. We had no success generating H_2^- (metastable H_2^- is only long-lived in very high rotational states [35, 36]). A few nA of F_2^- have been produced using a 10:1 Ar:CF_4 gas mixture. Gas mixtures containing other fluorine-containing compounds such as SF_6 and C_2F_6 did not produce any more current. A beam of $C_2H_2^-$ was produced from a 20:1 Ar:C_2H_6 mixture (interestingly, the acetylene anion could not be produced using an acetylene:argon mixture).

2.2.2 Cesium sputter source

Cesium sputter ion sources are among the most commonly used sources of negative ions. As the name implies, sputter sources utilize Cs sputtering of solid targets. The sputter source used in this work is a Peabody Scientific PS-120 source [34], and it shares some of the elements of the Duoplasmatron, which enables us to switch between sources relatively quickly.

Development of negative-ion sputter sources followed the discovery that when a material is sputtered by Cs^+ ions many of the sputtered particles are negatively charged [37]. The sputter source, as depicted in Fig. 2.2, operates by heating cesium in an oven to about 200 °C, releasing Cs vapor which travels into the source. A cylindrical tantalum ionizer is heated to about 1100 °C, and Cs atoms that come in contact with it are ionized. A voltage drop accelerates the Cs^+ ions toward the cathode, which contains the sputter target. The

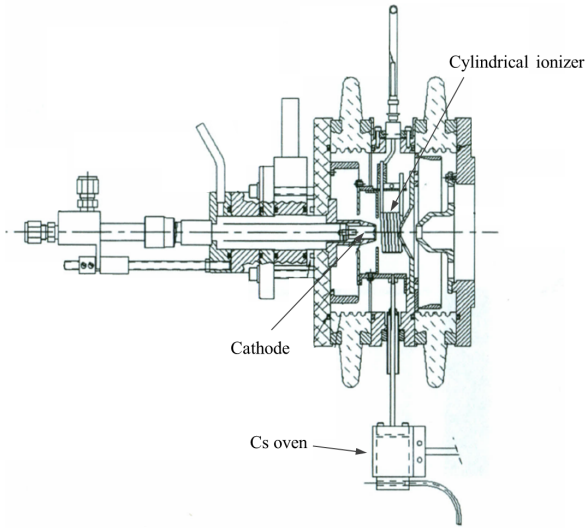

Figure 2.2: Diagram of the sputter source adapted from [34]. Cs vapor from the cesium oven flows into the source where it is ionized and accelerated toward the cathode target. Sputtered particles from the target with negative charge are extracted from the source.

Cs^+ ions impact the target with about 5 keV impact energy, sputtering particles from the target. Cs vapor also coats the surface of the cathode, and sputtered particles can undergo charge exchange with the atoms forming the film, increasing the emission of negative ions. A 1 g load of cesium lasts for about 10 days of operation.

The cathode target is a copper or aluminum cylinder with a hole drilled into the top flat face, which is packed with the solid target to be sputtered. The cathode is mounted on a manipulator allowing adjustment of the cathode position, which is used to optimize the sputtering efficiency. Typical cathodes last for a few 10's of hours of operation. Cathodes can be replaced while the source is operating by pulling the cathode out into the airlock by the control arm. The airlock is sealed and vented to atmosphere, and the cathode is then replaced. After replacing the cathode, the airlock is sealed and pumped before reopening to the source and the cathode is reinserted.

Negative ions are extracted through an exit aperture and accelerated to the desired beam energy. The energy of the beam is approximately the sum of the cathode voltage and extraction voltage. To prevent a large electron beam from exiting the source, permanent

magnets attached to the exterior of the source deflect the electrons enough that they don't pass through the exit aperture.

Extensive testing of this type of sputter source was done by Middleton [38] for almost every element on the periodic table. Using this as a guide we were able to generate several molecular anion beams. The most common target we used was LiF, from which a few molecular anions are produced. Aside from the strong atomic Li^- and F^- beams, molecular beams including LiF^-, F_2^- (the subject of Section 3.3), and LiF_2^- were produced. The current of the molecular beams is typically fractions of a nA after they are collimated and steered through the interaction region. Other targets include LiOH, which was used to generate LiO^- (the subject of Section 3.4); LiH was used to produce LiH^- beams; a mixture of LiF and MgCl was used to create FCl^-.

2.2.3 Experimental apparatus

The experimental apparatus employed in the molecular ion beam studies is shown schematically in Fig. 2.3. The apparatus consists of an ultra-high vacuum beamline containing the ion source, ion beam optics, laser beam optics, and imaging setup. Between the ion source and laser-interaction region are several elements used to steer, focus, and collimate the ion beam. The bending by the inflection magnet is proportional to the momentum-to-charge ratio of the ion beam, which allows for separation of beams of different species. An electrostatic quadrupole lens and two einzel lenses are used to focus the beam. Several electrostatic deflectors steer the beam horizontally and vertically through the beamline, and a few sets of four-jaw slits are used to collimate the beam and reduce the rate of scattered particles. Retractable Faraday cups at several points along the beamline are used to monitor the beam current. The purpose of all of these elements is to guide a well-collimated ion beam through the $1\times1\,\mathrm{mm}^2$ entrance aperture of the imaging spectrometer, where the laser-molecule interaction takes place, to the final 2-mm diameter Faraday cup in front of the imaging detector. A retractable beamviewer between the last Faraday cup and the imaging detector aids in tuning the beam to the last Faraday cup and reducing the rate of scattered ions on the

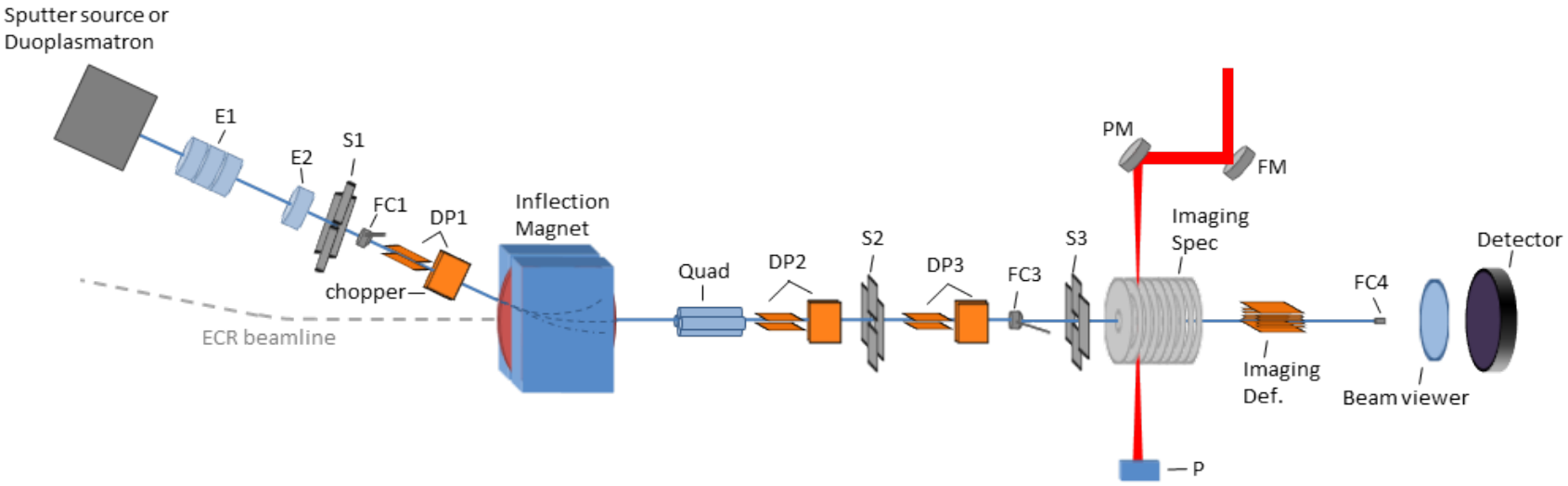

Figure 2.3: Top-view schematic of the setup used for the ion beam experiments (see Chapter 3). E – Electrostatic einzel lens used to focus the ion beam; DP – deflector plates, consisting of pairs of electrostatically biased parallel plates used to steer the ion beam horizontally and vertically. One pair of plates DP1 is used for chopping the ion beam (see text); S – four-jaw slits used to collimate the ion beam and reduce scatter; FC - removable Faraday cup, used to measure the current of the ion beam; Quad – electrostatic quadrupole lens used to focus the ion beam; FM – flat mirror used for aligning the laser beam; PM – 90° off-axis parabolic mirror which focuses the laser beam into the vacuum chamber; P – Power meter to monitor the laser power. The inflection magnet selects beams by their momentum-to-charge ratio. A removable beam viewer aids in tuning the ion beam through the interaction region to the final Faraday cup. The imaging spectrometer and imaging deflector are used as part of the LIMDI method (see text). The detector is a time- and position-sensitive delay-line detector [39].

detector. The ion beams are typically ∼1 mm across and beam currents range from a few picoamperes to a few nanoamperes.

A high rate of scattered particles hitting the detector can cause damage. To reduce this scatter, the ion beam is collimated and "chopped". Chopping is accomplished by a voltage pulse synchronized with the laser pulse that is applied to the first set of deflector plates before the inflection magnet, deflecting the ion beam away from its path. Since the ion beam only needs to be present in the laser-interaction region at the same time as the laser pulse, most of the ion beam can be dumped by the chopper. The width of the voltage pulse, triggered by a photodiode signal created by the laser pulse, ensures that about 90% of the beam is dumped. The ion beam that passes through in between voltage pulses arrives in the interaction region a few μs before to a few μs after the laser pulse. In principle, the duration of the chopped beam could be decreased even further, but the few-μs width accounts for time jitter of the voltage pulse and allows for easy crossing of the laser and ion beams. Thus, chopping converts the DC ion beam into a pulsed beam with a ∼10% duty cycle, which significantly reduces the scatter rate.

The laser beam is focused onto the ion beam by an aluminum 90° off-axis parabolic mirror ($f = 203\,mm$) outside of the vacuum chamber. The beamline entrance window is 1 mm-thick UV fused silica sealed with Torr Seal epoxy, which allows the base pressure to reach 1×10^{-9} Torr in the interaction region. The parabolic mirror creates a tight focus with minimum beam waist of ∼10 μm. It is mounted on a 3D translation stage used to optimize the crossing with the ion beam. The crossing of the beams is achieved by measuring the rate of a laser-driven process, such as dissociation or ionization, and scanning the translation stage to optimize the overlap. The position of the laser focus is usually determined to within 0.5 mm, much shorter than the Rayleigh length of the focused beam. In some experiments the ion beam is extremely weak, which makes the crossing procedure overly cumbersome. In these cases, it is often useful to adjust the inflection magnet to select a "stronger" ion beam with which the crossing with the laser beam is optimized. Then, the magnet is adjusted back to select the original beam, and since all other beamline elements are electrostatic (i.e. the tuning of the beam is only sensitive to its energy-to-charge ratio, and not mass) the crossing

with the laser is preserved.

The laser beam leaves the beamline through an exit window and is dumped onto a power meter. The average power of the laser is monitored over the course of the experiment. Additionally, a small fraction of the beam is focused on to a large-area photodiode which is used to monitor the shot-to-shot fluctuations in the pulse energy (see Appendix B).

The laser and ion beams are crossed inside the imaging spectrometer. The longitudinal electric field of the spectrometer accelerates or decelerates charged particles in order to separate ion and neutral fragments from each other by their time-of-flight (TOF) to the detector. A transverse electric field provided by the imaging deflector further separates the fragments in space on the detector. The imaging technique utilizing both the spectrometer and deflector is referred to as longitudinal and transverse field imaging (LATFI) [12].

The detector consists of a matched pair of microchannel plates (MCP) in a chevron configuration [40] stacked in front of a hex delay-line anode [39]. Position information is evaluated from the signals picked off each end of the delay-line wires. More detailed descriptions of the use of delay-line detectors can be found in Refs. [20, 41]. All of the detector signals provide timing information, and they are processed by a multi-hit time-to-digital converter (TDC) and then recorded. The timing signals are measured with respect to a photodiode signal generated by the laser pulse for every laser pulse (see Appendix C for a schematic of the detection electronics). While the time resolution of the TDC is 25 ps, jitter associated with the detector and its electronics limit the time resolution to about 200 ps [12, 20].

2.3 Momentum Imaging

The coincidence 3D momentum imaging technique described in this section (and in more detail in Refs. [12, 20]) allows for separation of fragmentation channels and enables the evaluation of the full 3D momentum of dissociation. From the momentum information, quantities such as kinetic energy release (KER) upon fragmentation and the direction of dissociation with respect to the laser polarization are also evaluated to study the fragmentation processes.

Using the measured TOF, the fragmentation channels are identified by plotting the co-

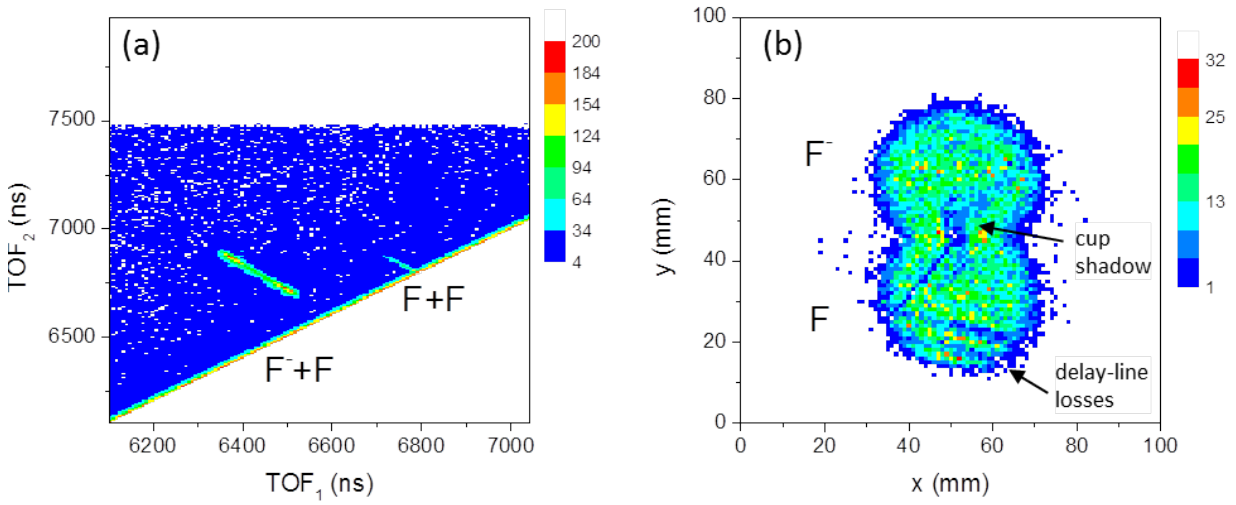

Figure 2.4: (a) Coincidence time-of-flight (CTOF) map showing fragmentation channels of a F_2^- ion beam. (b) Position spectrum showing the location of F^- and F fragments on the detector. Note that these fragments are separated spatially by the imaging deflector.

incidence time-of-flight map (CTOF), as shown in Fig. 2.4 for F_2^- as an example. From the coincidence time and position information of all the fragments, 3D momentum of all fragments is obtained. Detailed descriptions of the momentum imaging can be found in Refs. [12, 20], and a simpler example of "field-free" imaging explaining the same concepts is described in Ref. [42]. Briefly, let us consider the imaging in the x-direction, which is orthogonal to both the spectrometer and deflector electric fields so that the imaging in this direction is approximately field-free. For two-body breakup, the measured x-positions, x_1 and x_2, are given by

$$x_1 - x_0 = (v_{1x} + v_{0x})t_1 \tag{2.1}$$

$$x_2 - x_0 = (v_{2x} + v_{0x})t_2, \tag{2.2}$$

where x_0 is the initial position at which the molecule interacted with the laser, v_{0x} is the center-of-mass (CM) velocity, $v_{1,2x}$ are the breakup velocities of the two fragments in the CM frame, and $t_{1,2}$ are the measured TOFs. Note that these TOFs are the true times of flight relative to the time the laser pulse intersects the ion beam. The indexes (e.g. x_1 and

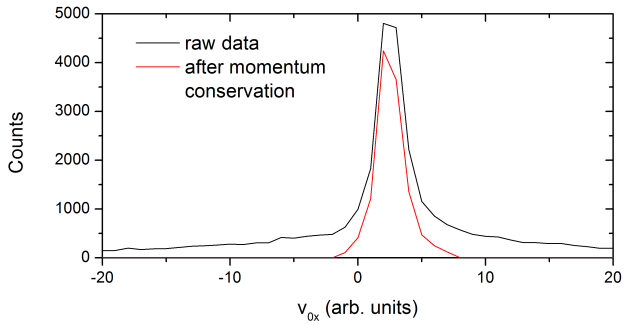

Figure 2.5: CM velocity distribution in the x-direction before and after selecting events that conserve momentum. Real events form a sharp distribution while random coincidences have a broad distribution.

x_2) refer to the order the fragments arrived in time. Additionally, momentum conservation dictates that in the CM frame

$$m_1 v_{1x} + m_2 v_{2x} = 0. \tag{2.3}$$

Using this system of three equations, three of the four unknown variables, v_{1x}, v_{2x}, v_{0x}, and x_0 can be solved for. The remaining unknown is replaced by an average value. Typically x_0 is approximated by an average value, as the spread in x_0 is about the size of the laser focus (usually $<$100 μm) which is smaller than the detector position resolution (about 0.25 mm) [12].

The imaging in the y- and z-directions proceeds in a similar way, but taking into account the effects of the deflector and spectrometer fields, respectively. To account for the electric field of the spectrometer, corrections to the kinematic time-of-flight formula for the z-direction are included based on simulations performed in SIMION [43]. Fringe fields from the spectrometer cause distortions in the x- and y-directions, which are also corrected based on SIMION simulations. Finally, from the CM-frame velocities, the 3D momentum of all fragments is obtained.

To distinguish real coincidences from false events, we evaluate the momentum of the center of mass using the x, y, and z CM velocities (v_{0x}, v_{0x}, and v_{0x}). Real events have a well-defined CM momentum while false coincidences are distributed randomly, as shown in Fig. 2.5.

The data analysis code was developed for positive and neutral fragments with a positive

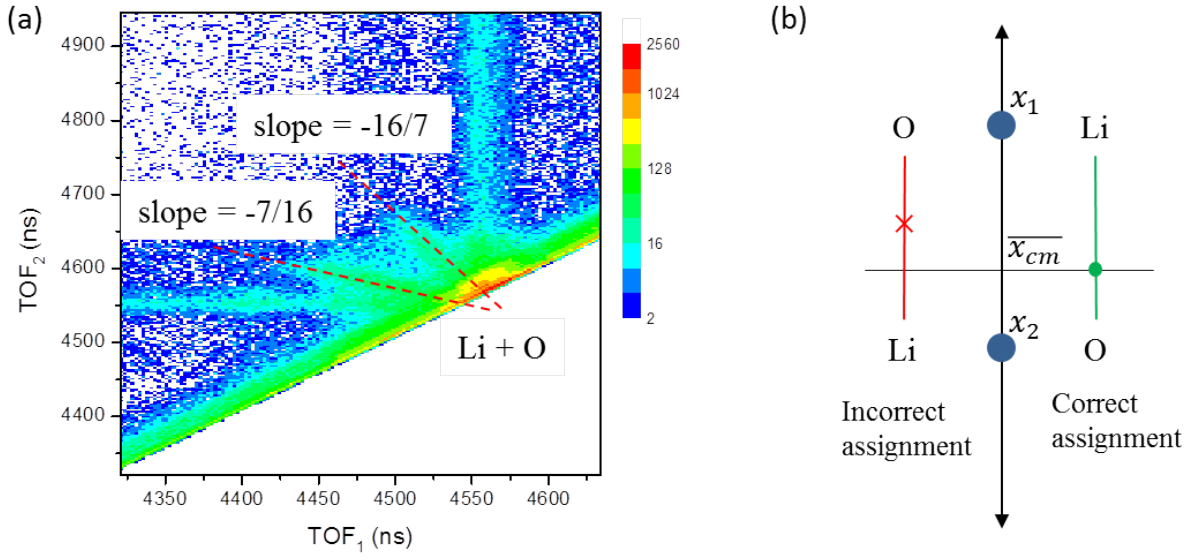

Figure 2.6: (a) CTOF map showing the Li + O neutral-neutral channel produced from a LiO^- beam. The two slopes indicate the time ordering of the fragments. Specifically, the -16/7 slope occurs when the O fragment is the first hit, and conversely the -7/16 slope occurs when the Li fragment arrives first. (b) Scheme for identifying neutral fragments by their position. The center-of-mass position is calculated for both mass assignments, and the correct assignment is chosen by comparing with an average CM position of all events identified by the CTOF slope.

spectrometer voltage, providing a field accelerating cations. When performing measurements on negative molecular ions breaking to anion fragments, a positive spectrometer voltage decelerates the ion fragments. Operating in this mode requires some modifications to the analysis software. Specifically, the analysis code assumes that the charged fragment hits the detector before neutral fragments, but for a positive spectrometer voltage the order is reversed for anion fragments. This simply requires reassigning the masses of the fragments, i.e. flipping the time order. The fringe fields of the decelerating spectrometer field also create different distortions that we simulated in SIMION and added to the analysis code. In the analysis code, these modifications are toggled automatically based on the input parameters for the spectrometer voltage and fragment charge.

On the other hand, the application of a negative spectrometer voltage accelerates the anion fragments so that they hit the detector first, which allows the use of the same imaging and analysis code as cation molecules for dissociation. The drawback to using a negative spectrometer voltage is that electrons are accelerated towards the detector which can interfere with the experiment at high enough rates; however, the imaging deflector steers most electrons away from the detector, enabling clean measurements of the ion beam fragments.

The other main difference in the analysis of fragmentation of molecular anions is the fragmentation channel involving only neutral fragments due to photodetachment of an electron and dissociation of the resulting neutral molecule. In coincidence measurements of ion and neutral fragments or two different ion fragments, identifying the fragments is simple because they are separated in time due to the spectrometer field. But, this is not the case with neutral-neutral channels, so other methods must be used to identify the fragments. The time-order of the neutral fragments, that is, which of the two neutral fragments hit the detector first, can be identified by the slope of the CTOF stripe as shown in Fig. 2.6(a). The linear approximation of the slope is simply given by the ratio of the fragment masses, m_1/m_2. Using the slope of the CTOF feature is sufficient provided that the time difference between the fragments is large enough. When the time difference is small, the fragments cannot be identified by their TOF, but their position information may be used instead. From the CM positions of known events, an average CM position is determined. Then, for each unknown

event, the CM position is calculated twice - once for each mass-order combination. The CM position closest to the average position corresponds to the correct mass assignment. This concept is shown schematically in Fig. 2.6(b).

This coincidence 3D momentum imaging technique is implemented in the studies on molecular anions in Chapter 3 and in the pump-probe studies on HD^+ and Ar_2^+ in Chapter 4.

2.4 Ultrafast Laser

The laser used in this work is the PULSAR, a KM Labs Ti:Sapphire based system capable of producing 21-fs pulses with 2-mJ pulse energy at 790-nm central wavelength [44]. The technology behind Ti:Sapphire lasers has been extensively covered in literature [24, 45–47], so in this section only a general overview of this laser technology is given along with some specifics of the PULSAR system. Several of the studies presented in this dissertation relied on manipulating the laser wavelength and pulse duration, and a brief description of the nonlinear optical techniques used to accomplish this are given. Knowledge and control of the spatial and temporal properties of the laser pulses is of great importance to understanding light-matter interactions, so the pulse characterization techniques used in this work are also concisely described.

2.4.1 Femtosecond Ti:Sapphire laser

A Ti:Sapphire laser oscillator contains a titanium-doped sapphire lasing medium that has a very broad fluorescence bandwidth (670-1070 nm) when pumped with 400-600 nm light [48]. While the gain bandwidth supports a large number of cavity modes, ultrashort pulse generation is achieved through mode-locking, in which the otherwise random cavity modes are phase-locked so that they constructively interfere within a very short period of time and eventually produce a single short pulse circulating in the cavity [47, 49]. The mode-locking mechanism commonly used in many modern solid-state lasers is the nonlinear optical Kerr effect, which passively acts as a very fast shutter only allowing high-intensity pulses to be

supported in the cavity [46, 49, 50].

The PULSAR oscillator produces pulses with central wavelength of 790 nm with about 80-nm bandwidth at a repetition rate of 75.2 MHz and average power of about 300 mW (which corresponds to ∼4 nJ pulse energy). Dispersion-compensating prisms in the oscillator reduce the pulse duration to ∼10 fs.

To increase the pulse energy from nJ to a few mJ, required for strong-field experiments, multipass amplification is used. To preserve the broad bandwidth and to prevent damaging the amplifier, the chirped-pulse amplification (CPA) technique is employed [46, 51]. A stretcher consisting of a pair of diffraction gratings stretches the pulse duration to tens of ps. Following the stretcher, the repetition rate is reduced to 10 kHz using a Pockels cell [50, 52]. In the PULSAR, amplification takes place in two stages. The first stage consists of 14 passes through a pumped Ti:Sapphire gain medium after which the pulse energy is almost 1 mJ. A second Pockels cell suppresses amplified spontaneous emission (ASE) from the gain medium. The second amplification stage further increases the pulse energy to about 3 mJ in 5 passes through another Ti:Sapphire medium. The amplifier crystals are cooled by a closed-loop compressed helium cryogenic cooling system, which allows for continuous operation of the laser and reduces thermal instabilities. Finally, a grating-based compressor reverses the stretching process, resulting in about 21-fs pulses with high peak power (∼0.1 TW).

Further details of the PULSAR system can be found in Ref. [44].

2.4.2 Few-cycle pulse generation

In some of the experiments presented in Chapter 5, the output of the PULSAR was spectrally broadened and compressed to sub-5 fs pulse duration. The generation of these ultrashort pulses was accomplished using a gas-filled hollow core fiber (HCF) and chirped-mirror setup as described in Ref. [53]. Spectral broadening in HCF's has been widely used in the generation of few-cycle pulses and detailed descriptions can be found in Refs. [54–59].

Briefly, self-phase modulation due to the nonlinear optical Kerr effect induces an intensity-dependent temporal phase that causes a broadening of the spectral content of the pulse [60].

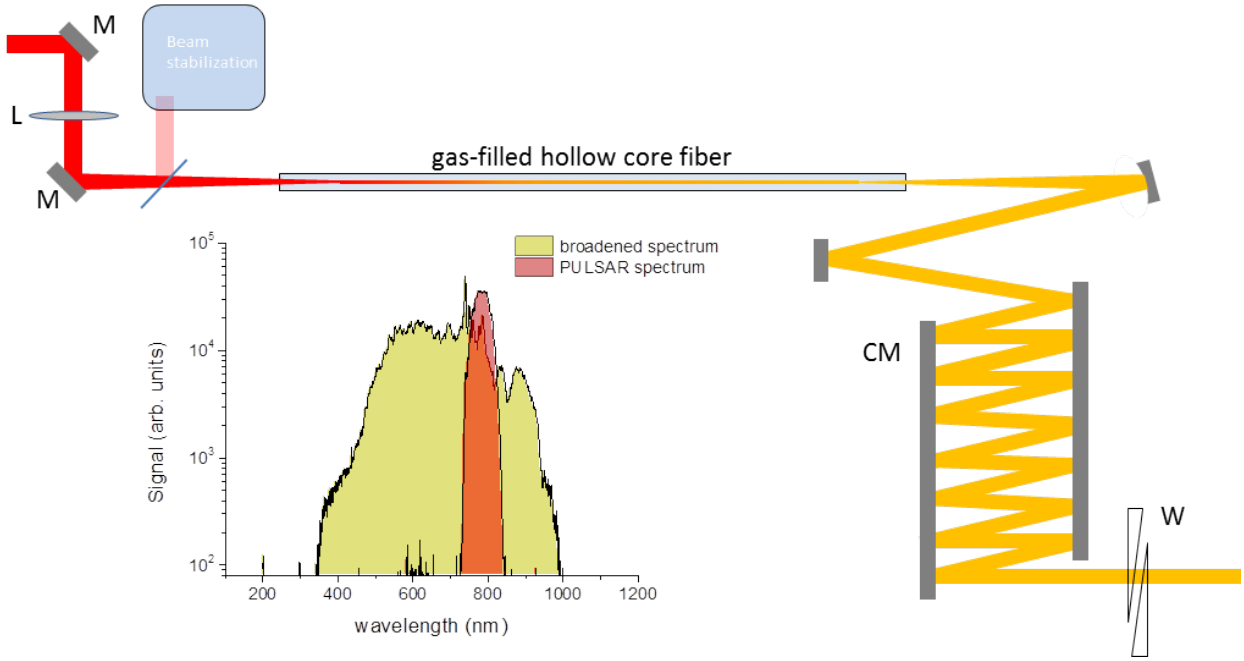

Figure 2.7: Schematic of the HCF spectral-broadening and pulse compression setup. M – motorized flat mirrors controlled by the beam stabilization system; L – a $f = 1.5\,\mathrm{m}$ focusing lens; CM – 7 pairs of chirped mirrors; W – glass wedges to compensate for dispersion. The amplified PULSAR spectrum with 70-nm bandwidth is broadened to over 500-nm bandwidth after passing through the HCF.

Coupling the laser beam into a HCF waveguide provides a long interaction distance over which the spectral broadening can take place. Noble gases, namely argon and neon, are used as a nonlinear medium. Propagation in the fiber causes positive dispersion which is compensated for with negative dispersion provided by multi-layered chirped mirrors [61].

The HCF throughput is very sensitive to the coupling of the laser beam into the fiber. The optimum coupling for a Gaussian beam occurs with a beam diameter of 0.64 times the HCF diameter [62, 63]. The length of the fiber is chosen such that sufficient broadening is achieved with minimum losses in the fiber. The stability of the pointing of the laser beam is very important to the coupling into the fiber. To achieve the high level of stability needed, the pointing of the laser beam is actively locked using a beam-pointing stabilization system from TEM-Messtechnik [64], in which a pair of position-sensitive detectors provide feedback to mirrors controlled by stepper and piezo motors.

In our setup, the laser beam is focused by a $f = 1.5\,\mathrm{m}$ lens into a 250-μm diameter, 1-m

long HCF, as illustrated by Fig. 2.7. The entrance and exit windows of the HCF chamber are oriented at Brewster's angle to maximize transmission. The intensity of the focused beam must be controlled to limit ionization of the gas. As neon has a higher ionization potential than argon, it is used for higher intensity applications. With neon, at the optimal gas pressure of about 1.5 bar, about 1 mJ pulses are broadened with a throughput of almost 50%. With argon-filled fiber at about 0.7 bar, a 0.45 mJ pulse is coupled into the fiber, also resulting in almost 50% throughput. With either gas, the broadened spectrum ranges from about 450 to 1000 nm. Finally, seven pairs of negatively-chirped mirrors compensate for the positive dispersion gained in the fiber as well as the positive dispersion along the path to the experimental apparatus. After the chirped mirrors the pulses are negatively chirped, and glass wedges in front of the experimental setup provide an adjustable amount of positive dispersion to optimize the pulse duration.

2.4.3 Second harmonic generation

The high peak intensity of ultrafast pulses allows one to capitalize on the nonlinear optical properties of materials. Nonlinear frequency conversion makes it possible to create wavelengths that are not directly accessible with lasers. Commonly employed frequency conversion processes include sum-frequency generation, difference-frequency generation, parametric amplification, and super-continuum generation [60]. One of the simplest and most commonly utilized is second harmonic generation, also referred to as frequency-doubling, in which light at twice the frequency of the fundamental field is generated through a 2^{nd}-order nonlinear process [60]. The intensity of the second harmonic light is given by

$$I(2\omega) = CI(\omega)^2 \mathrm{sinc}^2(\frac{\Delta kL}{2}),$$

where C depends on properties of the material, L is the length of the medium, and $\Delta k = k_2 - 2k_1$ is the wavevector mismatch between the fundamental and second harmonic fields. Clearly, the intensity of the second harmonic is maximized when Δk is minimized. This is

referred to as the phase-matching condition [60]. The wavevector mismatch may be written equivalently in terms of the index of refraction n and angular frequency frequency ω. The condition for perfect phase matching ($\Delta k = 0$) can be written as

$$n(2\omega) \times 2\omega - 2n(\omega) \times \omega = 0,$$

which yields,

$$n(2\omega) = n(\omega)$$

Perfect phase matching requires that the material's index of refraction is the same at the fundamental and second harmonic frequencies. However, materials in general are dispersive, meaning that the index of refraction increases or decreases as a function of ω. The most common solution for achieving phase matching is to make use of birefringent crystals. Uniaxial birefringent crystals consist of two orthogonal axes, namely the ordinary and extraordinary axes, which have different index of refraction [50]. With correct choice of crystal and alignment, the proper phase matching condition can be realized.

In the work presented in this dissertation, the second harmonic of 790-nm was produced using a beta-barium borate (BBO) crystal. The incident fundamental beam is polarized parallel to the ordinary axis of the crystal with index n_o, and the crystal is aligned at the angle at which an orthogonally polarized second harmonic beam experiences an index of refraction with $n_e(2\omega) = n_o(\omega)$. We used a 250-$\mu$m thick BBO with a cut angle of 29.2° from United Crystals [65]. Thicker BBO's allow for better conversion efficiency, and 250 μm is the greatest length that still provides good phase matching for the entire laser bandwidth.

Alignment of the BBO and polarization of the fundamental beam is important. If the incident beam is not polarized exactly along the ordinary axis, a fraction is projected on the extraordinary axis, which results in two delayed orthogonally polarized pulses. To align the BBO, the polarization of the fundamental field is measured after the BBO to ensure the incident polarization is maintained. Once the BBO axes are aligned, the incidence angle of the beam on the crystal is tuned to optimize the second harmonic generation. The phase

matching of different frequencies is very sensitive to the incidence angle, which is optimized by looking at the second harmonic spectrum. The second harmonic and remaining fundamental light are colinear, and a dichroic filter is used to dump the fundamental beam. Typically, the second harmonic conversion efficiency is about 30%, however better conversion can be achieved by reducing the laser beam size using a telescope and thus increasing the intensity.

2.4.4 Laser characterization and diagnostics

In strong-field laser studies, many processes are sensitive to various laser pulse parameters, and therefore knowledge of the spatial and temporal characteristics of the laser pulse is important. In the work presented in this dissertation, a few different tools are used to characterize the laser. The temporal electric field is determined using frequency-resolved optical gating (FROG), and two different types of FROG are discussed in Sec. 2.4.4. The pulse duration of the broadband few-cycle pulses is characterized through carrier-envelope phase tagging which is described in Sec. 2.4.5. The central wavelength and bandwidth of the laser is also determined by measuring the spectrum using a fiber-optic spectrometer from Ocean Optics [66]. The average power of the laser is measured with a Coherent FieldMax power meter [67], and fluctuations in the pulse energy are measured shot-to-shot by reflecting a small fraction of the laser beam on to a photodiode as described in Appendix B.

In the ion-beam experiments, the laser focusing element is located outside the vacuum system, so the focused beam can be redirected onto a charge-coupled device (CCD) camera, from which the area of the laser spot is obtained by fitting a Gaussian profile to the image. The peak intensity of the laser is given by

$$I_0 = 1.88\frac{\varepsilon}{A\tau},$$

where ε is the pulse energy, A the area, and τ the pulse duration (FWHM in intensity) [47]. The analysis of the CCD images utilizes an automated MATLAB code that I wrote which processes the images and performs curve fitting to determine the area. This method is

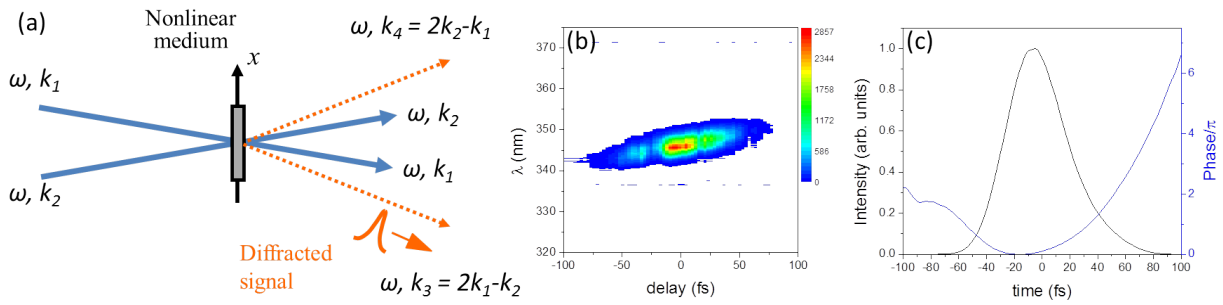

Figure 2.8: (a) Schematic drawing of the self-diffraction process used in the SD-FROG. (b) The spectrogram of the self-diffraction signal is used to reconstruct the electric field of the laser pulse. (c) Reconstructed intensity (black) and phase (blue) of the electric field.

detailed further in Appendix A.

Pulse characterization using FROG

SHG-FROG

Full characterization of the time-dependent electric field of the laser pulse is performed using frequency-resolved optical gating (FROG) [68]. The FROG technique utilizes the spectral information resulting from some process driven by two delayed replicas of the laser pulse, for example second- or third-harmonic generation. The delay-dependent spectrum, or spectrogram, shown in Fig. 2.8(b) is used to reconstruct the electric field of the laser pulse through an iterative phase retrieval algorithm [68].

Several FROG schemes exist that produce different signals. The FROG used to measure the 790-nm PULSAR pulses is a commercial second-harmonic FROG (SHG-FROG) from Mesa Photonics [69]. In SHG-FROG, the two delayed pulse replicas generate a second harmonic signal in a BBO crystal, and the spectrum of the second harmonic signal is measured as a function of the delay between the pulses, from which the electric field of the driving pulse is reconstructed.

SD-FROG

A home-built SD-FROG that I helped construct was used to measure second harmonic pulses. Since SHG crystals for 400-nm fundamental wavelengths are not common, another nonlinear process, self-diffraction, is exploited to generate a signal. In self-diffraction (SD),

two pulse replicas are crossed in a nonlinear medium at a shallow angle. The interference of the electric fields results in a periodic intensity distribution which causes a periodic nonlinear response in the medium that resembles a diffraction grating, and the first order diffracted beam provides a signal, as shown schematically in Fig. 2.8(a). Because the beams intersect at an angle, self-diffraction is not a phase-matched process, so high intensity is required to generate a signal.

In our setup, a "D"-shaped mirror splits the beam in two, and a 100-μm thick quartz plate is used as the nonlinear medium. The delay between the pulse replicas is controlled by a delay stage with a Thorlabs piezo-actuator which limits the delay range to about 150 fs. The self-diffraction signal is measured by a spectrometer integrated with a Labview code that also controls the delay stage. This home-built setup can easily be converted to other FROG configurations, such as SHG-FROG or transient-grating FROG. Further details regarding this FROG can be found in Appendix F.

2.4.5 Carrier-envelope phase tagging

An especially important property of few-cycle laser pulses is the carrier-envelope phase (CEP). For the electric field of an ultrashort laser pulse given by

$$E(t) = E_0(t)cos(\omega t + \varphi),$$

the CEP, φ, describes the offset between the peak of the carrier wave and the pulse envelope, $E_0(t)$, as depicted in Fig. 2.9(a). The CEP of ultrashort pulses has been shown to be a sensitive control knob for several physical process [7, 70–81], and several schemes have been developed to lock the laser CEP [70, 82–87]. While CEP-locking is useful for controlling processes, its implementation is often quite complicated. An alternative approach, especially useful for long measurements, involves measuring the random CEP of a free-running laser for every laser shot and correlating the measured CEP with each measured event. Such CEP-tagging measurements have been accomplished using, for example, a stereo-ATI phase

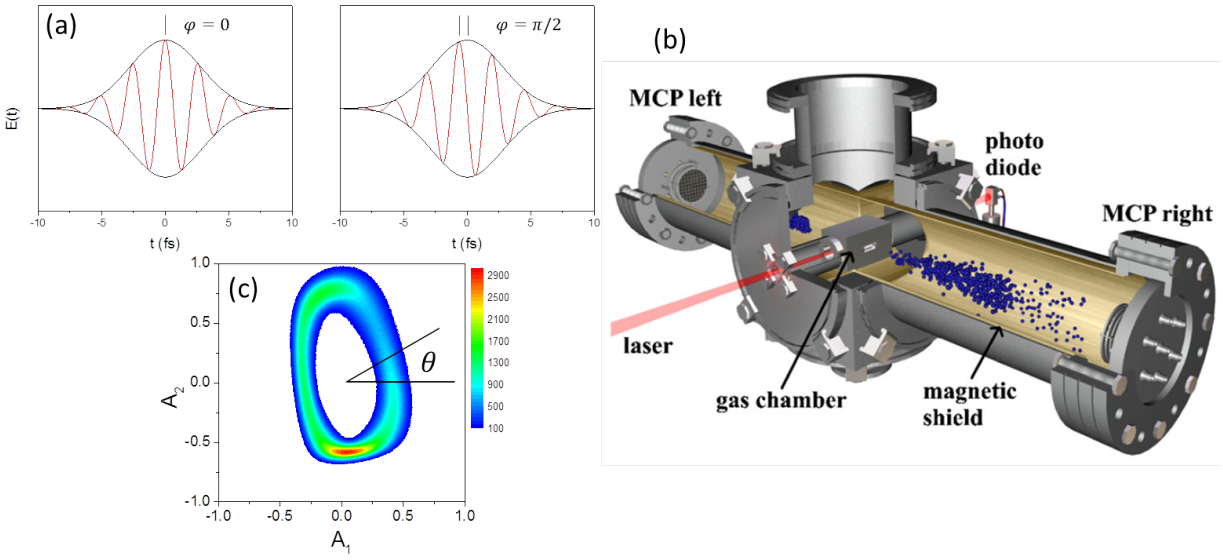

Figure 2.9: (a) Illustration of the electric field of ultrashort laser pulses with CEP $\varphi = 0$ and $\pi/2$. (b) Schematic of a stereo-ATI phasemeter adapted from Ref. [91]. (c) Parametric asymmetry plot, also called "phase potato", from the CEP-dependence measurements in Chap. 5. The angle θ is directly related to the CEP, φ.

meter as described in Refs. [53, 88–91].

The setup we use, implemented by Nora Kling [53], allows for shot-to-shot determination of the CEP in parallel to an event mode measurement. Briefly, the phase meter consists of two MCP detectors facing one another on either side of a gas cell containing xenon, as shown in Fig. 2.9(b). The energy distributions of photoelectrons emitted in each direction along the laser polarization are obtained for every laser shot. An asymmetry in the high-energy photoelectron yield between the two detectors has a periodic dependence on φ, given explicitly by $\mathcal{A} \simeq \frac{N_L(E)-N_R(E)}{N_L(E)+N_R(E)} \approxeq \sin(\varphi + \varphi_0)$, where $N_{L,R}(E)$ are the integrated electron yields at a specific energy on each of the detectors. By comparing the asymmetry in two energy regions, the parametric asymmetry plot shown in Fig. 2.9(c) is created. The angle θ defined in Fig. 2.9(c) is directly related to the CEP, and the conversion from θ to φ is accomplished by taking advantage of the randomness of the CEP of a free-running laser, as described in Refs. [53, 89, 90].

The phase meter was used to tag the CEP of every laser shot for the studies of D* emission from D_2 presented in Chapter 5.

Chapter 3

Fragmentation of Negatively-Charged Molecules

3.1 Scope

This chapter highlights the first experiments we performed utilizing the anion beams and the imaging technique described in Chap. 2. A brief overview of previous studies involving molecular anions is given in Sec. 3.2. Our studies of dissociation and photodetachment of F_2^- are presented in Sec. 3.3. Both 400-nm and 800-nm laser pulses are used to identify dissociation pathways and evaluate the vibrational population of F_2^-, and the role of dissociation in photodetachment is also explored. Two experiments involving LiO^- are presented in Sec. 3.4. In the first, multiphoton dissociation is used to determine the dissociation energy of the LiO^- ground state. In the second, a scheme to study the time-resolved decay by autodetachment of excited anions is presented. In Sec. 3.5, preliminary results of a few other molecular anions are briefly described, followed by a summary in Sec. 3.6.

3.2 Background and motivation

Negative ions have long been used as tools to study molecular dynamics [33, 92–95]. For example, detachment of the loosely bound "extra" electron initiates dynamics in the resulting neutral molecule that can then be probed [33, 92, 95]. Studying the dynamics of processes in molecular anions themselves is also interesting. Measurements of photodetachment of a dissociating molecular anion, for instance, has provided valuable information about the photodetachment process [96].

Molecular anions are often unstable, with electronic states lying in the continuum of the neutral molecule that quickly decay by autodetachment of the quasi-bound electron [33, 97–99]. These transient molecular anion states were the subject of several theoretical and experimental studies of collisions between gas-phase molecules and low energy electrons [97, 100–103]. In the case of electronically stable anion states, often times the electron detachment energy is smaller than the dissociation energy. Therefore, excitation can result in competition between electron autodetachment and dissociation [98].

Photoelectron spectra have provided valuable information about the structure of negative ions and neutral parent molecules [104–108]. Furthermore, time-resolved studies and coincidence measurements of photoelectrons and neutral molecular fragments have led to insight into dynamics of metastable molecular anions [32, 96, 98].

Studies of the interaction between ultrashort, intense laser pulses and molecular anions have been fairly rare (a few recent examples include Refs. [29, 30, 109]). Our aim is to extend strong-field molecular physics to the case of molecular anions by using strong laser fields to measure and control dissociation and electron detachment processes. Following the development of the capability to perform such measurements, as described in Chapter 2, the studies presented in the following sections are our first measurements of molecular-anion fragmentation using our powerful coincidence 3D momentum imaging technique.

3.3 Strong Field Fragmentation of F_2^-

3.3.1 Introduction

The F_2^- molecular anion was the first choice to test the application of our coincidence 3D momentum imaging technique to molecular anion fragmentation for a few reasons. The energy required to detach the "extra" electron in the majority of molecular anions is very small, a fraction of an eV in many cases, which is typically smaller than the energy required to dissociate the molecule. As a result, the absorption of photons predominantly leads to photodetachment into the neutral molecule or neutral fragments while dissociation into a pair anion and neutral fragments is extremely weak. However, in the case of halogen molecular anions like F_2^-, the strong electronegativity of the constituent atoms makes for relatively strongly bound diatomic anions. So, unlike most molecular anions, the ground state of F_2^- is well-separated by over 3 eV from the neutral ground state, as shown in Fig. 3.1. The relatively large electron detachment energy also means that there are multiple excited states that are electronically stable, unlike most anions which often have no stable excited states.

In Table 3.1, the final products of dissociation and photodetachment that we are interested in studying are listed. Our setup allows measurement of all these products simultaneously, providing a thorough test of our imaging techniques for fragmentation of molecular anions. The existence of only a few electronically stable repulsive states simplifies the interpretation of dissociation measurements, making F_2^- an ideal candidate for testing our imaging of dissociation of negative ions. We aim to identify the dissociation pathways and study their behavior for different laser pulse parameters, including wavelength, pulse duration, and intensity. Additionally, the dissociation measurement is used to evaluate the initial vibrational population of the F_2^- beam.

$F_2^- + n\omega \rightarrow$	$F + F^-$	photodissociation
	$F + F + e^-$	dissociative photodetachment
	$F_2 + e^-$	(nondissociative) photodetachment

Table 3.1: F_2^- fragmentation mechanisms.

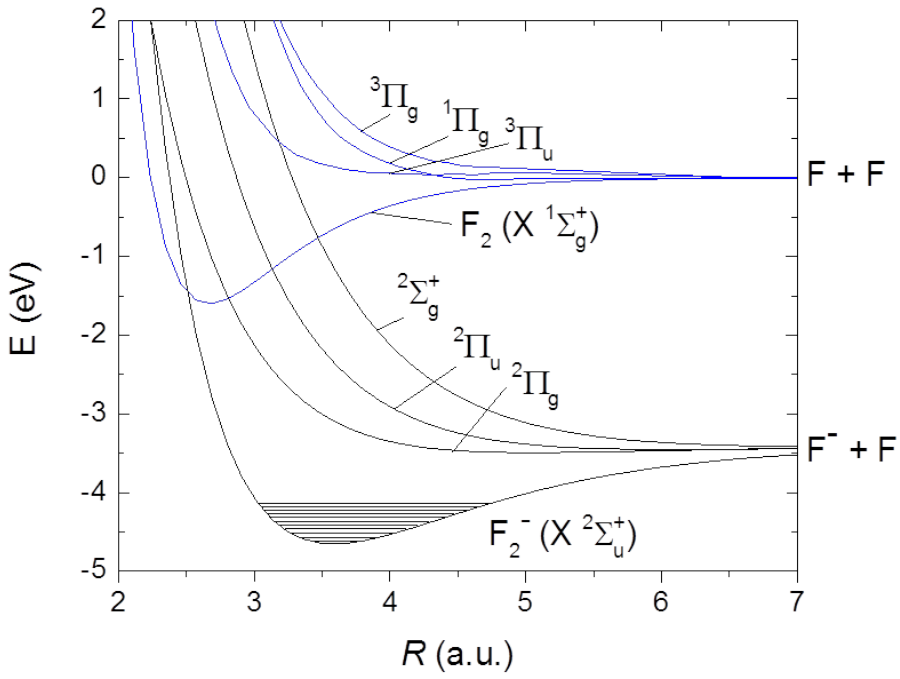

Figure 3.1: F_2^- (black) and F_2 (blue) potential energy curves adapted from Refs. [110, 111]. The horizontal lines in the $X\,^2\Sigma_u^+$ potential well indicate the energies of the ten lowest vibrational states of F_2^- calculated using a phase-amplitude method [112].

Photodetachment of F_2^- was previously studied [29] by measuring photoelectrons, and it was suggested that a sequential process, i.e. dissociation to F^-+F followed by photodetachment of the F^- fragment, competes with other processes. We provide complementary information to this previous work by measuring the heavy fragments and comparing photodetachment to F+F and F_2 final products and by exploring the role of dissociation in photodetachment resulting in F+F fragments.

3.3.2 Experimental details

The F_2^- beam was generated from a LiF target in a sputter source (Sec. 2.2.2), then accelerated to 6 keV and selected, steered, and collimated as described in Sec. 2.2.3. Because the process by which F_2^- is produced from LiF molecules is unknown, the population of excited rotational and vibrational states in the F_2^- beam was not known; however the KER distri-

bution resulting from photodissociation into F^- + F was used to evaluate the vibrational population, which was found to span a broad range of vibrational levels, as described in Sec. 3.3.3. The pulses of the PULSAR laser were optimized to the shortest duration by adjusting the compressor gratings and observing the supercontinuum generated by focusing the beam in air just in front of the experimental apparatus, resulting in $\lesssim$25-fs pulses. The second harmonic ($\sim$400-nm) beam was generated in a BBO crystal (see Sec. 2.4.3), with pulse durations estimated to be about 60 fs by evaluating the dispersion along the beam path from the BBO to the interaction region. The laser power was controlled by a half-wave plate followed by a polarizing beamsplitter cube. The polarization was aligned parallel to the spectrometer axis and the laser beam was focused onto the ion beam by a f=203 mm off-axis parabolic mirror. The imaging spectrometer and deflector separate ion and neutral fragments from each other by time and position, and the coincidence measurement of the fragments' time and position information allows the 3D momentum of each fragment to be evaluated (as described in Sec. 2.3). The use of the imaging deflector also facilitated measurement of the yield of neutral F_2 molecules produced by the laser interaction as well as fragmentation with low kinetic energy release [12, 28].

3.3.3 Results and Discussion

Dissociation

Results of dissociation of F_2^- by 400-nm, 60-fs pulses are shown in Fig. 3.2(a-c) for a variety of peak laser intensities. The kinetic energy release (KER) is evaluated from the momentum of the fragments in their center-of-mass frame. The angle θ is defined as the angle between the momentum of the F^- fragment and the laser polarization direction, as depicted in the cartoon in Fig. 3.2(d). Since θ is a polar angle, we plot $\cos\theta$, as in this representation an isotropic spherical distribution will be uniform in $\cos\theta$.

In Fig. 3.2(a), the KER distribution is shown for peak intensities ranging from 2×10^{11} to 5×10^{14} W/cm^2, and the distributions are scaled to match in total area. The distribution centered around just over 2 eV is consistent with a one-photon transition from the ground

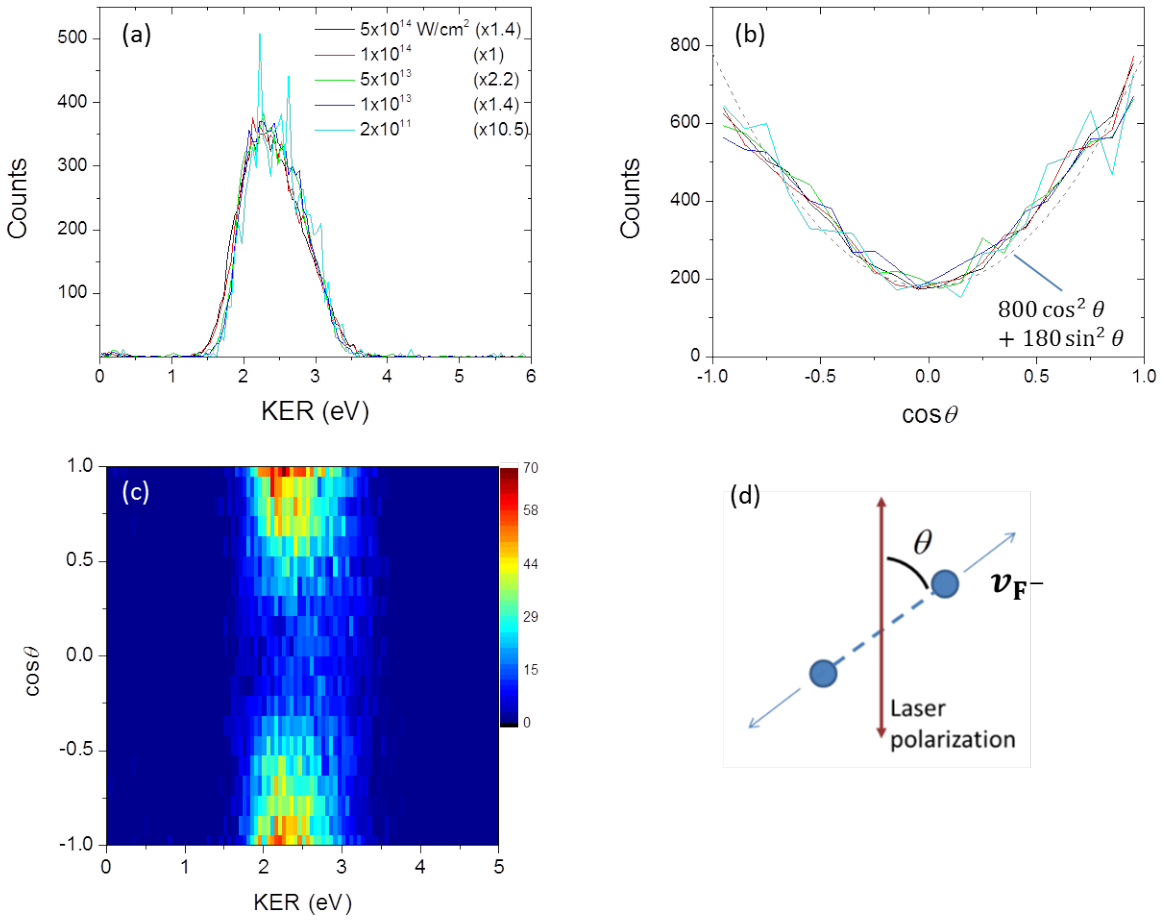

Figure 3.2: The (a) KER and (b) $\cos\theta$ distributions for dissociation of F_2^- into F^-+F by 60-fs, 400-nm pulses, for a variety of peak intensities. The $A\cos^2\theta + B\sin^2\theta$ fit of the angular distribution provides an estimate of the dissociation yield due to parallel and perpendicular transitions (see text). (c) 2D map of the F^-+F yield as a function of KER and $\cos\theta$. (d) definition of the angle θ.

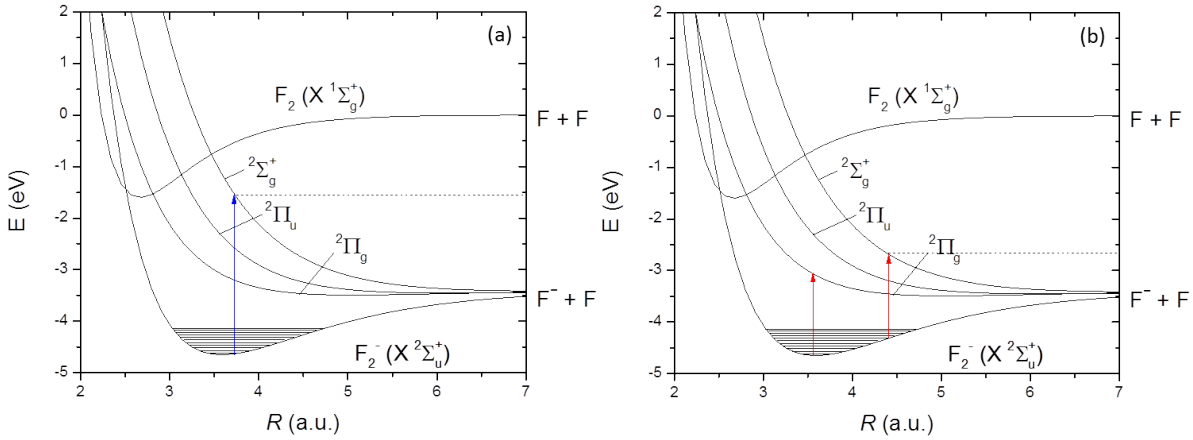

Figure 3.3: F_2^- potential energy curves (adapted from Ref. [110]). (a) The length of the blue arrow corresponds to the photon energy of 400-nm light (3.1 eV). (b) The length of the red arrows corresponds to the photon energy of 800-nm light (1.55 eV). The arrows depict the dominant dissociation pathways observed in the experiment.

electronic state of F_2^- to one of the three excited electronic states [see Fig. 3.3(a)]. One-photon transitions from the $X\,^2\Sigma_u^+$ ground state to the $^2\Pi_u$ state are parity forbidden, so that channel can be ruled out, leaving two possible dissociation pathways, namely $X\,^2\Sigma_u^+ \rightarrow {}^2\Sigma_g^+$ and $X\,^2\Sigma_u^+ \rightarrow {}^2\Pi_g$. These two pathways converge to the same F^-+F dissociation limit and overlap in KER ranging from 1.8 to 3.1 eV. So, the angular distributions are used to identify their relative contributions to the total dissociation yield.

The angular distribution of a parallel ($\Sigma \rightarrow \Sigma$) one-photon transition can be expressed as $P(\theta) \propto \cos^2\theta$, while the perpendicular ($\Sigma \rightarrow \Pi$) transition can be expressed as $P(\theta) \propto \sin^2\theta$ [113–115]. A fit of $A\cos^2\theta + B\sin^2\theta$ to the angular distributions shown in Fig. 3.2(b) indicate that the dominant contribution is due to the parallel transition. Using the fit coefficients, the branching ratio for the parallel transition, $A/(A+B) = 0.81 \pm 0.05$, shows that dissociation predominantly proceeds through transitions to the $^2\Sigma_g^+$ state. The higher yield due to the parallel transition can be explained qualitatively in terms of curve crossings in a dressed picture, which will be discussed in more detail later on.

The KER and angular distributions look nearly identical over the entire peak intensity range spanning over three orders of magnitude, indicating that multiphoton transitions

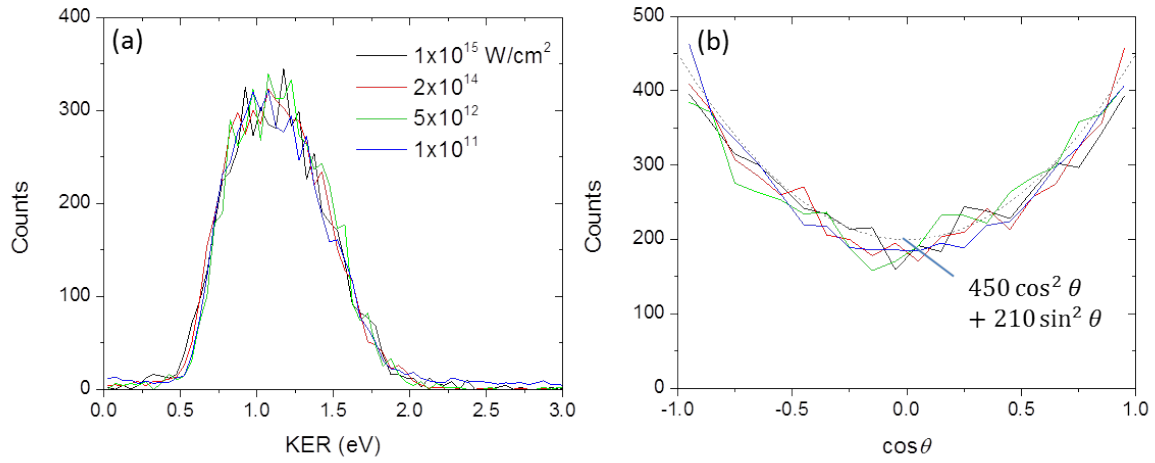

Figure 3.4: (a) KER and (b) $\cos\theta$ distributions for dissociation of F_2^- into F^-+F by 25-fs, 800-nm pulses, for a variety of peak intensities.

do not play an important role. For example, if two-photon absorption to the $^2\Pi_u$ state contributed at high intensity, we would expect to see a $\sin^4\theta$ contribution to the angular distribution and KER between 5 and 6 eV at higher intensities. Globally, the distributions seem to be insensitive to the intensity, further suggesting that one-photon absorption dominates.

The KER and angular distributions for dissociation by 25-fs, 800-nm pulses are shown in Fig. 3.4. Similar to the results using the second harmonic pulses, the KER and angular distributions change very little over the intensity range from 1×10^{11} to 1×10^{15} W/cm^2. This behavior, again, indicates that predominantly one-photon transitions are involved. The KER peaked at just over 1 eV, as shown in Fig. 3.4(a), is consistent with one-photon absorption. Furthermore, the angular distribution, shown in Fig. 3.4(b), indicates one-photon parallel and perpendicular contributions from transitions to the $^2\Sigma_g^+$ and $^2\Pi_g$ states, respectively. The branching ratio to the perpendicular pathway, based on the $A\cos^2\theta + B\sin^2\theta$ fit to the angular distribution, is 0.32 ± 0.03, which is about a factor of two greater than it was with 400-nm pulses.

Note that even though the peak laser intensity reaches over 10^{15} W/cm^2, this intensity accounts for only a very small fraction of the interaction volume. Lower intensities are overemphasized due to the overlap of the entire intensity profile with the ion beam. To more

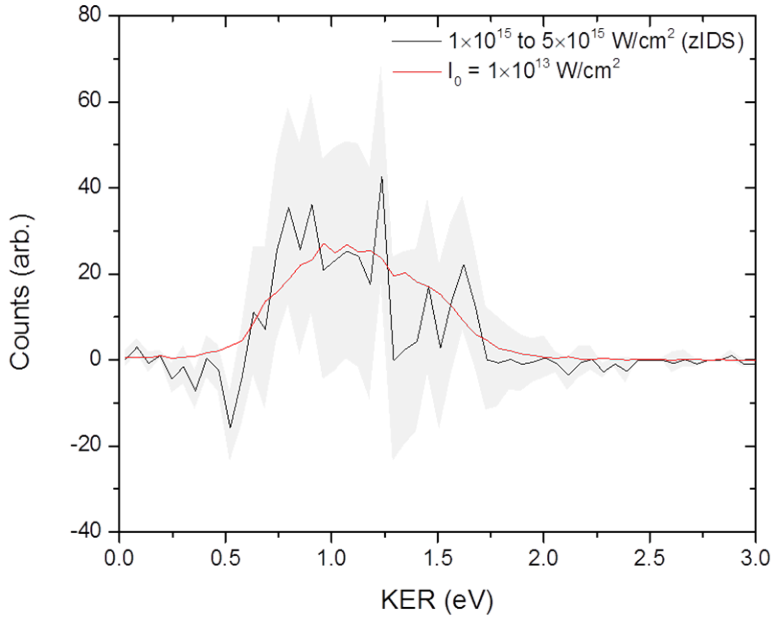

Figure 3.5: zIDS KER distribution for dissociation of F_2^- by 25-fs, 800-nm pulses with intensity ranging from 1×10^{15} to $5 \times 10^{15}\,\mathrm{W/cm^2}$. The distributions are normalized to match the integrated yield and the shaded area represents the statistical uncertainty.

closely look for high-intensity effects such as above threshold dissociation, we employ the z-scanning intensity difference spectra described by Sayler *et al.* [116]. The KER spectra for measurements at 1×10^{15} and $5 \times 10^{15}\,\mathrm{W/cm^2}$ are subtracted from one another and the differences in the laser focal volume are accounted for to obtain the KER spectrum for the intensity range from 1×10^{15} to $5{\times}10^{15}\,\mathrm{W/cm^2}$, shown in Fig. 3.5. While the statistics are too poor for this intensity slice to observe any small differences caused by high intensity, we can clearly see that there is no evidence of multiphoton absorption, as two-photon absorption would result in KER above 2 eV.

It is interesting that we do not observe any signatures of multiphoton dissociation even at very high intensities. There are a few plausible explanations for our observation of predominantly single-photon photodissociation at intensities up to $5 \times 10^{15}\,\mathrm{W/cm^2}$. Absorption of two 800-nm photons can result in photodetachment to $F_2 + e^-$, and absorption of three photons promotes the anion above the detachment threshold at all internuclear distances, so

it is possible that photodetachment is depleting any multiphoton dissociation. Also, keep in mind that two-photon absorption is really a *net*-2-photon process (for example, absorption of three photons and emission of one photon). Any such process that involves absorption of three or more photons would certainly compete with photodetachment or autodetachment.

The difference in angular distributions between the 400- and 800-nm pulses, namely the larger fraction of perpendicular transitions in the latter, can be understood using the help of light-dressed Floquet potentials [117]. In the Floquet picture, the Born-Oppenheimer potentials are dressed by the number of absorbed or emitted photons. For example, the $^2\Sigma_g^+$ state with one absorbed photon is denoted $^2\Sigma_g^+ - 1\omega$, where ω is the photon energy. The one-photon transition from the X $^2\Sigma_u^+$ state to the $^2\Sigma_g^+$ state is described by the coupling between the X $^2\Sigma_u^+ - 0\omega$ and $^2\Sigma_g^+ - 1\omega$ states, and transitions are most likely where the curves cross. The diabatic Floquet potentials for 400-nm and 800-nm photons are shown in Fig. 3.6. In the case of 400-nm pulses, coupling of the X $^2\Sigma_u^+ - 0\omega$ and $^2\Sigma_g^+ - 1\omega$ states are most likely at the crossing near the lowest vibrational level. Transitions from higher vibrational states are energetically allowed, but with lower probability than from states nearer to the crossing. There is no crossing with the $^2\Pi_g - 1\omega$, so while transitions from all vibrational states are also energetically allowed, they are expected to be weaker.

With 800-nm photons, the $^2\Sigma_g^+ - 1\omega$ and $^2\Pi_g - 1\omega$ curves both cross the X $^2\Sigma_u^+ - 0\omega$, but at different locations. The $^2\Sigma_g^+ - 1\omega$ crossing is around the $\nu = 8$ vibrational level and results in KER of about 0.8 eV, and therefore the parallel component is expected to be strongest around 0.8 eV. On the other hand, the $^2\Pi_g - 1\omega$ crossing is near the lowest vibrational level, so the perpendicular component is expected to be strongest at KER around 0.5 eV. Transitions from higher vibrational states contributing to higher KER are allowed, but are expected to be relatively weaker than transitions from vibrational levels near the crossings. In contrast to the 400-nm case where there is no $^2\Pi_g - 1\omega$ crossing, the existence of this crossing in the 800-nm case implies that the perpendicular pathway should contribute more significantly, which is what we observe. To provide a more quantitative explanation of the branching ratios we observe, the electronic transition dipole moments are needed to compute the dissociation probabilities, and unfortunately these quantities are unknown.

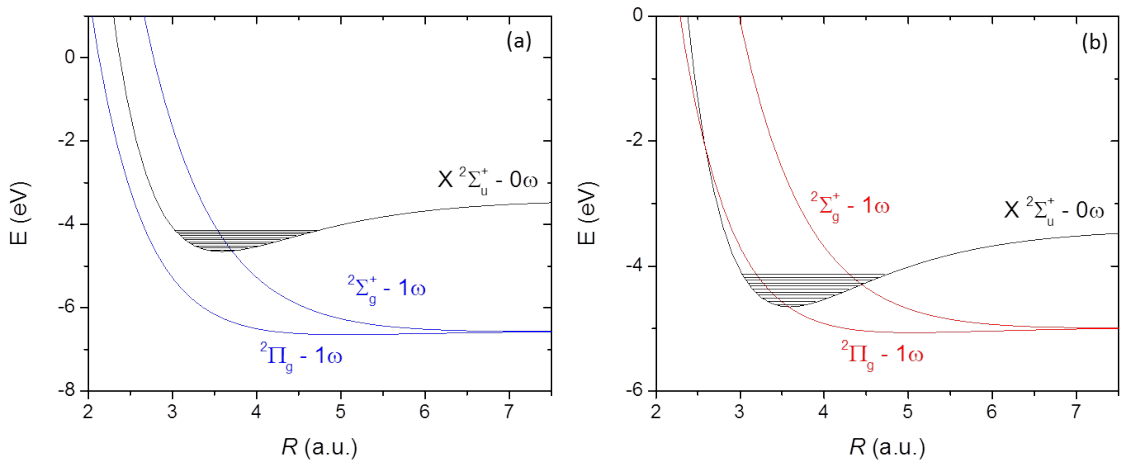

Figure 3.6: Diabatic Floquet potentials for (a) 400-nm photons and (b) 800-nm photons. Laser induced transitions are most likely at the curve crossings.

For 800-nm photons, because the $^2\Sigma_g^+ - 1\omega$ and $^2\Pi_g - 1\omega$ crossings with the X $^2\Sigma_u^+ - 0\omega$ ground state occur at different energies, as shown in Fig. 3.6(b), we expect the branching ratio to change with KER. To test this idea, $A\cos^2\theta + B\sin^2\theta$ is fit to the angular distributions associated with different slices in KER. The branching ratio of the $\sin^2\theta$ coefficient associated with the X $^2\Sigma_u^+ \rightarrow {}^2\Pi_g$ perpendicular transition, namely $B/(A+B)$, is plotted in Fig. 3.7(a) for each KER slice. Based on these results, a few observations can be made. First, the parallel transition dominates in the 0.7–1 eV range, which corresponds to the X $^2\Sigma_u^+ - 0\omega$ and $^2\Sigma_g^+ - 1\omega$ crossing. Lower KER shows slightly more perpendicular character, as expected based on the location of the X $^2\Sigma_u^+ - 0\omega$ and $^2\Pi_g - 1\omega$ crossing. The overall character at low KER is still strongly parallel, though, which may be due to the high intensity of the laser (6×10^{14} W/cm^2) allowing dissociation of vibrational states below the X $^2\Sigma_u^+ - 0\omega$ and $^2\Sigma_g^+ - 1\omega$ crossing. Curiously, at KER above 1 eV the relative perpendicular contribution grows linearly with KER. To understand this behavior, the KER spectra of the two pathways are calculated, as shown in Fig. 3.7(b). The KER spectra of the two transitions come from the next section where we use first order perturbation theory to obtain the transition probabilities and evaluate the vibrational population in the X $^2\Sigma_u^+$ ground state. The branching ratio is determined from the yields in each KER slice. Clearly, the change in the angular distributions

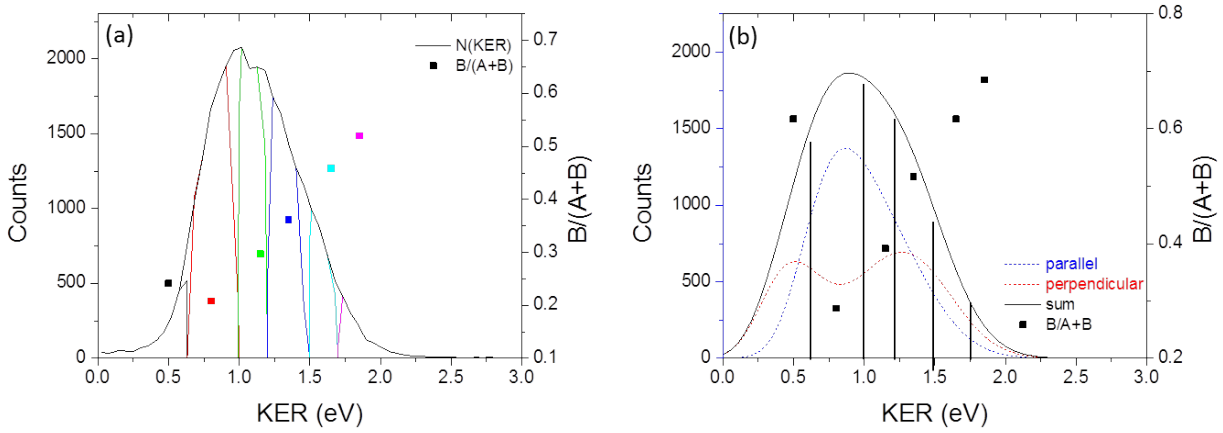

Figure 3.7: (a) Contributions of parallel and perpendicular dissociation pathways for different slices in KER. The relative magnitude of the $\sin^2\theta$ term in the fit of $A\cos^2\theta + B\sin^2\theta$ to the angular distribution indicates the relative contribution due to the perpendicular pathway. (b) Calculated KER spectra for the parallel and perpendicular transitions and the branching ratio, $B/(A+B)$, for each KER slice.

as a function of KER is reproduced by calculations.

Evaluation of the F_2^- vibrational population

As stated before, the process that results in the formation of F_2^- from LiF in the sputter source is unknown, and therefore the initial rovibrational population of the F_2^- beam is unknown. Based on our studies of dissociation of F_2^- described in Sec. 3.3.3, it appears that many vibrational states are populated. This is in contrast to F_2^- beams produced in other types of ion sources. For example, in Refs. [29, 109] F_2^- is produced by electron impact on NF_3 which leads mainly to the lowest vibrational states. In this section, we use first-order perturbation theory and the measured KER spectrum of dissociation of F_2^- to estimate the initial vibrational population of our F_2^- beam.

By energy conservation, the KER upon dissociation from each vibrational level of the initial $X\,^2\Sigma_u^+$ ground state is different, given explicitly by $\mathrm{KER}_\nu = E_\nu - E_\infty + \hbar\omega$. The KER from each level is not single-valued though, and sources of broadening like the laser bandwidth and instrumental broadening will be included later. The KER spectrum of each vibrational level should still be centered around KER_ν, however. Note that this expression

neglects distortions due to the strong field and therefore is only valid for low intensities. But, recall that we observe no significant differences in the KER spectra from peak intensities of 10^{11} up to $10^{15}\,\mathrm{W/cm^2}$, so we neglect any intensity-dependent distortions. Then, we expect that the yield at each KER, KER_ν, depends on the population in each vibrational state and the transition probability. By evaluating the transition probabilities using first order perturbation theory, we can find a vibrational population that produces a KER spectrum that matches the measured KER spectrum, as described below.

Using first-order perturbation theory for photoabsorption, the dissociation probability for a given vibrational level, ν, is given by

$$\frac{dP_\nu}{dE} \propto |D_\nu^{fi}|^2 e^{-(\frac{\omega-\omega_0}{\Delta\omega})^2}, \tag{3.1}$$

where D_ν^{fi} is the dipole transition matrix element, ω_0 is the photon energy, and $\Delta\omega$ is the laser bandwidth. The matrix elements are given by

$$D_\nu^{fi} = \langle F_E^f(R)|d(R)|F_\nu^i(R)\rangle, \tag{3.2}$$

where F_ν^i is the bound nuclear wave function in the initial electronic state, F_E^f is the continuum nuclear wave function in the final electronic state with energy $E = E_\nu + \omega_0$, and $d(R)$ is the transition dipole moment as a function of internuclear distance R. In principle, the total dissociation probability involves summing over all possible final states; however, in Sec. 3.3.3 we found that with 400-nm photons dissociation predominantly proceeds via a parallel transition to the $^2\Sigma_g^+$ state, so we only consider this final electronic state.

It is important to note that rotation of the molecule has been neglected for a few reasons. Determining the rotational population from our measured KER spectrum is out of the question due to our instrumental resolution (about 0.1 eV) being about two orders of magnitude greater than the spacing of rotational levels. We could include rotation, in principle, by adding the $\frac{J(J+1)}{2\mu R^2}$ centrifugal distortion to the potential curves and summing over all allowed transitions; however, we obtain nearly identical vibrational populations starting

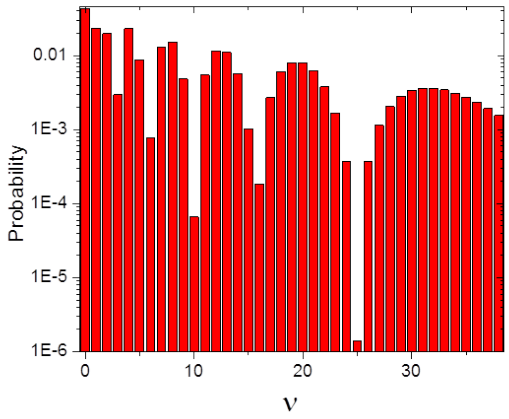

Figure 3.8: Transition probability for $X\,^2\Sigma_u^+ \rightarrow {}^2\Sigma_g^+$ transitions by absorption of one 400-nm photon.

with $J = 0$ or $J = 50$. This suggests that the featureless KER distribution does not allow us to determine the rotational population. So, for simplicity we treat this problem as if the rotational population is in $J = 0$.

The transition dipole moments are unfortunately not available for F_2^-, but we know that for the $\Sigma \rightarrow \Sigma$ transition in question $d(R)$ should scale as $R/2$ (see, for example Ref. [118]). The initial vibrational wave functions are the bound states of the F_2^- electronic ground state, and the final states are continuum wave functions of the $^2\Sigma_g^+$ state, with energy $E = E_\nu + \omega_0$. The bound vibrational wave functions are calculated numerically using a phase-amplitude method [112] with the potential energy curves from Ref. [110]. Then, the matrix elements are evaluated by numerically integrating Eq. 3.2 using the trapezoidal method, specifically, evaluating

$$D_\nu^{\Sigma_g\Sigma_u} = \int F_\nu^{X\,^2\Sigma_u^+}(R)\frac{R}{2}F_{E_{\nu+\omega_0}}^{^2\Sigma_g^+}(R)dR. \tag{3.3}$$

The square of the matrix elements for each vibrational level, which are directly proportional to the transition probabilities, are plotted in Fig. 3.8.

As a side note, the minimum in the matrix elements at $\nu = 25$ can be associated with the well-known Cooper minima effect [119]. The Cooper minima effect originally referred to minima in atomic photoabsorption cross sections due to the dipole moment approaching zero. In this case, the transition amplitude is reduced nearly to zero due to the overlap integral

of the vibrational functions, a vibrational form of a Cooper minimum effect as described in Ref. [9].

After determining the matrix elements, the contribution to the KER due to a specific vibrational state can be written as

$$f_\nu(\mathrm{KER}) = A_\nu \frac{dP_\nu(E)}{dE} = A_\nu |D_\nu^{fi}|^2 e^{-(\frac{\omega-\omega_0}{\sigma})^2}, \tag{3.4}$$

where A_ν is the population in state ν. The transition probability given by Eq. 3.1, where the width, $\Delta\omega$, is the laser bandwidth, is convoluted with our instrumental KER resolution. This results in a total broadening as indicated by the width of the gaussian function, $\sigma = \sqrt{\Delta\omega^2 + \sigma_{inst.}^2}$. The laser spectrum was measured to be approximately gaussian with $\Delta\omega = 60\,\mathrm{meV}$ and the instrumental resolution is estimated to be $\sigma_{inst.} = 0.125 \times \sqrt{\mathrm{KER}}$ [12].

The final KER distribution is a sum over all vibrational states:

$$f(\mathrm{KER}) = \sum_\nu A_\nu |D_\nu^{fi}|^2 e^{-(\frac{\omega-\omega_0}{\sigma})^2}, \tag{3.5}$$

and the set of A_ν coefficients defining the vibrational population is found by fitting this distribution to the measured KER.

The ground state of F_2^- supports 35 vibrational levels, and using 35 parameters to fit the fairly featureless measured KER distribution will not have a unique result. So, we choose to constrain the values of A_ν so that they follow a smooth function. Several functions were tested: flat (constant), linear, Boltzmann-like, to name a few. But, to match our measured KER, we found the function had to peak at an intermediate value of ν. Two functions that fit this criterion are

$$P_\nu = \frac{a_1}{\sqrt{2\pi}a_2} e^{-\frac{1}{2}(\frac{E_\nu - a_3}{a_2})^2} \tag{3.6}$$

$$P_\nu = 2a_1 \sqrt{\frac{E_\nu - a_3}{\pi a_2^3}} e^{-\frac{E_\nu - a_3}{a_2}}, \tag{3.7}$$

which are Gaussian and Maxwell-Boltzmann-like distributions, respectively. Constraining

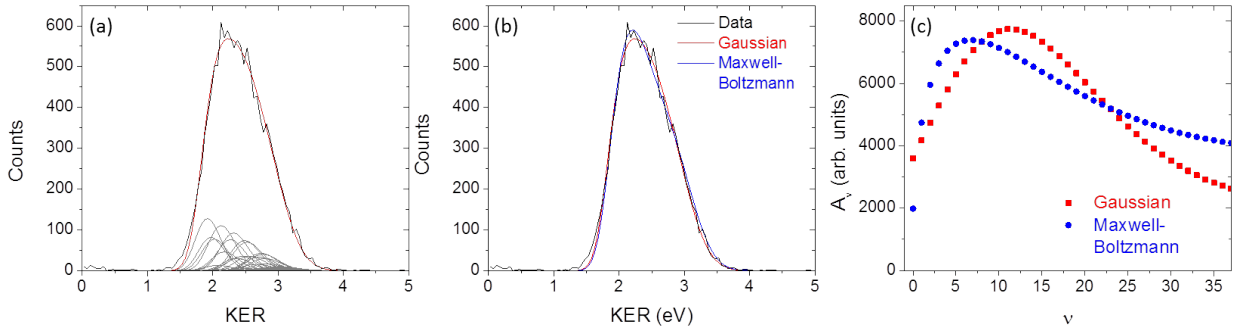

Figure 3.9: Results of fitting the vibrational population. (a) Contributions from each vibrational state in grey for the Gaussian model. The total KER in red provides a good fit to the measured KER in black. (b) Comparison of Gaussian and Maxwell-Boltzmann-like fit functions. (c) A_ν distributions obtained using the Gaussian and Maxwell-Boltzmann-like fit functions.

A$_\nu$ to these distributions reduces the number of fit parameters from 35 to just three: a_1, a_2, and a_3.

The results of the fits are shown in Fig. 3.9. The KER due to the individual vibrational states is shown in Fig. 3.9(a). Note that the individual KER distributions overlap significantly, which explains why there is not much structure in the KER distribution. This also illustrates why allowing the population of each of the 35 states to be an adjustable fit parameter would not be useful – the peaks overlap enough that the entire KER distribution could be fit using only 5–10 of the vibrational levels. Results using the Gaussian and Maxwell-Boltzmann-like fit functions are shown in Fig. 3.9(b-c) and indicate that in either case, the P_ν distribution has a broad maximum in the vicinity of ν=10, and relatively little population occupies the lowest vibrational states, in contrast to the vibrationally cold F_2^- beams used in Refs. [29, 109].

If accurate, the population we obtained should also be able to reproduce the other KER spectrum measured using 800-nm pulses. Recall that unlike the 400-nm case where a single pathway dominates, with 800-nm photons two pathways contribute, a parallel transition to the $^2\Sigma_g^+$ state and a perpendicular transition to the $^2\Pi_g$ state. That is, the total KER

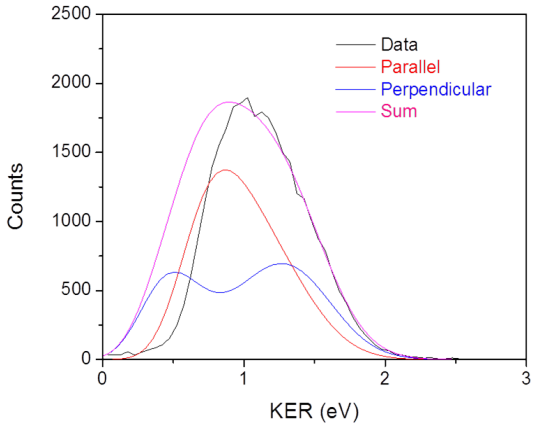

Figure 3.10: Calculated KER spectrum for 800-nm pulses using the population estimated by fitting the KER spectrum for 400-nm pulses.

distribution is given by

$$f_\nu(\text{KER}) = A_\nu(|D_\nu^{\parallel}|^2 + |D_\nu^{\perp}|^2)e^{-(\frac{\omega-\omega_0}{\sigma})^2} \tag{3.8}$$

So, to include both of these pathways, the matrix elements for each transition are needed. Unfortunately, the dipole couplings are not available and we do not know the R-dependence of the perpendicular transition. But, we can still perform a rough estimate by approximating $d(R)$ as a constant for the perpendicular pathway, making the matrix element simply the overlap integral of the bound and continuum nuclear wave functions, i.e employing the Franck-Condon principle [120]. The relative magnitude of the two pathways (i.e. $\frac{|D_\nu^{\parallel}|^2}{|D_\nu^{\perp}|^2}$) becomes an additional fit parameter which we base off the measured branching ratio discussed in Sec. 3.3.3. The resulting KER spectra are plotted in Fig. 3.10. Note that the calculated KER spectrum matches the general shape of the measured KER distribution, but fails to accurately reproduce the low KER portion below 1 eV. This may be due in part to inaccurate matrix elements of the perpendicular transition. Or, it may be evidence that we overestimated the population in the lower vibrational levels. Regardless, even given the crudeness of our estimated population, it is clear that it is not peaked at $\nu = 0$ and that high vibrational levels are populated.

In continuation of this work, we have initiated a collaboration with the group of Daniel Strasser at the Hebrew University of Jerusalem [109], in which we will study the dissociation, photodetachment, and multiple detachment of F_2^- beams employing different initial vibrational populations, specifically a relatively "cold" vibrational population peaked at $\nu = 0$ in their work in contrast with our broad highly excited ("hot") distribution.

Photodetachment

In the photoelectron imaging studies of F_2^- in 1300-nm, 135-fs, 3.4×10^{13} W/cm^2 by Hultgren and Kiyan [29], the measured photoelectron momentum distributions were interpreted as being the result of competition between direct photodetachment, $F_2^- \rightarrow F_2$, and a sequential photodetachment process in which dissociation into F^-+F is followed by photodetachment of the F^- atom. On the other hand, through measurements of the final molecular products, both F_2 and F+F, we aim to provide complementary information about photodetachment pathways and the role dissociation plays in it.

We first compare the relative yields of dissociative, F+F, and nondissociative, F_2, photodetachment of F_2^-. The F+F events are analyzed using the coincidence method described in Sec. 2.3, and the yield of F_2 is determined by gating on the TOF and position of F_2 to separate it from the background. To calculate the branching ratio between F_2 and F+F the yields are corrected for their different detection efficiencies. The "true" number of F+F events, N_{F+F}, is related to the measured number, M_{F+F}, by $M_{F+F} = \varepsilon_F \varepsilon_F N_{F+F}$, where ε_F is the detection efficiency of the F fragment. Similarly, for F_2, $M_{F_2} = \varepsilon_{F_2} N_{F_2}$. The detection efficiency was estimated to be about $30\% \pm 5\%$ using the method described in Ref. [12], and we assume the same efficiency for F and F_2.

The branching ratios of dissociative and nondissociative photodetachment are shown in Fig. 3.11 for 25-fs, 800-nm pulses and 60-fs, 400-nm pulses at a variety of laser intensities. In general, the yield of F_2 is about an order of magnitude lower than that of F+F. Note that for some intensities, there are multiple data points from separate measurements that are very different. This is an illustration of our limited ability to measure the yield of the F_2.

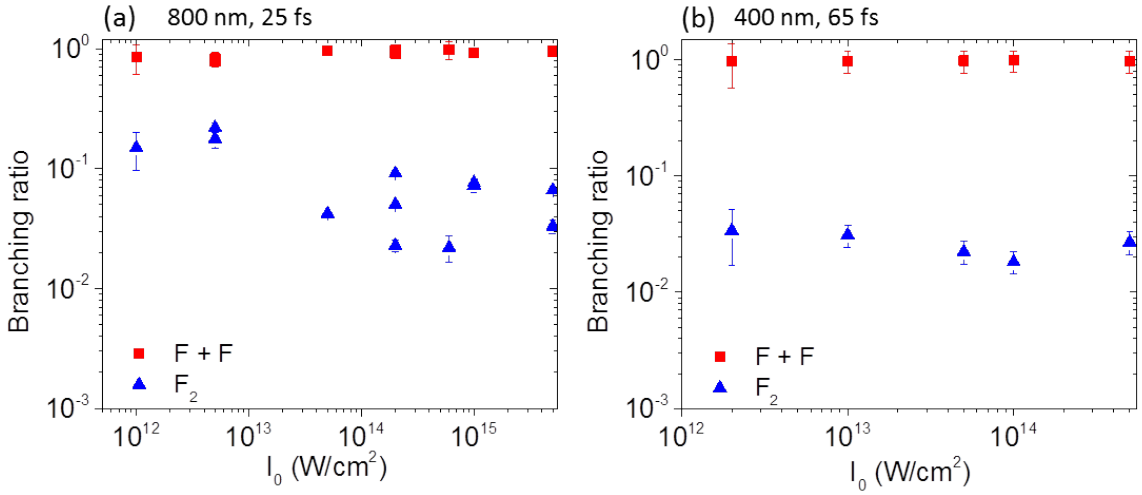

Figure 3.11: Intensity dependence of branching ratios of the final products of photodetachment, F_2 and F+F for (a) 800-nm, 25-fs pulses and (b) 400-nm, 60-fs pulses.

In contrast to the measurement of F+F in coincidence, the F_2 yield is obtained by gating on the time-of-flight and position to reduce the number of random background events. However, the gating does not subtract the background completely, and depending on the measurement this can result in significantly different yields of F_2.

While F_2 is formed by photodetachment to the ground electronic state, there are several competing processes that result in fragmentation into F+F. The sequential photodetachment process suggested in Ref. [29] involves dissociation into F^-+F followed by photodetachment of the F^- atom. In this case, the fragments gain kinetic energy on the repulsive potential before being excited to a relatively flat curve of F_2, so the KER is expected to be similar to the KER upon dissociation into F^-+F. So, to study this mechanism, we compare the KER distributions of F+F with F^-+F.

The KER distributions for fragmentation into F+F are shown for three different sets of laser parameters in Fig. 3.12: 25-fs and 125-fs pulses at 800 nm, as well as 60-fs, 400-nm pulses. The F^-+F KER is overlayed with the F+F KER to indicate regions of KER in which the sequential photodetachment process is expected to contribute. The F+F KER matches the F^-+F KER at the high-KER side of the distributions, but clearly other dissociative photodetachment processes play a role, especially at low KER. For the sequential detachment

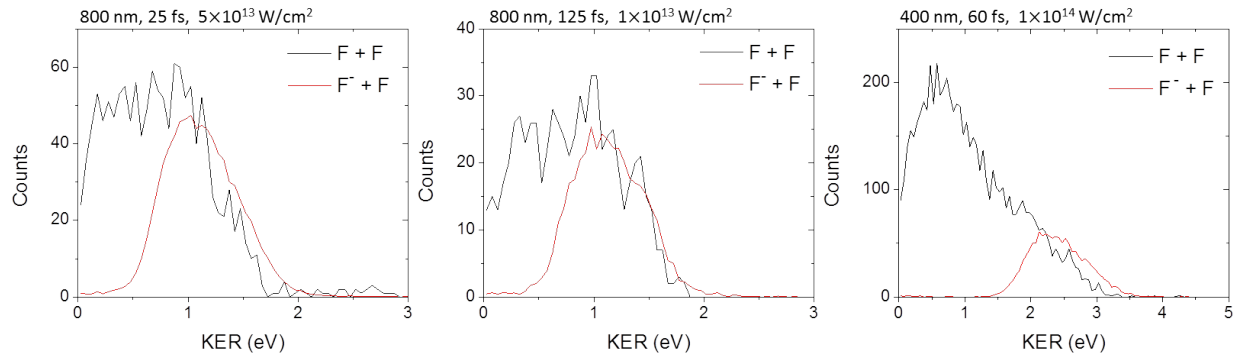

Figure 3.12: Dissociative photodetachment (F+F) KER for three different sets of laser parameters. The corresponding dissociation (F^-+F) KER (red lines) is overlayed to indicate the KER range in which sequential photodetachment contributes.

of the F^- fragment to occur, significant stretching of the molecule must occur, but 25-fs does not provide very much time for the dissociating wave packet to propagate, as shown by the dashed lines in Fig. 3.13(a). By solving the classical equation of motion on the $^2\Sigma_g^+$ curve, we find that the internuclear separation reaches about 6 a.u. in 25-fs, while 125-fs pulses allow for stretching to over 13 a.u. within the FWHM duration of the laser pulse. With 60-fs, 400-nm pulses, dissociating molecules stretch to about 10 a.u. during the pulse. With longer pulses, one might expect an enhancement in the high KER that overlaps with the dissociation KER due to photodetachment of F^- fragments of dissociating molecules. But, the KER spectra for 25- and 125-fs pulses look very similar – any enhancement with longer pulses in the high KER region is weak. In the future, measurements with better statistics may provide a clearer answer to this question.

In addition to the sequential photodetachment process, direct dissociative photodetachment is also possible if the molecule is promoted to the vibrational continuum of F_2, for example, by the absorption of three 800-nm photons or two 400-nm, as shown in Fig. 3.13(b). Absorption of three 800-nm photons from any of the vibrational states of F_2^- results in energy ranging from 0.1 eV to about 1.3 eV above the dissociation limit of F_2. So, the F+F KER extends over this range if the detached electron carries little energy. If the electron acquires any energy the KER is lowered. So, in the KER distributions for 800-nm pulses shown in Fig. 3.12, absorption of three 800-nm photons can be used to explain the low KER, up to

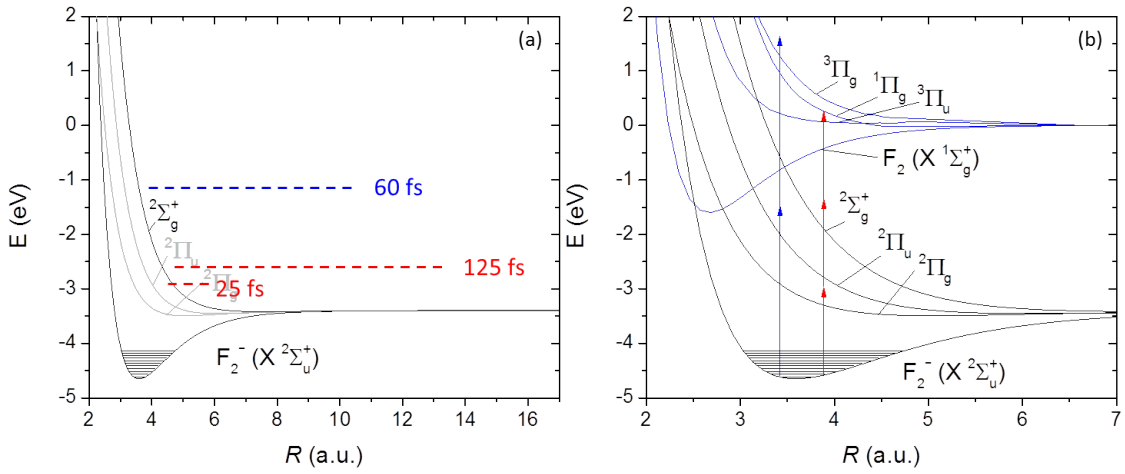

Figure 3.13: (a) Classical estimate of the F^-+F stretching on the $^2\Sigma_g^+$ curve during 25-, 60-, and 125-fs pulses. Dashed lines represent the stretching distance during the pulses. The initial R position is chosen to correspond to the peaks in the measured KER spectra. (b) Direct photodetachment pathways involving the absorption of two 400-nm photons or three 800-nm photons.

about 1.3 eV

By the same logic, absorption of two 400-nm photons results in KER between 1.6 eV and 2.8 eV if the detached electron carries little or no energy. The measured KER peaks at just under 1 eV but also extends down to 0 eV, which by energy conservation implies that the electron must carry up to at least about 1.6 eV. In the photoelectron measurements of Ref. [29], the photoelectron energy distribution peaks at about 1 eV and extends out to almost 5 eV, so our suggestion that the electron takes around 1 eV is in agreement with Ref. [29]. Note though that measurements in Ref. [29] were performed using 1300-nm photons, so our study using 400-nm and 800-nm photons is not a direct comparison. Absorption of one 400-nm photon from high-lying vibrational states is sufficient for photodetachment, but the resulting neutral molecule will be a bound F_2. Also, note that transitions to one of the excited states of F_2^- quickly followed by photodetachment before much stretching occurs may also contribute to low-KER breakup. This is similar to the sequential mechanism discussed previously, however in this case ionization of the dissociating wave packet occurs before the F^- fragment can be treated as a separate atom.

3.3.4 Summary

In summary, we have explored dissociation and photodetachment of F_2^- in intense 400-nm and 800-nm laser fields. We found that dissociation occurs predominantly via one-photon transitions to the $^2\Sigma_g^+$ and $^2\Pi_g$ states. By identifying a dominant dissociation pathway for 400-nm pulses and employing first order perturbation theory, we evaluated the initial vibrational population of the F_2^- beam, and found that the population spans a broad range of vibrational levels and is peaked in the vicinity of ν=10. Our ability to detect neutral molecular fragments allowed us to study dissociative, F+F, and non-dissociative, F_2, photodetachment, providing complementary information to past photoelectron imaging studies of F_2^- [29]. The yield of F+F was about an order of magnitude higher than that of F_2, indicating that fragmentation plays an important role in photodetachment. Sequential photodetachment – dissociation followed by photodetachment of the F^- fragment – was identified by the F+F KER that overlapped with the F^-+F KER, but other competing processes contribute just as much or even more. Direct photodetachment to the second or higher ionization thresholds explains the low KER features.

Building on this work, future studies on F_2^- may include pump-probe measurements in which the role of dissociation followed by photodetachment of the F^- fragment can be studied more closely. Studies utilizing the third harmonic will allow for single-photon photodetachment. Longterm, coincidence measurements of the electrons and heavy fragments will provide a more complete understanding of the photodetachment mechanisms, however detecting electrons from ion beam targets is a challenging task. Bunching the ion beam will help provide additional target density that may enable these measurements in the future.

3.4 Strong field fragmentation of LiO^-

3.4.1 Introduction

The LiO^- molecule is an example of an anion in which the energy required to detach an electron is less than the dissociation energy. In the electronic ground state at the equilibrium

internuclear separation, the energy required to detach the electron is 0.42 eV [121] while the bond dissociation energy (that is, the depth of the potential well from the lowest vibrational level) is about 3 eV (see Sec. 3.4.2). As shown in Fig. 3.14, the lowest electronic states of LiO^- lie just below the neutral LiO threshold. Vibrationally excited LiO^- overlaps in energy with the neutral LiO ground state, and coupling between the electronic and nuclear degrees of freedom can lead to decay to the LiO ground state by autodetachment [122, 123]. Typically, "autodetachment" (and equivalent "autoionization") refers to *electronic* autodetachement, which is the decay of resonances lying higher in energy than the detachment/ionization threshold due to electron-electron correlation [97]. Electronic autodetachment in molecules is possible even when the nuclei are fixed. In other words, it is possible when the electronic energy is greater than the detachment threshold. This process is identical to that in atomic systems [97].

Unlike electronic autodetachment, vibrational autodetachment is unique to molecules. It was described as a breakdown of the Born-Oppenheimer approximation as early as 1966 by R. Stephen Berry [128]. The exchange of energy between the vibrating nuclei and an electron which then gains sufficient energy to leave the molecule is described by the coupling of the initial and final wave functions through the nuclear kinetic energy operator (i.e. the non-adiabatic coupling terms that are neglected in the Born-Oppenheimer approximation). This mechanism is not limited to autodetachment/autoionization; it also results in predissociation of highly excited molecules (for example, H_2 [129]). Vibrational autodetachment, and equivalent vibrational autoionization in neutral and positively charged molecules, has been the topic of many studies of energy redistribution in molecules [33, 122, 123, 130–133].

In the case of LiO^-, the electronic energy is below the electron detachment threshold at all internuclear distances (i.e. the potential curves of the anion do not cross the curves of neutral LiO), but nuclear motion can bring the total energy of the system above the detachment threshold, in which case decay to $LiO + e^-$ by vibrational autodetachment may occur.

In studying the fragmentation of LiO^- or anions with similar electronic structure, the overlap between the anion and neutral potential wells results in competition between disso-

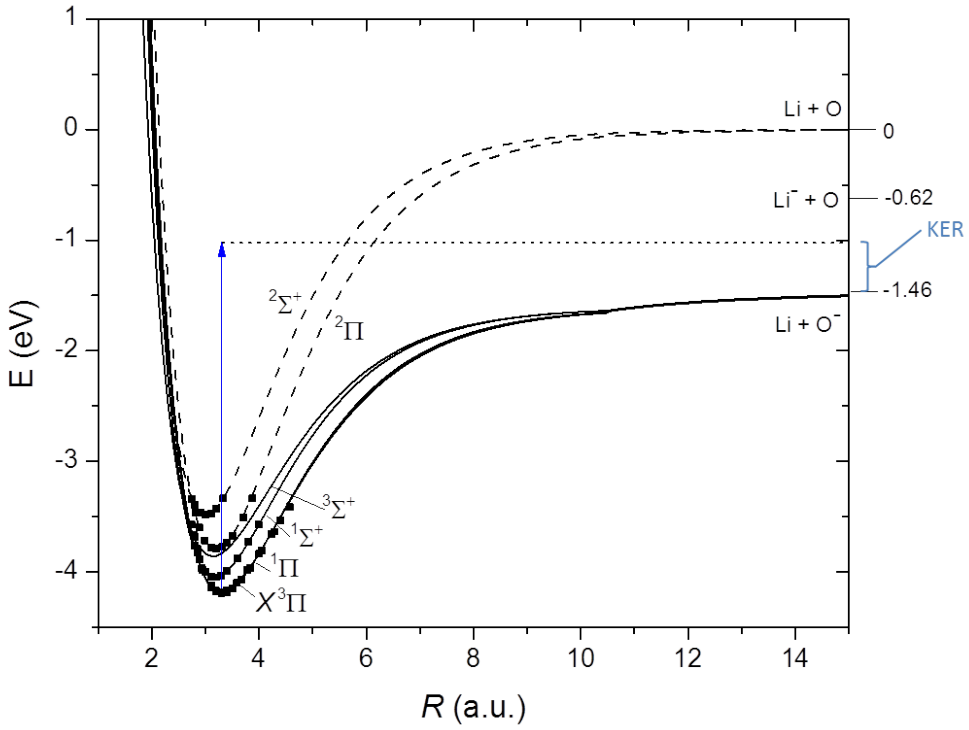

Figure 3.14: Potential energy curves of LiO^- based on the calculations by Bauschlicher *et al.* [124] spanning a bond-length range extending from 2.8 to 4.4 a.u. The calculated data points are shown as small squares, while the lines are Morse potential fits to these points and the dissociation limits [125, 126]. The calculated value of potential depth, D_0, of LiO was taken from Ref. [127]. The KER upon photodisoociation by the absorption of one 395-nm photon, depicted by the blue arrow, can be used to determine D_0 (see text).

$LiO^- + \omega \rightarrow$	$LiO + e^-$	photodetachment
	LiO^-(vib. excited) $\rightarrow LiO + e^-$	autodetachement
	$Li + O^-$	dissociation

Table 3.2: LiO^- fragmentation mechanisms.

ciation and autodetachment. In the case of LiO^-, the absorption of a single 395-nm photon can result in the competition between photodetachement, autodetachment, and dissociation, as shown in Table 3.2. This leads to some interesting questions: How do dissociation and autodetachment rates compare? What is the lifetime of the anion with respect to autodetachment (and how can it be measured)? How do autodetachment rates compare between anions (for example, LiO^- and LiH^-)?

Using a LiO^- beam, we aim to begin working towards answering some of these questions. The first task is to measure the fragmentation of LiO^-. Results of dissociation into $Li+O^-$ fragments by 395-nm and 790-nm pulses are presented below. While studying the pathways that lead to fragmentation, we were able to provide new information regarding the dissociation energy of the LiO^- ground state, as shown in Sec. 3.4.2. Preliminary work toward studying autodetachment of LiO^- is discussed in Sec. 3.4.3. A pump-probe scheme for resolving the autodetachment lifetimes is presented, as well as some preliminary results that suggest a lifetime on the order of a few hundred femtoseconds.

3.4.2 Employing Resonance-Enhanced Multiphoton Dissociation for measuring the dissociation energy of LiO^-

Introduction

The structure of molecules is the foundation upon which molecular sciences are built. The quest to determine the fundamental structure parameters of a molecule, such as the bond length, vibration and rotation constants, and dissociation energy, D_0, have been pursued by theorists and experimentalists for decades. The dissociation energy, for example, tells us how strongly bound a molecule is, i.e. how much energy it takes to dissociate it from

the ground state into its constituents (also in their ground states). Given its importance, a multitude of methods have been developed and applied through the years to determine D_0 (see for example the data compilation by Darwent [134]).

This information is as valuable for molecular ions, however the experimental techniques may differ due to the low density of ion beams in comparison to gas phase targets. One powerful method for obtaining D_0 is photo-fragment spectroscopy, in which the dissociation energy can be determined from the known photon energy and the measured kinetic energy release (KER) upon dissociation, assuming the KER can be measured with high enough precision [135]. We note that this technique has also been employed to measure additional structure and dynamics information [136–143].

In this work we demonstrate that dissociation driven by multiphoton absorbtion in a strong laser field can also be used to determine the dissociation energy, especially in cases that dissociation is enhanced by a resonant transition to an intermediate state. We picked LiO^- – the strongest base currently known [144] – as the test case, as it has convenient stepping states that enable Resonance-Enhanced Multi-Photon Dissociation (REMPD) [145] at 790 nm, and we find that our measured value of D_0 does not agree with calculated values.

The potential energy curves of the LiO^- molecular anion, shown in Fig. 3.14, are based on calculations by Bauschlicher *et al.* [124]. The lowest Π and Σ^+ curves of LiO^- and the lowest $^2\Pi$ and $^2\Sigma^+$ potentials of LiO were calculated around the equilibrium internuclear distance, specifically from $R = 2.8$ to 4.4 a.u, shown by the solid points. In these calculations only the relative energies were obtained, so we related them to the lowest Li + O dissociation limit using the value of D_0 for the $^2\Pi$ ground state of LiO from Ref. [127]. The energy of the $Li+O^-$ limit of the anion states is based on the electron affinity of oxygen [125, 126]. Then, we fit Morse potentials to each curve, resulting in those shown in Fig. 3.14. The $Li+O^-$ curves are expected to have a $-\frac{\alpha}{2R^4}$ polarization potential dependence at large R, and we match the Morse potentials with the R^{-4} potential at $R = 10$ a.u. using the polarizability of Li from Ref. [146]. Note that these are only approximate potentials, but they are sufficient to obtain D_0 which depends only on the dissociation limit and the shape of the potential near its minimum.

Using these potentials, D_0 of the $X\,^3\Pi$ ground electronic state of LiO^- was found to be 2.7 eV. As shown below, our measurements suggest that this value must be *at least* 0.3 eV greater. However, given that the potentials were generated using a few different measurements and calculations, it is important to discuss the accuracy of the theoretical value of D_0. The accuracy of D_0 depends on the accuracy of the calculated potentials of Ref. [124] – particularly the energy gap between the anion and neutral curves, as well as the accuracy of D_0 of LiO from Ref. [127] and the $Li+O^-$ dissociation limit. The $Li+ O^-$ limit is assumed to be the most accurate quantity of this group, as the electron affinity of oxygen has been measured spectroscopically with very high precision (better than 10^{-6} eV) [125, 126]. D_0 of LiO is less well-known, ranging from 3.4 to 3.8 eV (see Ref. [127] and references therein). We chose to use the calculated value obtained by Langhoff *et al.* of 3.79 eV because it appeared to be the most accurate of the available values and because it was the largest available value – which in turn gives us the largest starting value of D_0 for LiO^- and the closest to our measured value. The energy gap between the LiO^- and LiO curves from the calculations of Bauschlicher *et al.* [124] agree to within about 0.01 eV with values of the adiabatic electron affinity of LiO^- reported elsewhere [121].

As depicted in Fig. 3.14, D_0 can be determined experimentally by beam-fragment spectroscopy. In essence, D_0 is the difference between the measured KER upon dissociation of the LiO^- beam into $Li + O^-$ and the known photon energy. Of course, this assumes that the $\nu = 0$ vibrational level is populated and neglects the existence of a rotationally excited LiO^- target and ignores the effects of laser intensity on the resulting KER. These effects will be discussed further in the following sections.

Experimental method

To conduct this measurement on LiO^- we produced these ions from LiOH in a sputter source, accelerated them to 7 keV, and selected the LiO^- beam using an inflection magnet, as described in chapter 2. The beam was then directed, after proper focusing and collimation, through the interaction region and finally deflected into a small (2-mm diameter) Faraday

cup, which is used to monitor the beam current for normalization of measurements to each other. The deflection of the anion beam between the interaction region and the Faraday cup enables the measurement of neutral molecules produced by photodetachment as well as neutral fragments with low KER, which otherwise would be "lost" in the Faraday cup [12].

The fragments of LiO^-, both charged and neutrals, are measured by a time- and position-sensitive detector (see chapter 2). The time and position signals are recorded event by event relative to a time signal produced by scattering some of the laser light onto a photodiode. This measured information is analyzed with the coincidence three-dimensional momentum imaging method we have used for positive molecular ions in the past [5, 12, 20, 21]. In a nutshell, from the time and position information we determine the momenta of both fragments in the parent LiO^- center-of-mass frame. Then, the angular and KER distributions are evaluated. It is important to note that the laser interaction with the molecular ions takes place inside a spectrometer which accelerates the anions toward the detector, and thus enables identification of the charged fragments. Further details of the experimental method and its application to anion molecular beams are provided in Chap. 2, and for cations in Refs. [5, 12, 20, 21].

A potential source of contamination to the $^7LiO^-$ beam is $^6LiOH^-$, which has the same mass to charge ratio and therefore cannot be separated by our inflection magnet. We estimate that $^6LiOH^-$ comprises no more than a few percent of the total beam, given the low ($\sim 7\%$) isotopic abundance of ^6Li. $LiOH^-$ is also linear centered around the oxygen atom, and we do not observe any $Li + OH^-$ which is expected to be the dominant dissociation channel [147]. Given this observation and the significant bond rearrangement that would need to occur, we do not expect $^6LiH^- + O$ or $^6LiH + O^-$ to contaminate our measurements of $Li + O^-$ and $Li^- + O$.

Results and Discussion

As discussed above, by measuring photodissociation with a large enough photon energy the dissociation energy can be determined. To that end, we produced 395-nm photons by second

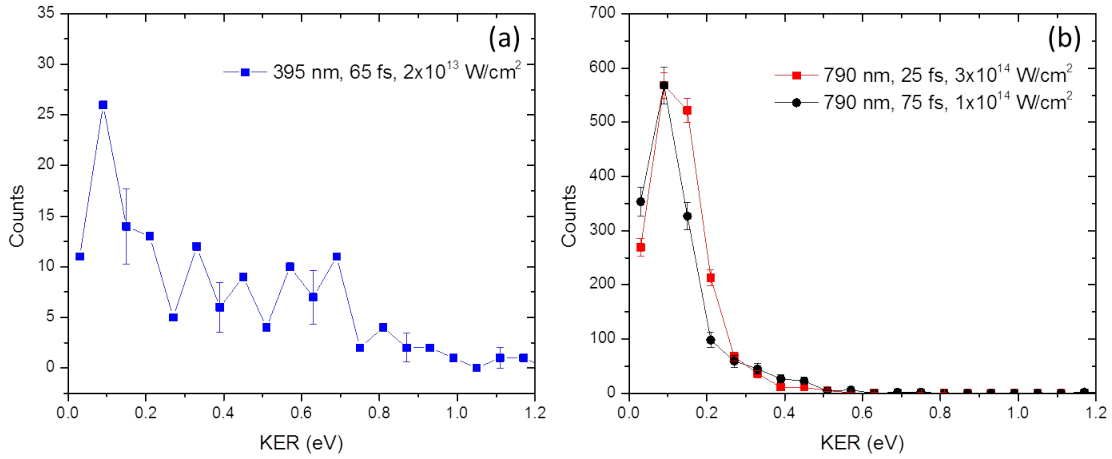

Figure 3.15: The measured KER distribution of $\mathrm{Li} + \mathrm{O}^-$ fragments following photo dissociation of LiO^- by (a) 65-fs, 395-nm, and $2{\times}10^{13}$-W/cm^2 pulses, and (b) 25-fs, $3{\times}10^{14}$-W/cm^2 (red) and 75-fs, $1{\times}10^{14}$-W/cm^2 (black), 790-nm pulses. The 75-fs data was multiplied by a factor of 2.04 to match the peak height of the 25-fs distribution. Error bars are due to statistical uncertainty.

harmonic generation of our 790 nm laser beam in a type I beta-barium borate (BBO) crystal. The 395-nm laser beam is then crossed with the ion beam and the resulting products of the interaction are measured downstream as described briefly above. The laser polarization is linear and aligned along the spectrometer axis. The KER spectrum of $\mathrm{Li} + \mathrm{O}^-$ products, measured in coincidence, is shown in figure 3.15(a). This KER distribution is peaked at about 0.1 eV and extends down to 0.05 eV or even lower, therefore suggesting that the dissociation energy of LiO^- is closer to the the photon energy of about 3.1 eV and not 2.7 eV as suggested by theory (using the curves from Ref. [124] and the dissociation energy of LiO from [127], as described in Sec. 3.4.2).

It is important to note the low number of counts in this spectrum, which are the result of a very long (72 hours) measurement with very low counting rate (about 2 events per hour). This low counting rate is mainly due to the low $X\,{}^3\Pi$ to ${}^3\Sigma^+$ transition probability resulting from the overlap of the initial and final nuclear wave functions, as shown in figure 3.16(a). Of course, the low target density of the 0.01 nA LiO^- beam does not help.

The width of the KER peak is largely due to the bandwidth of the laser pulse (about

100 meV FWHM based on the measured spectrum). The high-KER tail extending out to 0.7 eV may be due to dissociation from higher vibrational states, although it may also just be noise due to the extremely low statistics. Also, only vibrational levels below the LiO threshold may be populated, as higher vibrational levels decay to LiO+e^- by vibrational autodetachment much faster than the flight time from the ion source to the interaction region (see Sec. 3.4.3). If the peak at 0.1 eV is assumed to be due to dissociation from $\nu = 0$, then dissociation from the higher vibrational states that may be populated can result in KER up to about 0.5 eV.

Note that while we are only discussing the triplet states for simplicity, this interpretation applies to the singlet states as well. The $^3\Pi$ and $^1\Pi$ states are likely both populated in the ion beam, however they are nearly degenerate and have the same D_0 (within our experimental resolution). While the excited $^1\Sigma^+$ and $^3\Sigma^+$ states are also bound, radiative decay to the $^3\Pi$ and $^1\Pi$ states is expected to occur on a much shorter timescale than the flight time from the ion source to the interaction region, so we only expect the Π states to be populated when the ion beam reaches the interaction region.

In order to improve the count rate of this measurement, i.e. improve its efficiency, we have implemented a REMPD scheme (which is analogous to resonance-enhanced multiphoton ionization - REMPI [24, 148, 149]) in which we used the fundamental 790 nm photons of our laser, taking advantage of the $^3\Sigma^+$ stepping state. The excitation scheme is shown by the red arrows in figure 3.16. Resonant excitation to a few vibrational states around $\nu = 17 - 18$ is achieved due to the bandwidth (∼100 meV FWHM) of the laser, which is larger than the spacing of about 60 meV between these vibrational levels. The vibrational wave packet that is produced is then excited to the vibrational continuum more efficiently by the absorption of another photon.

The resulting KER upon LIO^- photodissociation into $Li + O^-$ by 25-fs, 790-nm, and 3×10^{14}-W/cm^2 pulses is shown in Fig. 3.15(b). For a more direct comparison with the measurement using 395-nm, 65-fs positively chirped pulses, we repeated the 790-nm measurement with 75-fs positively chirped pulses. The resulting KER, also shown in Fig. 3.15(b), is very similar to the KER distribution obtained with 25-fs pulses, which only suggests that the

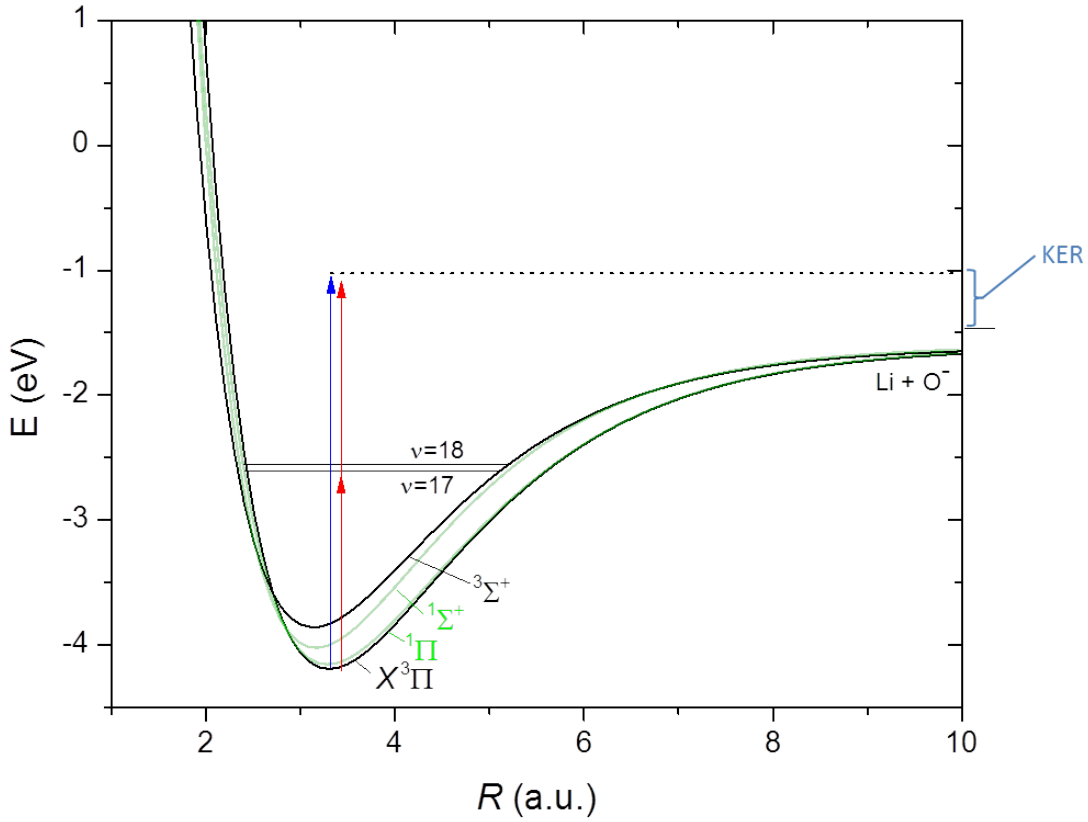

Figure 3.16: The lowest potential energy curves of LiO^- connecting to the lowest dissociation limit $Li + O^-$, separated into triplet (black) and singlet (green) curves. This subset of states are the same as the ones shown in figure 3.14. In the two-photon pathway, the first photoabsorption launches a vibrational wave packet, which is photodissociated later during the same laser pulse.

pulse chirp does not significantly change the observed KER distribution.

It is important to note the improved counting rate of the 790-nm measurements compared to the 390-nm measurements, by about a factor of 100, in spite of the fact that two photons are needed instead of one. This is due to the resonant nature of the first bound-bound step and improved nuclear wave function overlap in the second bound-free step. Theoretical treatment is needed to determine the relative importance of the two.

The KER distribution obtained using 790-nm pulses is very similar to the low-statistic one measured for the doubled frequency photons. Assuming that the KER peak at 0.1 eV is due to dissociation starting from $\nu = 0$, this suggests that the dissociation energy of LiO^- is 3.0 ± 0.1 eV, larger than the predicted value of 2.7 eV based on theory. The 0.1-eV uncertainty is based on the width of the peak. As the measured KER is very low, it is possible that the dissociation is not possible from the lowest vibrational states at these photon energies. That is, the KER peak may be due to dissociation from a higher vibrational level, which would mean D_0 is even larger than 3.0 eV. However, there is some evidence that the peak may actually be due to $\nu = 0$. If all vibrational levels below the LiO threshold were populated, the resulting KER could extend up to about 0.5 eV, and the tail of our measured distribution does extend all the way to 0.5 eV. Furthermore, if the LiO^- target is rotationally excited, the potential well is shallowed by the centrifugal distortion. This would result in a measurement of a smaller D_0 than the true D_0. So, any rotational excitation of the LiO^- beam would also imply that D_0 is even larger than our measured value. Unfortunately, the rovibrational population of the beam is unknown, and further work is needed to determine it (either by a measurement or modeling of the formation of LiO^- from LiOH that occurs in the sputter source). Therefore, our measurement of 3.0 eV places a *lower limit* on the value of D_0.

This result may be due to other factors as well. We originally obtained the dissociation energy from theory using a reported value of D_0 for the ground state of LiO and the separation between the LiO and LiO^- states. So, the reason the theoretical value of D_0 is too low may also be due to inaccuracies in either of these two values. That is, the dissociation energy of LiO is actually greater than reported in literature (although, recall that we are using the largest value that has been reported). Or, the separation between LiO and LiO^-

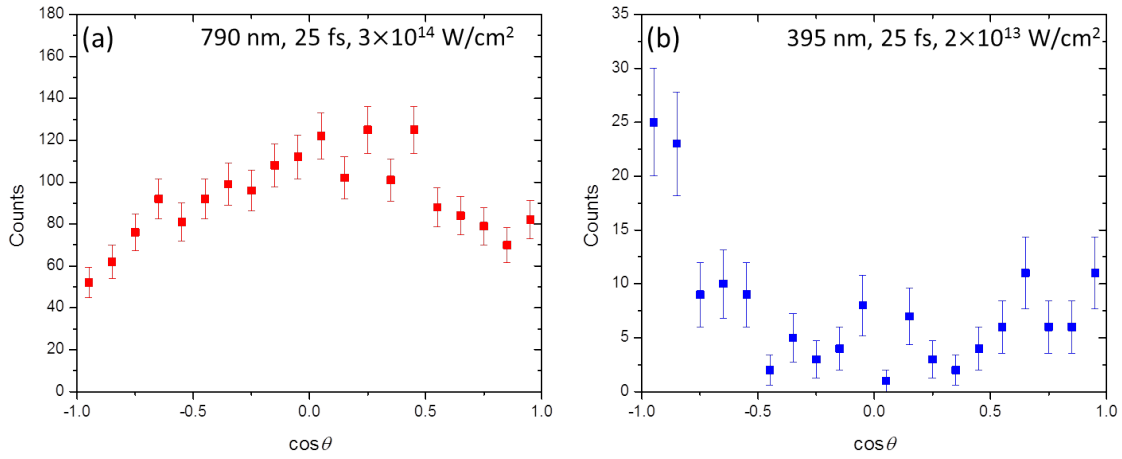

Figure 3.17: Angular distributions for dissociation of LiO^- to $Li+O^-$ by (a) 790-nm, 25-fs, 3×10^{14}-W/cm^2 pulses and (b) 395-nm, 65-fs, 2×10^{13}-W/cm^2 pulses.

(and consequently the electron affinity of LiO) is greater than what has been reported. One possible explanation of why the theoretical value of D_0 is smaller than our measurement is that the calculated LiO^- potentials do not include spin-orbit coupling. This effect alone could deepen the potential well and result in a D_0 closer to our measurement.

The coincidence 3D-momentum imaging method also provides angular distributions of dissociation relative to the laser polarization, which are shown in figure 3.17 for both 790-nm and 395-nm pulses. It is immediately apparent that the two distributions are significantly different. The dissociation caused by two 790 nm photons, i.e the REMPD process, is aligned perpendicular to the laser polarization, which is the expected behavior for $\Delta\Lambda = 1$ transitions [113–115], suggesting the $X\,^3\Pi$ — $^3\Sigma^+$ transitions are dominant in this case (as opposed to a permanent dipole transition within the $X\,^3\Pi$ state). In contrast, photodissociation following the absorption of a single 395-nm photon is predominantly aligned along the laser polarization, which is typical for transitions with $\Delta\Lambda = 0$ [113–115]. This suggests that photodissociation by 395-nm photons is primarily due to a permanent dipole transition to the vibrational continuum within the $X\,^3\Pi$ ground state.

As a consistency check, we also studied dissociation into $L^- + O$ fragments. Even though the potential energy curves are not available for states resulting in these final products, all

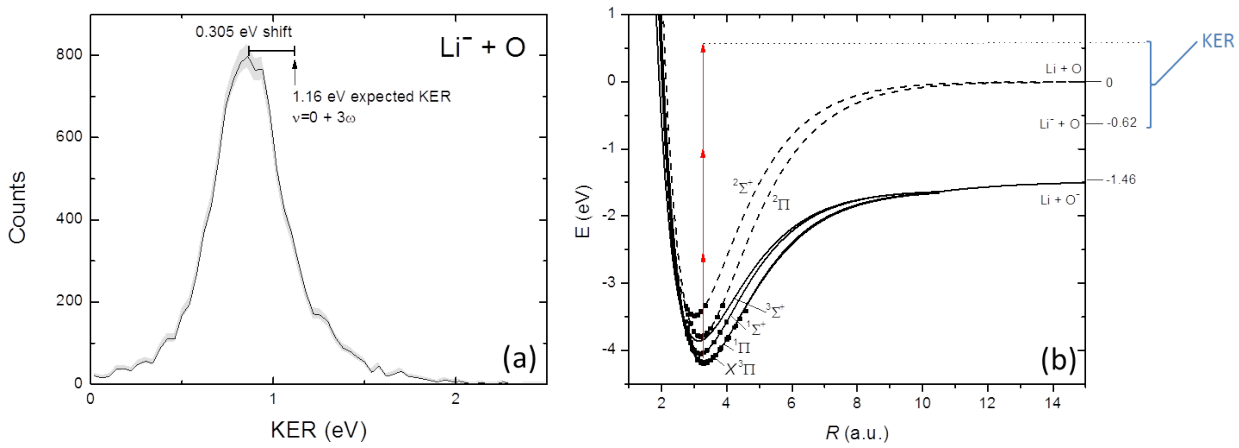

Figure 3.18: (a) Measured KER distribution of Li^- + O by 790-nm, 25-fs, 3×10^{14}-W/cm^2 pulses. The shaded area represents the statistical error. The peak of the KER distribution is shifted by 0.305 eV from the expected KER produced by LIO^- in $\nu = 0$ absorbing three 790-nm photons. (b) Photon picture of three-photon absorption resulting in dissociation into Li^- + O final products.

that is needed to predict the KER is the known dissociation limit [150].

Based on the photon picture shown in Fig. 3.18(b), the absorption of three 790-nm photons from $\nu = 0$ results in a final energy 1.16 eV above the $Li^- + O$ dissociation limit; however, the measured KER distribution is peaked 0.305 eV lower, as shown in Fig. 3.18(a). This result is consistent with our observations in the $Li + O^-$ channel and is further evidence that D_0 must be larger by at least 0.3 eV.

Summary

In summary, we have evaluated the dissociation energy of LiO^- through photo-fragmentation by measuring the KER upon dissociation into $Li+O^-$. Resonance-enhanced two-photon absorption was used to increase the rate of dissociating LiO^- by about two orders of magnitude over single-photon photodissociation. This REMPI-like process involves exciting LiO^- to a stepping state from which photodissociation is more efficient. Using the measured KER distribution, we set a lower limit on the dissociation energy of 3.0 ± 0.1 eV, which is 0.3 eV larger than the value based on theory.

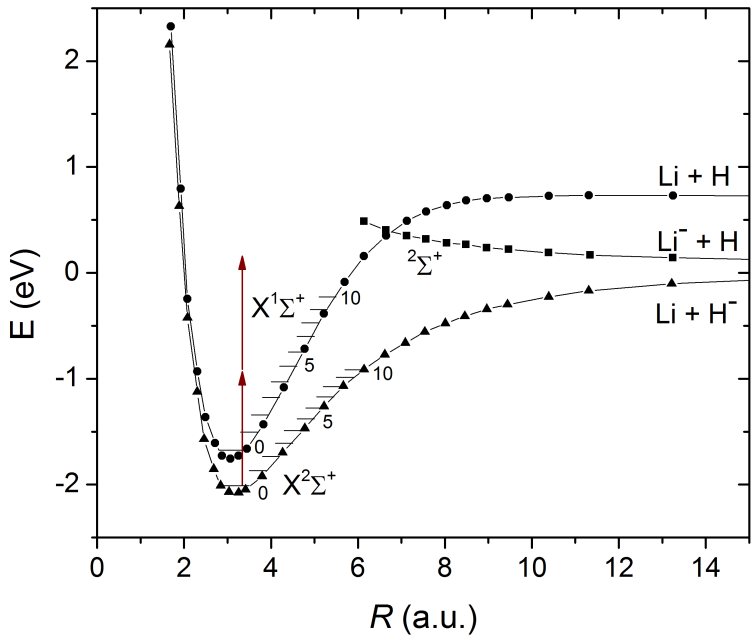

Figure 3.19: Potential energy curves of LiH^- and LiH from Ref. [151]. To study time-resolved autodetachment of LiH^- using the pump-probe scheme described in this section, 1100-nm photons (shown by the brown arrows) may be used. Unlike LiO^-, only a single pathway is involved, which could greatly simplify the interpretation of the measurement.

3.4.3 Pump-probe studies of autodetachment of LiO^-

As shown in Fig. 3.20(a), the potential wells of LiO^- and LiO overlap with one another. Therefore, vibrationally excited LiO^- decays to the ground state of LiO through vibrational autodetachment of an electron due to the redistribution of energy between the nuclear and electronic degrees of freedom [122, 123], as outlined in Sec. 3.4.1.

To measure the autodetachment lifetimes of vibrationally excited LiO^-, a pump-probe scheme that involves measuring dissociation from anion states that have not yet undergone autodetachment was proposed by Brett Esry. Specifically, LiO^- molecules in the $^3\Pi$ ground electronic state are excited by a 790-nm pump pulse to the $^3\Sigma^+$ state, as illustrated in Fig. 3.20(a). The vibrational states that are populated by the pump pulse can decay to vibrational states of the $^2\Pi$ and $^2\Sigma^+$ states of LiO that are lower in energy. A probe pulse arriving after a controlled delay excites the anions that have not yet autodetached out of the potential well causing their dissociation into $Li+O^-$. The yield of $Li+O^-$ as a function of delay is a measure of the autodetachment rate from the excited vibrational states of the $^3\Sigma^+$

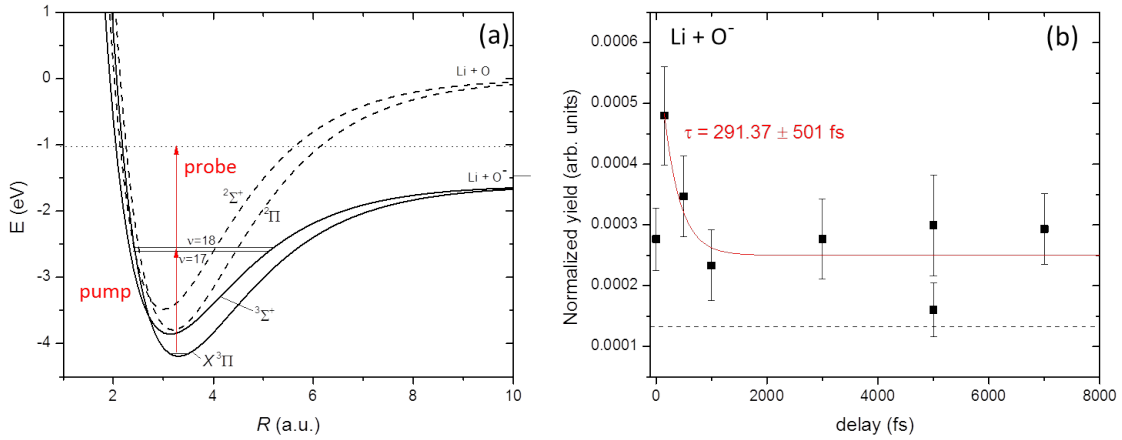

Figure 3.20: (a) The LiO^- and LiO potentials and illustrated pump-probe scheme. The pump pulse excites LiO^- to vibrational states that decay by autodetachment. The probe pulse photodissociates states that have not yet autodetached, resulting in dissociation to $Li+O^-$. (b) The yield of $Li+O^-$ normalized to the yield of LiO plotted as a function of pump-probe delay. The pump and probe pulses were each 75 fs, 790 nm, and 1×10^{13} W/cm^2. The red line is an exponential decay fit to the data, which reveals a lifetime of about 300 fs.

state. Note that while this description is only given for the triplet states of LiO^-, the same applies to the singlet states (i.e. pumping the $^1\Pi$ state to the $^1\Sigma^+$ state and probing in a similar way), as well as permanent dipole transitions (i.e. vibrational transitions within the $^3\Pi$ state), and a combination of all of these transitions contributes to the signal. A simpler system in which the same phenomena can be studied is LiH^-, as described in Sec. 3.5.1. Using the same scheme presented in this section, excitation by the pump pulse is only possible by a permanent dipole transition, as illustrated in Fig. 3.19. Reducing the number of pathways to one would significantly simplify the interpretation of the experiment. However, performing a pump-probe experiment following the scheme described in this section requires photon energies that are not presently available to us.

Utilizing the pump-probe technique described in chapter 4, we attempted to implement the above scheme. The 75-fs, 790-nm pump and probe pulses had a peak intensity of 1×10^{13} W/cm^2 each. The intensity of both pulses was kept relatively low to minimize the amount of dissociation to $Li+O^-$ by a single pulse. The pump pulse launches a vibrational wave packet, as the large bandwidth of the laser (100 meV) allows a few vibrational states

around ν=17–18 to be populated by exciting $LiO^-(\nu = 0)$. Because the autodetachment rate is a function of the R-dependent coupling between the initial and final states, we use 75-fs pulses to average over the motion of the vibrational wave packet, which has a ∼50-fs vibrational period for $\nu = 17$. In the future, a narrow bandwidth (< 60 meV) pump pulse could be used to populate a single vibrational level, but this pulse was not available at the time of this measurement.

The measured yield of $Li+O^-$ normalized to the yield of LiO to account for fluctuations of the ion beam is plotted as a function of pump-probe delay in Fig. 3.20(b). The maximum yield occurs at a delay of 150 fs. The drop at zero-delay could be due to destructive interference of the overlapped pulses. Beyond 150 fs, the yield appears to drop and is fairly flat after 1 ps. The yield due to a single pulse is indicated by the dashed line. The large error bars are due to the very low rate of $Li+O^-$, about 5 events per hour. Each delay point represents 4-6 hours of data collection. We observe the yield of $Li+O^-$ decreasing as a function of delay, as expected, and fitting an exponential decay function to the results yields a lifetime of about 300-fs.

Typical lifetimes with respect to vibrational autodetachment of diatomic anions were previously reported to range from a few ps to a few ns based on the calculations by Acharya *et al.* [123]. While our preliminary estimate of a 300-fs lifetime is shorter than the expected ps-ns lifetimes based on theory, we do not have a high degree of confidence in this result due to the extremely low statistics of the measurement. But, this measurement demonstrates that such a measurement is possible and is a significant step towards future studies of vibrational autodetachment rates.

3.5 Other anions

In addition to the studies using F_2^- and LiO^- molecular anion targets, a few other experiments have been performed yielding preliminary results. Not all of these measurements were successful and the results are preliminary, but they provide guidance for future experiments. Brief highlights of some of the other molecular-anion projects are given below.

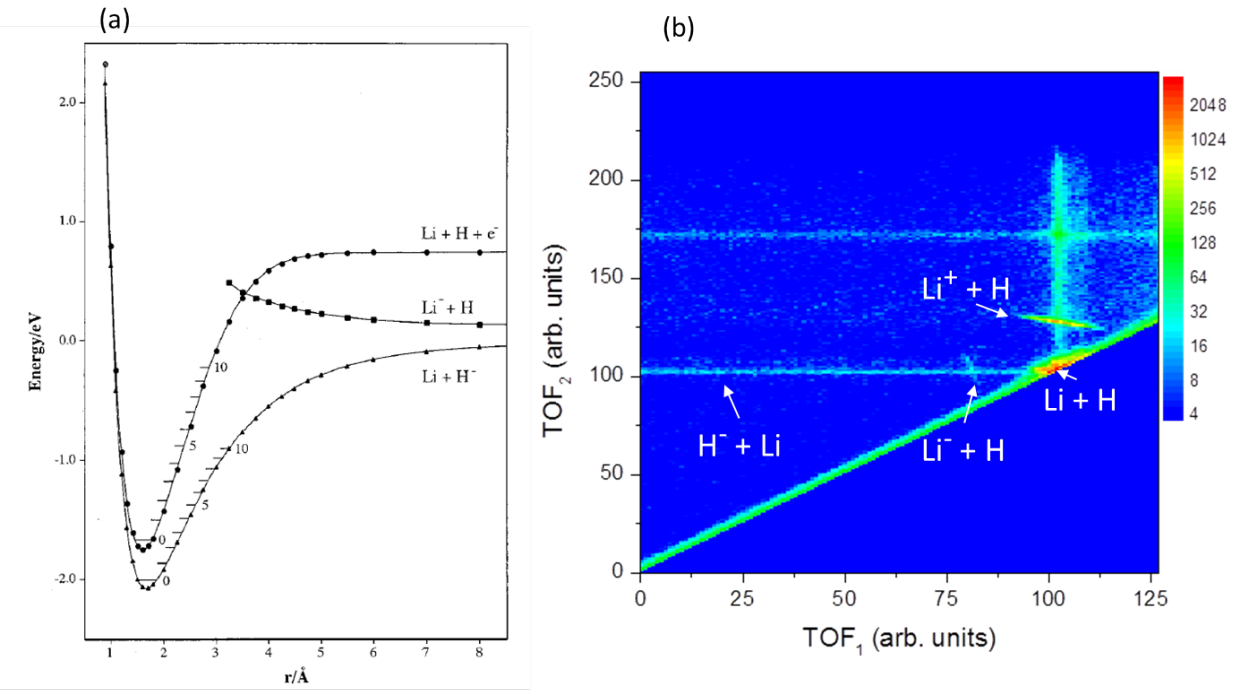

Figure 3.21: (a) LiH^- and LiH potentials from Ref. [151]. (b) Coincidence time-of-flight map for fragmentation of LiH^- by 800-nm, 25-fs, $1\times10^{14}\,W/cm^2$ pulses.

3.5.1 LiH^-

The structure of LiH^- is very similar to LiO^- (see Sec. 3.4), and therefore it is another good candidate for studies of autodetachment lifetimes using the pump-probe scheme described in Sec. 3.4.3 or other approaches. We chose to study the isotopologue LiD^-, as the smaller mass ratio between the fragments makes measurements easier for us to perform. Also, the $^7LiH^-$ beam is contaminated by a $^6LiH_2^-$ beam that has the same mass-to-charge ratio. While the natural abundance of the ^6Li isotope is only about 10%, LiH_2^- has a much higher current than LiH^-, so the level of contamination is high. On the other hand, $^7LiD^-$ is a cleaner target. $^7LiH_2^-$ is a possible contaminant, but we use a high-purity LiD target in the sputter source so any H-containing beams are not formed.

The potential energy curves of LiH^- and LiH [151] in Fig. 3.21(a) show that the dissociation energy of LiH^- is about 2 eV, so the absorption of one 395-nm photon or two 790-nm photons is needed to excite the molecule out of the potential well, but is also high above the threshold for detachment. Absorption of 800-nm photons primarily results in photode-

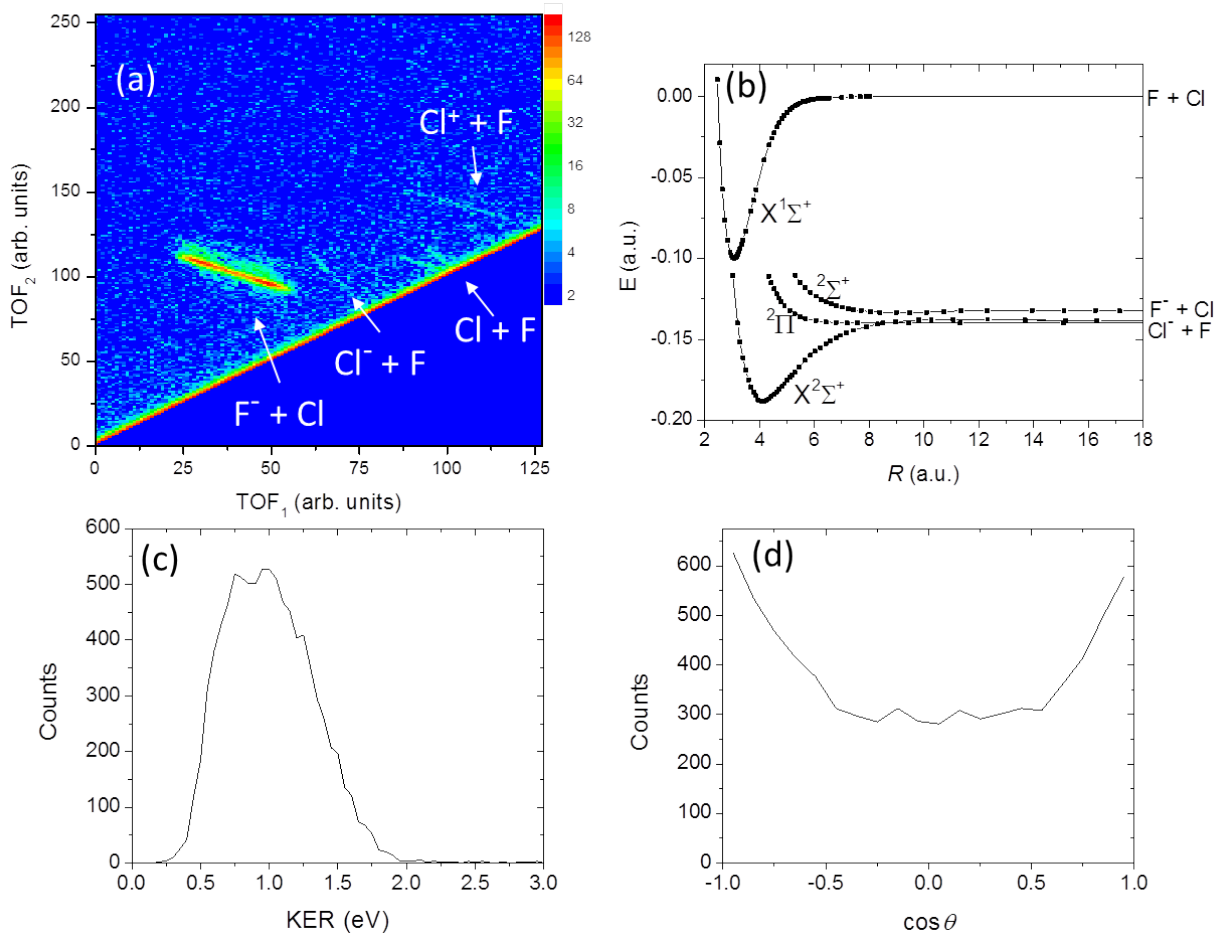

Figure 3.22: (a) Coincidence time-of-flight map for fragmentation of ClF^- by 800-nm, 25-fs, 1×10^{15} W/cm^2 pulses. (b) ClF^- and ClF potential energy curves adapted from Ref. [152]. (c) KER and (d) $\cos\theta$ distributions for F^-+Cl breakup.

tachment to neutral LiH, which is the strongest channel by several orders of magnitude. But, we also observe dissociation into Li^-+H as well as dissociative photodetachment into Li+H and even ionization resulting in Li^++H, as shown in Fig. 3.21(b). We were unable to observe dissociation into H^-+Li, which is needed for performing the pump-probe measurements described in Sec. 3.4.3. In the future, using 500-nm or 1000-nm photons may cause more dissociation to Li+H^-, and generation of these wavelengths is under development.

3.5.2 ClF^-

The ClF^- molecular anion is essentially a heteronuclear version of F_2^-, and there are two experimentally distinguishable final products, Cl^-+F and F^-+Cl, which are separated by about 0.2 eV, as shown in Fig. 3.22(b). The ClF^- beam was produced in the sputter source using a cathode containing a roughly 1:1 mixture of LiF and MgCl powders. Dissociation into Cl^-+F final products from the $X\,^2\Sigma^+$ ground state occurs by an electronic transition to the $^2\Pi$ state or by a permanent dipole transition to the vibrational continuum of the electronic ground state. Dissociation into F^-+Cl final products proceeds via a transition to the $^2\Sigma^+$ state. In our preliminary measurements, F^-+Cl was observed to be the dominant final product, as can be seen in Fig. 3.22(a), and the KER associated with it, shown in Fig. 3.22(b), was consistent with a one-photon transition from high vibrational states of the ground state to the $^2\Sigma^+$ state. The angular distribution, shown in Fig. 3.22(d), is also consistent with a $\Sigma \rightarrow \Sigma$ transition. On the other hand, the KER of the much weaker Cl^-+F breakup can be associated with a one-photon transition from low vibrational states of the ground state to the $^2\Pi$ state. Note that the nonadiabatic coupling between the $^2\Sigma^+$ states at 9.5 a.u. can drive charge exchange. A signature of the charge exchange process would appear as Cl^-+F with KER equal to the F^-+Cl KER plus the difference in the dissociation limits, 0.2 eV. However, no such feature was observed in the measured KER spectrum. The coincidence time-of-flight map shows that in addition to F^-+Cl and Cl^-+F, photodetachment and two-electron removal resulting in fragmentation into Cl+F and Cl^++F, respectively, are also observed.

3.5.3 LiF_2^-

Observing 3-body breakup of triatomic anions in which one of the fragments is an anion would be interesting, as multiple bonds would be broken without detaching the weakly bound "extra" electron. Also particularly interesting to study would be 3-body breakup involving all neutral fragments, which is otherwise difficult to measure. Preliminary explorations of the fragmentation of polyatomic anions were performed on LiF_2^-. This anion is a good candidate

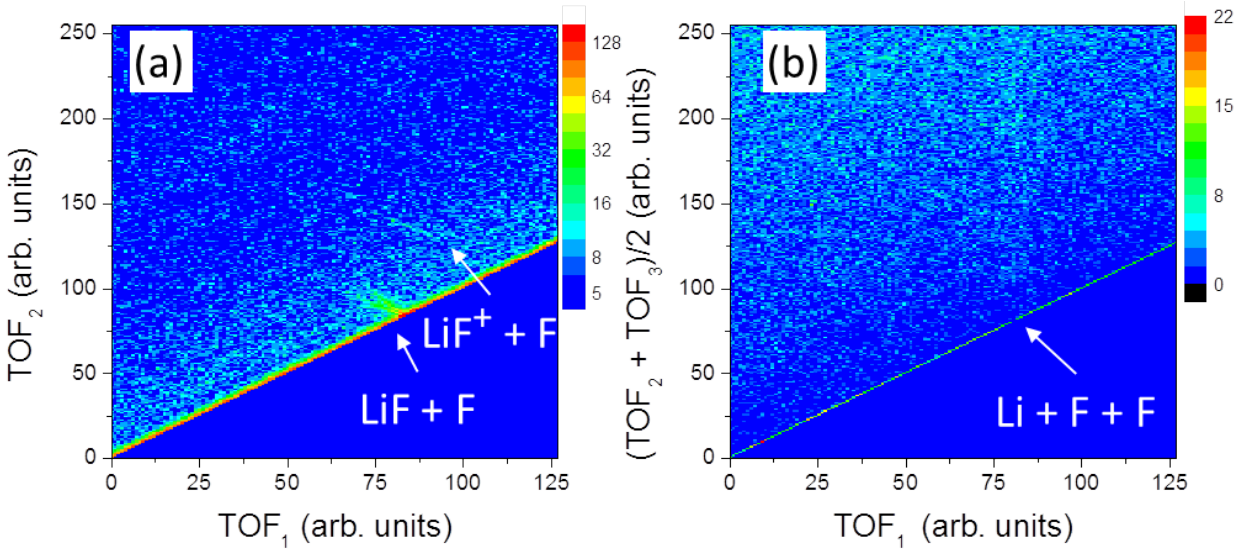

Figure 3.23: (a)-(b) Coincidence time-of-flight spectra for 2- and 3-body fragmentation of LiF_2 by 800-nm, 25-fs, 8×10^{14} W/cm^2. The 3-body spectrum has the TOF of the first fragment on the x-axis and the average of the TOFs of the second and third fragments on the y-axis.

for studying 3-body breakup as the electron detachment energy (about 7 eV) is greater than the Li-F bond strength (3 eV), and breaking both Li-F bonds may be energetically preferable to electron detachment. Unfortunately, no 3-body breakup was observed, though we did observe two-body breakup into LiF+F and LiF^++F and also the neutral LiF_2 molecule. Work towards identifying other possible candidate anions for studying 3-body breakup is in progress.

3.6 Summary

In summary, our new capability to generate molecular anion beams and measure their fragmentation using a coincidence 3D momentum imaging technique has been employed to study the fragmentation of a few molecular anions. Measurements of the dissociation and photodetachment revealed information about the fragmentation process. The dissociation pathways were identified, and the existence of a dominant pathway allowed for a simple estimate of the vibrational population of the F_2^- beam using first order perturbation theory and the measured KER distribution. The role of a sequential photodetachment process in which dis-

sociation into F^-+F is followed by photodetachment of the resulting F^- fragment was also explored. Photodetachment resulting in F+F is about an order of magnitude more likely than F_2, and sequential and direct photodetachment processes were suggested to contribute to the F+F yield. The sequential and direct photodetachment processes were found to be identifiable by their KER.

Dissociation of LiO^- into Li+O^- was studied and used to evaluate the bond dissociation energy of LiO^-, which was found to be 0.3 eV greater than values based on theory. Resonance-enhanced two-photon excitation drastically increased the rate of dissociation compared to single-photon photodissociation. Furthermore, autodetachment of LiO^- was explored using a pump-probe scheme, and preliminary results indicate an autodetachment lifetime of about 300 fs. A few additional anion beams have also been investigated, yielding preliminary results that will guide future work.

Future studies on molecular anions will build on the work presented in this chapter. Pump-probe measurements of dynamics in molecular anions provide an avenue to study unique processes such as autodetachment. Bunching the ion beam should increase the target density by about a factor of 10, which will have a large impact on the feasibility of future experiments.

Chapter 4

Pump-probe studies of fragmentation of a fast molecular ion beam

4.1 Scope

The pump-probe studies of molecular fragmentation presented in this chapter focus on enhanced ionization of HD^+ and Ar_2^+ molecular ions by a strong laser field. We develop a method for evaluating the yield of ionization of dissociating molecules as a function of pump-probe delay, and enhanced ionization of the dissociating HD^+ and Ar_2^+ wave packets was observed at surprisingly long time delays corresponding to large internuclear distances. A brief introduction to the concepts used to describe enhanced ionization is presented in Sec. 4.2. The pump-probe technique used to perform these measurements is described in Sec. 4.3, and its application to the studies of fragmentation of Ar_2^+ and HD^+ is presented in Sec. 4.4 and 4.5, respectively. The results of the two targets are compared to each other in Sec. 4.6 and to theory in Sec. 4.7. A summary of the results and future directions is presented in Sec. 4.8.

4.2 Introduction

Enhancement in the ionization of H_2^+ at internuclear distances larger than the equilibrium distance is a topic that has received a great deal of attention in the past [24, 153–162]. The charge resonance enhanced ionization (CREI) mechanism proposed by Zuo and Bandrauk [153] and studied in parallel by Seidman, Ivanov, and Corkum [163], describes enhanced ionization at particular internuclear distances based on a static-field tunnel ionization picture with fixed internuclear distance, R. Several experimental studies have used this model to at least qualitatively understand structures in the kinetic energy release of Coulomb-exploding H_2^+ [24, 154–156, 158, 159, 162], however the double-peak structure predicted by Zuo and Bandrauk [153] is often not observed, likely because of the motion of the nuclei [160, 164]. Furthermore, this model is not as useful at lower laser intensities where the tunneling picture is less applicable.

An alternative interpretation of the structures observed in the Coulomb explosion of H_2^+ proposed by Esry *et al.* [157] identified them as above threshold Coulomb explosions (ATCE). The ATCE phenomenon is understood using a frequency domain picture that describes enhancement at particular internuclear separations using Floquet potentials. Dissociation and ionization are treated on equal footing using photon-dressed Floquet potentials. Enhancements in the KER are associated with curve crossings that correspond to the opening of multiphoton ionization channels. This picture serves as the motivation for the pump-probe studies of our group.

To study the effect of the internuclear distance on the ionization yield, others have utilized the pump-probe technique, which is among the most common tools used to study molecular dynamics [1, 165–167]. In this technique, a dissociating H_2^+ wave packet is launched by the same pump pulse that ionized the target H_2. This dissociating wave packet is later ionized by the probe pulse [158, 162, 168]. The dissociation dynamics are mapped through the observation of the delay-dependent KER upon Coulomb explosion.

In experiments using a neutral H_2 target, H_2^+ is "born" and dissociated in a strong laser field that distorts the H_2^+ potentials, making it more difficult to describe the time evolution

of the dissociating wave packet. On the other hand, by using a molecular ion as a target, a relatively weak pump pulse can be applied to initiate dissociation, and the dissociation dynamics can be more easily described in terms of well-understood H_2^+ dissociation mechanisms such as bond softening and above threshold dissociation [24, 169–171]. In this work, a weak pump pulse, not strong enough to ionize, is used to dissociate a molecular ion, either HD^+ or Ar_2^+, and a strong probe pulse later ionizes the dissociating wave packet.

Studying dynamics using an ion-beam target, however, is difficult due to the low target density. The time required to obtain sufficient statistics at each pump-probe delay step demands long-term stability of the laser and ion beams as well as their crossing, which is difficult to achieve. Specifically, drifting of the laser or ion beam makes the comparison of measured yields difficult. In spite of these difficulties, we have successfully demonstrated that such measurements can be performed.

This chapter includes pump-probe studies of HD^+ and Ar_2^+ ion-beam targets. The completion of the HD^+ studies spanned two Ph.D projects. Mohammad Zohrabi led the technical developments and obtained preliminary results as part of his Ph.D [172]. After he graduated, Mohammad as a postdoc and I as senior grad student led the successful experimental effort and obtained good quality results for HD^+. Then, after Mohammad moved on to a new job, I completed the analysis, presented this project at conferences, and prepared the results for publication. It is important to note, though, that this project could not have been completed without the contributions of Mohammad. The HD^+ section consists mainly of results, as many details are discussed in Mohammad's Ph.D. thesis. On the other hand, the Ar_2^+ pump-probe measurements were performed more recently, and I led the effort to conduct the measurements and develop the analysis of this data, which is described in detail in the following sections. For this reason, even though the Ar_2^+ project was a follow-up to the HD^+ studies, it is presented first in this chapter.

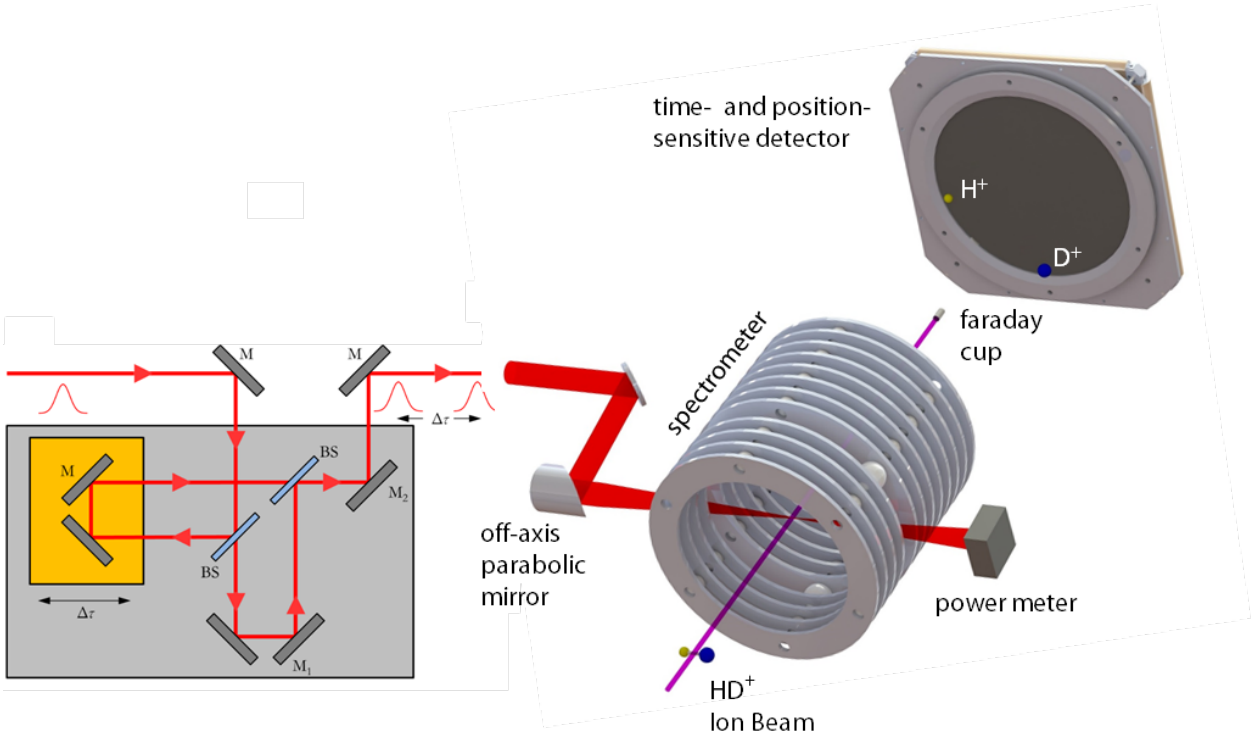

Figure 4.1: Schematic of the experimental setup. The laser beam is split into pump and probe pulses in a Mach-Zehnder interferometer. The laser beam is focused onto the HD^+ ion beam in an imaging spectrometer. The electric field of the spectrometer separates the ions in time, and the time- and position- information of every fragment is measured on a time- and position-sensitive delay-line detector.

4.3 Experimental method

The experimental setup used to perform the pump-probe measurements presented in this chapter employs the developments described by Mohammad Zohrabi in his Ph.D. dissertation [172]. Briefly, the laser beam was split into pump and probe pulses in a Mach-Zehnder interferometer, as illustrated in Fig. 4.1. The delay between the pulses was controlled by a linear translation stage that adjusts the optical path length in one arm with a resolution of 0.2 μm (0.67 fs) and maximum range of 25 mm (∼80 ps). The laser beam was focused onto the ion beam by a 90° off-axis parabolic mirror ($f = 203$ mm). The HD^+ beam was generated by electron impact ionization in an electron-cylcotron resonance (ECR) ion source, and the Ar_2^+ beam was generated by a similar process in a duoplasmatron ion source (see Sec. 2.2.1). The ion beam intersects the laser beam inside an imaging spectrometer, which provides a longitudinal electric field that separates fragments from each other by their time of flight, allowing the identification of dissociation events (H^++D or H+D^+) and ionization events (H^++D^+), or the respective Ar^+ + Ar and Ar^++ Ar^+ channels in the case of Ar_2^+. Moreover, the measurement of the fragments in coincidence as well as their times and positions allows for the evaluation of the 3D momentum of each fragment.

4.4 Pump-probe studies of ionization of a fast Ar_2^+ beam

The pump-probe studies of the ionization of Ar_2^+ presented in this section are a follow-up to previous studies on HD^+ ionization described in Sec. 4.5 in which enhanced ionization of the dissociating HD^+ was observed at delays corresponding to surprisingly large internuclear distances of over 30 a.u. The aim of the Ar_2^+ studies in this section was to explore whether ionization at large internuclear distances is a general phenomenon not unique to only H_2^+ by observing it in another system. One advantage of using Ar_2^+ as a target is its slow nuclear motion compared to HD^+. Dissociation occurs on much longer timescales, making dynamics easier to study. Moreover, dissociation of Ar_2^+ can be described by a single pathway involving

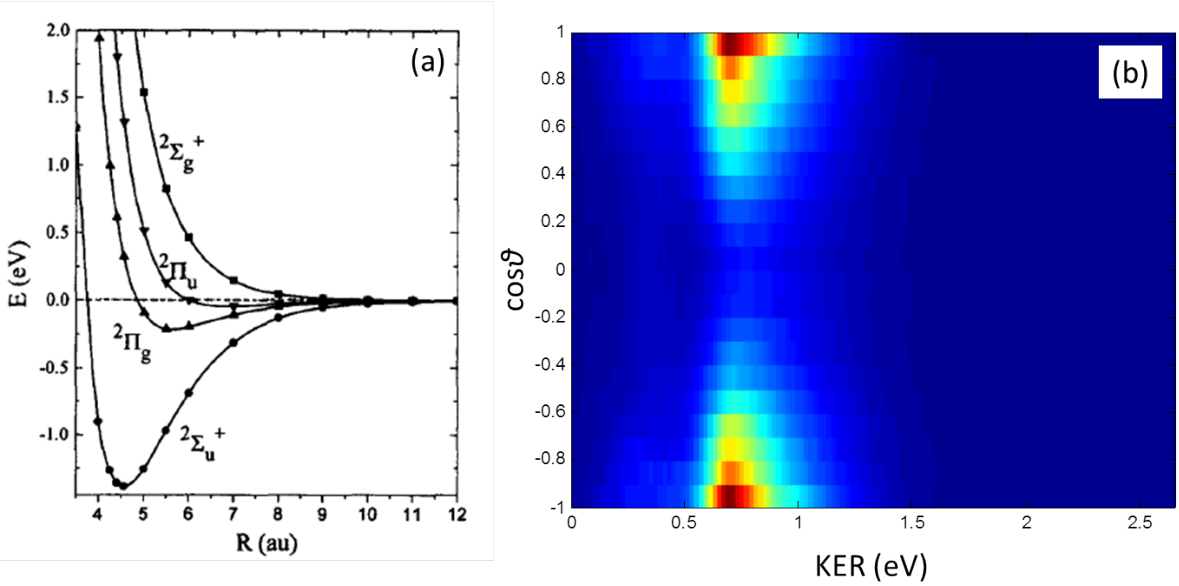

Figure 4.2: (a) Ar_2^+ potentials from Ref. [173]. (b) A map of the Ar^++Ar yield as a function of the KER and cosθ. The angular distribution is aligned predominantly along the laser polarization direction and the KER distribution is centered around 0.7 eV.

two states, as explained below, making it essentially a heavy analogue of H_2^+. Thus, we aim to study similar dynamics as in H_2^+ with better time resolution thanks to the slower motion of the more massive Ar_2^+.

Three possible dissociation pathways exist in Ar_2^+ involving transitions from the $X\,^2\Sigma_u^+$ ground state to the $X\,^2\Sigma_g^+$, $^2\Pi_u$, and $^2\Pi_g$ states shown in Fig. 4.2(a). The distribution of the Ar^++Ar yield, mapped as a function of KER and $\cos\theta$, where θ is the angle between the laser polarization and the momentum of the Ar^+ fragment, is shown in Fig. 4.2(b). The angular distribution is predominantly aligned along the laser polarization, consistent with a parallel $\Delta\Lambda = 0$ transition [113–115]. The transition to the $^2\Pi_g$ state has $\Delta\Lambda = 1$ and therefore the angular distribution is expected to peak around $\cos\theta = 0$. Because one-photon $u \to u$ transitions are forbidden, the $^2\Pi_u$ state is inactive. The very low yield at $\cos\theta = 0$ suggest that the $^2\Pi_g$ state does not play a significant role. Furthermore, the KER distribution centered at 0.7 eV is consistent with a near-resonant one-photon transition from the $X\,^2\Sigma_u^+$ ground state to the $^2\Sigma_g^+$ state. We neglect any initial population in the weakly bound $^2\Pi_g$ state, as the radiative lifetime of the $^2\Pi_g$ state is expected to be much shorter than the Ar_2^+

flight time from the ion source to the interaction region. Also, one-photon absorption from the $^2\Pi_g$ state would result in KER of about 1.2 to 1.5 eV which we do not observe. Therefore, we approximate the dissociation of Ar_2^+ as only a single pathway, specifically a one-photon $X\,^2\Sigma_u^+ \rightarrow X\,^2\Sigma_g^+$ transition.

In the pump-probe measurement of the ionization of Ar_2^+, the delay between the pump and probe pulses was controlled using a Mach-Zehnder interferometer, as described in Sec. 4.3, and the pulse energy was split evenly between the 790-nm, 25-fs pump and probe pulses. The peak intensities of the pump and probe pulses was 8×10^{14} W/cm^2. While an advantage of using an ion beam target is that a weak pump pulse can be used to initiate dissociation, strong pump and probe pulses were used in this measurement to maximize the counting rate. Scans over the delay ranges of 2, 4, and 12 ps were conducted with respective delay step sizes of 40, 60, and 150 fs. Each data set consists of the sum of multiple scans (typically 3-4) in order to average over fluctuations in the measurement.

The yield of Ar^++Ar^+ mapped as a function of pump-probe delay and KER is shown in Fig. 4.3. The tail feature extending to low KER with increasing delay, labeled "I" in Fig. 4.3(a), is due to ionization of the dissociating Ar_2^+. On the other hand, the feature with a roughly constant KER around 5 eV, labeled "II", is due to ionization of bound Ar_2^+. Under closer inspection, some structure is observed in the KER around 5 eV at delays between about 200 and 500 fs, as shown more clearly in Fig. 4.3(b). The structure is the result of ionization of the oscillating bound nuclear wave packet initiated by the pump laser pulse. This feature resembles the well-resolved stripes that result from the ionization of a bound D_2^+ wave packet [174].

The delay-independent feature at low KER, labeled "III" in Fig. 4.3(a), is the result of random coincidences between Ar^+ fragments from different molecules that dissociate during the same laser pulse and happen to pass our momentum conservation condition. Unfortunately, at large delays the random coincidences contribute at the same KER as ionization of the dissociating wave packet. So, to correctly evaluate the ionization yield of the dissociating wave packet as a function of delay, these random coincidences must be removed. Ideally, the laser parameters could be adjusted to minimize the rate of random coincidences, but in

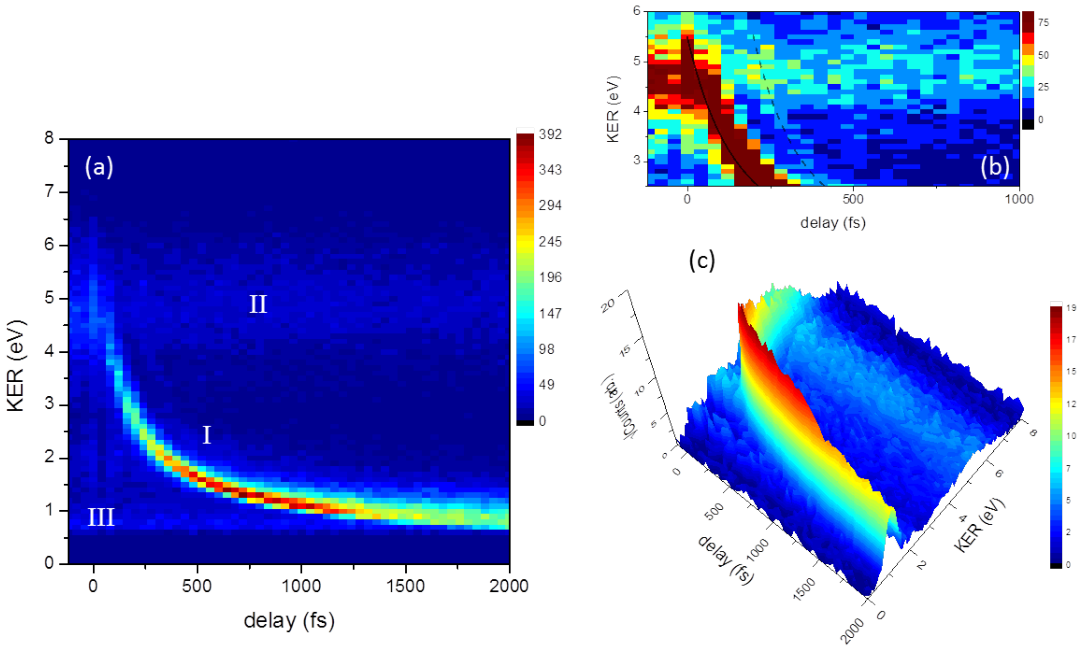

Figure 4.3: (a) Ar^++Ar^+ ionization yield mapped as a function of pump-probe delay and KER. The tail extending to lower KER with increasing delay (I) is due to ionization of the dissociating Ar_2^+ wave packet. The component with KER around 5 eV (II) is due to ionization of bound Ar_2^+. The delay-independent feature at low KER (III) is due to random coincidences between Ar^+ ions. (b) Zoomed-in plot of the feature at high KER associated with ionization of the bound wave packet, marked by the dashed lines. (c) 3D visualization of the ionization map.

practice this is difficult because to reduce random coincidences one must reduce the rate of dissociation without sacrificing the ionization rate. Decreasing the laser spot size may improve the contrast between ionization and random coincidences by increasing the intensity (which may increase the ionization rate) and decreasing the interaction volume (which will lower the dissociation rate). Efforts to improve the experiment may be attempted in the future. Alternatively, we suggest a scheme which involves subtracting the random coincidences using the measured data. This provides an approximate but accurate-enough evaluation of the ionization yield as a function of delay.

4.4.1 Subtraction of random coincidences

In this section, two methods for generating and subtracting random Ar^++Ar^+ coincidences are presented. In the first, the measurement of the Ar^++Ar dissociation channel is used to statistically evaluate the contribution of random coincidences. In the second, the measured random coincidences that are clearly separated from the true events are used to generate a random coincidences map as a function of delay, which is then subtracted from the ionization map.

Statistical method for subtracting random coincidences

Assuming that all of the random coincidences originate from dissociating molecules, which is by orders of magnitude the dominant fragmentation channel, the rate of producing a random pair of Ar^+ ions from the dissociation of two molecules into Ar^++Ar in the same laser pulse is described by Poisson statistics as

$$R_{rand} = \frac{1}{2} e^{-R_{diss}} R_{diss}^2, \tag{4.1}$$

where R_{rand} is the rate of random coincidences and R_{diss} is the rate of Ar^++Ar dissociation events per laser pulse. R_{diss} is related to the measured number of Ar^++Ar events by

$$R_{diss} = \frac{M_{diss}}{N \varepsilon_{\mathrm{Ar}} \varepsilon_{\mathrm{Ar}^+}}, \tag{4.2}$$

where M_{diss} is the measured number of Ar^++Ar events, N is the number of laser shots, and $\varepsilon_{\mathrm{Ar}^+}$ and $\varepsilon_{\mathrm{Ar}}$ are the detection efficiencies of Ar^+ and Ar fragments, respectively (evaluated using the method based on Ref. [12] and described in Sec. 3.3.3). Similarly, the measured number of random coincidences, M_{rand} and the rate of random coincidences are related by

$$R_{rand} = \frac{M_{rand}}{N \varepsilon_{\mathrm{Ar}^+}^2}. \tag{4.3}$$

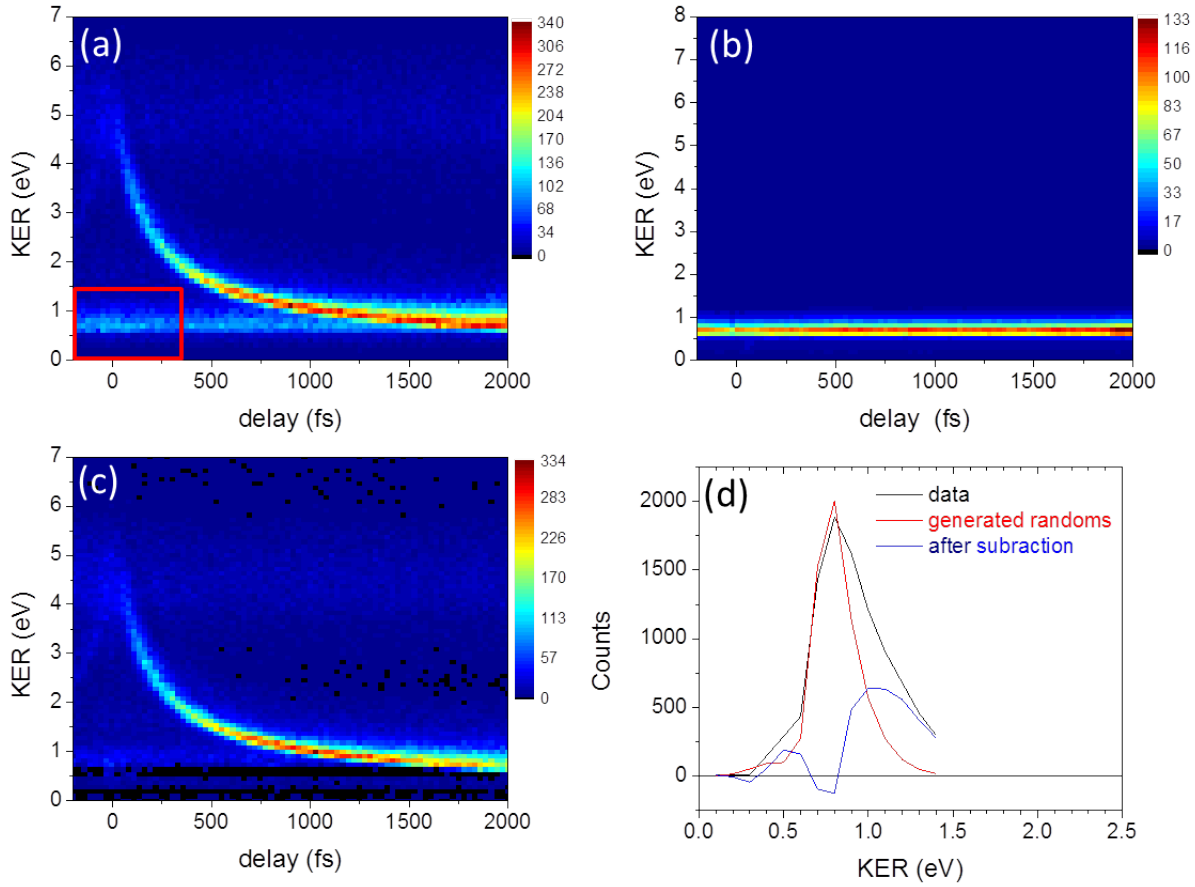

Figure 4.4: (a) Measured Ar^++Ar^+ events mapped as a function of pump-probe delay and KER. (b) Map of random coincidences generated by applying Poisson statistics to the measured dissociation yield as a function of delay and KER. (c) Ionization map after subtraction of random coincidences. (d) KER distribution integrated over the delay range marked by the red box in panel (a) before and after subtraction indicates that the subtraction is effective at lower KER but does not work as well for higher KER.

The dissociation rate is determined for each delay step and KER bin. Similarly, the number of random coincidences, M_{rand}, can be solved for by substituting equation 4.3 into equation 4.1, resulting in

$$M_{rand} = \frac{c\,N\,\varepsilon_{\mathrm{Ar}^+}^2}{2} e^{-R_{diss}}\,R_{diss}^2 \tag{4.4}$$

where we include a scaling factor, c, since only a fraction of the random Ar^++Ar^+ pairs pass the momentum conservation conditions we impose.

From this expression, we can generate the yield of random coincidences in each delay step and at each KER bin using the measured KER distribution of Ar^++Ar for each delay step.

The resulting random coincidences map binned as a function of delay and KER, shown in Fig. 4.4(b), is then subtracted from the measured Ar^++Ar^+ data, leading to the ionization map shown in Fig. 4.4(c). The constant, c, is used as a fit parameter to optimize the subtraction. For the subtraction shown in Fig. 4.4, $c = 1$ was used. The quality of the subtraction is illustrated in Fig. 4.4(d) by comparing the yield of random coincidences corresponding to the "boxed" region in panel (a). Clearly, while the subtraction does remove a large fraction of the random coincidences, reducing their total yield by about 65%, it does not adequately suppress the random coincidences with KER above about 0.8 eV. Nevertheless, a comparison of the ionization yield maps before and after subtracting the generated random coincidences is shown in Fig. 4.4(a) and (c), respectively. After subtraction, the "tail" associated with the ionization of dissociating Ar_2^+ shows a hint of enhancement in the vicinity of 1000 fs delay, but a cleaner method of subtracting the random coincidences is needed to verify this observation.

This method of subtraction - using the measured dissociation events and Poisson statistics to determine the probability distribution of random Ar^+-Ar^+ coincidences as a function of KER - is correct in principle, but it relies on identical analysis and experimental conditions for the dissociation and ionization channels. In addition, the number of random coincidences we calculate in equation 4.4 uses the average dissociation rate and does not account for fluctuations in the rate. In terms of the analysis, consider that if the dissociation channel was analyzed in such a way that events with high KER were excluded, the KER distribution of generated random coincidences would also be missing the high-KER component. To rule out this source of error, both channels were analyzed carefully to ensure that no data was lost in the analysis. We adjusted the size of the "gates" used to select these channels on the CTOF map (see Sec. 2.3) to be large enough, and both channels were analyzed with identical conditions on the center-of-mass momentum.

On the other hand, differences in the *measurement* of these two channels are harder to control and can cause the problems we encounter in the random coincidences subtraction. Specifically, losses of high-KER Ar^+ + Ar due to reduced detection efficiency on part of the detector would result in the missing high-KER component of the random coincidences

distribution. It is likely that an unknown issue is affecting the measurement of high-KER $Ar^+ + Ar$. In addition, we do not consider random coincidences of one ion from an Ar^++Ar^+ event and the other ion from an Ar^++Ar event. This could result in higher KER; however, we believe it is reasonable to neglect this source of random coincidences because the rate of ionization is about two orders of magnitude lower than the dissociation rate. Thus, these types of random coincidences would contribute at most about 1% to the total random coincidences spectrum. Since the discrepancy between the measured and generated random coincidences could be due to a variety of factors that need further work to understand, we instead propose another method for generating and subtracting random coincidences.

Subtraction using the measured random coincidences "directly"

We propose another approach that can be used to provide a better approximate subtraction of the random coincidences. Instead of using the dissociation rate to generate the distribution of random coincidences, the measured random coincidences themselves, at short delays, are used to generate a random coincidences map over all delays; therefore, we expect this method to work better. At small time delays (e.g. the boxed region of Fig. 4.4(a)), the random coincidences are separated from the true coincidence events. So, in essence, these measured random coincidences are duplicated to generate the total random coincidences spectrum at all delays for subtraction. First, the random coincidences associated with each delay step in the marked regions are selected, as illustrated in Fig. 4.5(a). Short delays where the pump and probe pulses overlap are excluded because the increased peak intensity may produce $Ar^+ + Ar$ with different KER and dissociation rate, and therefore affect the KER and yield of the random coincidences. Then, the KER spectra in each delay step within the selected regions are duplicated and randomly time-ordered to produce a full map of random coincidences, as shown in Fig. 4.5(b). The exact time ordering has no meaningful effect on the location or magnitude of the enhancement after subtraction. This spectrum is then subtracted from the measured delay–KER spectrum of $Ar^+ + Ar^+$ events, resulting in Fig. 4.5(b). In Fig. 4.5(d), the integrated yield within the boxed regions of panel (a) is

shown before and after subtraction. One can easily see that this method is more effective by comparing Fig. 4.4(d) and 4.5(d).

We should note that directly subtracting the measured random coincidences this way is only accurate if the rate of random coincidences is constant over all delay steps. The rate of random coincidences is directly related to the dissociation rate, which is measured simultaneously and fluctuates by no more than 5% over the course of the measurement. Therefore, we expect the yield in the ionization channel after subtraction to be accurate to within a few percent. Other errors associated with this method are discussed in Sec. 4.4.2. We also note that this method is more straightforward than the statistical method described previously in Sec. 4.4.1. In this method there is no need to carefully match the analysis conditions of the $Ar^+ + Ar^+$ and $Ar^+ + Ar$ channels nor adjust a scaling parameter, c.

4.4.2 Evaluation of enhanced ionization

After subtraction of the random coincidences using the method described in Sec. 4.4.1, it is clear that ionization of the dissociating wave packet is enhanced at delays of a couple hundred femtoseconds, as shown in Fig. 4.5(c). While our primary goal was to simply identify any enhancement at long time delays, there is some use in exploring the location and magnitude of the enhancement more quantitatively. The methods described in this section to quantify the enhancement serve two purposes: they allow us to show that the enhancement we observe is statistically significant, and they provide a prescription for future measurements that may focus more specifically on the exact magnitude of the enhancement.

To quantify the location and magnitude of the enhancement, the events associated with this process must be carefully selected. To aid in setting a gate on these events, a function is fit to the "tail" feature, as shown in Fig. 4.6(a). The fit function that provided a good fit was a double-exponential decay, $f(\Delta t) = A_1 e^{-\Delta t/\tau_1} + A_2 e^{-\Delta t/\tau_2}$, where Δt is the delay. Since this function is only used to select the events of interest, it is only important that this function follows the general shape of the tail, not to provide a perfect fit.

The difference between the measured KER and the value of $f(\Delta t)$ at each delay step,

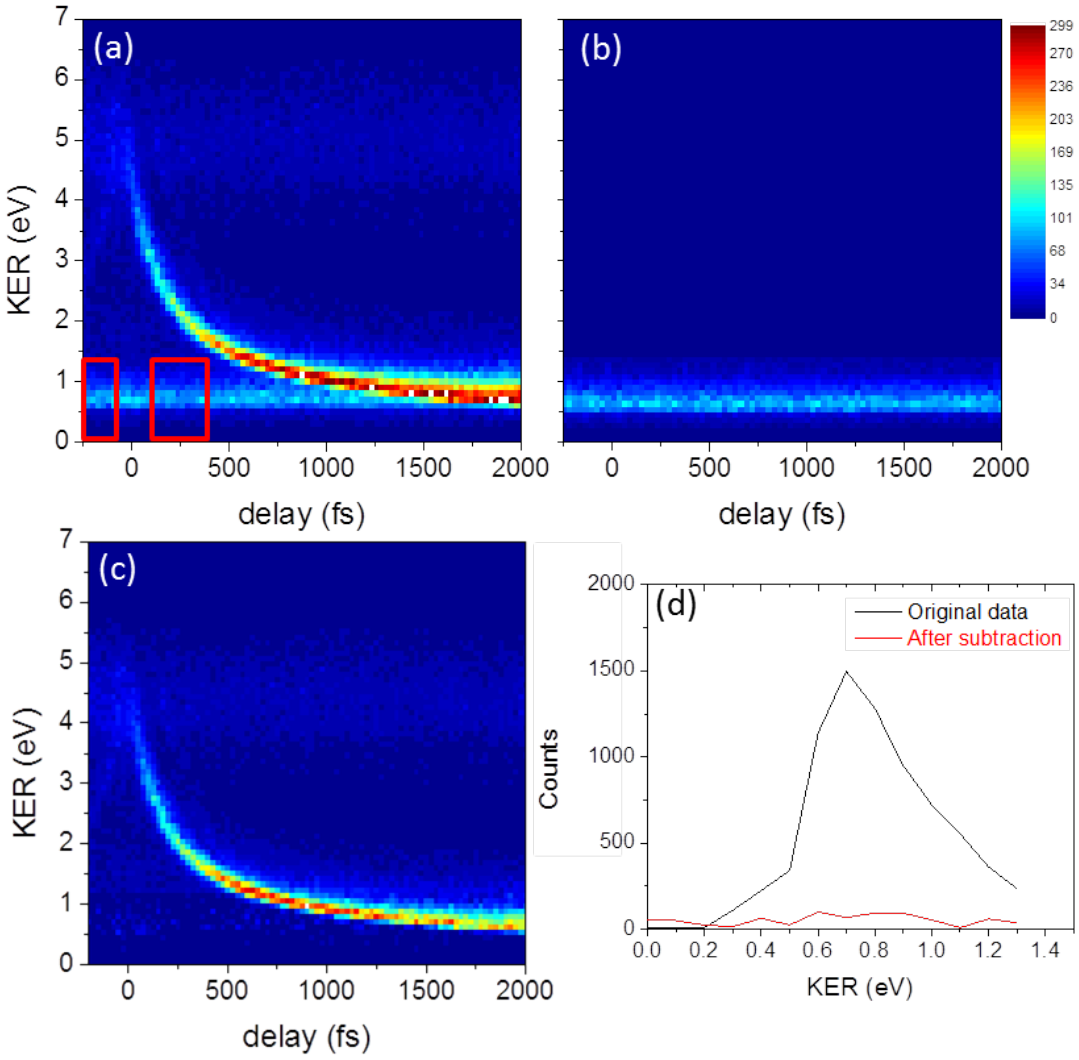

Figure 4.5: Subtraction of random coincidences from the delay-KER map of $Ar^+ + Ar^+$ events using the measured random coincidences "directly". (a) The red rectangles indicate regions where the random coincidences are clearly separated from the true coincidence events. Short delays where the pulses overlap are excluded. (b) Random coincidences spectrum generated by duplicating and randomly time-ordering the KER spectra associated with the selected random coincidences. (c) $Ar^+ + Ar^+$ yield after subtraction of the random coincidences. (d) The Ar^++Ar^+ yield before and after subtraction integrated over the red rectangles in panel (a).

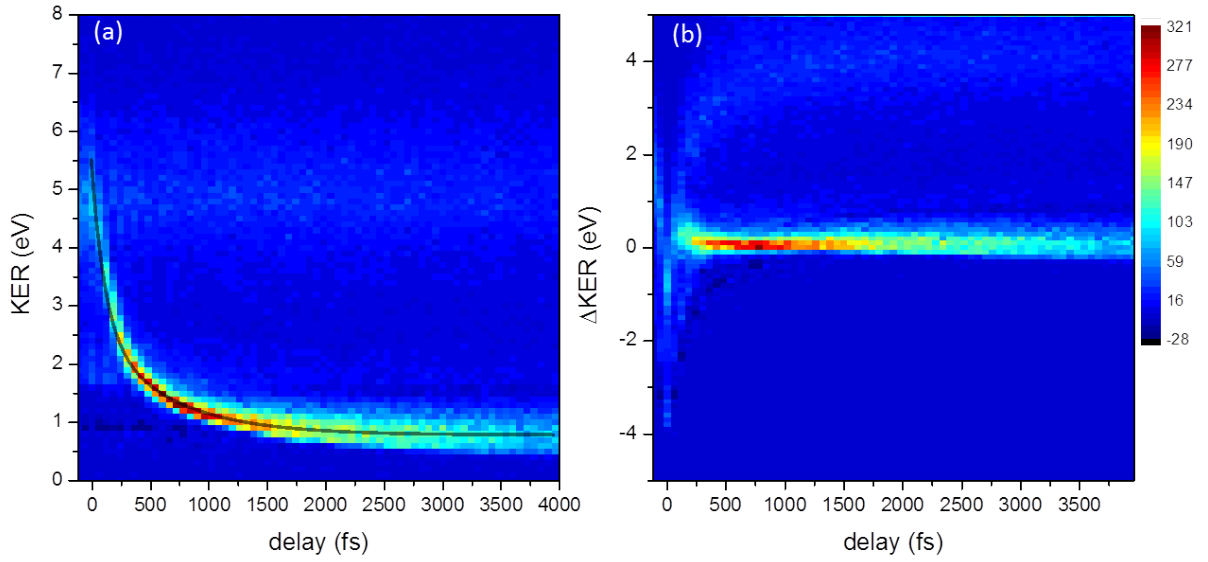

Figure 4.6: (a) Ionization map with double exponential decay fit to the "tail". (b) "Straightened" ionization map generated by evaluating the difference between the measured KER and the value of the fit function at each delay step (see text).

which we refer to as ΔKER, is then determined. This results in a "straightened" tail as shown in Fig. 4.6(b). To select events associated with the tail, a gate in ΔKER is applied. The ΔKER distributions for a few values of delay plotted in Fig. 4.7(a) show that the ΔKER distribution is approximately the same over all delays. This allows us to apply a uniform ΔKER gate indicated by the dashed lines in Fig. 4.7(a). By integrating the yield within the gate for each delay step, the $Ar^+ + Ar^+$ yield as a function of delay, shown in Fig. 4.7(b), is obtained.

The choice of gate width and position introduces some uncertainty to the evaluation of the yield. To quantify this uncertainty, the yield is evaluated for several different gate choices, as shown in Fig. 4.8. The integrated yields shown in Fig. 4.8(b) corresponding to all possible combinations of the gates shown in Fig. 4.8(a) are used to estimate the uncertainty introduced by the gating. The standard deviation of the yields resulting from the different gate choices is evaluated at each delay and plotted relative to the statistical error in Fig. 4.8(c). The error, σ_{gate}, is then estimated by a function that fits the general

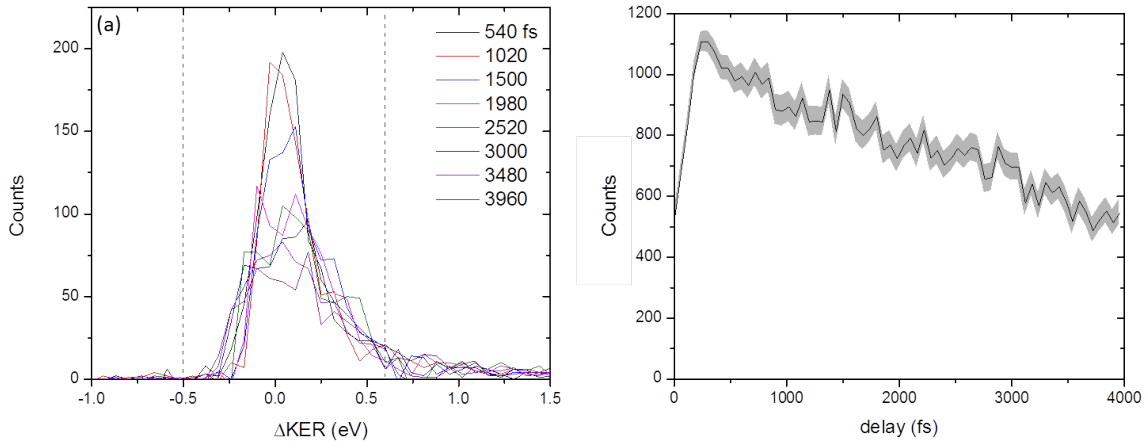

Figure 4.7: (a) ΔKER distributions plotted for several different delay steps. (b) Integrated yield evaluated using the dashed ΔKER gates shown in panel (a). The shaded area indicates the statistical error of the integrated yield.

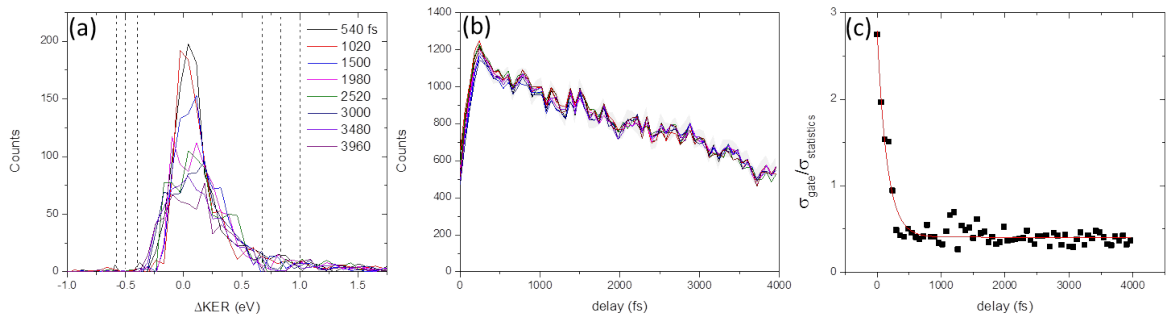

Figure 4.8: (a). ΔKER distributions plotted for several delay steps with dashed lines indicating different gates. (b) Integrated yields as functions of delay corresponding to each of the gate combinations in panel (a). (c) Standard deviation relative to the statistical error of the yields from 9 different ΔKER gates as a function of delay. The red line is an exponential decay fit to provide an analytical expression for σ_{gate}(delay).

trend, as shown by the red line in Fig. 4.8(c).

An additional error is introduced by the subtraction of random coincidences. Recall that random coincidences spectra are selected at a few delay steps where they are separated from true $Ar^+ + Ar^+$ events, then duplicated and randomly time-ordered to generate a full map of random coincidences that is then subtracted from the measured data. The randomized time order in the subtraction procedure introduces an additional uncertainty, as shown in Fig. 4.9. The integrated yields are plotted for a few versions of the randomized time ordering

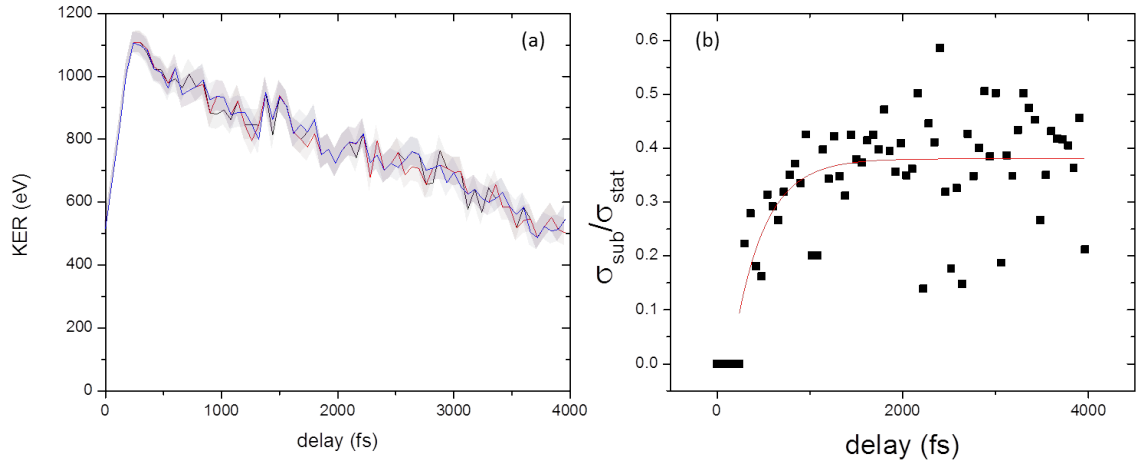

Figure 4.9: (a) Integrated yields evaluated for different randomized subtractions of random coincidences. (b) Standard deviation of the results of subtracted randoms with different time order relative to the statistical error of the yields plotted as a function of delay. The red line is a fit function that provides an approximate analytic form of σ_{sub}(delay).

of random coincidences. The standard deviation of the yields is shown in panel (b). The ionization tail only overlaps with the random coincidences at large delays, which explains why the subtraction of random coincidences introduces very little additional error at short delays.

All of the above errors are added in quadrature to obtain the total uncertainty. This procedure was repeated to evaluate the enhancement and estimate the error for three different pump-probe scans with ranges of 2, 4, and 12 ps. The integrated yields (normalized to match the peak height) are shown in Fig. 4.10(a), with the error indicated by the shaded areas.

To determine the magnitude of the enhancement, the ratio of the maximum yield and the average yield near the end of the scan, as indicated by Y_1 and Y_2 in Fig. 4.10(a), is calculated. The number of delay points used to evaluate Y_2 introduces another error of about 2% from the standard deviation of Y_2 using the final 4 delay steps up to the final 8 steps of the scan. The exact value of this error for each scan was evaluated and included in the error bar on the enhancement, shown in 4.10(b). These error bars include each independent source of error described in this section added in quadrature. The magnitudes of the enhancement for the three measurements are shown in Fig. 4.10(b). The dashed line and shaded area indicate the

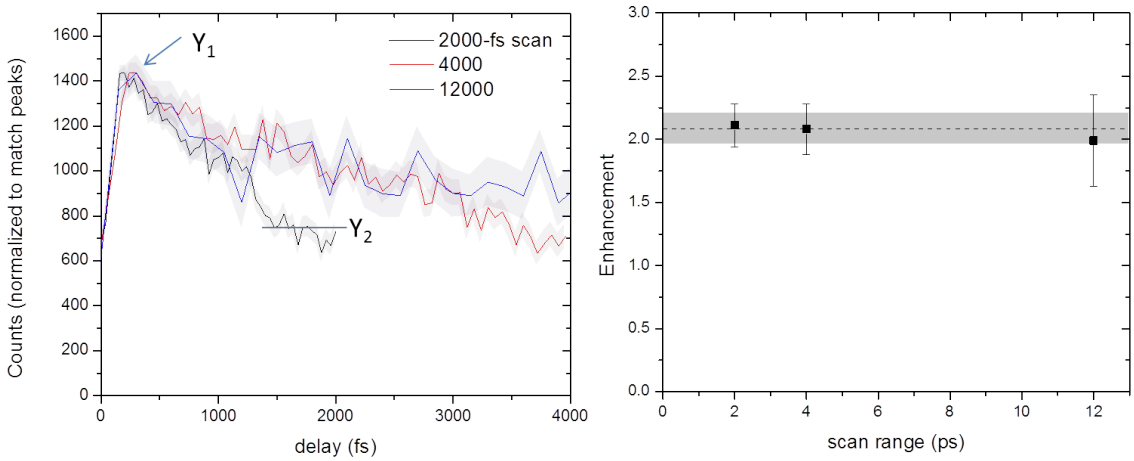

Figure 4.10: (a) Integrated yields plotted as a function of delay for three separate pump-probe scans. (b) Enhancement (defined as the ratio of Y_1/Y_2, see panel (a)) obtained from the three measurements. The dashed line and shaded area indicate the weighted mean and the error of the weighted mean, respectively.

weighted mean and error of the weighted mean. We observe an enhancement of 2.08 ± 0.12 at about 300-fs delay.

Improved method for selecting data

One issue with the previous method used to determine the gate on the ionization "tail" is that at short delays where the slope of the tail is steeper, the ΔKER distribution is broader, and therefore the uniform gate on ΔKER doesn't work as well at short delays. To improve the quality of the selection of Ar^++Ar^+ events on the ionization tail, especially at short delays, we propose another method.

Instead of calculating ΔKER - the difference between the measured KER and the value of the fit function at each delay step - we calculate the perpendicular distance between the curve and each data point (i.e. the shortest distance between the point and the fitted curve). This distance, which we refer to as y', as illustrated in Fig. 4.11(a), narrows the distribution at short delays where the slope of the tail on the delay–KER map is steep. This will enable us to use a uniform gate (on y' now) to more accurately select the true Ar^++Ar^+ events.

To calculate y', the minimum distance between the delay and KER coordinates associated

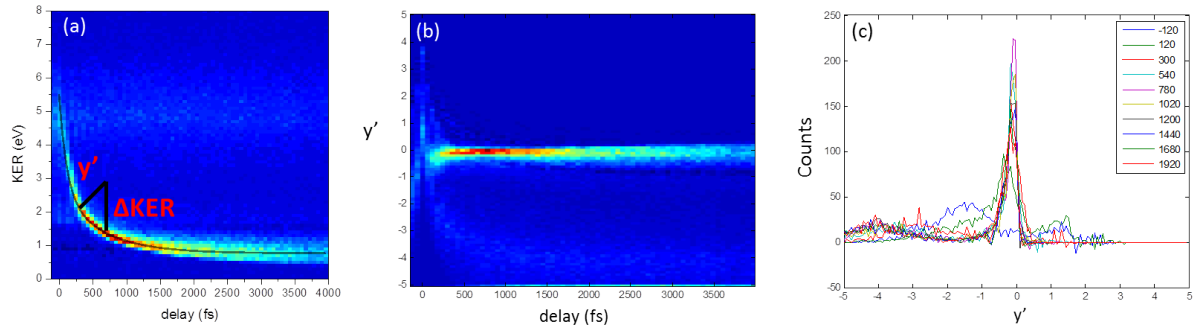

Figure 4.11: (a) delay–KER map of $Ar^+ + Ar^+$ events. Lines illustrate the difference between the definitions of y' and ΔKER. (b) Ionization events mapped as a function of delay and y'. (c) y' distributions plotted for several delay steps.

with each event and the fit curve $f(\Delta t)$. The distance, r, between a point (x_0, y_0) and a function $f(x)$ is given by

$$r = \sqrt{(x_0 - x)^2 + (y_0 - y)^2}. \tag{4.5}$$

Or,

$$r = \sqrt{(x_0 - x)^2 + (y_0 - f(x))^2}. \tag{4.6}$$

The value y' is defined as the minimum value of r, which can be found from

$$\frac{\partial}{\partial x} r = 0. \tag{4.7}$$

The value of x that minimizes y' is solved for to determine y' event by event. The resulting map of ionization events as a function of delay and y', as shown in Fig. 4.11(b), displays a similar "straightened" tail as in the previous section. The $N(y')$ distributions, shown in Fig. 4.11(c), demonstrate that these distributions are narrow and fairly uniform at all delays.

Following the same prescription as in the previous section, we estimate the uncertainty introduced by applying the gate on y' and evaluate the enhancement as shown in Fig. 4.12. While the location of the enhancement is the same as with the previous method (around 300 fs), the magnitude of the enhancement is larger using this analysis method, specifically 2.5 ± 0.11 compared with the previous result of 2.08 ± 0.12. The relative error is also reduced

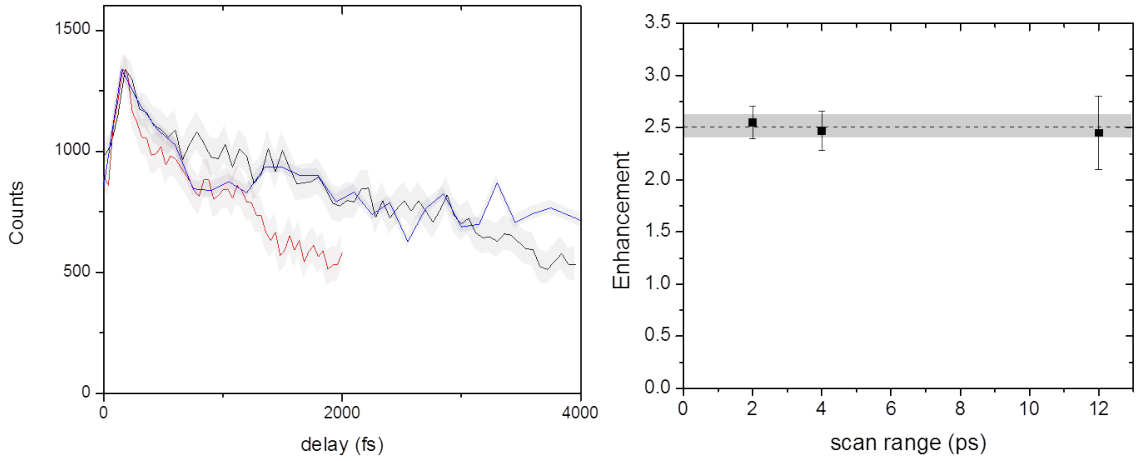

Figure 4.12: (a). Integrated yields for scans of 2-, 4-, and 12-ps range. (b). Evaluated enhancement for the three scans. The dashed line and shaded area indicate the weighted average and the error.

(4.4% compared to 5.8%). This is most likely due to the improved ability to select the events at short delays.

In summary, we have presented a few methods for subtracting random coincidences from the delay–KER spectrum of $Ar^+ + Ar^+$ events. We also described two methods for selecting the events within the "tail" associated with ionization of the dissociating Ar_2^+ wave packet and quantifying enhancement of the ionization yield. We identify an enhancement of 2.5 ± 0.11 at delays around 300 fs that is statistically significant (a 22σ effect). Though the exact magnitude of the enhancement was not a primary goal of these studies, the methods presented in this section provide a guide for studying this phenomenon more quantitatively in the future.

4.5 Pump-probe studies of ionization of a fast HD^+ beam

Our pump-probe studies of the ionization of HD^+ revealed an ionization enhancement of the dissociating wave packet at surprisingly long delays corresponding to large internuclear

separations where the fragments are expected to behave like separate atoms. This study was motivated by a prediction of enhanced ionization at large internuclear distances based on a model proposed by Esry *et al.* [157] in which the same multiphoton concepts are used to describe dissociation and ionization with light-dressed potentials.

A detailed description of the experimental method can be found in Ref. [172]. Briefly, synchronized pump and probe laser pulses were obtained using a Mach-Zehnder interferometer. The linearly polarized 23-fs, 790-nm pulses (at 10 kHz) provided by the PULSAR laser [44] were focused onto an ion-beam target by an $f = 203$-mm off-axis parabolic mirror. The pump- and probe-pulse intensities were 7.6×10^{13} and 3.3×10^{14} W/cm^2, respectively.

The 7 keV HD^+ beam was generated by fast electron impact ionization in an electron cyclotron resonance (ECR) ion source, selected, and electrostatically focused into a well-collimated beam. The ion beam was steered through a spectrometer where it intersected the laser beam. Fragments generated in the laser interaction region were separated from each other by their time-of-flight by the longitudinal field of the spectrometer. The time and position information for every fragment (except electrons) was measured by a delay line detector and recorded event-by-event. The coincidence measurement of the fragments and their time- and position-information allows for the 3D momentum of each fragment to be obtained [5, 12, 20, 21].

The ionization yield, i.e. the number of $H^+ + D^+$ events, as a function of the pump-probe delay and kinetic energy release (KER) is shown in Fig. 4.13. The high-KER delay-independent feature is the result of ionization of the bound wave packet [158, 167, 168, 174–176]. The tail extending to low KER with increasing delay is due to ionization of the dissociating HD^+ wave packet [158, 167, 168, 174–176]. The enhancement we observe at about 25-fs delay corresponds to an internuclear separation of about 12 a.u., which is consistent with previous observations of enhancement in the range of 4–15 a.u. in measurements on the neutral molecular hydrogen target [154, 156, 168] as well as the cation [23, 25, 160]. The exact location and width of the enhancement depends on the laser pulse parameters such as the peak intensity. In contrast, the broad enhancement feature centered around 250-fs delay, which corresponds to an internuclear separation of about 45 a.u., has not been previously

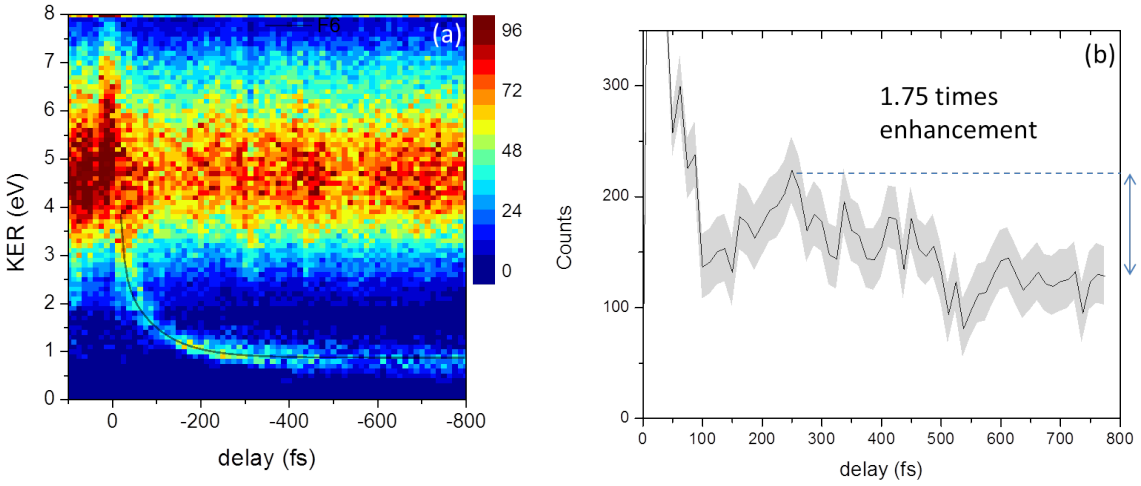

Figure 4.13: (a) The yield of $H^+ + D^+$ events mapped as a function of the pump-probe delay and KER. The high-KER component is due to the ionization of bound HD^+. The tail extending to lower KER is due to ionization of the dissociating HD^+ wave packet, and it exhibits a broad enhancement around 250 fs. (b) The integrated yield indicates a 1.75 ± 0.33 times enhancement in the ionization of the dissociating wave packet at a delay of 250 fs.

observed. Enhancement at such large internuclear distances is surprising given that the interaction between the ionic and atomic fragments is extremely weak (i.e. the potentials are practically flat at this distance).

Following the procedure outlined in Sec. 4.3, the enhancement was quantified. Random coincidences were subtracted by duplicating and randomly time-ordering the separated random coincidences at short time delays, as described in Sec. 4.4.1. The integrated yield as a function of delay was determined following the method described in Sec. 4.4.2 by evaluating the distance from a double-exponential decay fit function, y', and selecting events by placing a gate on the y' distributions. We obtained a 1.75 ± 0.33 times enhancement at a delay of about 250 fs, as shown in Fig. 4.13(b), where the uncertainty associated with random subtraction and selection of the events is estimated as described in Sec. 4.4.1.

One may ask why this enhancement was not observed in previous pump-probe measurements on neutral hydrogen molecules. The primary difference between measurements on H_2 and H_2^+ targets is how the dissociating wave packet is launched. In experiments starting from a neutral molecule, an intense pump pulse is needed to ionize and dissociate the

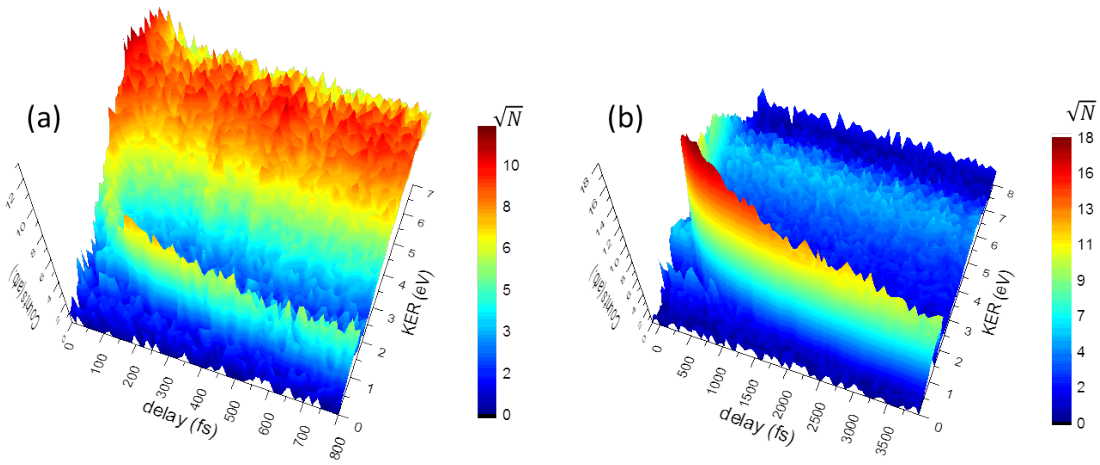

Figure 4.14: Maps of the ionization of HD^+ (a) and Ar_2^+ (b) as a function of pump-probe delay and KER. Note that the z-axis is a $\sqrt{N}$ scale to emphasize the weaker features.

molecule. The dissociating wave packet therefore originates from a different vibrational population. Furthermore, the potentials could be distorted by the strong field associated with the intense pump pulse, which may wash out the enhancement. In our measurement on the molecular ion, a relatively weak pump pulse is used which reduces distortions due to intensity, and dissociation is dominated by bond softening.

4.6 Comparison of HD^+ and Ar_2^+ results

The successful pump-probe measurements of HD^+ and Ar_2^+ dissociation and ionization, described in the previous sections, provide the opportunity to compare the two systems. The respective ionization maps, shown in Fig. 4.14, display a few interesting similarities and differences. The most important similarity between the two measurements is that each exhibits enhancement of the ionization rate of the dissociating wave packet at large time delays, suggesting that this may be a general phenomenon. The magnitude of the enhancement is slightly larger for Ar_2^+, 2.5 ± 0.11 times compared to 1.75 ± 0.33 times enhancement for HD^+. This could be due to the symmetries of the states that contribute to dissociation, and will be further discussed in Sec. 4.7. The location of the enhancement, broadly peaked at around 300 fs for Ar_2^+ and 250 fs for HD^+, corresponds to internuclear distances of 14-20 a.u. and

Ar_2^+				HD^+		
delay (fs)	I_{bound}/D	$I_{diss.}/D$		delay (fs)	I_{bound}/D	$I_{diss.}/D$
500	0.0079 ± 0.001	0.015 ± 0.001		200	0.33 ± 0.01	0.041 ± 0.004
1000	0.0076 ± 0.002	0.014 ± 0.001		500	0.36 ± 0.01	0.032 ± 0.005
1500	0.0074 ± 0.002	0.013 ± 0.001		700	0.31 ± 0.01	0.027 ± 0.005
2000	0.0072 ± 0.002	0.011 ± 0.001				

Table 4.1: Rates of ionization of the bound wave packet (I_{bound}) and dissociating wave packet($I_{diss.}$) relative to the dissociation rate (D) for Ar_2^+ and HD^+.

about 40-50 a.u., respectively.

The most striking difference between these measurements is the relative yields of ionization of the bound and dissociating wave packets. As clearly visible in Fig. 4.14, in HD^+ ionization of the bound wave packet dominates, while in Ar_2^+ it is a much smaller feature than the ionization of the dissociating molecule. By integrating the ionization yields of the bound and dissociating wave packets, we can quantify this difference, as shown in Table 4.1. The ionization yields are evaluated relative to the measured dissociation rates at a few different delays near and far from the enhancement feature. In Ar_2^+, ionization of the bound wave packet is about a factor of 2 weaker than ionization of the dissociating wave packet. For HD^+, the opposite is true, ionization of the bound wave packet is about a factor of 10 larger than ionization of the dissociating wave packet.

This raises some questions: Are these differences due to suppressed ionization of bound Ar_2^+? Or, are they due to enhanced ionization of dissociating Ar_2^+? To answer, we need to normalize the measurements of HD^+ and Ar_2^+ to each other. The normalized dissociation rates are calculated using Eq. 4.8. The rates are normalized by the number of laser pulses, the ion beam current, laser focal area, and velocity of the ion beam in each measurement. More simply, the integral of the ion-beam current over the course of the measurements also accounts for the number of laser pulses, and the relative rates can be written as

$$\frac{D_{HD^+}}{D_{Ar_2^+}} = \frac{M_{HD^+}}{M_{Ar_2^+}} \times \frac{I_{Ar_2^+}}{I_{HD^+}} \times \frac{A_{HD^+}}{A_{Ar_2^+}} \times \frac{v_{HD^+}}{v_{Ar_2^+}} = 0.12, \tag{4.8}$$

where M is the measured number of events, I is the integrated ion-beam current, A is the cross-section area of the laser spot (assuming similar Gaussian profiles), and v is the velocity

of the ion beam, all of which are measured quantities. We find that $D_{HD^+}/D_{Ar_2^+} = 0.12$, that is the dissociation rate of Ar_2^+ is nearly an order of magnitude greater than HD^+.

Using this normalization factor, we can compare the rates of ionization of the bound wave packets of the two molecules, and similarly the dissociating wave packets. Specifically,

$$\frac{I^{diss.}_{Ar_2^+}}{I^{diss.}_{HD^+}} = \frac{I^{diss.}_{Ar_2^+}/D_{Ar_2^+}}{I^{diss.}_{HD^+}/D_{HD^+}} \times \frac{D_{Ar_2^+}}{D_{HD^+}} = 3.4 \pm 0.4, \tag{4.9}$$

and

$$\frac{I^{bound}_{Ar_2^+}}{I^{bound}_{HD^+}} = \frac{I^{bound}_{Ar_2^+}/D_{Ar_2^+}}{I^{bound}_{HD^+}/D_{HD^+}} \times \frac{D_{Ar_2^+}}{D_{HD^+}} = 0.2 \pm 0.03. \tag{4.10}$$

From these values, we see that the differences between ionization of Ar_2^+ and HD^+ are due in part to an enhancement of the ionization of dissociating Ar_2^+ by a factor of about 3 relative to HD^+ and a suppression of the ionization of bound Ar_2^+ by about a factor of 5 relative to HD^+.

Additionally, from these values we find that the total ionization rates, (I_{bound}+$I_{diss.}$), are within about a factor of 2 of each other, given by

$$\frac{I_{Ar_2^+}}{I_{HD^+}} = \frac{I^{diss.}_{Ar_2^+} + I^{bound}_{Ar_2^+}}{I^{diss.}_{HD^+} + I^{bound.}_{HD^+}} = \frac{(I^{diss.}_{Ar_2^+} + I^{bound}_{Ar_2^+})/D_{Ar_2^+}}{(I^{diss.}_{HD^+} + I^{bound.}_{HD^+})/D_{HD^+}} \times \frac{D_{Ar_2^+}}{D_{HD^+}} = 0.4 \pm 0.1. \tag{4.11}$$

While we have identified more clearly the differences between the two measurements, there are still some unanswered questions about the sources of these differences. For example, why is the ionization of bound Ar_2^+ suppressed? The ionization potentials do not provide an explanation, as the vertical ionization potentials (I_p) from R_0 of HD^+ and Ar^+ are similar (about 29 eV and 24 eV respectively). In fact, while the I_p of HD^+ is greater than Ar_2^+, its ionization rate is also greater. Perhaps the enhanced dissociation rate of Ar_2^+ depletes the population of bound Ar_2^+. Further work is needed to answer this and other questions regarding the comparison of the ionization of HD^+ and Ar_2^+.

4.7 Comparison with theory

The motivation for studying the enhancement of ionization at large internuclear distance was the general model suggested by Esry *et al.* [157, 161] in which dissociation and ionization are described using the same multiphoton concepts. In essence, Floquet potentials, which have long been used to describe dissociation of H_2^+ [24], are used so that we can understand the dynamics in terms of curve crossings. In the Floquet representation, the exchange of photons with the laser field is represented by adding an index n to the field-free Born-Oppenheimer potentials and shifting them in energy by $\pm n\omega$, where ω is the carrier frequency of the laser field in atomic units. We should point out that while the Floquet picture applies to a CW laser field, the picture can still be used as a qualitative description of laser-induced transitions in short laser pulses. In practice, the time dependence of the laser field can be introduced through the coupling matrix elements. Laser-induced transitions are described by the coupling between the resulting diabatic Floquet potentials, and transitions are most likely where the curves cross. For example, bond softening in HD^+ is due to the coupling between the $1s\sigma$ state without photons ($1s\sigma - 0\omega$) and the $2p\sigma$ state dressed by one photon ($2p\sigma - 1\omega$), as depicted in Fig. 4.15(a).

In the same manner, the $1/R$ ionization potential is dressed by n photons, resulting in the $1/R - n\omega$ curves plotted in Fig. 4.15(a). These curves are the ionization threshold potentials, i.e. they assume the electron is "born" with zero energy. Employing this model we expect an ionization enhancement of the dissociating HD^+ at critical values of R where the ionization threshold potentials cross the dissociation potential on which the dissociating wave packet is propagating.

The observed ionization enhancement in HD^+ at around 250-fs delay is associated with the crossing between the $2p\sigma - 1\omega$ dissociation potential and the $1/R - 10\omega$ ionization threshold. The KER of H^++D^+ near the ionization enhancement time delay is about 1 eV, which by energy conservation is simply the difference between the initial energy and the asymptotic $1/R - 10\omega$ limit. The initial energy associated with this KER is around the $\nu = 7$ level of HD^+, which is 0.3 eV below the crossing between the ground state and the

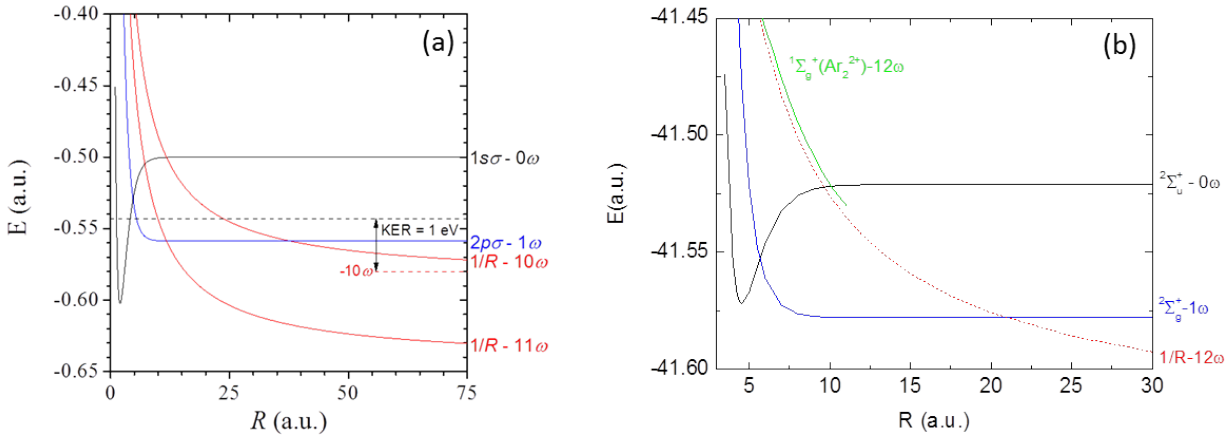

Figure 4.15: (a) The diabatic Floquet potentials used to describe dissociation and ionization of HD^+, adapted from Ref. [177]. Enhancement is expected at the crossings of the dressed ionization thresholds and the dissociation potential at 12 and 38 a.u. (b) The diabatic Floquet potentials used to describe dissociation and ionization of Ar_2^+ adapted from Ref. [173]. The $^1\Sigma_g^+$ curve of Ar_2^{2+} is approximated by a $1/R$ curve, and ionization enhancement is expected where the $1/R - 12\omega$ and $X\,^2\Sigma_g^+$ curves cross at about 21 a.u.

dissociation potential (i.e. E= -0.542 a.u.). Solving the classical equations of motion on the $2p\sigma$ potential assuming an initial energy of -0.542 a.u. results in an internuclear distance of 45 a.u. after 250 fs, in fairly good agreement with the location of the $1/R - 10\omega$ crossing at 38 a.u. Note that the crossing only represents the threshold where the channel opens, and if the ionized electron carries some energy, the crossing shifts to larger R and therefore longer delays.

While the Floquet picture is successful in providing qualitative support of the enhancement we observe in ionization of HD^+, some discrepancies arise in comparing with the Ar_2^+ data. The relevant Floquet potentials for Ar_2^+ are shown in Fig. 4.15(b). The coupling between the ground state with no photons, $X\,^2\Sigma_u^+ - 0\omega$, and the excited $X\,^2\Sigma_g^+$ state with one photon, $X\,^2\Sigma_g^+ - 1\omega$, causes dissociation, and the coupling is strongest where the curves cross. Using the same approach, the $^1\Sigma_g^+$ ionization threshold of Ar^++Ar^+, adapted from Ref. [178], is dressed by 12 photons. Since only a partial curve is available, we approximate the ionization threshold by a $1/R$ curve that closely resembles the threshold. Ionization of the dissociating wave packet is most likely near the crossing of the $X\,^2\Sigma_g^+ - 1\omega$ and $^1\Sigma_g^+ - 12\omega$

curves at an internuclear separation of 21 a.u. This corresponds to a time delay of about 600 fs, much larger than the observed enhancement at about 300 fs.

More importantly, recent TDSE calculations for ionization of H_2^+ performed by Brett Esry's group cast additional doubts on the unified Floquet picture. While the calculations predict enhancement at large internuclear distances, the location is inconsistent with the Floquet picture. However, while studying this problem theoretically, Esry's group recently discovered another explanation for enhancement at large internuclear distance. They show that the ionization enhancement we observe experimentally is the result of a two-center interference effect extending to surprisingly large internuclear distances. This explanation is similar to the description of suppressed ionization of bound molecules [179] at smaller internuclear distances, in which two-center interference can result in enhancement or suppression of ionization depending on the symmetry of the states involved in dissociation. The surprising extension of this effect to large internuclear distances where one would expect the fragments to behave as separate atoms is the topic of a future publication [180].

4.8 Summary

In summary, we have explored the ionization of bound and dissociating HD^+ and Ar_2^+ by a strong laser field using a pump-probe technique. A surprising ionization enhancement of the dissociating wave packet was observed at long delays corresponding to large internuclear distances for both molecules. We presented a few methods for evaluating the enhancement, from which we determined the magnitude and location of the enhancement and estimated the uncertainties associated with the methods. We found statistically significant enhancement in both studies: 2.5±0.11 times enhancement broadly peaked at about 300-fs delay for Ar_2^+, and 1.75±0.33 times enhancement broadly peaked at about 250-fs delay for HD^+. While the goals of these measurements were simply to observe whether or not there is enhancement at large delays, the methods presented in this chapter may be used in the future to quantitatively study the magnitude of the enhancement.

These studies were the first successful pump-probe measurements performed on ion-beam

targets and will pave the way for future studies of dynamics using ion beams. Each of these experiments and any other "scanning" measurement would benefit greatly from increased target density. To that end, improvements to the setup with the goal of increasing the target density by more than a factor of 10 are in progress. The high current molecular ion beams produced by the duoplasmatron ion source (see Sec. 2.2.1) allow us to produce a wide array of high-density beams. Additionally, bunching the ion beam should increase the target density by a factor of 10 or more, and these together will enable other dynamics studies in the future.

Chapter 5

Studies on excited D* formation from D_2

5.1 Scope

This chapter is based on the work leading to Refs. [181, 182] and also provides a description of the experimental method used specifically for these projects. These experiments rely on the detection of excited atomic fragments from molecules, specifically, D* (D(nl) with $n \geq 2$) fragments from D_2. An introduction to the D_2 excited state structure that is involved in the production of D* fragments is presented in Sec. 5.2. The experimental method and the apparatus used to perform state-selective measurements by utilizing field ionization of highly excited Rydberg atoms is described in Section 5.3. The results of state-selective measurements of D* formation from D_2 are presented in Section 5.4. These studies focus on gaining insight into the production mechanisms of D* fragments through observing the CEP control of their emission as well as measuring the n-state population. A method we developed for evaluating the detection efficiency of excited atoms is presented in Section 5.5. Understanding the detection efficiency is particularly important in some cases in which different excited states are detected by different mechanisms. Sections 5.4 and 5.5 are formatted differently from the rest of the chapter, as Section 5.4 is a draft of a paper we plan to submit

for publication [182] and Section 5.5 is a manuscript that has already been published [181]. The experimental setup used in these projects was originally intended for high-resolution measurements of dissociative double ionization of diatomic molecules such as O_2 and CO, a project that is also briefly described in Section 5.6. Finally, a summary of the work presented in this chapter is presented in Section 5.7.

5.2 Background and motivation

Molecular dynamics such as bond cleavage, bond rearrangement, charge exchange, and electron loss proceed through a variety of mechanisms including nonadiabatic couplings and electron-electron correlations. Processes driving these dynamics, including predissociation and autoioinization, can be challenging to fully treat theoretically and experimental results are difficult to interpret. Thus, the hydrogen molecule is often chosen for studies of these phenomena due to its relative simplicity. The excited states of H_2 have proved to be a fruitful testing ground for studying molecular dynamics, and the spectroscopy and dynamics of Rydberg and doubly excited H_2 have received considerable interest over the past several decades [130, 183–187].

The Born-Oppenheimer potentials describing the $1s\sigma(nl\lambda)$ Rydberg states of H_2 consist of an infinite series of bound electronic states that closely resemble the H_2^+ ground state. The excited electron occupies a diffuse orbital resembling an excited orbital of the hydrogen atom and can be labeled by quantum numbers $nl\lambda$, where n is the principal quantum number, l is the angular momentum, and λ is the projection of the angular momentum on the internuclear axis. On average, the Rydberg electron is located at large distances from the ionic core and only interacts weakly with it. For sufficiently high n the curves are nearly identical to the $X^2\Sigma_g^+$ ground state of H_2^+. A few of these potentials that run parallel to the ground state of the molecular ion are shown in Fig. 5.1.

Born-Oppenheimer curves, however, do not adequately describe the excited states of H_2. Non-adiabatic effects play an important role in the dynamics of the Rydberg states. For example, predissociation of the molecule is induced by coupling between vibrational and

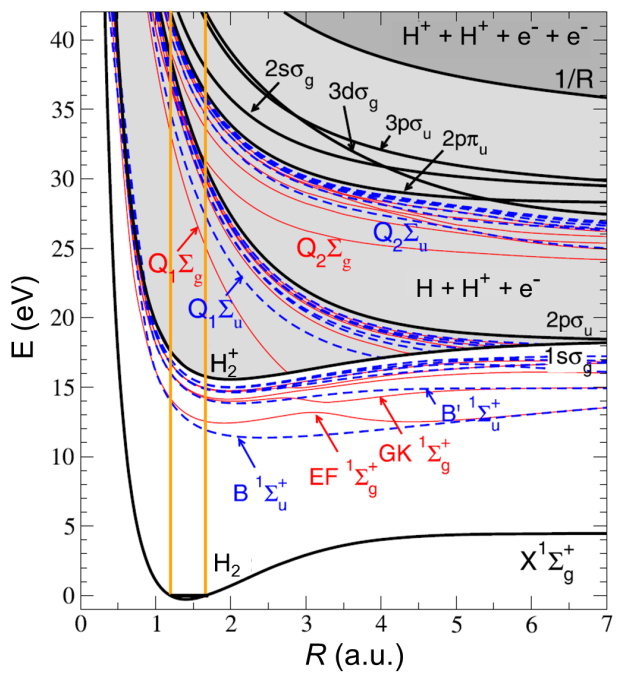

Figure 5.1: H_2 and H_2^+ potentials adapted from Ref. [187]. The solid black curves show the ground state of H_2, several H_2^+ ionization thresholds, and the 1/R double ionization threshold. A few of the lowest excited states of H_2 with $^1\Sigma_u^+$ (dashed blue lines) and $^1\Sigma_g^+$ (solid red lines) symmetry below the first ionization threshold are shown. In addition the first few doubly excited states of the Q_1 and Q_2 series are shown. The yellow lines indicate the Franck-Condon region starting from the vibrational ground state of H_2.

electronic degrees of freedom by the nuclear kinetic energy operator, which drives population from a bound vibrational state to the vibrational continuum of another electronic state, resulting in dissociation to $H(1s) + H(nl)$ [129]. Similarly, if the total energy is greater than the ionization threshold, the same type of coupling causes autoionization of the molecule leading to $H_2^+ + e^-$ or $H^+ + H + e^-$. The nonadiabatic coupling matrix elements, predissociation yields, autoionization rates and linewidths have been calculated [129, 188, 189], and this information has been used in describing measurements involving dissociation [129, 190–193] and autoionization [131, 194] from Rydberg states.

The doubly-excited states that lie above the ionization threshold may decay by autoionization due to electron-electron correlation, the same mechanism as atomic autoionization, resulting in $H_2^+ + e^-$ or $H^+ + H + e^-$, or dissociate into either $H^+ + H^-$ or two neutral fragments. The structure and properties of these states and the competition between de-

cay pathways have been studied extensively, and *ab initio* potentials, resonance widths, dipole transition moments, and dissociation rates have been reported for the hydrogen molecule [132, 183, 184, 186, 187, 195–198]. The doubly-excited states and Rydberg states with total energy over the ionization threshold make up what are known as the "super-excited states" [130]. The structure and dynamics of superexcited states of H_2 have been the focus of numerous theoretical and experimental studies [130, 132, 185, 187, 187, 191, 197, 199–203, 203, 204, 204, 205, 205–207]. The Q_1 series of doubly-excited states above the first ionization threshold are built on the $2p\sigma_u$ state of H_2^+. Theses states dissociate primarily to $H(1s)$ + $H(nl)$ and become electronically stable at some critical internuclear distance where they cross the ionization threshold. The lowest Q_1 state has the shortest lifetime and is the largest contributor to autoionization while the higher Q_1 states are longer-lived by about an order of magnitude and are more likely to dissociate into two neutral fragments [183, 184, 195]. The Q_2 states above the second ionization threshold are built on the second excited state of H_2^+ and dissociate to $H(n = 2)$ + $H(nl)$. Similarly to the Q_1 states, the autoionization rates of the lower states are higher and decrease for higher states.

Most of the measurements involving the excited states of H_2 produced by photoexcitation or collisional excitation focus on ion and electron emission or fluorescence from the radiative decay of excited atoms or molecular states. In this work, we focus on the direct measurement of excited atomic fragments from dissociation. While measurements of fluorescence are a powerful tool for studying the production of excited atoms, direct measurements of the atoms provide complementary information about the dissociation through the momentum of the fragments. Clearly, numerous channels can result in the production of excited atomic fragments through predissociation of Rydberg states and dissociation from doubly-excited states that do not autoionize. Furthermore, avoided crossings between the Q_1 states and the $1s\sigma(nl\lambda)$ Rydberg series can result in many dissociation channels being populated.

Excited states of H_2^+ also contribute to H* production [208, 209]. States lying just below the double-ionization threshold, the $1/R$ Coulomb potential in Fig. 5.1, dissociate to H^+ + H* fragments. The coincidence measurement of H^++H* allows one to distinguish these H* fragments originating from H_2^{+*} from the fragments of H_2, as demonstrated in Ref. [208].

We use the D_2 isotopologue of H_2 to study the production of D* fragments by ultrafast, intense laser fields with the aim of gaining insight into the mechanisms that result in D* production. The dense manifolds of excited states provide numerous dissociation pathways that can interfere. These interferences may complicate the interpretation of some spectra but can also be used to control the emission of D* fragments via the carrier-envelope phase of few-cycle pulses. We measure the n-state population of the D* fragments as well as the CEP dependence of the emission of D* in different n-state groups. These measurements, presented in Sec. 5.4, may help improve the understanding of the complicated excited state dynamics.

5.3 Experiment

Rydberg atoms have been intensely studied using a variety of experimental techniques [210]. Common techniques include measurements of the fluorescence due to the radiative decay of excited states as well as field ionization (by static or microwave fields) and measurement of the resulting ions. In addition, excited atoms can be detected directly through interactions with a detector surface, as done in this work. Transfer of an atom's internal energy to a surface has been well-studied and can be described by Auger de-excitation [211] as illustrated in Fig. 5.2, by which an electron is ejected from the detector surface, initiating the electron cascade that produces a measurable signal. Detection by this mechanism requires that the internal energy of the atom is greater than the work function of the detector surface.

Direct detection of excited atoms using MCP detectors by an Auger or similar process has been demonstrated previously [208, 209, 212–214]. Detection of all excited states of D* is made possible, as the potential energy of $D(n = 2)$, 10.2 eV, is greater than the work function of the MCP surface that is about 6 eV [40].

In addition to the direct detection of D* atoms in our method, field ionization by a static electric field is utilized to select the range of excited n, l states that are measured. Two flat high-transmission meshes preceding the MCP, illustrated in Fig. 5.3(a), facilitate field ionization of highly excited atoms. The front mesh is grounded while a positive voltage is

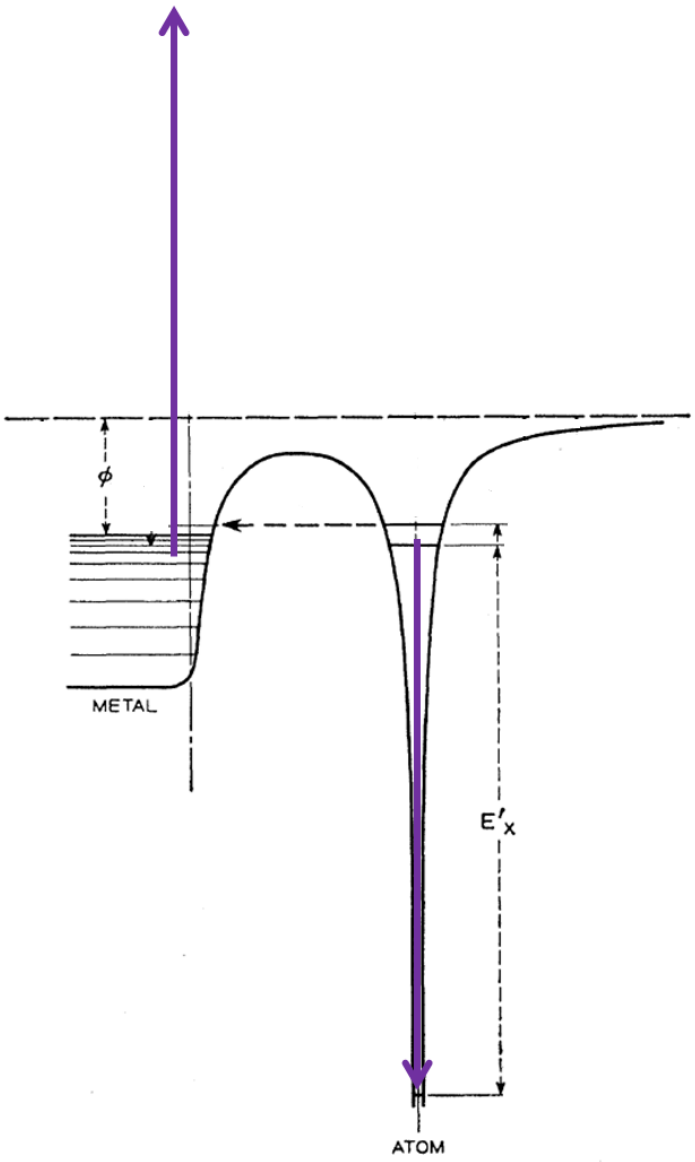

Figure 5.2: Schematic diagram illustrating the Auger de-excitation of an excited atom near a metal surface (adapted Ref. [211]). The de-excitation of the atom with internal energy E_x results in the ejection of an electron from the surface with energy $E_x - \phi$, where ϕ is the work function.

applied to the second mesh. The electric field between the meshes field ionizes highly excited atoms. The resulting positive ions (and any other positive ions) are repelled by the field so that they are not detected. Similarly, a negative voltage on the front MCP surface repels all electrons. This ensures that only excited neutral atoms are detected. Furthermore, by controlling the voltage on the middle mesh, we can control the range of excited states that can be detected.

The threshold electric field strength required for field ionization can be written as the classical over-the-barrier threshold, $1/16n^4$, for which the potential barrier in the direction of the electric field is lowered to the binding energy of the electron in state n [210]. Note that this approach, also known as the saddle-point method, ignores the Stark shifting of the Rydberg state as well as the spatial distribution of the electronic wave function. For these reasons we instead use the scaling law based on the semiclassical model presented by Chu and Rakovic [215],

$$f_{FI} = 1/5.783n^4, \tag{5.1}$$

where f_{FI} is the electric field strength in atomic units for which 50% of all atoms with principal quantum number n are ionized. This threshold is based on the ionization probability plotted in Fig. 5.3(b). Both models have the same n^{-4} functional form and only differ by a scaling factor. Also, it should be noted that the field strength for ionization of state n is not a hard cutoff. For example, the threshold field strength for $n = 20$ is about 5700 V/cm. While 50% of the $n = 20$ population is ionized, 10% of $n = 19$ and 85% of $n = 21$ are ionized. Similarly, at the threshold for $n = 40$, 25% of $n = 39$ and 68% of $n = 41$ are ionized (see Appendix E for more details). This tenuous definition of n based on the field strength should be kept in mind in the following sections.

To study specific subsets of n-states, measurements are performed with different static field strengths. With the field between the meshes set to the threshold for ionization of the state $n = n'$, D* atoms in states $2 \leq n \lesssim n'$ are measured. Similarly, if in another measurement the field strength is decreased to the threshold for $n = n' + 1$, atoms in states $2 \leq n \lesssim n + 1'$ are measured. Then, any differences between the two measurements are

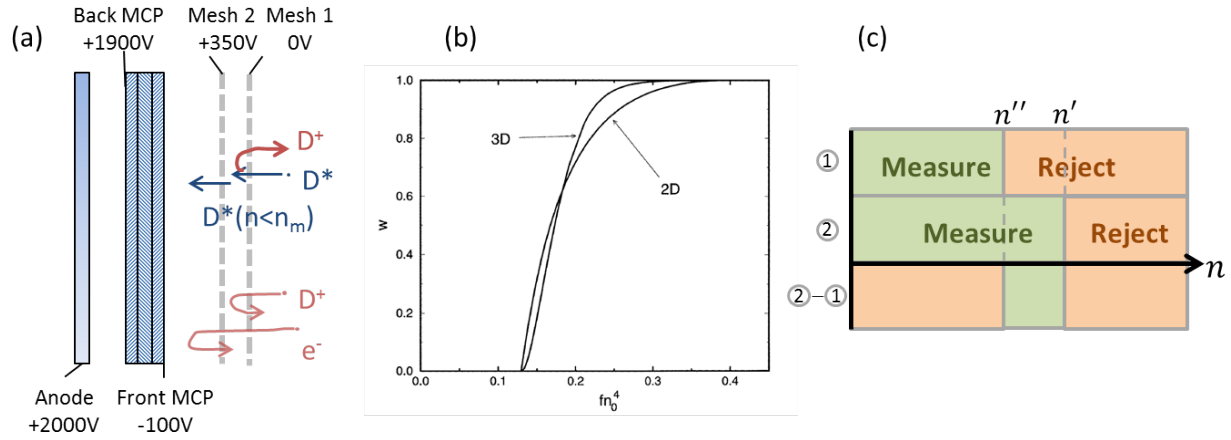

Figure 5.3: (a) Schematic of the MCP detector and meshes used to field ionize and detect highly excited D* atoms. The field between the meshes is controlled to ionize atoms in states above n_m. The positive voltage on the second mesh repels all ions, and the negative voltage on the front MCP repels all electrons. (b) Ionization probability plotted as a function of fn^4, where f is the electric field strength in atomic units and n is the principal quantum number of hydrogen (adapted from Ref. [215]). (c) Measurement scheme for studying specific subsets of n-states.

mainly due to the atoms in state $n = n'$. This scheme, as illustrated in Fig. 5.3(c), can be used to identify the contributions of a specific n-state or range of n-states to any spectrum or to map the n-state population, as discussed in Sec. 5.4. The total range of excited states that can be identified in our apparatus extends from $n = 16$ to $n = 44$. Atoms in states between $n = 2$ and 15 are also detected, but can not be identified using the field ionization method due to limitations on the maximum voltage that can be applied to the meshes. Highly excited atoms with $n > 44$ are field ionized by the weak field in the region between the second mesh and the MCP surface and the resulting ions do not have sufficient kinetic energy to be detected efficiently.

The D* atoms are formed in our experiments by focusing the laser beam onto an effusive D_2 gas jet, as shown in Fig. 5.4. The flow of gas into the chamber through the hypodermic needle is controlled by a needle valve backed by a driving pressure of a few psi. The effusive jet density is monitored by measuring the pressure inside the chamber using an ionization gauge. The base pressure is about 1×10^{-9} Torr, and with gas flow it is typically between 1×10^{-8} and 1×10^{-7} Torr. The target density is the primary variable used to control the

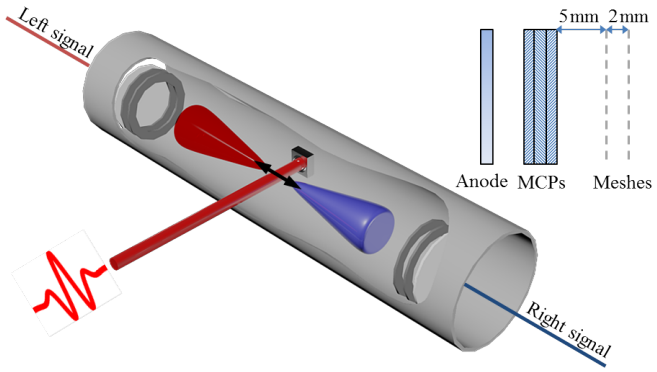

Figure 5.4: Schematic of the experimental apparatus used to measure D* fragments from D_2.

rate of fragments hitting the detectors, which is typically limited to under 1 event per laser shot, well below the maximum rate limit of our data acquisition system. Two detectors facing each other are located on either side of the gas jet. The detectors, referred to as "left" and "right", are 157 mm (left) and 162 mm (right) away from the gas jet. The laser beam is focused by a $f = 75$ mm spherical mirror mounted on a 3D translation stage inside the vacuum chamber.

The laser polarization is linear in most cases and is aligned along the axis connecting the two detectors. The D* fragments emitted within a 14.5° cone around the polarization are detected on either detector. For each laser shot, the time-of-flight of D* fragments is recorded event-by-event with respect to a photodiode signal generated by a small fraction of the laser beam. The flight of the neutral fragments is not influenced by any external fields, so, neglecting the transverse motion, the kinetic energy release of the fragmentation is simply given by

$$\mathrm{KER} = m_D(l_{L,R}/t)^2, \tag{5.2}$$

where m_D is the mass of D, $l_{L,R}$ is the respective distance to the left or right detector, and t is the measured time-of-flight. The partner fragment that is not measured is either D or D^+,

and the mass difference between D and D^+ is neglected in evaluating the KER. In addition, the initial center-of-mass velocity of the D_2 molecules due to the thermal motion of the jet is neglected. The transverse velocity due to the thermal motion of the jet introduces a small uncertainty in the KER (e.g. 60 meV at 1 eV KER). The effective temperature of the jet was measured to be a low temperature of about 100 K (see Sec. 5.6.1). Since we do not measure the position of the fragments that hit the detectors, the angular spread on the detectors is another source of uncertainty of about 1% in the fragment velocity. The maximum time-of-flight that can be measured is 52 μs due to the finite time window of the time-to-digital converter (TDC) used in our data acquisition stystem. As a result, fragmentation with KER < 0.2 eV is not measured. A detailed description of the detection electronics can be found in Appendix E.

A removable spectrometer consisting of four high-transmission meshes (two on either side of the gas jet) operating in a Wiley-McLaren configuration [216], not shown in Fig. 5.4, allows ion time-of-flight spectrometry to be performed using either detector. For example, ionization of Ar is measured to optimize the laser pulse parameters. This spectrometer is not used in the D* measurements. All of the spectrometer and detector meshes are electroformed copper meshes with 88% transmission, 90.1 lines/inch, and 14-μm line width [217]. Electroformed meshes are extremely flat and uniform, which make them ideal for reducing electric field distortions.

5.4 State-selective studies and carrier-envelope phase control of D* formation from D_2 by strong laser fields

This section contains a draft of a manuscript we have prepared to submit for publication in the near future, following the submission of two related papers. Experimental studies of D* formation by strong-field excitation of D_2 were carried out using the methods described in

Sec. 5.3. The aim of these studies was to gain insight into the processes driving D* formation by measuring the excited state population and using the carrier-envelope phase of few-cycle pulses to control the formation of specific ranges of excited states.

State-selective studies and carrier-envelope phase control of the formation of Rydberg D* fragments from D_2 in a strong field

Ben Berry, M Zohrabi, Bethany Jochim, T Severt, Peyman Feizollah, U Ablikim, K D Carnes, B D Esry, and I Ben-Itzhak
J.R. Macdonald Laboratory, Physics Department, Kansas State University, Manhattan, KS 66506, USA
(Dated: March 29, 2018)

We implement a state-selective technique that utilizes field ionization to identify the n-state of D* (Rydberg D(n,l) with $16 \lesssim n \lesssim 44$) fragments produced in ultrafast, intense laser fields. The carrier-envelope phase (CEP) is shown to be a sensitive control knob for D* production, and the CEP-dependent spatial asymmetry and yield show significant differences between subsets of n-states. We also use this technique to measure the population of n-states produced by the strong field. Due to the long time-of-flight to the detector, much of the initial population decays by spontaneous emission. By simulating the decay, we link the measured distribution to the initial n-state population created by the laser. Additionally, we study the effects of laser intensity, pulse duration, and wavelength on the n-state distribution and kinetic energy release (KER) of the D* fragmentation channels.

I. INTRODUCTION

The excited states of H_2 have been of considerable interest for decades [1–7], as they provide opportunities to probe nonadiabatic interactions and electron-electron correlations in one of the simplest molecular systems through processes including predissociation and autoionization. Studies involving doubly excited states in molecular systems have been mainly focused on H_2 because it still poses significant theoretical and experimental challenges. These states which lie above the ionization threshold (i.e. the $1s\sigma_g$ state of H_2^+) may autoionize resulting in $H_2^+ + e^-$, $H^+ + H + e^-$ or dissociate into either $H^+ + H^-$ or two neutral fragments. The structure and properties of these doubly excited states including *ab initio* potentials, resonance widths, dipole transition moments, and dissociation rates have been reported [3, 4, 6–11]. Similarly, in the Rydberg states below the ionization threshold, nonadiabatic coupling between the electronic and nuclear degrees of freedom may lead to autoionization or predissociation of the molecule [12–15]. These decay mechanisms have been the focus of studies involving photoexcitation of H_2 [5, 10, 12, 16, 17].

The study of multiphoton excitation to autoionizing states of hydrogen by measuring ion or electron decay products is difficult because of the large number of ions and electrons created directly by the laser field that have nothing to do with the relevant excited states. Instead, detection schemes that are sensitive to the final excited state must be used. For example, fluorescence of excited hydrogen atoms has been used to identify dissociation channels and lifetimes of doubly-excited states of H_2 [16, 17]. Alternatively, measurements of the excited H(nl) fragments from dissociating molecules that do not autoionize provide direct information about excited-state dynamics through their momentum and final state. In this case, field ionization has been utilized to identify the final states of the excited atomic fragments [18].

We detect excited D* atoms (D(nl) with $n \geq 2$) produced by strong field excitation of D_2 and employ a field ionization technique to distinguish the final states of Rydberg D* fragments with $n \gtrsim 16$. This method allows us to distinguish the final n-states of the D* products and measure the kinetic energy release (KER) upon dissociation. In this paper, we study the carrier-envelope-phase (CEP) dependence of D* formation by intense, few-cycle laser pulses and use the field ionization technique to explore state-selective CEP effects in different subsets of n-states, providing more differential information about the strong field excitation. In addition, we measure the n-state distribution of the D* fragments and study the dependence of the excited population on various laser parameters, such as intensity, pulse duration, and wavelength.

The CEP of few cycles laser pulses has been used to control the direction of proton emission from H_2 [19, 20], H_2^+ [21, 22], and recently several other systems [23–26]. A general theoretical description of this type of CEP control reveals that it arises from interference between pathways that involve different numbers of photons [27, 28]. For example, spatial asymmetry (e.g. asymmetry in proton emission from H_2 along the polarization direction) results from interference between pathways differing by an odd number of photons, while the CEP dependence of the yield is the result of interference between pathways differing by an even number of photons [28]. In D* production from D_2, the dense manifolds of excited states provide a multitude of pathways that can interfere. By studying the CEP dependence of D* formation state-selectively, we observe differences between subsets of excited states that are likely due to different interfering pathways.

II. EXPERIMENTAL METHOD

The apparatus employed in these measurements consists of two detectors facing one another on either side of

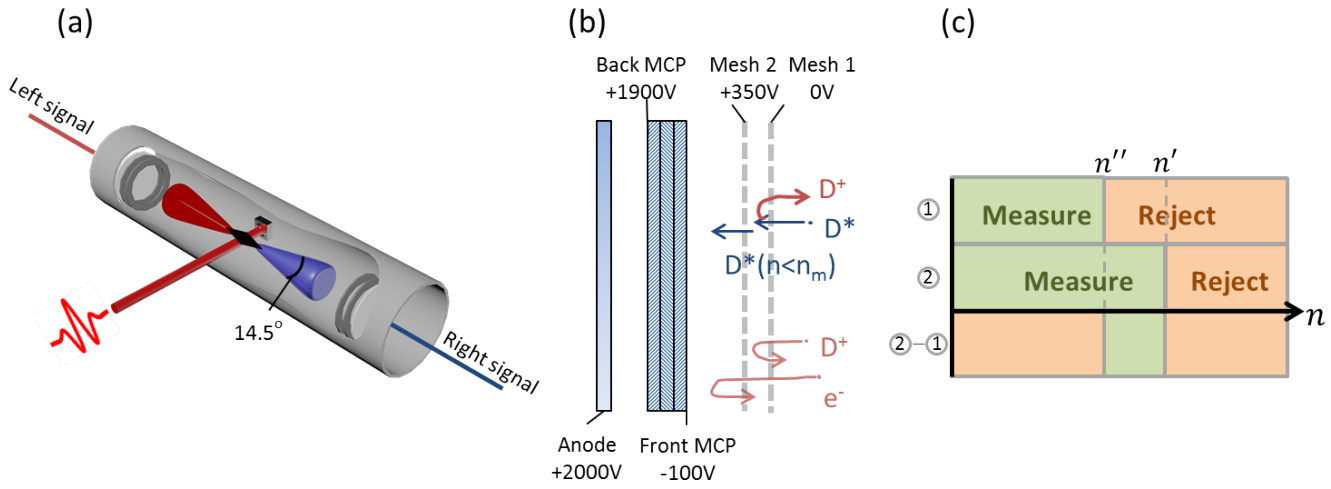

FIG. 1. (a) Schematic of the apparatus used to measure D* fragments from D_2. (b) Schematic of the MCP detector and meshes used to field ionize and detect D* atoms. (c) Measurement scheme for studying specific subsets of n-states.

an effusive gas jet of D_2, as shown in Fig. 1(a). The laser beam is back-focused onto the jet by a $f = 75$ mm spherical mirror. The laser polarization is linear and aligned along the axis of the apparatus. The time of flight of fragments emitted along the polarization direction (within a 14.5° cone) is measured on either detector. The detectors consist of a z-stack of microchannel plates (MCP) preceded by two electrically isolated high-transmission electroformed meshes, as shown in Fig. 1(b). The front mesh is grounded, and a positive voltage is applied to the second mesh to repel all ions. A negative voltage is applied to the front of the MCP stack to repel electrons.

Detection of excited neutral fragments is possible in general if the internal energy of the fragment is greater than the work function of the MCP (~ 6 eV for lead glass MCPs [29]). Transfer of the internal energy of the fragment to the detector surface occurs by Auger-like mechanisms [30], liberating electrons that initiate the electron cascade which produces a measurable signal. The internal energy of $D(n = 2)$, 10.2 eV, is sufficient to activate the MCP, and therefore detection of all excited states of hydrogen is possible as demonstrated experimentally in Refs. [31, 32].

We further restrict the range of excited states that are detected by field ionizing atoms in highly excited Rydberg states and repelling them. Specifically, the electric field between the two meshes field ionizes highly excited D* atoms above some n_{FI}, and the resulting D^+ ions are repelled. Adjusting the voltage between the meshes provides control of the range of excited states that are detected. The threshold field strength for ionization of hydrogen Rydberg states follows the scaling law,

$$f_{FI} = 1/5.783 n_{FI}^4, \tag{1}$$

where f_{FI} is the field strength in atomic units for which 50% of the population in n_{FI} is ionized [33]. A small slice of n-states can be obtained through the subtraction of two measurements. In one measurement, the states $2 \leq n \lesssim n'$ are measured, followed $2 \leq n \lesssim n''$ in another measurement, with $n'' > n'$. Subtracting these two measurements results in the range $n' \lesssim n \lesssim n''$, as shown schematically in Fig. 1(c). This type of measurement has also been used to determine the detection efficiency of excited neutral atoms [34].

In principle, all excited states can be detected, but atoms in states above $n \simeq 44$ are field ionized between the second mesh and MCP and the resulting ions are not energetic enough to be detected. Also, experimental limitations on the voltage that can be applied to the meshes allow us to field ionize only states with $n \gtrsim 16$. This limits the identifiable range of excited states from $n = 16$ to 44.

The D* fragments from D_2 were produced by the strong laser field of our laser, known as PULSAR, which provides 21-fs pulses centered at 785 nm with 10-kHz repetition rate and 2-mJ pulse energy [35]. The pulse energy is monitored shot-to-shot using a photodiode. For the CEP measurements employing sub-5 fs pulses, the spectrum is broadened by self-phase modulation in a neon-filled hollow-core fiber. The output spectrum from the fiber spans from 450 nm to 1000 nm, and chirp compensation mirrors compress the pulses to below 5-fs duration (FWHM in intensity). The CEP of every pulse is tagged using a stereo-ATI phase meter [22, 35–40].

The time-of-flight (TOF) of each D* fragment and CEP of the pulse are recorded event-by-event. As the flight of the neutral fragments is not influenced by any external field, the kinetic energy release (KER) is simply evaluated to be

$$\mathrm{KER} = m_D (l_{L,R}/t_{L,R})^2, \tag{2}$$

where $t_{L,R}$ and $l_{L,R}$ are the TOF and the distance from the laser interaction to the detector on the left or right

side, respectively. The partner fragment that is not measured is either D or D^+, a the mass difference between D and D^+ is neglected in the evaluation of the KER. We also neglect the initial CM-velocity of the molecule due to its thermal motion, which introduces an uncertainty in the KER of a few percent (e.g., 60 meV at KER of 1 eV). The transverse temperature of the jet was measured to be approximately 100 K in a separate coincidence measurement of double ionization of O_2, in which one O^+ fragment was measured on each detector, providing the needed information to obtain the center-of-mass velocity distribution, and therefore the temperature [41].

Typical TOF and KER spectra are shown in Fig. 2 for 5-fs, 8×10^{13} W/cm^2 pulses. The spectra include the entire measured range of D*, from $n = 2$ to $n \simeq 44$. The KER extends beyond 18 eV with several structures. Fragmentation with KER below 0.2 eV is not measured due to the 52-μs maximum time window of the time-to-digital converter (TDC) used.

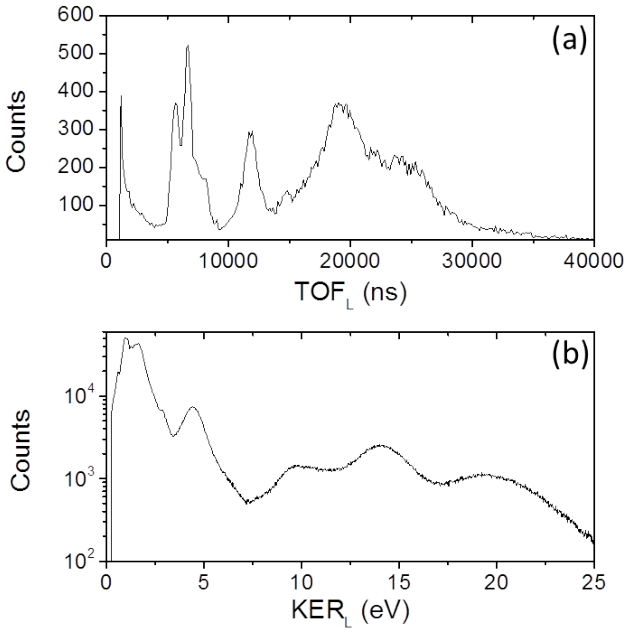

FIG. 2. (a) The TOF and (b) KER spectra of D* fragments with $2 \leq n \leq 44$ from D_2 produced by by 5-fs pulses with peak intensity $I_0 = 8 \times 10^{13}$ W/cm^2.

III. CARRIER-ENVELOPE PHASE EFFECTS IN D* EMISSION

The general theory of CEP effects presented by Roudnev and Esry [27] and further detailed in Ref. [28] describe all CEP effects as interference between different photon-number channels. In short, the Hamiltonian of a system exposed to a laser field is periodic in CEP, φ, which permits the use of the Floquet representation in which the wave function is expanded as a Fourier series

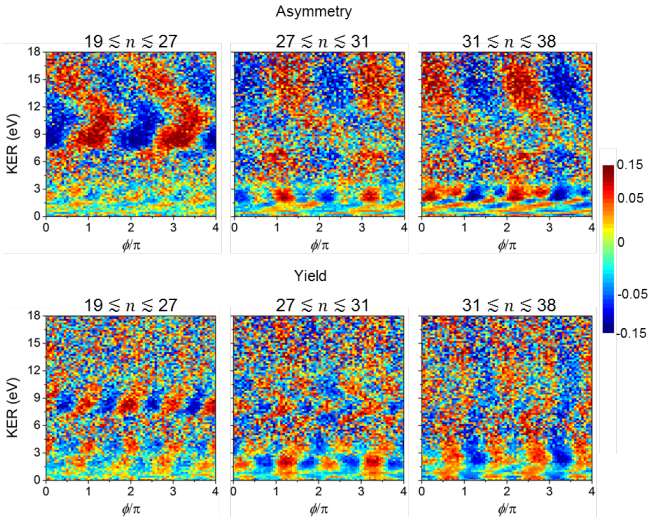

FIG. 3. Spatial asymmetry (top) and yield (bottom) mapped as functions of CEP and KER for different subsets of n-states, as labeled on the panels. Note that for visualization purposes 2π was randomly added to ϕ for half of the events to extend the plot to 4π.

in φ. The expansion coefficients correspond to the amplitudes of m-photon absorption or emission. It follows that the CEP dependence of any observable results from the interference of the m-photon amplitudes. This, of course, requires that at least two different m-photon components be populated to observe any CEP effect, and the CEP-dependence of an observable is given by an oscillating function with periodicity $2\pi/\Delta m$, where $\Delta m = m - m'$.

This general framework allows for meaningful interpretation and prediction of CEP effects without performing detailed calculations. CEP effects in molecular fragmentation appear, for example, as spatial asymmetry in the emission of a fragment as well as CEP-dependence of the yield of a final product [28]. Spatial asymmetry is the result of interference of opposite-parity channels (and therefore odd Δm) that contribute at the same KER, while CEP-dependence of the yield is the result of interference between photon processes in which Δm is even. Therefore, the asymmetry is expected to show oscillations in φ with periods of $2\pi/k, k = 1, 3, 5, ...$, while the yield oscillates with periods having $k = 2, 4, 6, ...$

The asymmetry in D* production is evaluated experimentally as the yield difference between the two detectors ("left" and "right") normalized by the cycle-averaged yield. Specifically,

$$A(\mathrm{KER}, \varphi) = \frac{N_L(\mathrm{KER}, \varphi) - N_R(\mathrm{KER}, \varphi) - A_0}{\langle N_L(\mathrm{KER}, \varphi) + N_R(\mathrm{KER}, \varphi)\rangle_\varphi}, \quad (3)$$

where $N_{L,R}$ are the respective yields on each detector. The cycle-averaged asymmetry, $A_0 = \langle N_L(\mathrm{KER}, \varphi) - N_R(\mathrm{KER}, \varphi)\rangle_\varphi$, which accounts for differences in detection efficiency between the two detectors, for example, is subtracted so that the asymmetry oscillates about zero.

The CEP-dependence of the yield is defined as the sum of the yields on the two detectors for a given CEP, normalized by the cycle-averaged yield,

$$Y(\mathrm{KER},\varphi) = \frac{N_L(\mathrm{KER},\varphi) + N_R(\mathrm{KER},\varphi)}{\langle N_L(\mathrm{KER},\varphi) + N_R(\mathrm{KER},\varphi)\rangle_\varphi} - 1. \quad (4)$$

Similar to Eq. 3, the cycle-averaged yield is subtracted so that the yield oscillates about zero.

The CEP-dependent asymmetry and yield of D* production, shown in Fig. 3, each show the characteristic oscillations predominantly with the lowest expected periodicity, in agreement with the general theory [27, 28]. Compared to other reported CEP-dependent oscillations [19, 22], the observed modulation depth of about 20% is relatively high. The large CEP effect may be in part due to the dense excited-state manifolds of D_2 that provide numerous interfering pathways. However, the high density of states also makes it difficult to identify the specific pathways involved. Our ability to distinguish the final n-state of the D* fragments allows us to observe CEP effects in different subsets of n-states. This is accomplished by generating, for example, the asymmetry map for one measurement of $2 \leq n \leq 31$, and then adjusting the field ionization conditions and repeating the measurement for the range $2 \leq n \leq 38$. Subtracting the asymmetry maps of these two measurements results in the asymmetry map for the $31 \lesssim n \lesssim 38$ range.

As shown in Fig. 3, this procedure was repeated to map the CEP dependence of the spatial asymmetry and yield for a few sets of n-states. We observe strong CEP dependence in a few KER ranges: near and below 2 eV, around 9 eV, and from 12 to 18 eV. Previous measurements have correlated D* with D^+ fragments for KER greater than 4 eV [31]. In addition, this high KER range resembles that of D^++D^+ breakup. This suggests that excited states of D_2^+, lying just below and closely following the $1/R$ Coulomb potential, may be important contributors to the features at high KER. On the other hand, in the Franck-Condon overlap region with the D_2 ground state, as shown in Fig. 4, the Q_1 doubly-excited states of D_2 result in similar KER and may also play a role. Measuring D*+D^+ fragmentation in coincidence might help better identify the contributions of the Q_1 and excited H_2^+ states. However, identifying $D^+ + D^*$ pairs is difficult in our setup due to the high rate of D^+ ions from dissociative single and double ionization.

The features at lower KER (below 4 eV) are most likely associated with either D*+D or D*+D^+, though based on Ref. [31] the former is more likely. Pairs of D* fragments were not observed in coincidence in our measurements or in previous measurements [31, 32], so we neglect pathways that result in D*+D*. However, the KER below 4 eV has previously been shown to resemble the KER spectrum that comes from D_2^+ dissociation [31, 32], i.e. $D_2^+ + n\hbar\omega \rightarrow D^+ + D$. This suggests that dissociation from the $1s\sigma(nl\lambda)$ Rydberg series of D_2 may be contributing to the lower KER features.

The strong CEP oscillations at KER of around 8-9 eV

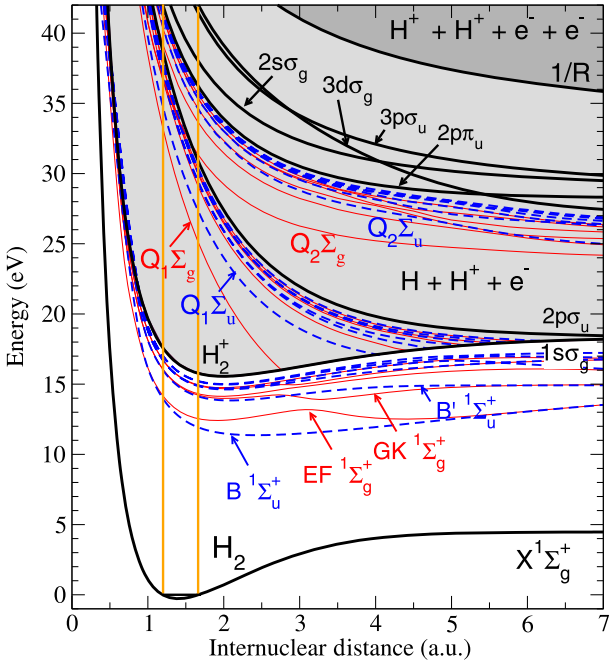

FIG. 4. H_2 and H_2^+ potentials from Ref. [7]. The solid black curves show the ground state of H_2, several H_2^+ ionization thresholds, and the $1/R$ double ionization threshold. A few of the lowest excited states of H_2, with $^1\Sigma_u^+$ (dashed blue lines) and $^1\Sigma_g^+$ (solid red lines) symmetries, below the first ionization threshold are shown. In addition the first few doubly excited states of the Q_1 and Q_2 series are shown. The yellow lines indicated the Franck-Condon region from the ground vibrational state of H_2.

are associated predominantly with the range of n-states between 19 and 27. On the other hand, the oscillations at lower KER are much more pronounced in the higher n-state subsets, 27–31 and 31–38. In comparing these two subsets (27–31 and 31–38) the asymmetry and yield oscillations are different in their phase offset, slopes, and contours. This implies that the amplitudes and phases of the m-photon pathways are quite different for the different ranges of n-states even though the fragmentation channels are very close together in energy.

To further illustrate the differences between the n-state ranges, Fourier analysis of the asymmetry and yield maps was performed with respect to φ. To perform the Fourier transforms, multiples of 2π were randomly added to the CEP associated with each event, which increased the range of φ and therefore improved the resolution of the transform [42]. The discrete Fourier transform was evaluated using a FFT algorithm along the φ dimension of the asymmetry and yield maps in Fig. 3. The resulting power spectrum maps the frequency components of the oscillations that are directly related to Δm, the difference in photon number between interfering pathways. The spectra, shown in Fig. 5, illustrate the expected frequencies of $\Delta m = 1$ in the asymmetry and $\Delta m = 2$ in the yield. They also clearly show the difference in

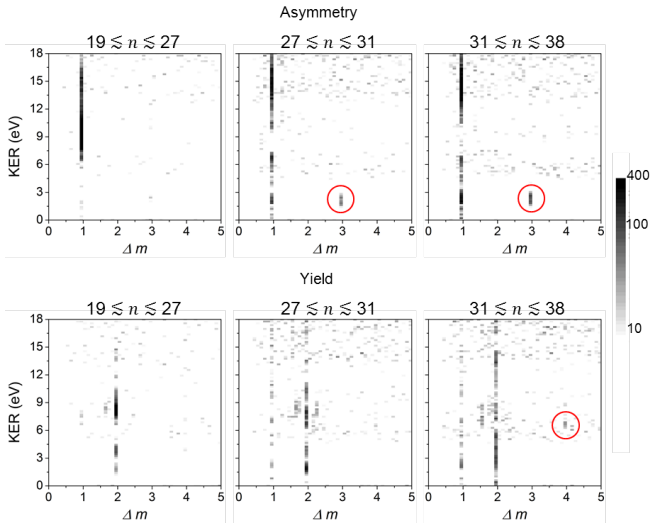

FIG. 5. Fourier transforms of the spatial asymmetry and yield maps shown in Fig. 3.

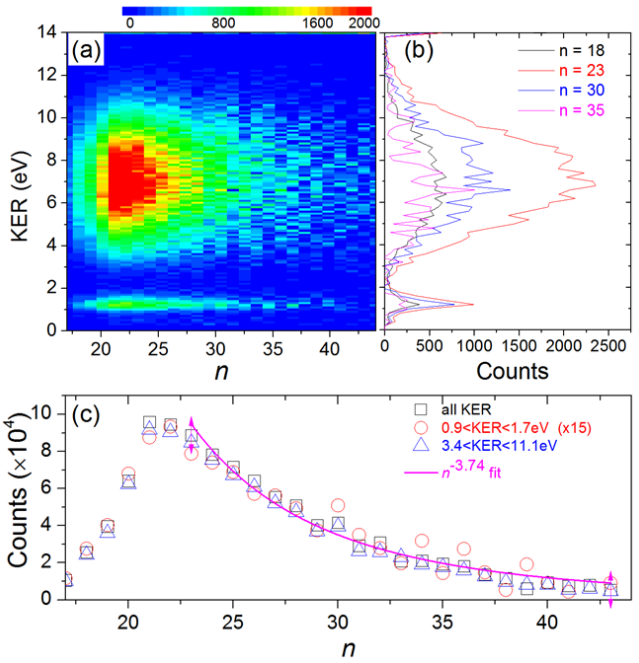

FIG. 6. (a) The D* yield is mapped as function of detected n-state and KER. (b) 1D KER distributions for a few representative values of n show that the shape of the KER distribution does not change significantly with n-state. (c) The n-state population in the "high" and "low" KER regions are similar, and the population of states above $n = 20$ matches a $n^{-3.74}$ dependence.

magnitude and KER of the CEP effects for the different n-state subsets. Furthermore, higher order oscillations are observed in the asymmetry of the two higher ranges of n with $\Delta m = 3$, and in the highest range of n in the yield with $\Delta m = 4$. These contributions are the result of the interference of pathways differing by 3 and 4 photons, respectively, resulting in the same KER (see Ref. [42] for further details).

IV. D* POPULATION

By controlling the strength of the electric field between the detector meshes, we are able to measure the yield and KER distributions of approximately one n-state at a time. The D* yield is mapped as a function of the n-state and KER in Fig. 6(a) over the range $17 \leq n \leq 43$ for 25-fs, 800-nm pulses with peak intensity of $I_0 = 1 \times 10^{14}\,\mathrm{W/cm^2}$. Two main features are observed: an intense, broad distribution peaked at 7 eV, and a weaker narrow distribution at about 1 eV. The 1D KER distribution is plotted in Fig. 6(b) for a few representative n-states, which seem to be very similar to one another. This is not surprising, given that the excited states are densely packed in energy. The n-state distributions associated with the "low" and "high" KER regions, shown in Fig. 6(c), have nearly identical shapes. The high KER is likely due to dissociative ionization into $D^* + D^+$, while the low KER is most likely $D^* + D$, so different molecular states contribute the two KER regions but curiously they are associated with approximately the same n-state distributions.

The most curious feature of the n-state distribution is that it is peaked at about $n = 23$. The measured n-state distribution, however, is not necessarily identical to the initial n population produced by the laser field. The time-of-flight of the fragments ranges from 10 to 30μs, which is much longer than the lifetimes of many excited states with $n < 20$. Thus, the maximum at $n = 23$ may be simply a result of the radiative decay in flight.

The high n-states ($n > 20$), are long-lived compared to the flight time, so the shape of the distribution for the highest values of n is expected to match the shape of the initial n-state population. As shown in Fig. 6(c), a $n^{-3.74}$ fit to the high-n tail of the measured n-state distribution matches the data fairly well. This is not far off from the expected n^{-3} dependence of cross-sections for both collisional- and photo-excitation in atoms [18]. Radiative decay of the shorter-lived states may be the main factor causing the maximum at $n = 23$. To relate the initial and measured n-state populations, we model the decay in flight by spontaneous emission to attempt to reproduce the local maximum in the data. The rate equation of a nl state of hydrogen is given by

$$\frac{dN_{nl}}{dt} = -\sum_{\substack{n'<n \\ l'=l\pm1}} A_{n'l',nl} N_{nl} + \sum_{\substack{n'>n \\ l'=l\pm1}} A_{nl,n'l'} N_{n'l'}, \quad (5)$$

where N_{nl} indicates the population in state nl and $A_{n'l',nl}$ is the transition rate from state nl to $n'l'$. The first term in Eq. 5 accounts for population decaying from state nl to all states lower in energy that obey the selec-

tion rule $l' = l \pm 1$. The second term accounts for feeding the state nl by transitions from higher-lying states. The equations for all states form a set of coupled first-order equations that was solved numerically. We used the Euler method [43] to numerically integrate the rate equations as in this case it was the fastest and the results agreed well with other solvers.

The transition rates are given by the spontaneous emission rates [18]

$$A_{n'l',nl}(s^{-1}) = \frac{8}{3} \times 10^9 (\frac{\omega_{n'n}}{0.5})^3 \frac{max(l,l')}{2l+1} |\langle n'l'|r|nl\rangle|^2, \quad (6)$$

which depend on the square of the dipole matrix element $\langle n'l'|r|nl\rangle$. For hydrogen, these matrix elements have analytic solutions [44], given by

$$\langle n'l-1|r|nl\rangle = \frac{(-1)^{n'-l}}{4(2l-1)!}\sqrt{\frac{(n+l)!(n'+l-1)!}{(n-l-1)!(n'-l)!}}\frac{(4nn')^{l+1}(n-n')^{n+n'-2l-2}}{(n+n')^{n+n'}}\times$$
$$\times [F(-(n-l-1),-(n'-l),2l,-\frac{4nn'}{(n-n')^2})-$$
$$(\frac{n-n'}{n+n'})^2 F(-(n-l+1),-(n'-l),2l,-\frac{4nn'}{(n-n')^2})],$$

where F is the hypergeometric function. The lifetimes associated with our calculated decay rates agree well (to within 0.1 ns) with values reported in literature [45].

The rate equations are then used to relate the measured n-state population to an initial n-state population. To accomplish this, a model initial population is assumed, then propagated in time, and the final distribution is compared with the measurement. The $n^{-3.74}$ distribution we found to fit the measured population of high n-states, which have lifetimes longer than the flight time to the detector, requires that the initial population obey a $n^{-3.74}$ dependence for high n-states above $n = 20$. So, as a first guess, we assume a $n^{-3.74}$ dependence for the entire range of n-states. The population in lower n-states that decay quickly may have a different n-dependence, and may be peaked at some value for example, but these states decay quickly enough that our measurement is not sensitive to this part of the distribution.

Additionally, the angular momentum, l, influences the decay rate. To address the initial distribution of l, we try a couple approaches. First, the population is assumed to be in only $l = 0$ states. Second, a statistical distribution related to the number of absorbed photons, $P(l,m) = m!/l!(m-1)!$, where m is the number of photons, is used. About 20 photons are required to excite the ground state of D_2 to the Q_1 states that may play a role in D* production, so $m = 20$ is used as a first guess.

Typical results of the simulations are shown in Fig. 7. A comparison of the simulated "final" n-state population after 10 μs with the measured population, shown in Fig. 7(b), reveals some similarities. Namely, the general shape of the distributions is very similar, and as expected the high-n tail matches. The shape of the distribution appears to be relatively insensitive to the choice of l-distribution, meaning that our measurement is not sensitive to the initial population of l-states. But, the

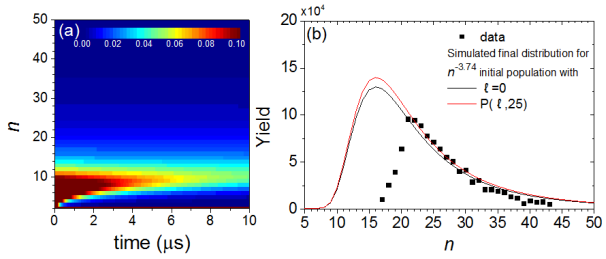

FIG. 7. (a) Simulation of the decay by spontaneous emission of a $n^{-3.74}$ distribution over 10 μs. (b) Final n-state distributions compared with the measurement. Two different initial l-distributions result in approximately the final n-state distribution.

location of the maximum differs, $n = 23$ in the measurement and $n = 16$ from the simulation. The difference in peak position is still an open question and may be due to issues associated with decreased detection efficiency of fragments in states below $n = 20$.

Finally, we have also conducted measurements of the n-state population for a variety of laser conditions. In general, the KER is sensitive to the laser parameters, but the n-state distribution is not, as shown in Fig. 8. The sensitivity of the KER certainly suggests that dissociation channels are being populated differently, but the same distributions of high-n states are being populated.

V. SUMMARY

In summary, we have used a field ionization detection scheme to state-selectively study the strong field formation of D* fragments from D_2. We observed that the CEP dependence of D* formation from D_2 varies signif-

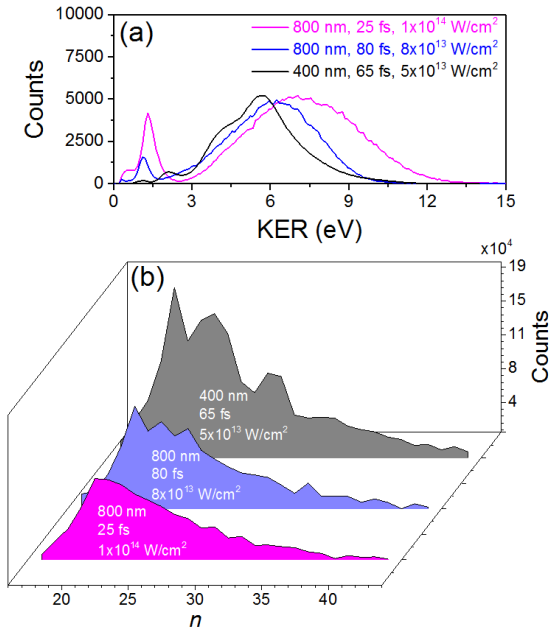

FIG. 8. (a) The measured KER distributions of D* formation from D_2 by a few different laser pulse parameters. (b) The n-state distributions measured using different laser pulse parameters are very similar to one another.

icantly for different subsets of n-states. The oscillations in the CEP-dependent spatial asymmetry and yield agree with the general theory describing CEP effects [27, 28], and the differences between subsets of n-states indicate that the while the fragmentation pathways are densely packed in energy, the multiphoton transition amplitudes and phases are very different in each subset of n-states.

Our state-selective detection technique also allows for measurements of the n-state population of the D* fragments. Unfortunately, the n-state distributions measured long after the laser interaction cannot be uniquely linked to the initial population due to decay by spontaneous emission, but we can still conclude that highly excited states (up to at least $n = 44$) are populated and that the population in states above $n = 20$ follow a $n^{-3.74}$ distribution.

Now that we have the ability to study the formation of D* fragments from D_2 state-selectively, the processes leading to D* formation can be explored in more detail. To fully understand D* formation, though, further work is needed. In particular, coincidence measurements of D* + D^+ will help clarify their contributions to the total D* yield. This work may also be helpful to the development of theoretical treatments of multiphoton excitation of H_2 producing highly excited fragments.

VI. ACKNOWLEDGMENTS

We gratefully acknowledge Kanaka Raju P. and C. W. Fehrenbach for assistance with the laser beam. This work was supported by the Chemical Sciences, Geosciences, and Biosciences Division, Office of Basic Energy Sciences, Office of Science, U.S. Department of Energy, Grant No. DE-FG02-86ER1349. The PULSAR laser was provided by Grant No. DE-FG02-09ER16115 from the same funding agency.

[1] N. Kouchi, M. Ukai, and Y. Hatano, Journal of Physics B: Atomic, Molecular and Optical Physics **30**, 2319 (1997).
[2] R. L. Platzman, Radiation Research **17**, 419 (1962), http://www.rrjournal.org/doi/pdf/10.2307/3571104.
[3] C. Bottcher and K. Docken, Journal of Physics B: Atomic and Molecular Physics **7**, L5 (1974).
[4] S. L. Guberman, The Journal of Chemical Physics **78**, 1404 (1983), http://dx.doi.org/10.1063/1.444882.
[5] M. Glass-Maujean, The Journal of Chemical Physics **89**, 2839 (1988), http://dx.doi.org/10.1063/1.454987.
[6] F. Martín, Journal of Physics B: Atomic, Molecular and Optical Physics **32**, R197 (1999).
[7] A. Palacios, J. L. Sanz-Vicario, and F. Martín, Journal of Physics B: Atomic, Molecular and Optical Physics **48**, 242001 (2015).
[8] I. Sánchez and F. Martín, The Journal of Chemical Physics **106**, 7720 (1997), http://dx.doi.org/10.1063/1.473773.
[9] I. Sánchez and F. Martín, The Journal of Chemical Physics **110**, 6702 (1999), http://dx.doi.org/10.1063/1.478576.
[10] M. Glass-Maujean, C. Jungen, H. Schmoranzer, A. Knie, I. Haar, R. Hentges, W. Kielich, J. K., and A. Ehresmann, Physical Review Letters **104**, 183002 (2010).
[11] I. Sánchez and F. Martín, Phys. Rev. Lett. **79**, 1654 (1997).
[12] M. Glass-Maujean, J. Breton, and P. M. Guyon, Physical Review Letters **40**, 181 (1978).
[13] M. Glass-Maujean, S. Klumpp, L. Werner, A. Ehresmann, and H. Schmoranzer, The Journal of Chemical Physics **128**, 094312 (2008), http://dx.doi.org/10.1063/1.2835006.
[14] P. M. Dehmer and W. A. Chupka, The Journal of Chemical Physics **66**, 1972 (1977), http://dx.doi.org/10.1063/1.434154.
[15] J. L. Dehmer, P. M. Dehmer, J. B. West, M. A. Hayes, M. R. F. Siggel, and A. C. Parr, The Journal of Chemical Physics **97**, 7911 (1992), http://dx.doi.org/10.1063/1.463466.
[16] M. Glass-Maujean, The Journal of Chemical Physics **85**, 4830 (1986), http://dx.doi.org/10.1063/1.451717.
[17] A. Azarm, D. Song, K. Liu, S. Hosseini, Y. Teranishi, S. H. Lin, A. Xia, F. Kong, and S. L. Chin, Journal of Physics B: Atomic, Molecular and Optical Physics **44**, 085601 (2011).
[18] T. F. Gallagher, *Rydberg Atoms* (Cambridge University Press, 1994).

[19] M. F. Kling, C. Siedschlag, A. J. Verhoef, J. I. Khan, M. Schultze, T. Uphues, Y. Ni, M. Uiberacker, M. Drescher, F. Krausz, and M. J. J. Vrakking, Science **312**, 246 (2006), http://science.sciencemag.org/content/312/5771/246.full.pdf

[20] H. Xu, J.-P. Maclean, D. E. Laban, W. C. Wallace, D. Kielpinski, R. T. Sang, and I. V. Litvinyuk, New Journal of Physics **15**, 023034 (2013).

[21] T. Rathje, A. M. Sayler, S. Zeng, P. Wustelt, H. Figger, B. D. Esry, and G. G. Paulus, Phys. Rev. Lett. **111**, 093002 (2013).

[22] N. G. Kling, K. J. Betsch, M. Zohrabi, S. Zeng, F. Anis, U. Ablikim, B. Jochim, Z. Wang, M. Kübel, M. F. Kling, K. D. Carnes, B. D. Esry, and I. Ben-Itzhak, Physical Review Letters **111**, 163004 (2013).

[23] F. Süßmann, S. Zherebtsov, J. Plenge, N. G. Johnson, M. Kübel, A. M. Sayler, V. Mondes, C. Graf, E. Rühl, G. G. Paulus, D. Schmischke, P. Swrschek, and M. F. Kling, Review of Scientific Instruments **82**, 093109 (2011), http://dx.doi.org/10.1063/1.3639333.

[24] B. Bergues, M. Kübel, N. G. Johnson, B. Fischer, N. Camus, K. J. Betsch, O. Herrwerth, A. Senftleben, A. M. Sayler, T. Rathje, T. Pfeifer, I. Ben-Itzhak, R. R. Jones, G. G. Paulus, F. Krausz, R. Moshammer, J. Ullrich, and M. F. Kling, Nature Communications **3**, 813 (2012).

[25] K. J. Betsch, N. G. Johnson, B. Bergues, M. Kübel, O. Herrwerth, A. Senftleben, I. Ben-Itzhak, G. G. Paulus, R. Moshammer, J. Ullrich, M. F. Kling, and R. R. Jones, Physical Review A: Atomic, Molecular, and Optical Physics **86**, 063403 (2012).

[26] A. S. Alnaser and I. V. Litvinyuk, Journal of Physics B: Atomic, Molecular and Optical Physics **50**, 032002 (2017).

[27] V. Roudnev and B. D. Esry, Phys. Rev. Lett. **99**, 220406 (2007).

[28] J. J. Hua and B. D. Esry, Journal of Physics B: Atomic, Molecular and Optical Physics **42**, 085601 (2009).

[29] J. L. Wiza, Nuclear Instruments and Methods **162**, 587 (1979).

[30] H. Hagstrum, Physical Review **96**, 336 (1954).

[31] B. Manschwetus, T. Nubbemeyer, K. Gorling, G. Steinmeyer, U. Eichmann, H. Rottke, and W. Sandner, Phys. Rev. Lett. **102**, 113002 (2009).

[32] J. McKenna, S. Zeng, J. J. Hua, A. M. Sayler, M. Zohrabi, N. G. Johnson, B. Gaire, K. D. Carnes, B. D. Esry, and I. Ben-Itzhak, Phys. Rev. A: At., Mol., Opt. Phys. **84**, 043425 (2011).

[33] M. J. Rakovic and S.-I. Chu, Journal of Physics B: Atomic, Molecular and Optical Physics **31**, 1989 (1998).

[34] B. Berry, M. Zohrabi, D. Hayes, U. Ablikim, B. Jochim, T. Severt, K. D. Carnes, and I. Ben-Itzhak, Review of Scientific Instruments **86**, 046103 (2015), http://dx.doi.org/10.1063/1.4916953.

[35] X. Ren, A. M. Summers, K. R. P, A. Vajdi, V. Makhija, C. W. Fehrenbach, N. G. Kling, K. J. Betsch, Z. Wang, M. F. Kling, K. D. Carnes, I. Ben-Itzhak, C. Trallero-Herrero, and V. Kumarappan, Journal of Optics **19**, 124017 (2017).

[36] T. Wittmann, B. Horvath, W. Helml, M. G. Schatzel, X. Gu, A. L. Cavalieri, G. G. Paulus, and R. Kienberger, Nature Physics **5**, 357 (2009).

[37] A. M. Sayler, T. Rathje, W. Müller, K. Rühle, R. Kienberger, and G. G. Paulus, Opt. Lett. **36**, 1 (2011).

[38] N. G. Johnson, O. Herrwerth, A. Wirth, S. De, I. Ben-Itzhak, M. Lezius, B. Bergues, M. F. Kling, A. Senftleben, C. D. Schröter, R. Moshammer, J. Ullrich, K. J. Betsch, R. R. Jones, A. M. Sayler, T. Rathje, K. Rühle, W. Müller, and G. G. Paulus, Phys. Rev. A **83**, 013412 (2011).

[39] T. Rathje, N. G. Johnson, M. Möller, F. Süßmann, D. Adolph, M. Kübel, R. Kienberger, M. F. Kling, G. G. Paulus, and A. M. Sayler, Journal of Physics B: Atomic, Molecular and Optical Physics **45**, 074003 (2012).

[40] N. G. Kling, *Controlling the dynamics of electrons and nuclei in ultrafast strong laser fields*, Ph.D. thesis, Kansas State University (2013).

[41] B. Berry, *Imagaing laser-induced fragmentation of molecular beams, from positive to negative molecules*, Ph.D. thesis, Kansas State University (2018).

[42] M. Zohrabi, *Quantum control of molecular fragmentation in strong laser field*, Ph.D. thesis, Kansas State Universtiy (2014).

[43] W. H. Press, *Numerical Recipes* (Cambridge University Press, 2007).

[44] W. Gordon, Annalen der Physik **394**, 1031 (1929).

[45] J. M. Harriman, Phys. Rev. **101**, 594 (1956).

5.5 Determining the detection efficiency of D* atoms

Using the detection scheme presented in Sec. 5.3, we developed a method for determining the detection efficiency of excited neutral atoms, which was published in Review of Scientific Instruments [181]. This method compares the yields of excited atoms detected by different mechanisms and is presented here as published.

Note: Determining the detection efficiency of excited neutral atoms by a microchannel plate detector

Ben Berry, M. Zohrabi, D. Hayes, U. Ablikim, Bethany Jochim, T. Severt, K. D. Carnes, and I. Ben-Itzhak
J.R. Macdonald Laboratory, Physics Department, Kansas State University, Manhattan, Kansas 66506, USA

(Received 13 January 2015; accepted 24 March 2015; published online 3 April 2015)

We present a method for determining the detection efficiency of neutral atoms relative to keV ions. Excited D* atoms are produced by D_2 fragmentation in a strong laser field. The fragments are detected by a micro-channel plate detector either directly as neutrals or as keV ions following field ionization and acceleration by a static electric field. Moreover, we propose a new mechanism by which neutrals are detected. We show that the ratio of the yield of neutrals and ions can be related to the relative detection efficiency of these species. © *2015 AIP Publishing LLC.* [http://dx.doi.org/10.1063/1.4916953]

Measurements involving excited neutral atoms are typically achieved through field ionization and detection of the resulting ions or by detection of fluorescence from the decay of excited states.[1] Field ionization only provides access to highly excited Rydberg states, while fluorescence studies are restricted to allowed atomic transitions. Directly measuring metastable excited neutrals can provide some advantages over other methods, such as gaining access to all excited states, and it has been shown that these measurements are possible using micro-channel plate (MCP) detectors.[2–5]

Particle detection by MCP detectors relies on electron emission and multiplication in the micron-size channels.[6] For light ions, the detection efficiency saturates at around 2-3 keV impact energy, typically at a value equal to the active open area of the detector.[7] In the detection of excited neutral atoms, electron emission and amplification are possible if the internal potential energy of the atom is greater than the work function of the MCP surface (a few eV). Some basic ideas describing this phenomenon exist;[8] however, quantitatively describing the electron emission rate from the MCP surface (i.e., the detection efficiency) has proven difficult.

In addition to detection via the potential energy of the atom, we propose another mechanism. In normal operating conditions, the electric field due to the bias voltage of the MCP is strong enough to field ionize atoms in highly excited Rydberg states. This process always results in the emission of one electron that begins the charge-amplification process.

In this work, we present a method for determining the detection efficiencies of each of these mechanisms, relative to the detection of keV ions (ε_{ion}). This simple scheme allows one to determine the relative efficiencies of both the "potential energy" detection (ε_{PE}) and field ionization within the MCP channel (ε_{FI}) independently. This information may be used to characterize a detector and optimize it for detection of neutrals. To evaluate the efficiencies, we use D* (excited atomic deuterium fragments) formation by laser-induced fragmentation of D_2. The D* potential energy (10.2-13.6 eV) is much greater than the work function of the MCP. The method presented here applies to other species, though they may have different detection efficiencies.

Laser pulses of central wavelength near 800 nm and duration of 30 fs at 10 kHz (corresponding to a peak intensity $I_0 \sim 3 \times 10^{13}$ W/cm^2) are focused on an effusive D_2 gas jet by a spherical mirror (f = 75 mm).[9] The laser polarization is oriented along the axis of the setup shown in Fig. 1, directing fragments emitted in the polarization direction toward either of two MCP detectors where the time of flight is measured.

Each detector is preceded by two high-transmission copper electroformed meshes (88% transmission, 90 lines/in.). For detecting only D* fragments, +150 V is applied to the front mesh to repel any positive ions. A voltage on the second mesh creates an electric field that field ionizes atoms in highly excited states. The direction of the field dictates whether these ions are repelled or detected. The electric field strength is adjustable, which allows control over the range of excited states that are measured and the mechanism by which they are detected. The threshold static electric field strength for field ionization follows the scaling law[11] $E_{th} = \frac{1}{5.783n^4}$. The front MCP is operated at −200 V when detecting neutrals only, and at −1800 V when field ionizing D* between the meshes and accelerating the ions to keV kinetic energy. These negative voltages ensure no electrons are detected. Timing signals are picked off from the back of the MCP stack, and the count rate is kept low enough, much less than one event per laser shot, to avoid saturation.

Determining the detection efficiencies by internal potential energy (ε_{PE}) and field ionization within the channel (ε_{FI}), relative to keV ions (ε_{ion}), requires a series of related measurements.

The electric field inside the MCP channels field ionizes excited states with n quantum number n_{MCP} and above. We estimate the field strength as the MCP voltage divided by its thickness, a good approximation based on SIMION simulations of the electric field near the MCP surface. Setting a repelling field between the meshes (E_{FI}) equal in strength to the MCP field results in the measurement of D* by the potential energy mechanism alone. In hydrogen, $n = 2$ has sufficient excitation to be detected, so D* in states $2 \le n \le n_{MCP}$ are

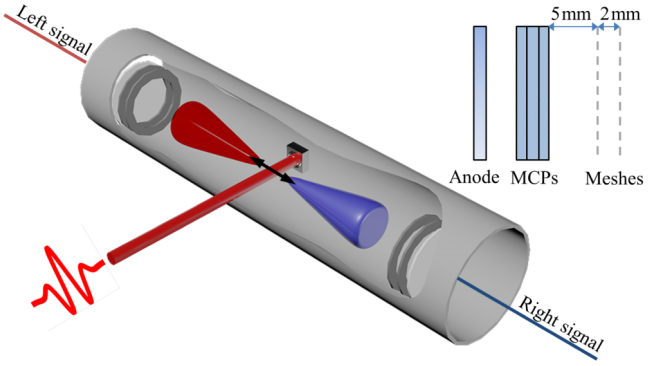

FIG. 1. Schematic of double-sided time-of-flight spectrometer used to measure D* fragments from D_2, along with a diagram of the z-stack MCP detector.[10]

measured (Fig. 2)

$$M_1 = \sum_{n=2}^{n_{MCP}} N_n \, \varepsilon_{PE}, \tag{1}$$

where M_1 is the number of measured D* and N_n is the number produced by the laser in state n. We assume that ε_{PE} is independent of n, as all excited states are much higher in energy than the work function of the MCP, and occupy a narrow energy range (10.2-13.6 eV).

Repeating this measurement with the same E_{FI}, but switching the field direction so that field-ionized D* are detected as D^+ results in

$$M_2 = \sum_{n=2}^{n_{MCP}} N_n \, \varepsilon_{PE} + \sum_{n=n_{MCP}}^{\infty} N_n \, \varepsilon_{ion} \, . \tag{2}$$

In a second pair of measurements, E_{FI} is increased above the MCP field. The mesh field ionizes D* with $n \geq n_L$, where $n_L < n_{MCP}$. Again, in one measurement the field ionized D* are repelled and in the other they are detected

$$M_3 = \sum_{n=2}^{n_L} N_n \, \varepsilon_{PE}, \tag{3}$$

$$M_4 = \sum_{n=2}^{n_L} N_n \, \varepsilon_{PE} + \sum_{n=n_L}^{\infty} N_n \, \varepsilon_{ion} \, . \tag{4}$$

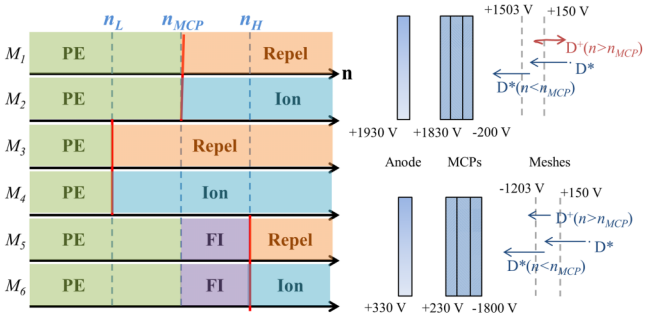

FIG. 2. Left: schematic diagram of the three pairs of measurements involved in determining the relative detection efficiencies, corresponding to measurements $M_1 - M_6$ listed in the text. Right: example detector configurations for repelling (top) and detecting (bottom) field ionized D*.

The difference between M_1 and M_3 is the yield of D* with $n_L \leq n \leq n_{MCP}$ measured as neutrals by the potential energy mechanism.

$$[M_1 - M_3] = \sum_{n=2}^{n_{MCP}} N_n \, \varepsilon_{PE} - \sum_{n=2}^{n_L} N_n \, \varepsilon_{PE}$$
$$= \sum_{n=n_L}^{n_{MCP}} N_n \, \varepsilon_{PE} = \varepsilon_{PE} \sum_{n=n_L}^{n_{MCP}} N_n \, .$$

Similarly, the yield of D* in the same range of n detected as ions is given by

$$[M_4 - M_3] - [M_2 - M_1] = \sum_{n=n_L}^{\infty} N_n \, \varepsilon_{ion} - \sum_{n=n_{MCP}}^{\infty} N_n \, \varepsilon_{ion}$$
$$= \varepsilon_{ion} \sum_{n=n_L}^{n_{MCP}} N_n \, .$$

As the number of D* in each excited state, N_n, produced by the laser field is unknown, the absolute detection efficiencies cannot be determined, but the relative efficiency $\varepsilon_{PE}/\varepsilon_{ion}$ is given by dividing the two expressions above

$$\frac{[M_1 - M_3]}{[M_4 - M_3] - [M_2 - M_1]} = \frac{\varepsilon_{PE} \sum_{n=n_L}^{n_{MCP}} N_n}{\varepsilon_{ion} \sum_{n=n_L}^{n_{MCP}} N_n} = \frac{\varepsilon_{PE}}{\varepsilon_{ion}} \, . \tag{5}$$

In a similar fashion, we can determine the relative detection efficiency of D* by field ionization inside the MCP channel, $\varepsilon_{FI}/\varepsilon_{ion}$, by performing an additional pair of measurements. Now, E_{FI} is set to be weaker than the field inside the MCP, field ionizing $n \geq n_H$, where $n_H > n_{MCP}$. D* in the states between n_{MCP} and n_H are detected by field ionization in the MCP while all states below n_{MCP} are still detected because of their potential energy. Once more, measurements are performed repelling and detecting the ions from all the higher excited states ionized between the meshes

$$M_5 = \sum_{n=2}^{n_{MCP}} N_n \, \varepsilon_{PE} + \sum_{n=n_{MCP}}^{n_H} N_n \, \varepsilon_{FI}, \tag{6}$$

$$M_6 = \sum_{n=2}^{n_{MCP}} N_n \, \varepsilon_{PE} + \sum_{n=n_{MCP}}^{n_H} N_n \, \varepsilon_{FI} + \sum_{n=n_H}^{\infty} N_n \, \varepsilon_{ion} \, . \tag{7}$$

Computing the differences between the measured yields as before gives the yield in states $n_{MCP} \leq n \leq n_H$ detected by field ionization in the MCP,

$$[M_5 - M_1] = \sum_{n=2}^{n_{MCP}} N_n \, \varepsilon_{PE} + \sum_{n=n_{MCP}}^{n_H} N_n \, \varepsilon_{FI} - \sum_{n=2}^{n_{MCP}} N_n \, \varepsilon_{PE}$$
$$= \sum_{n=n_{MCP}}^{n_H} N_n \, \varepsilon_{FI} = \varepsilon_{FI} \sum_{n=n_{MCP}}^{n_H} N_n \, ,$$

and as field-ionized keV ions,

$$[M_2 - M_1] - [M_6 - M_5] = \sum_{n=n_{MCP}}^{\infty} N_n \, \varepsilon_{ion} - \sum_{n=n_H}^{\infty} N_n \, \varepsilon_{ion}$$
$$= \sum_{n=n_{MCP}}^{n_H} N_n \, \varepsilon_{ion} = \varepsilon_{ion} \sum_{n=n_{MCP}}^{n_H} N_n \, .$$

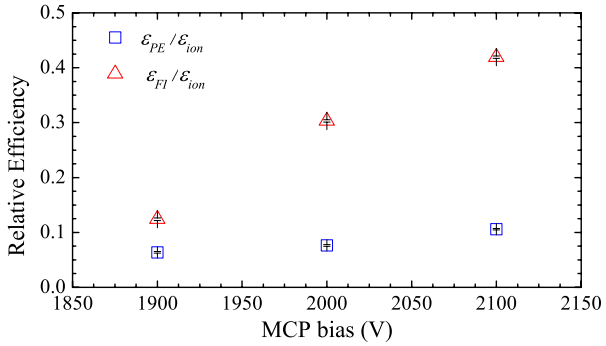

FIG. 3. Measured relative efficiencies $\varepsilon_{PE}/\varepsilon_{ion}$ (blue squares) and $\varepsilon_{FI}/\varepsilon_{ion}$ (red triangles) as functions of MCP bias voltage.

Finally, dividing these expressions results in the relative efficiency for $\varepsilon_{FI}/\varepsilon_{ion}$,

$$\frac{[M_5 - M_1]}{[M_2 - M_1] - [M_6 - M_5]} = \frac{\varepsilon_{FI} \sum_{n=n_{MCP}}^{n_H} N_n}{\varepsilon_{ion} \sum_{n=n_{MCP}}^{n_H} N_n} = \frac{\varepsilon_{FI}}{\varepsilon_{ion}}. \quad (8)$$

If the absolute efficiencies are needed, the ion detection efficiency can be determined using the method described by Gaire *et al.*[12] In Fig. 3, we show the relative efficiencies evaluated using Eqs. (5) and (8). We observe that as the MCP bias voltage is increased (i.e., the MCP gain is increased), both relative efficiencies also increase. At these MCP voltages, the ion detection efficiency is saturated (likely to the open area). This was determined by directing D^+ created in the laser interaction toward the detector with a weak electric field and detecting ions with 2 keV impact energy. At the MCP voltages mentioned above, the D^+ rate was constant, indicating that the ion detection efficiency was saturated. Therefore, the increase with detector gain is mainly due to increases in the neutral detection efficiency.

Furthermore, we observe that ε_{FI} is significantly greater than ε_{PE}, which is not unexpected. While field ionization within the MCP channel always results in the release of an electron that can start the charge-amplification process, these results suggest that transferring internal energy to the surface does not. Previous studies[2] have found that, depending on the species and detector conditions, the efficiency of "potential energy" detection can range from 10^{-4} to 0.5. We were limited to a maximum bias of 2100 V due to technical issues; however, we expect the efficiency would improve with increased voltage.

It should be noted that while these efficiency measurements only require one detector, we made use of the two detectors in our experimental setup by operating one at constant settings while evaluating the efficiency on the other. This allowed us to correct for fluctuations in target density and laser power that change the number of D* produced in the interaction, by using the yield on the detector held constant for normalization.

In summary, we have presented a simple technique for determining the relative detection efficiency of a MCP detector for neutral particles. In addition to the well-known "potential energy" detection mechanism for excited neutrals, we suggest that highly excited neutrals can be detected by field ionization inside the MCP. The relative detection efficiencies of each of these mechanisms is measured using the experimental scheme described herein.

This work was supported by the Chemical Sciences, Geosciences, and Biosciences Division, Office of Basic Energy Sciences, Office of Science, U.S. Department of Energy, Grant No. DE-FG02-86ER1349. The PULSAR laser was provided by Grant No. DE-FG02-09ER16115 from the same funding agency. B.J. is supported by the Department of Energy Office of Science Graduate Fellowship Program (DOE SCGF), made possible in part by the American Recovery and Reinvestment Act of 2009, administered by ORISE-ORAU under contract no. DE-AC05-06OR23100.

[1]T. F. Gallagher, *Rydberg Atoms* (Cambridge University Press, 1994).
[2]H. Hotop, "Detection of Metastable Atoms and Molecules," *Atomic, Molecular, and Optical Physics: Atoms and Molecules*, Experimental Methods in the Physical Sciences edited by F. Dunning and R. G. Hulet (Academic Press, 1996), Vol. 29B, p. 191.
[3]W. Vassen, C. Cohen-Tannoudji, M. Leduc, D. Boiron, C. Westbrook, A. Truscott, K. Baldwin, G. Birkl, P. Cancio, and M. Trippenbach, Rev. Mod. Phys. **84**, 175 (2012).
[4]B. Manschwetus, T. Nubbemeyer, K. Gorling, G. Steinmeyer, U. Eichmann, H. Rottke, and W. Sandner, Phys. Rev. Lett. **102**, 113002 (2009).
[5]J. McKenna, S. Zeng, J. J. Hua, A. M. Sayler, M. Zohrabi, N. G. Johnson, B. Gaire, K. D. Carnes, B. D. Esry, and I. Ben-Itzhak, Phys. Rev. A **84**, 043425 (2011).
[6]J. L. Wiza, Nucl. Instrum. Methods **162**, 587 (1979).
[7]J. Oberheide, P. Wilhelms, and M. Zimmer, Meas. Sci. Technol. **8**, 351 (1997).
[8]H. Hagstrum, Phys. Rev. **96**, 336 (1954).
[9]Using the JRML laser known as PULSAR - a KM-Labs laser providing 2 mJ, down to 21 fs FTL pulses at a 10 kHz repetition rate with a central wavelength of about 790 nm.
[10]Photonis detection-grade MCPs: 25 micron pore size, 32 micron center-to-center, 40:1 aspect ratio, 8 degree bias angle.
[11]M. J. Rakovic and S.-I. Chu, J. Phys. B: At., Mol. Opt. Phys. **31**, 1989 (1998).
[12]B. Gaire, A. M. Sayler, P. Q. Wang, N. G. Johnson, M. Leonard, E. Parke, K. D. Carnes, and I. Ben-Itzhak, Rev. Sci. Instrum. **78**, 024503 (2007).

5.6 Doppler-free imaging of double ionization

The apparatus described in Sec. 5.3 was originally intended for use in coincidence measurements of dissociative double-ionization of molecules. The scheme, developed by Lundqvist and coworkers [218], involves the TOF measurement of both dissociating ionic fragments in coincidence, one on each detector. These TOFs are given explicitly by

$$t_L = \frac{l_L + z_i}{(v'_L - v_{CM})} \tag{5.3}$$

$$t_R = \frac{l_R - z_i}{(v'_R + v_{CM})}, \tag{5.4}$$

where $t_{L,R}$ are the measured TOFs on the left and right sides, $l_{L,R}$ are the distances from the center of the gas jet to each detector, z_i is the position of the interaction along the device axis, v_{CM} is the initial center-of-mass velocity of the molecule in the lab frame, and $v'_{L,R}$ are the velocities of the two fragments in the center-of-mass frame. In addition to the TOF formulas, momentum conservation dictates that

$$m_L v'_L = m_R v'_R \tag{5.5}$$

This system of three equations allows solving for the three unknown variables: v_{CM}, v'_L, and v'_R, while z_i is replaced by an average value. Because of the geometry of the setup, v_{CM} adds to the velocity of one fragment and subtracts from the velocity of the other and essentially cancels out. It follows that the solution for the velocity in the center-of-mass frame is independent of v_{CM}. As a result, the measurement is free of Doppler broadening due to the center-of-mass motion, hence the name "Doppler free".

$$v'_R = \frac{1}{1 + \frac{m_R}{m_L}}\left(\frac{l_R - z_i}{t_R} + \frac{l_L + z_i}{t_L}\right). \tag{5.6}$$

The unknown value z_i is replaced by an average value and is used as a parameter to symmetrize the velocity distribution. This introduces a small uncertainty of less than 0.1%. For completeness, v_{CM} can also be solved for and is given by

$$v_{CM} = \frac{1}{1+\frac{m_R}{m_L}}\left(\frac{m_R}{m_L}\frac{l_R - z_i}{t_R} - \frac{l_L + z_i}{t_L}\right). \tag{5.7}$$

Then, the kinetic energy release upon dissociation, given by

$$\mathrm{KER} = \frac{1}{2}m_R v_R'^2 + \frac{1}{2}m_L v_L'^2, \tag{5.8}$$

is unaffected by Doppler broadening, which allows for measurements of KER with vibrational resolution [218, 219].

This "Doppler-free" technique was used by Lundqvist and coworkers to resolve the vibrational structure of metastable states of CO^{2+} [218], O_2^{2+} [219], N_2^{2+} [220], and NO^{2+} [221]. The primary limiting factor regarding the energy resolution was the rotational temperature of the gas target (300 K or 25 meV). These measurements were important in identifying metastable states of the doubly-charged molecules and determining their energies and lifetimes.

In the long run, we aim to extend these types of studies by, for example, comparing multiphoton double-ionization by a strong laser field with double-electron capture (or double ionization) in collisions with highly charged ions. Preliminary results from measurements of double ionization of O_2 using collisions with 19 MeV F^{4+} ions as well as strong laser fields are shown in Fig. 5.5(a-b). The coincidence TOF maps reveal several structures in the collisions measurement which are likely associated with different electronic states of the dication. Conversely, laser measurement shows much less structure.

To better visualize this structure, the TOF maps shown in Fig. 5.5(a-b) are rotated by 45° and projected onto the diagonal line, i.e. onto t_{sum}, defined by

$$t_{sum} = \frac{t_L + t_R}{2}, \tag{5.9}$$

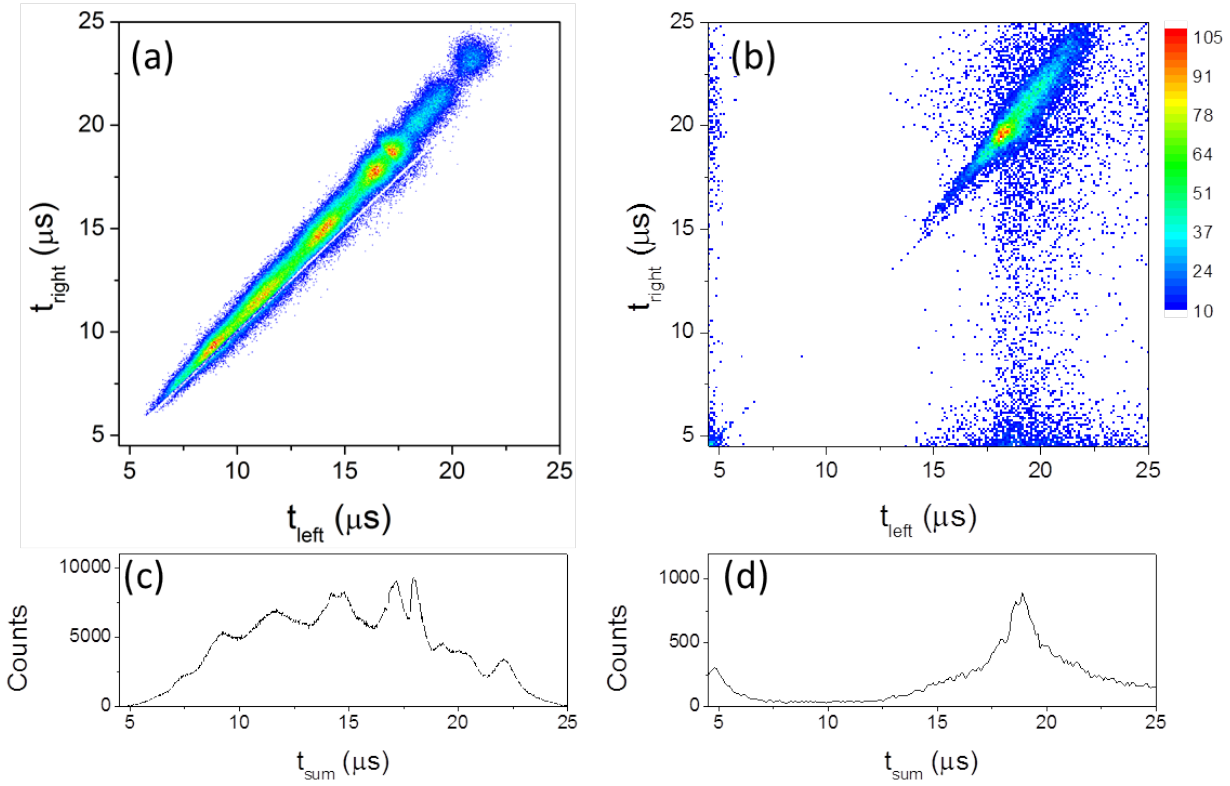

Figure 5.5: Coincidence time-of-flight maps for the double ionization of O_2 (a) by collisions with 19 MeV F^{4+} ions and (b) by multiphoton ionization using 25-fs, 800-nm, 1×10^{13} W/cm^2 pulses. (c)-(d) Projected t_{sum} distributions with $-2 < t_{diff} < 6\,\mu$s for each of these cases (see text).

as shown in Fig. 5.5(c-d). The other coordinate in this rotated frame is the time difference, $t_{diff} = t_L - t_R$. To minimize the effect of random background coincidences in the projected spectra, the t_{sum} projection shown in Fig. 5.5(d) is gated on events with $-2 < t_{diff} < 6\,\mu$s. The peaks in Fig. 5.5(c) are due to dissociation from several different electronic states of O_2^{2+}, however we have been unable to match them with the structure measured by Lundqvist *et al.* [219], and further work will need to be done to identify the states associated with the peaks in each measurement. The single peak in the laser measurement, shown in Fig. 5.5(d), does not quite match the t_{sum} of the dominant peaks in the collision measurement, indicating the different electronic states are likely being populated.

Clearly, we were unable to obtain vibrational resolution in these preliminary measurements. There are a few potential sources of broadening affecting the energy resolution. The

relatively large acceptance angle of the detectors, 14.5°, could smear out the KER, as we treat the breakup as 1D. By using position-sensitive detectors, 3D momentum imaging could improve the energy resolution. Alternatively, limiting the angular acceptance of the detectors with small apertures (like Lundqvist *et al.* [218]) could improve the resolution. In the laser measurements, the high intensity of the laser pulses could cause smearing of the KER in addition to the instrumental resolution.

5.6.1 Evaluation of the gas jet temperature

Employing the Dopper-free technique described above, the coincidence measurement of both ionic fragments allows for the solution of the initial center-of-mass velocity of the molecule. The effective temperature of the jet can then be determined from the distribution of v_{CM}. A typical v_{CM} distribution is shown in Fig. 5.6.

The thermal velocity distribution in one dimension can be described by the Maxwell-Boltzmann velocity distribution

$$f(v) = \sqrt{\frac{m}{2\pi kT}} e^{-\frac{mv^2}{2kT}}$$

where m is the mass of the molecule, k is the Boltzmann constant, and T is the effective temperature. The temperature can then be related to the width of the measured v_{CM} distribution by fitting the velocity distribution to our measured v_{CM} distribution. As shown in Fig. 5.6(a), a Maxwell-Boltzmann distribution with T=100 K has the same width as the measured distribution. Note that our measured v_{CM} distribution is not exactly Gaussian and has extra structure, therefore the Maxwell-Boltzmann distribution only gives an approximate temperature. The source of the structure and left/right asymmetry in the measured v_{CM} distribution is likely an unknown experimental artifact. In Fig. 5.6(b), the thermal energy distribution is plotted. For reference, room temperature ($\sim$ 300 K) corresponds to a thermal energy of 0.04 eV. The evaluated temperature of 100 K is not different from what one would expect for an effusive jet in which the temperature is similar to, though somewhat cooler than

the source temperature. The molecular flow through the long, narrow needle transversely cools the jet.

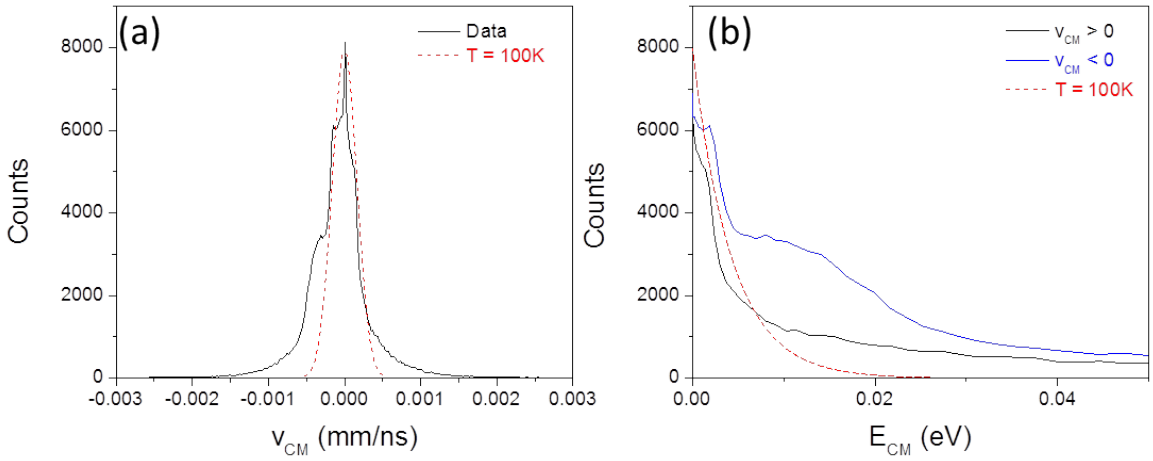

Figure 5.6: (a) Measured center-of-mass velocity distribution of O_2 (solid black line) with a Maxwell-Boltzmann velocity distribution overlayed (dashed red line) that was used to determine the jet temperature. (b) Center-of-mass kinetic energy distributions. The structure and asymmetry in the measured distributions are likely due to an unknown experimental artifact, but the width of the distribution provides an approximate temperature of 100 K (see text).

5.7 Summary and outlook

In summary, new insight into the multiphoton excitation of D_2 has been gained through the development of a state-selective scheme for directly detecting excited atomic D* fragments from D_2. The production of D* fragments was found to depend on the CEP of sub-5-fs pulses, and the CEP effects were quite different for different sets of excited states. Furthermore, the n-state population of the D(nl) fragments was measured and found to have a $n^{-3.74}$ dependence. This state-selective detection scheme was also used to develop a method for determining the detection efficiency of excited neutral atoms by MCP detectors. Improvements to the experimental apparatus including the addition of position sensitive detectors and the ability to detect ions in coincidence with the excited neutral fragments will be pursued by other students in the future. Coincidence measurements of $D^+ + D^*$ will further

help in identifying fragmentation pathways of D_2. Implementing position-sensitive detectors will improve the KER resolution which may be particularly useful in future measurements.

Chapter 6

Summary and Outlook

To conclude, several examples of studies of laser-induced fragmentation of molecules were presented in this dissertation with the aim of working towards improving our understanding of the interactions of molecules with intense, ultrashort laser pulses. The technical developments that were achieved enabled these studies that provided new information about the fragmentation of positive, negative, and neutral molecules. The main findings are summarized here.

Studies of dissociation and photodetachment of F_2^- and LiO^- led to new information about the fragmentation of molecular anions by strong laser fields. Measurements of the dissociation of F_2^- under various laser conditions enabled us to identify the dissociation pathways and evaluate the initial vibrational population of the F_2^- beam. The photodetachment of F_2^- was also found to predominantly result in breakup into F+F fragments. We were able to suggest direct and sequential processes that contribute to the F+F yield that were identified by their KER. Studies involving the dissociation of LiO^- into $Li+O^-$ utilized resonance-enhanced two-photon excitation to determine the bond dissociation energy of LiO^-, which we found to be at least 0.3 eV greater than values based on theory. Furthermore, the vibrational autodetachment of LiO^- was explored using a pump-probe scheme to measure autodetachment lifetimes, and preliminary results suggest a lifetime of about 300 fs.

The generation and use of the fast molecular anion beams that made these studies possible

was the primary technical achievement of this work. In addition, the coincidence 3D momentum imaging technique developed for positive ions was adapted to the case of negative ions. Further work on molecular anions is already in progress. Studies of the photodetachment of H^- by single-photon and multiphoton absorption will hopefully provide new information about photodetachment. Furthermore, ionization of H by recollision of the photodetached electron can be explored at low laser intensities with linear and circular polarization. The fragmentation of $C_2H_2^-$ offers the opportunity to study bond rearrangement. Future studies will build on the studies we have performed on dissociation, photodetachment, and autodetachment of molecular anions. In the long run we plan to use photodetachment of molecular anion beams to generate fast beams of neutral molecules. All of these experiments will benefit from bunching of the ion beam, which will be implemented in the near future and is expected to increase the target density by a factor of 10 or more.

Ionization of positively charged molecular ions was successfully studied by employing a pump-probe technique, which enabled us to observe enhanced ionization of dissociating HD^+ and Ar_2^+ at surprisingly large internuclear separation where the fragments are expected to behave like separate atoms. Pump-probe and other "scanning" measurements would benefit greatly from increased target density. The duoplasmatron ion source that was implemented into our system as part of this work and used to generate Ar_2^+ provides high currents of positive ions. Along with bunching of the ion beam, these developments should further our abilities to study dynamics in future experiments.

Finally, the development of an approach to state-selectively study the production of D* fragments from D_2 led to new insight into the multiphoton excitation of D_2. The carrier-envelope phase dependence of D* formation was found to change for different ranges of excited states of the D* fragments. Moreover, we used this state-selective method to measure the excited state population of the D* fragments. In the near future, improvements to the apparatus including the ability to measure the position of fragments on the detectors and to measure D^+ ions in coincidence with D* fragments will be used to further our understanding of D* formation.

Bibliography

[1] A. H. Zewail, "Femtochemistry: Atomic-scale dynamics of the chemical bond", J. Phys. Chem. A **104**, 5660 (2000), http://dx.doi.org/10.1021/jp001460h.

[2] P. B. Corkum and F. Krausz, "Attosecond science", Nature Physics **3**, 381 (2007), http://dx.doi.org/10.1038/nphys620.

[3] A. H. Zewail, "Laser femtochemistry", Science **242**, 1645 (1988), http://science.sciencemag.org/content/242/4886/1645.

[4] F. Krausz and M. Ivanov, "Attosecond physics", Reviews of Modern Physics **81**, 163 (2009), https://link.aps.org/doi/10.1103/RevModPhys.81.163.

[5] P. Q. Wang, A. M. Sayler, K. D. Carnes, J. F. Xia, M. A. Smith, B. D. Esry, and I. Ben-Itzhak, "Dissociation of $H_2{}^+$ in intense femtosecond laser fields studied by coincidence three-dimensional momentum imaging", Phys. Rev. A: At., Mol., Opt. Phys. **74**, 043411 (2006), https://link.aps.org/doi/10.1103/PhysRevA.74.043411.

[6] J. McKenna, A. M. Sayler, F. Anis, B. Gaire, N. G. Johnson, E. Parke, J. J. Hua, H. Mashiko, C. M. Nakamura, E. Moon, et al., "Enhancing high-order above-threshold dissociation of H_2^+ beams with few-cycle laser pulses", Phys. Rev. Lett. **100**, 133001 (2008), https://link.aps.org/doi/10.1103/PhysRevLett.100.133001.

[7] N. G. Kling, K. J. Betsch, M. Zohrabi, S. Zeng, F. Anis, U. Ablikim, B. Jochim, Z. Wang, M. Kübel, M. F. Kling, et al., "Carrier-envelope phase control over pathway interference in strong-field dissociation of H_2^+", Physical Review Letters **111**, 163004 (2013), https://link.aps.org/doi/10.1103/PhysRevLett.111.163004.

[8] I. Ben-Itzhak, *Progress in Ultrafast Laser Science IV* (Springer, 2009), vol. 91, chap. Molecular ion beams interrogated with ultrashort intense laser pulses.

[9] J. McKenna, F. Anis, B. Gaire, N. G. Johnson, M. Zohrabi, K. D. Carnes, B. D. Esry, and I. Ben-Itzhak, "Suppressed dissociation of H_2^+ vibrational states by reduced dipole coupling", Phys. Rev. Lett. **103**, 103006 (2009), https://link.aps.org/doi/10.1103/PhysRevLett.103.103006.

[10] J. McKenna, A. M. Sayler, B. Gaire, N. G. Johnson, M. Zohrabi, K. D. Carnes, B. D. Esry, and I. Ben-Itzhak, "Permanent dipole transitions remain elusive in HD^+ strong-field dissociation", Journal of Physics B: Atomic, Molecular and Optical Physics **42**, 121003 (2009), http://stacks.iop.org/0953-4075/42/i=12/a=121003.

[11] J. McKenna, A. M. Sayler, B. Gaire, N. G. Johnson, K. D. Carnes, B. D. Esry, and I. Ben-Itzhak, "Benchmark measurements of $H_3{}^+$ nonlinear dynamics in intense ultrashort laser pulses", Phys. Rev. Lett. **103**, 103004 (2009), https://link.aps.org/doi/10.1103/PhysRevLett.103.103004.

[12] B. Gaire, Ph.D. thesis, Kansas State University (2011), http://hdl.handle.net/2097/8852.

[13] J. McKenna, A. M. Sayler, B. Gaire, N. G. Kling, B. D. Esry, K. D. Carnes, and I. Ben-Itzhak, "Frustrated tunnelling ionization during strong-field fragmentation of D_3^+", New Journal of Physics **14**, 103029 (2012), http://stacks.iop.org/1367-2630/14/i=10/a=103029.

[14] A. M. Sayler, J. McKenna, B. Gaire, N. G. Kling, K. D. Carnes, and I. Ben-Itzhak, "Measurements of intense ultrafast laser-driven $D_3{}^+$ fragmentation dynamics", Phys. Rev. A: At., Mol., Opt. Phys. **86**, 033425 (2012), https://link.aps.org/doi/10.1103/PhysRevA.86.033425.

[15] A. M. Sayler, J. McKenna, B. Gaire, N. G. Kling, K. D. Carnes, B. D. Esry, and I. Ben-Itzhak, "Elucidating isotopic effects in intense ultrafast laser-driven D_2H^+ fragmentation", Journal of Physics B: Atomic, Molecular and Optical Physics **47**, 031001 (2014), http://stacks.iop.org/0953-4075/47/i=3/a=031001.

[16] J. McKenna, A. M. Sayler, B. Gaire, N. G. Johnson, E. Parke, K. D. Carnes, B. D. Esry, and I. Ben-Itzhak, "Intensity dependence in the dissociation branching ratio of ND^+ using intense femtosecond laser pulses", Phys. Rev. A: At., Mol., Opt. Phys. **77**, 063422 (2008), https://link.aps.org/doi/10.1103/PhysRevA.77.063422.

[17] J. McKenna, A. M. Sayler, F. Anis, N. G. Johnson, B. Gaire, U. Lev, M. A. Zohrabi, K. D. Carnes, B. D. Esry, and I. Ben-Itzhak, "Vibrationally cold CO^{2+} in intense ultrashort laser pulses", Physical Review A: Atomic, Molecular, and Optical Physics **81**, 061401 (2010), https://link.aps.org/doi/10.1103/PhysRevA.81.061401.

[18] M. Zohrabi, J. McKenna, B. Gaire, N. G. Johnson, K. D. Carnes, S. De, I. A. Bocharova, M. Magrakvelidze, D. Ray, I. V. Litvinyuk, et al., "Vibrationally resolved structure in O_2^+ dissociation induced by intense ultrashort laser pulses", Phys. Rev. A: At., Mol., Opt. Phys. **83**, 053405 (2011), https://link.aps.org/doi/10.1103/PhysRevA.83.053405.

[19] L. Graham, M. Zohrabi, B. Gaire, U. Ablikim, B. Jochim, B. Berry, T. Severt, K. J. Betsch, A. M. Summers, U. Lev, et al., "Fragmentation of CD^+ induced by intense ultrashort laser pulses", Physical Review A: Atomic, Molecular, and Optical Physics **91**, 023414 (2015), https://link.aps.org/doi/10.1103/PhysRevA.91.023414.

[20] A. M. Sayler, Ph.D. thesis, Kansas State Universtiy (2008), http://hdl.handle.net/2097/2611.

[21] I. Ben-Itzhak, P. Q. Wang, J. F. Xia, A. M. Sayler, M. A. Smith, K. D. Carnes, and B. D. Esry, "Dissociation and ionization of $H_2{}^+$ by ultrashort intense laser pulses probed by coincidence 3d momentum imaging", Physical Review Letters **95**, 073002 (2005), https://link.aps.org/doi/10.1103/PhysRevLett.95.073002.

[22] A. Giusti-Suzor, F. H. Mies, L. F. DiMauro, E. Charron, and B. Yang, "Dynamics of H_2^+ in intense laser fields", J. Phys. B: At., Mol. Opt. Phys. **28**, 309 (1995), http://stacks.iop.org/0953-4075/28/i=3/a=006.

[23] I. D. Williams, P. McKenna, B. Srigengan, I. M. G. Johnston, W. A. Bryan, J. H. Sanderson, A. El-Zein, T. R. J. Goodworth, W. R. Newell, P. F. Taday, et al., "Fast-beam study of H_2^+ ions in an intense femtosecond laser field", Journal of Physics B: Atomic, Molecular and Optical Physics **33**, 2743 (2000), http://stacks.iop.org/0953-4075/33/i=14/a=311.

[24] J. H. Posthumus, "The dynamics of small molecules in intense laser fields", Reports on Progress in Physics **67**, 623 (2004), http://stacks.iop.org/0034-4885/67/i=5/a=R01.

[25] D. Pavičić, T. W. Hänsch, and H. Figger, "Vibrationally resolved strong-field dissociation of $D_2{}^+$ in ion beams", Phys. Rev. A: At., Mol., Opt. Phys. **72**, 053413 (2005), https://link.aps.org/doi/10.1103/PhysRevA.72.053413.

[26] J. D. Alexander, C. R. Calvert, R. B. King, O. Kelly, L. Graham, W. A. Bryan, G. R. A. J. Nemeth, W. R. Newell, C. A. Froud, I. C. E. Turcu, et al., "Photodissociation of D_3^+ in an intense, femtosecond laser field", Journal of Physics B: Atomic, Molecular and Optical Physics **42**, 141004 (2009), http://stacks.iop.org/0953-4075/42/i=14/a=141004.

[27] E. Lötstedt, T. Kato, and K. Yamanouchi, "Classical dynamics of laser-driven D_3^+", Physical Review Letters **106**, 203001 (2011), https://link.aps.org/doi/10.1103/PhysRevLett.106.203001.

[28] B. Gaire, J. McKenna, M. Zohrabi, K. D. Carnes, B. D. Esry, and I. Ben-Itzhak, "Dynamics of $D_3{}^+$ slow dissociation induced by intense ultrashort laser pulses", Physical Review A: Atomic, Molecular, and Optical Physics **85**, 023419 (2012), https://link.aps.org/doi/10.1103/PhysRevA.85.023419.

[29] H. Hultgren and I. Y. Kiyan, "Photodetachment dynamics of $F_2{}^-$ in a strong laser field", Physical Review A: Atomic, Molecular, and Optical Physics **84**, 015401 (2011), https://link.aps.org/doi/10.1103/PhysRevA.84.015401.

[30] Y. Albeck, D. M. Kandhasamy, and D. Strasser, "Multiple detachment of the SF_6^- molecular anion with shaped intense laser pulses", The Journal of Physical Chemistry A **118**, 388 (2014), pMID: 24369787, http://dx.doi.org/10.1021/jp4116436.

[31] B. J. Greenblatt, M. T. Zanni, and D. M. Neumark, "Photodissociation of I_2–$(Ar)_n$ clusters studied with anion femtosecond photoelectron spectroscopy", Science **276**, 1675 (1997), http://science.sciencemag.org/content/276/5319/1675.

[32] R. E. Continetti, "Coincidence spectroscopy", Annual Review of Physical Chemistry **51**, 165 (2001).

[33] J. Simons, "Molecular anions", The Journal of Physical Chemistry A **112**, 6401 (2008), pMID: 18630888, http://dx.doi.org/10.1021/jp711490b.

[34] "Peabody scientific", www.peabody-scientific.com.

[35] O. Heber, R. Golser, H. Gnaser, D. Berkovits, Y. Toker, M. Eritt, M. L. Rappaport, and D. Zajfman, "Lifetimes of the negative molecular hydrogen ions: H_2^-, D_2^-, and HD^-", Physical Review A: Atomic, Molecular, and Optical Physics **73**, 060501 (2006), https://link.aps.org/doi/10.1103/PhysRevA.73.060501.

[36] L. Lammich, L. H. Andersen, G. Aravind, and H. B. Pedersen, "Experimental characterization of the metastable D_2^- ion by photofragment imaging", Physical Review A: Atomic, Molecular, and Optical Physics **80**, 023413 (2009), https://link.aps.org/doi/10.1103/PhysRevA.80.023413.

[37] V. E. Krohn, "Emission of negative ions from metal surfaces bombarded by positive cesium ions", Journal of Applied Physics **33**, 3523 (1962), http://dx.doi.org/10.1063/1.1702439.

[38] R. Middleton, Tech. Rep., Department of Physics, University of Pennsylvania (1990).

[39] RoentDek, "Roentdek handels gmbh", http://www.roentdek.com.

[40] J. L. Wiza, "Microchannel plate detectors", Nuclear Instruments and Methods **162**, 587 (1979), http://www.sciencedirect.com/science/article/pii/0029554X79907341.

[41] A. Staudte, Ph.D. thesis, Goethe University Frankfurt (2005).

[42] I. Ben-Itzhak, *Fragmentation Processes: Topics in Atomic and Molecular Physics* (Cambridge University Press, 2013), chap. Fragmentation of molecular-ion beams in intense ultrashort laser pulses.

[43] SIMION, "Simion industry standard charged particle optics simulation software", http://simion.com.

[44] X. Ren, A. M. Summers, K. R. P, A. Vajdi, V. Makhija, C. W. Fehrenbach, N. G. Kling, K. J. Betsch, Z. Wang, M. F. Kling, et al., "Single-shot carrier-envelope-phase tagging using an $f--2f$ interferometer and a phase meter: a comparison", Journal of Optics **19**, 124017 (2017), http://stacks.iop.org/2040-8986/19/i=12/a=124017.

[45] T. Brabec and F. Krausz, "Intense few-cycle laser fields: Frontiers of nonlinear optics", Reviews of Modern Physics **72**, 545 (2000), https://link.aps.org/doi/10.1103/RevModPhys.72.545.

[46] J.-C. Diels and W. Rudolph, *Ultrashort Laser Pulse Phenomena* (Academic Press, 2006).

[47] Z. Chang, *Fundamentals of Attosecond Optics* (CRC Press, 2011).

[48] P. F. Moulton, "Spectroscopic and laser characteristics of Ti:Al_2O_3", J. Opt. Soc. Am. B **3**, 125 (1986), http://josab.osa.org/abstract.cfm?URI=josab-3-1-125.

[49] D. E. Spence, P. N. Kean, and W. Sibbett, "60-fsec pulse generation from a self-mode-locked Ti:Sapphire laser", Opt. Lett. **16**, 42 (1991), http://ol.osa.org/abstract.cfm?URI=ol-16-1-42.

[50] E. Hecht, *Optics* (Addison-Wesley, 2001), 4th ed.

[51] D. Strickland and G. Mourou, "Compression of amplified chirped optical pulses", Optics Communications **55**, 447 (1985), http://www.sciencedirect.com/science/article/pii/0030401885901518.

[52] R. Goldstein, "Pockels cell primer", Laser Focus (1968).

[53] N. G. Kling, Ph.D. thesis, Kansas State University (2013), http://hdl.handle.net/2097/16821.

[54] M. Nisoli, S. D. Silvestri, and O. Svelto, "Generation of high energy 10 fs pulses by a new pulse compression technique", Applied Physics Letters **68**, 2793 (1996), http://dx.doi.org/10.1063/1.116609.

[55] M. Nisoli, S. D. Silvestri, O. Svelto, R. Szipöcs, K. Ferencz, C. Spielmann, S. Sartania, and F. Krausz, "Compression of high-energy laser pulses below 5 fs", Opt. Lett. **22**, 522 (1997), http://ol.osa.org/abstract.cfm?URI=ol-22-8-522.

[56] B. Schenkel, J. Biegert, U. Keller, C. Vozzi, M. Nisoli, G. Sansone, S. Stagira, S. D. Silvestri, and O. Svelto, "Generation of 3.8-fs pulses from adaptive compression of a cascaded hollow fiber supercontinuum", Opt. Lett. **28**, 1987 (2003), http://ol.osa.org/abstract.cfm?URI=ol-28-20-1987.

[57] A. Baltuska, M. Uiberacker, E. Goulielmakis, R. Kienberger, V. S. Yakovlev, T. Udem, T. W. Hansch, and F. Krausz, "Phase-controlled amplification of few-cycle laser pulses", IEEE Journal of Selected Topics in Quantum Electronics **9**, 972 (2003).

[58] T. Pfeifer, C. Spielmann, and G. Gerber, "Femtosecond x-ray science", Reports on Progress in Physics **69**, 443 (2006), http://stacks.iop.org/0034-4885/69/i=2/a=R04.

[59] M. Nisoli and G. Sansone, "New frontiers in attosecond science", Progress in Quantum Electronics **33**, 17 (2009), http://www.sciencedirect.com/science/article/pii/S0079672708000244.

[60] R. W. Boyd, *Nonlinear Optics* (Academic Press, 2008), 3rd ed.

[61] R. Szipöcs, C. Spielmann, F. Krausz, and K. Ferencz, "Chirped multilayer coatings for broadband dispersion control in femtosecond lasers", Opt. Lett. **19**, 201 (1994), http://ol.osa.org/abstract.cfm?URI=ol-19-3-201.

[62] R. Abrams, "Coupling losses in hollow waveguide laser resonators", IEEE Journal of Quantum Electronics **8**, 838 (1972).

[63] L. Gallmann, T. Pfeifer, P. Nagel, M. Abel, D. Neumark, and S. Leone, "Comparison of the filamentation and the hollow-core fiber characteristics for pulse compression into the few-cycle regime", Applied Physics B **86**, 561 (2007), http://dx.doi.org/10.1007/s00340-006-2503-8.

[64] "Tem messtechnik gmbh", www.tem-messtechnik.de.

[65] "United crystals", www.unitedcrystals.com.

[66] "Ocean optics", www.oceanoptics.com.

[67] "Coherent", www.coherent.com.

[68] R. Trebino, *Frequency-Resolved Optical Gating: The Measurement of Ultrashort Laser Pulses* (Springer, 2012).

[69] "Real-time ultrafast laser pulse measurement", https://www.mesaphotonics.com.

[70] M. F. Kling, C. Siedschlag, A. J. Verhoef, J. I. Khan, M. Schultze, T. Uphues, Y. Ni, M. Uiberacker, M. Drescher, F. Krausz, et al., "Control of electron localization in molecular dissociation", Science **312**, 246 (2006), http://science.sciencemag.org/content/312/5771/246.

[71] F. Süßmann, S. Zherebtsov, J. Plenge, N. G. Johnson, M. Kübel, A. M. Sayler, V. Mondes, C. Graf, E. Rühl, G. G. Paulus, et al., "Single-shot velocity-map imaging of attosecond light-field control at kilohertz rate", Review of Scientific Instruments **82**, 093109 (2011), http://dx.doi.org/10.1063/1.3639333.

[72] B. Bergues, M. Kübel, N. G. Johnson, B. Fischer, N. Camus, K. J. Betsch, O. Herrwerth, A. Senftleben, A. M. Sayler, T. Rathje, et al., "Attosecond tracing of correlated electron-emission in non-sequential double ionization", Nature Communications **3**, 813 (2012), http://dx.doi.org/10.1038/ncomms1807.

[73] K. J. Betsch, N. G. Johnson, B. Bergues, M. Kübel, O. Herrwerth, A. Senftleben, I. Ben-Itzhak, G. G. Paulus, R. Moshammer, J. Ullrich, et al., "Controlled directional ion emission from several fragmentation channels of CO driven by a few-cycle laser field", Physical Review A: Atomic, Molecular, and Optical Physics **86**, 063403 (2012), https://link.aps.org/doi/10.1103/PhysRevA.86.063403.

[74] H. Xu, J.-P. Maclean, D. E. Laban, W. C. Wallace, D. Kielpinski, R. T. Sang, and I. V. Litvinyuk, "Carrier-envelope-phase-dependent dissociation of hydrogen", New Journal of Physics **15**, 023034 (2013), http://stacks.iop.org/1367-2630/15/i=2/a=023034.

[75] T. Rathje, A. M. Sayler, S. Zeng, P. Wustelt, H. Figger, B. D. Esry, and G. G. Paulus, "Coherent control at its most fundamental: Carrier-envelope-phase-dependent electron localization in photodissociation of a H_2^+ molecular ion beam target", Phys. Rev. Lett. **111**, 093002 (2013), https://link.aps.org/doi/10.1103/PhysRevLett.111.093002.

[76] V. Roudnev, B. D. Esry, and I. Ben-Itzhak, "Controlling HD^+ and H_2^+ dissociation with the carrier-envelope phase difference of an intense ultrashort laser pulse", Phys. Rev. Lett. **93**, 163601 (2004), https://link.aps.org/doi/10.1103/PhysRevLett.93.163601.

[77] V. Roudnev and B. D. Esry, "HD^+ in a short strong laser pulse: Practical consideration of the observability of carrier-envelope phase effects", Phys. Rev. A: At., Mol., Opt. Phys. **76**, 023403 (2007), https://link.aps.org/doi/10.1103/PhysRevA.76.023403.

[78] V. Roudnev and B. D. Esry, "General theory of carrier-envelope phase effects", Phys. Rev. Lett. **99**, 220406 (2007), https://link.aps.org/doi/10.1103/PhysRevLett.99.220406.

[79] J. J. Hua and B. D. Esry, "The role of mass in the carrier–envelope phase effect for H_2^+ dissociation", Journal of Physics B: Atomic, Molecular and Optical Physics **42**, 085601 (2009), http://stacks.iop.org/0953-4075/42/i=8/a=085601.

[80] F. Anis, Ph.D. thesis, Kansas State Universtiy (2009).

[81] A. S. Alnaser and I. V. Litvinyuk, "Subfemtosecond directional control of chemical processes in molecules", Journal of Physics B: Atomic, Molecular and Optical Physics **50**, 032002 (2017), http://stacks.iop.org/0953-4075/50/i=3/a=032002.

[82] D. J. Jones, S. A. Diddams, J. K. Ranka, A. Stentz, R. S. Windeler, J. L. Hall, and S. T. Cundiff, "Carrier-envelope phase control of femtosecond mode-locked lasers and direct optical frequency synthesis", Science **288**, 635 (2000), http://science.sciencemag.org/content/288/5466/635.

[83] C. Li, E. Moon, H. Mashiko, C. M. Nakamura, P. Ranitovic, C. M. Maharjan, C. L. Cocke, Z. Chang, and G. G. Paulus, "Precision control of carrier-envelope phase in grating based chirped pulse amplifiers", Opt. Express **14**, 11468 (2006), http://www.opticsexpress.org/abstract.cfm?URI=oe-14-23-11468.

[84] J. Rauschenberger, T. Fuji, M. Hentschel, A.-J. Verhoef, T. Udem, C. Gohle, T. W. Hänsch, and F. Krausz, "Carrier-envelope phase-stabilized amplifier system", Laser Physics Letters **3**, 37 (2006), http://stacks.iop.org/1612-202X/3/i=1/a=006.

[85] M. Nisoli, G. Sansone, S. Stagira, J.-P. Caumes, C. Vozzi, S. De Silvestri, M. Pascolini, L. Poletto, P. Villoresi, and G. Tondello, "Single-atom effects in high-order harmonic generation: role of carrier-envelope phase in the few-optical-cycle regime", Applied Physics B **78**, 873 (2004), http://dx.doi.org/10.1007/s00340-004-1482-x.

[86] T. J. Yu, K.-H. Hong, H.-G. Choi, J. H. Sung, I. W. Choi, D.-K. Ko, J. Lee, J. Kim, D. E. Kim, and C. H. Nam, "Precise and long-term stabilization of the carrier-envelope phase of femtosecond laser pulses using an enhanced direct locking technique", Opt. Express **15**, 8203 (2007), http://www.opticsexpress.org/abstract.cfm?URI=oe-15-13-8203.

[87] B. Langdon, J. Garlick, X. Ren, D. J. Wilson, A. M. Summers, S. Zigo, M. F. Kling, S. Lei, C. G. Elles, E. Wells, et al., "Carrier-envelope-phase stabilized terawatt class laser at 1 kHz with a wavelength tunable option", Opt. Express **23**, 4563 (2015), http://www.opticsexpress.org/abstract.cfm?URI=oe-23-4-4563.

[88] T. Wittmann, B. Horvath, W. Helml, M. G. Schatzel, X. Gu, A. L. Cavalieri, G. G. Paulus, and R. Kienberger, "Single-shot carrier-envelope phase measurement of few-cycle laser pulses", Nature Physics **5**, 357 (2009), http://dx.doi.org/10.1038/nphys1250.

[89] A. M. Sayler, T. Rathje, W. Müller, C. Kürbis, K. Rühle, G. Stibenz, and G. G. Paulus, "Real-time pulse length measurement of few-cycle laser pulses using above-threshold ionization", Opt. Express **19**, 4464 (2011), http://www.opticsexpress.org/abstract.cfm?URI=oe-19-5-4464.

[90] A. M. Sayler, T. Rathje, W. Müller, K. Rühle, R. Kienberger, and G. G. Paulus, "Precise, real-time, every-single-shot, carrier-envelope phase measurement of ultrashort laser pulses", Opt. Lett. **36**, 1 (2011), http://ol.osa.org/abstract.cfm?URI=ol-36-1-1.

[91] T. Rathje, N. G. Johnson, M. Möller, F. Süßmann, D. Adolph, M. Kübel, R. Kienberger, M. F. Kling, G. G. Paulus, and A. M. Sayler, "Review of attosecond resolved measurement and control via carrier–envelope phase tagging with above-threshold ionization", Journal of Physics B: Atomic, Molecular and Optical Physics **45**, 074003 (2012), http://stacks.iop.org/0953-4075/45/i=7/a=074003.

[92] S. Wolf, G. Sommerer, S. Rutz, E. Schreiber, T. Leisner, L. Wöste, and R. S. Berry, "Spectroscopy of size-selected neutral clusters: Femtosecond evolution of neutral silver trimers", Phys. Rev. Lett. **74**, 4177 (1995), https://link.aps.org/doi/10.1103/PhysRevLett.74.4177.

[93] D. M. Neumark, "Time-resolved photoelectron spectroscopy of molecules and clusters", Annual Review of Physical Chemistry **52**, 255 (2001), pMID: 11326066, http://dx.doi.org/10.1146/annurev.physchem.52.1.255.

[94] A. Stolow, A. E. Bragg, and D. M. Neumark, "Femtosecond time-resolved photoelectron spectroscopy", Chemical Reviews **104**, 1719 (2004), pMID: 15080710, http://dx.doi.org/10.1021/cr020683w.

[95] D. M. Neumark, "Probing chemical dynamics with negative ions", The Journal of Chemical Physics **125**, 132303 (2006), http://dx.doi.org/10.1063/1.2216709.

[96] R. Mabbs, K. Pichugin, and A. Sanov, "Time-resolved imaging of the reaction coordinate", The Journal of Chemical Physics **122**, 174305 (2005), http://dx.doi.org/10.1063/1.1887170.

[97] J. C. Y. Chen, *Advances in Radiation Chemistry* (Wiley and Sons, 1969), chap. Theory of Transient Negative Ions of Simple Molecules, pp. 245–377.

[98] M. A. Yandell, S. B. King, and D. M. Neumark, "Time-resolved radiation chemistry: Photoelectron imaging of transient negative ions of nucleobases", Journal of the American Chemical Society **135**, 2128 (2013), pMID: 23350789, http://dx.doi.org/10.1021/ja312414y.

[99] K. D. Jordan and P. D. Burrow, "Temporary anion states of polyatomic hydrocarbons", Chem. Rev. **87**, 557 (1987), http://dx.doi.org/10.1021/cr00079a005.

[100] T. Oster, A. Kühn, and E. Illenberger, "Gas phase negative ion chemistry", International Journal of Mass Spectrometry and Ion Processes **89**, 1 (1989), http://www.sciencedirect.com/science/article/pii/0168117689850311.

[101] E. Illenberger and J. Momigny, *Gaseous Molecular Ions: An Introduction to Elementary Processes Induced by Ionization* (Steinkopff-Verlag Heidelberg, 1992), http://www.springer.com/us/book/9783662073858.

[102] J. Kalcher and A. F. Sax, "Gas phase stabilities of small anions: Theory and experiment in cooperation", Chem. Rev. **94**, 2291 (1994), http://dx.doi.org/10.1021/cr00032a004.

[103] F. B. Dunning, "Electron-molecule collisions at very low electron energies", Journal of Physics B: Atomic, Molecular and Optical Physics **28**, 1645 (1995), http://stacks.iop.org/0953-4075/28/i=9/a=006.

[104] J. Ho, K. M. Ervin, and W. C. Lineberger, "Photoelectron spectroscopy of metal cluster anions: Cu_n^-, Ag_n^-, and Au_n^-", The Journal of Chemical Physics **93**, 6987 (1990), http://dx.doi.org/10.1063/1.459475.

[105] M. K. Gilles, M. L. Polak, and W. C. Lineberger, "Photoelectron spectroscopy of the halogen oxide anions FO^-, ClO^-, BrO^-, IO^-, $OClO^-$, and OIO^-", The Journal of Chemical Physics **96**, 8012 (1992), http://dx.doi.org/10.1063/1.462352.

[106] D. R. Bates, "Negative ions: Structure and spectra", Advances In Atomic, Molecular, and Optical Physics **27**, 1 (1990), http://www.sciencedirect.com/science/article/pii/S1049250X08601482.

[107] P. G. Wenthold, D. A. Hrovat, W. T. Borden, and W. C. Lineberger, "Transition-state spectroscopy of cyclooctatetraene", Science **272**, 1456 (1996), http://science.sciencemag.org/content/272/5267/1456.

[108] R. A. Bachorz, W. Klopper, M. Gutowski, X. Li, and K. H. Bowen, "Photoelectron spectrum of valence anions of uracil and first-principles calculations of excess electron binding energies", The Journal of Chemical Physics **129**, 054309 (2008), http://dx.doi.org/10.1063/1.2965128.

[109] A. Shahi, Y. Albeck, and D. Strasser, "Intense-field multiple-detachment of F_2^-: Competition with photodissociation", The Journal of Physical Chemistry A **121**, 3037 (2017), pMID: 28388045, http://dx.doi.org/10.1021/acs.jpca.6b13008.

[110] J. G. Dojahn, E. C. M. Chen, and W. E. Wentworth, "Characterization of homonuclear diatomic ions by semiempirical Morse potential energy curves. 1. the halogen anions", The Journal of Physical Chemistry **100**, 9649 (1996), http://dx.doi.org/10.1021/jp953601z.

[111] I. A. Delyagina, D. B. Kokh, and A. M. Pravilov, "Study of the covalent and triplet ionic-pairing states of the fluorine molecule with the mrdci method", Optics and Spectroscopy **94**, 170 (2003), http://dx.doi.org/10.1134/1.1555174.

[112] E. Y. Sidky and I. Ben-Itzhak, "Phase-amplitude method for calculating resonance energies and widths for one-dimensional potentials", Phys. Rev. A: At., Mol., Opt. Phys. **60**, 3586 (1999), https://link.aps.org/doi/10.1103/PhysRevA.60.3586.

[113] R. N. Zare and D. R. Herschbach, "Doppler line shape of atomic fluorescence excited by molecular photodissociation", Proceedings of the IEEE **51**, 173 (1963).

[114] A. M. Sayler, P. Q. Wang, K. D. Carnes, B. D. Esry, and I. Ben-Itzhak, "Determining laser-induced dissociation pathways of multielectron diatomic molecules: Application to the dissociation of O_2^+ by high-intensity ultrashort pulses", Phys. Rev. A: At., Mol., Opt. Phys. **75**, 063420 (2007), https://link.aps.org/doi/10.1103/PhysRevA.75.063420.

[115] A. Hishikawa, S. Liu, A. Iwasaki, and K. Yamanouchi, "Light-induced multiple electronic-state coupling of O_2^+ in intense laser fields", The Journal of Chemical Physics **114**, 9856 (2001), http://dx.doi.org/10.1063/1.1368383.

[116] A. M. Sayler, P. Q. Wang, K. D. Carnes, and I. Ben-Itzhak, "Determining intensity dependence of ultrashort laser processes through focus z -scanning intensity-difference spectra: application to laser-induced dissociation of H_2^+", Journal of Physics B: Atomic,

Molecular and Optical Physics **40**, 4367 (2007), http://stacks.iop.org/0953-4075/40/i=22/a=006.

[117] J. Posthumus, *Molecules and Clusters in Intense Laser Fields* (Cambridge University Press, 2001), https://doi.org/10.1017/CBO9780511564116.

[118] W. J. Stevens, M. Gardner, A. Karo, and P. Julienne, "Theoretical determination of bound-free absorption cross sections in Ar_2^+", The Journal of Chemical Physics **67**, 2860 (1977), http://aip.scitation.org/doi/abs/10.1063/1.435153.

[119] J. W. Cooper, "Photoionization from outer atomic subshells. a model study", Physical Review **128**, 681 (1962), https://link.aps.org/doi/10.1103/PhysRev.128.681.

[120] B. H. Bransden and C. J. Joachain, *Physics of Atoms and Molecules* (Pearson United Kingdom, 2003), 2nd ed.

[121] B. Mintz, B. Chan, M. B. Sullivan, T. Buesgen, A. P. Scott, S. R. Kass, L. Radom, and A. K. Wilson, "Structures and thermochemistry of the alkali metal monoxide anions, monoxide radicals, and hydroxides", J. Phys. Chem. A **113**, 9501 (2009), http://dx.doi.org/10.1021/jp9034826.

[122] J. Simons, "Propensity rules for vibration-induced electron detachment of anions", Journal of the American Chemical Society **103**, 3971 (1981), http://dx.doi.org/10.1021/ja00404a002.

[123] P. K. Acharya, R. A. Kendall, and J. Simons, "Vibration-induced electron detachment in molecular anions", Journal of the American Chemical Society **106**, 3402 (1984), http://dx.doi.org/10.1021/ja00324a003.

[124] C. W. Bauschlicher, H. Partridge, and L. G. M. Pettersson, "Franck-condon factors for photodetachment from LiO^-, NaO^-, and KO^-", The Journal of Chemical Physics **99**, 3654 (1993), http://dx.doi.org/10.1063/1.466163.

[125] D. M. Neumark, K. R. Lykke, T. Andersen, and W. C. Lineberger, "Laser photodetachment measurement of the electron affinity of atomic oxygen", Phys. Rev. A: At., Mol., Opt. Phys. **32**, 1890 (1985), https://link.aps.org/doi/10.1103/PhysRevA.32.1890.

[126] C. Blondel, W. Chaibi, C. Delsart, C. Drag, F. Goldfarb, and S. Kröger, "The electron affinities of O, Si, and S revisited with the photodetachment microscope", The European Physical Journal D - Atomic, Molecular, Optical and Plasma Physics **33**, 335 (2005), http://dx.doi.org/10.1140/epjd/e2005-00069-9.

[127] S. R. Langhoff, C. W. B. Jr., and H. Partridge, "Theoretical study of the diatomic alkali and alkaline–earth oxides", The Journal of Chemical Physics **84**, 4474 (1986), http://dx.doi.org/10.1063/1.450019.

[128] R. S. Berry, "Ionization of molecules at low energies", The Journal of Chemical Physics **45**, 1228 (1966), https://doi.org/10.1063/1.1727742.

[129] M. Glass-Maujean, S. Klumpp, L. Werner, A. Ehresmann, and H. Schmoranzer, "The study of the $D'\,^1\Pi_u$ state of H_2: Transition probabilities from the ground state, predissociation yields, and natural linewidths", The Journal of Chemical Physics **128**, 094312 (2008), http://dx.doi.org/10.1063/1.2835006.

[130] R. L. Platzman, "Superexcited states of molecules", Radiation Research **17**, 419 (1962), http://www.rrjournal.org/doi/abs/10.2307/3571104.

[131] J. L. Dehmer, P. M. Dehmer, J. B. West, M. A. Hayes, M. R. F. Siggel, and A. C. Parr, "Vibrational autoionization in H_2: Vibrational branching ratios and photoelectron angular distributions near the $\nu^+ = 3$ threshold", The Journal of Chemical Physics **97**, 7911 (1992), http://dx.doi.org/10.1063/1.463466.

[132] M. Glass-Maujean, C. Jungen, H. Schmoranzer, A. Knie, I. Haar, R. Hentges, W. Kielich, J. K., and A. Ehresmann, "H_2 superexcited states: experimental and theoretical characterization of their competing decay-channel fluorescence, dissociation,

and ionization", Physical Review Letters **104**, 183002 (2010), https://link.aps.org/doi/10.1103/PhysRevLett.104.183002.

[133] S. Pratt, "Vibrational autoionization in polyatomic molecules", Annu. Rev. Phys. Chem. **56**, 281 (2004), http://dx.doi.org/10.1146/annurev.physchem.56.092503.141204.

[134] B. deB. Darwent, *Bond Dissociation Energies in Simple Molecules* (Nat. Stand. Ref. Data Ser., Nat. Bur. Stand. (U.S.), 1970), http://nvlpubs.nist.gov/nistpubs/Legacy/NSRDS/nbsnsrds31.pdf.

[135] S. North, D. A. Blank, and Y. T. Lee, "Determination of the barrier height to CH_3CO dissociation", Chemical Physics Letters **224**, 38 (1994), http://www.sciencedirect.com/science/article/pii/0009261494005060.

[136] H. Helm, D. P. de Bruijn, and J. Los, "Fast neutral-beam photofragment spectroscopy of H_2 $c^3\Pi_u^-$", Physical Review Letters **53**, 1642 (1984), https://link.aps.org/doi/10.1103/PhysRevLett.53.1642.

[137] B. Buijsse, E. R. Wouters, and W. J. van der Zande, "Diagnostic value of photofragment anisotropy measurements: Predissociation mechanisms of the $e^1\Pi_u$ state of N_2", Physical Review Letters **77**, 243 (1996), https://link.aps.org/doi/10.1103/PhysRevLett.77.243.

[138] W. Koot, W. J. van der Zande, and J. Los, "Vibrational wave function of a radiatively dissociating level of H_2 obtained from the kinetic–energy distribution of the H fragments", Physical Review Letters **58**, 2746 (1987), https://link.aps.org/doi/10.1103/PhysRevLett.58.2746.

[139] L. Dinu, Y. J. Picard, and W. J. van der Zande, "Predissociation and autoionization of triplet Rydberg states in molecular hydrogen", The Journal of Chemical Physics **121**, 3058 (2004), http://dx.doi.org/10.1063/1.1773157.

[140] C. Pernot, J. Durup, J.-B. Ozenne, J. A. Beswick, P. C. Cosby, and J. T. Moseley, "Angular distributions and separation energies of predissociation photofragments of O_2^+ $(b\,^4\Sigma_g^-, v' = 4, N', F')$", The Journal of Chemical Physics **71**, 2387 (1979), http://dx.doi.org/10.1063/1.438644.

[141] M. Tadjeddine, R. Abouaf, P. C. Cosby, B. A. Huber, and J. T. Moseley, "Predissociation photofragment spectroscopy of O_2^+ quartet states", The Journal of Chemical Physics **69**, 710 (1978), http://dx.doi.org/10.1063/1.436638.

[142] C. W. Walter, P. C. Cosby, and H. Helm, "Photoexcitation and predissociation intensities of the $c'\,^1\Sigma_u^+$ (v=3 and 4), $c\,^1\Sigma_u$ (v=3 and 4), and $b'\,^1\Sigma_u^+$ (v=10, 12, 13, and 15) states of N_2", The Journal of Chemical Physics **112**, 4621 (2000), http://dx.doi.org/10.1063/1.481090.

[143] E. R. Wouters, B. Buijsse, J. Los, and W. J. van der Zande, "Dissociation dynamics of quasibound levels in the $g\,^3\Sigma_g^+$ state of H_2: Characterization of the continuum", The Journal of Chemical Physics **106**, 3974 (1997), http://dx.doi.org/10.1063/1.473115.

[144] Z. Tian, B. Chan, M. B. Sullivan, L. Radom, and S. R. Kass, "Lithium monoxide anion: A ground-state triplet with the strongest base to date", Proceedings of the National Academy of Sciences **105**, 7647 (2008), http://www.pnas.org/content/105/22/7647.abstract.

[145] D. Ursrey, F. Anis, and B. D. Esry, "Multiphoton dissociation of HeH^+ below the $He^+(1s)$+H$(1s)$ threshold", Phys. Rev. A: At., Mol., Opt. Phys. **85**, 023429 (2012), https://link.aps.org/doi/10.1103/PhysRevA.85.023429.

[146] A. Miffre, M. Jacquey, M. Büchner, G. Trénec, and J. Vigué, "Measurement of the electric polarizability of lithium by atom interferometry", Phys. Rev. A **73**, 011603 (2006), https://link.aps.org/doi/10.1103/PhysRevA.73.011603.

[147] M. Kas, J. Loreau, J. Livin, and N. Vaeck, "Ab initio study of the neutral and anionic alkali and alkaline earth hydroxides: Electronic structure and prospects for sympathetic cooling of OH^-", The Journal of Chemical Physics **146**, 194309 (2017), https://doi.org/10.1063/1.4983627.

[148] C. R. Scheper, W. J. Buma, C. A. de Lange, and W. J. van der Zande, "Photoionization and photodissociation dynamics of H_2 after (3+1) resonance-enhanced multiphoton ionization via the $B\,^1\Sigma_u^+$ state", The Journal of Chemical Physics **109**, 8319 (1998), http://dx.doi.org/10.1063/1.477495.

[149] J. H. Posthumus, B. Fabre, C. Cornaggia, N. de Ruette, and X. Urbain, "Laser-intensity dependent vibrational excitation and alignment of molecular ions in the ultrafast multiphoton regime", Phys. Rev. Lett. **101**, 233004 (2008), https://link.aps.org/doi/10.1103/PhysRevLett.101.233004.

[150] G. Haeffler, D. Hanstorp, I. Kiyan, A. E. Klinkmüller, U. Ljungblad, and D. J. Pegg, "Electron affinity of Li: A state-selective measurement", Phys. Rev. A **53**, 4127 (1996), https://link.aps.org/doi/10.1103/PhysRevA.53.4127.

[151] D. T. Chang, K. Reimann, G. Surratt, G. I. Gellene, P. Lin, and R. R. Lucchese, "First principles determination of the photoelectron spectrum of LiH^-", The Journal of Chemical Physics **117**, 5757 (2002), http://dx.doi.org/10.1063/1.1502246.

[152] A. A. Vassilakis, A. Kalemos, and A. Mavridis, "Accurate first principles calculations on chlorine fluoride ClF and its ions $ClF^{\pm}$", Theoretical Chemistry Accounts **133**, 1436 (2014), http://dx.doi.org/10.1007/s00214-013-1436-7.

[153] T. Zuo and A. D. Bandrauk, "Charge-resonance-enhanced ionization of diatomic molecular ions by intense lasers", Phys. Rev. A: At., Mol., Opt. Phys. **52**, R2511 (1995), http://link.aps.org/doi/10.1103/PhysRevA.52.R2511.

[154] G. N. Gibson, M. Li, C. Guo, and J. Neira, "Strong-field dissociation and ionization

of H_2^+ using ultrashort laser pulses", Physical Review Letters **79**, 2022 (1997), http://link.aps.org/doi/10.1103/PhysRevLett.79.2022.

[155] D. Pavičić, A. Kiess, T. W. Hänsch, and H. Figger, "Intense-laser-field ionization of the hydrogen molecular ions $H_2{}^+$ and $D_2{}^+$ at critical internuclear distances", Phys. Rev. Lett. **94**, 163002 (2005), https://link.aps.org/doi/10.1103/PhysRevLett.94.163002.

[156] A. Rudenko, B. Feuerstein, K. Zrost, V. L. B. de Jesus, T. Ergler, C. Dimopoulou, C. D. Schroeter, R. Moshammer, and J. Ullrich, "Fragmentation dynamics of molecular hydrogen in strong ultrashort laser pulses", Journal of Physics B: Atomic and Molecular Physics **38**, 487 (2005).

[157] B. D. Esry, A. M. Sayler, P. Q. Wang, K. D. Carnes, and I. Ben-Itzhak, "Above threshold coulomb explosion of molecules in intense laser pulses", Physical Review Letters **97**, 013003 (2006), http://link.aps.org/doi/10.1103/PhysRevLett.97.013003.

[158] T. Ergler, A. Rudenko, B. Feuerstein, K. Zrost, C. D. Schröter, R. Moshammer, and J. Ullrich, "Ultrafast mapping of H_2^+ (D_2^+) nuclear wave packets using time-resolved coulomb explosion imaging", Journal of Physics B: Atomic, Molecular and Optical Physics **39**, S493 (2006), http://stacks.iop.org/0953-4075/39/i=13/a=S22.

[159] A. Staudte, D. Pavičić, S. Chelkowski, D. Zeidler, M. Meckel, H. Niikura, M. Schöffler, S. Schössler, B. Ulrich, P. P. Rajeev, et al., "Attosecond strobing of two-surface population dynamics in dissociating $H_2{}^+$", Phys. Rev. Lett. **98**, 073003 (2007), https://link.aps.org/doi/10.1103/PhysRevLett.98.073003.

[160] I. Ben-Itzhak, P. Q. Wang, A. M. Sayler, K. D. Carnes, M. Leonard, B. D. Esry, A. S. Alnaser, B. Ulrich, X. M. Tong, I. V. Litvinyuk, et al., "Elusive enhanced ionization structure for $H_2{}^+$ in intense ultrashort laser pulses", Physical Review A: Atomic, Molecular, and Optical Physics **78**, 063419 (2008), http://link.aps.org/doi/10.1103/PhysRevA.78.063419.

[161] B. D. Esry and I. Ben-Itzhak, "Time-dependent dynamics of an intense laser-induced above-threshold coulomb explosion", Physical Review A: Atomic, Molecular, and Optical Physics **82**, 043409 (2010), https://link.aps.org/doi/10.1103/PhysRevA.82.043409.

[162] H. Xu, F. He, D. Kielpinski, R. Sang, and I. Litvinyuk, "Experimental observation of the elusive double-peak structure in r-dependent strong-field ionization rate of H_2^+", Scientific Reports **5**, 13527 (2015), http://dx.doi.org/10.1038/srep13527.

[163] T. Seideman, M. Y. Ivanov, and P. B. Corkum, "Role of electron localization in intense-field molecular ionization", Phys. Rev. Lett. **75**, 2819 (1995), https://link.aps.org/doi/10.1103/PhysRevLett.75.2819.

[164] S. Chelkowski, C. Foisy, and A. D. Bandrauk, "Electron-nuclear dynamics of multi-photon H_2^+ dissociative ionization in intense laser fields", Physical Review A: Atomic, Molecular, and Optical Physics **57**, 1176 (1998), https://link.aps.org/doi/10.1103/PhysRevA.57.1176.

[165] A. Mokhtari, P. Cong, J. L. Herek, and A. H. Zewail, "Direct femtosecond mapping of trajectories in a chemical reaction", Nature **348**, 225 (1990), http://dx.doi.org/10.1038/348225a0.

[166] H. Stapelfeldt, E. Constant, and P. B. Corkum, "Wave packet structure and dynamics measured by Coulomb explosion", Phys. Rev. Lett. **74**, 3780 (1995), http://link.aps.org/doi/10.1103/PhysRevLett.74.3780.

[167] T. Ergler, A. Rudenko, B. Feuerstein, K. Zrost, C. D. Schröter, R. Moshammer, and J. Ullrich, "Time-resolved imaging and manipulation of H_2 fragmentation in intense laser fields", Physical Review Letters **95**, 093001 (2005), https://link.aps.org/doi/10.1103/PhysRevLett.95.093001.

[168] A. S. Alnaser, I. Litvinyuk, T. Osipov, B. Ulrich, A. Landers, E. Wells, C. M. Maharjan, P. Ranitovic, I. Bochareva, D. Ray, et al., "Momentum-imaging investigations of the

dissociation of D_2^+ and the isomerization of acetylene to vinylidene by intense short laser pulses", Journal of Physics B: Atomic, Molecular and Optical Physics **39**, S485 (2006), http://stacks.iop.org/0953-4075/39/i=13/a=S21.

[169] P. H. Bucksbaum, A. Zavriyev, H. G. Muller, and D. W. Schumacher, "Softening of the H_2^+ molecular bond in intense laser fields", Physical Review Letters **64**, 1883 (1990), https://link.aps.org/doi/10.1103/PhysRevLett.64.1883.

[170] A. Giusti-Suzor, X. He, O. Atabek, and F. H. Mies, "Above-threshold dissociation of H_2^+ in intense laser fields", Physical Review Letters **64**, 515 (1990), https://link.aps.org/doi/10.1103/PhysRevLett.64.515.

[171] G. Jolicard and O. Atabek, "Above-threshold-dissociation dynamics of H_2^+ with short intense laser pulses", Phys. Rev. A: At., Mol., Opt. Phys. **46**, 5845 (1992), https://link.aps.org/doi/10.1103/PhysRevA.46.5845.

[172] M. Zohrabi, Ph.D. thesis, Kansas State Universtiy (2014), http://hdl.handle.net/2097/18401.

[173] F. X. Gadea and I. Paidarová, "*Ab initio* calculations for Ar_2^+, He_2^+ and He_3^+, of interest for the modelling of ionic rare-gas clusters", Chemical Physics **209**, 281 (1996), http://www.sciencedirect.com/science/article/pii/0301010496001073.

[174] T. Ergler, A. Rudenko, B. Feuerstein, K. Zrost, C. D. Schröter, R. Moshammer, and J. Ullrich, "Spatiotemporal imaging of ultrafast molecular motion: Collapse and revival of the $D_2{}^+$ nuclear wave packet", Physical Review Letters **97**, 193001 (2006), http://link.aps.org/doi/10.1103/PhysRevLett.97.193001.

[175] I. A. Bocharova, A. S. Alnaser, U. Thumm, T. Niederhausen, D. Ray, C. L. Cocke, and I. V. Litvinyuk, "Time-resolved coulomb-explosion imaging of nuclear wave-packet dynamics induced in diatomic molecules by intense few-cycle laser pulses", Physical Review A: Atomic, Molecular, and Optical Physics **83**, 013417 (2011), https://link.aps.org/doi/10.1103/PhysRevA.83.013417.

[176] K. Schnorr, A. Senftleben, M. Kurka, A. Rudenko, G. Schmid, T. Pfeifer, K. Meyer, M. Kübel, M. F. Kling, Y. H. Jiang, et al., "Electron rearrangement dynamics in dissociating I_2^{n+} molecules accessed by extreme ultraviolet pump-probe experiments", Phys. Rev. Lett. **113**, 073001 (2014), https://link.aps.org/doi/10.1103/PhysRevLett.113.073001.

[177] B. D. Esry and H. R. Sadeghpour, "Adiabatic formulation of heteronuclear hydrogen molecular ion", Physical Review A: Atomic, Molecular, and Optical Physics **60**, 3604 (1999), https://link.aps.org/doi/10.1103/PhysRevA.60.3604.

[178] N. Saito, Y. Morishita, I. Suzuki, S. Stoychev, A. Kuleff, L. Cederbaum, X.-J. Liu, H. Fukuzawa, G. Prümper, and K. Ueda, "Evidence of radiative charge transfer in argon dimers", Chemical Physics Letters **441**, 16 (2007), http://www.sciencedirect.com/science/article/pii/S0009261407005404.

[179] J. Muth-Böhm, A. Becker, and F. H. M. Faisal, "Suppressed molecular ionization for a class of diatomics in intense femtosecond laser fields", Phys. Rev. Lett. **85**, 2280 (2000), https://link.aps.org/doi/10.1103/PhysRevLett.85.2280.

[180] Y. Yu, "In preparation" (2017).

[181] B. Berry, M. Zohrabi, D. Hayes, U. Ablikim, B. Jochim, T. Severt, K. D. Carnes, and I. Ben-Itzhak, "Note: Determining the detection efficiency of excited neutral atoms by a microchannel plate detector", Review of Scientific Instruments **86**, 046103 (2015), http://dx.doi.org/10.1063/1.4916953.

[182] B. Berry, M. Zohrabi, B. Jochim, T. Severt, P. Feizollah, U. Ablikim, J. Rajput, K. R. P, D. Hayes, K. D. Carnes, et al., "State-selective studies and carrier-envelope phase control of the formation of Rydberg D* fragments from D_2 in a strong field", In preparation (2017).

[183] C. Bottcher and K. Docken, "Autoionizing states of the hydrogen molecule", Journal

of Physics B: Atomic and Molecular Physics **7**, L5 (1974), http://stacks.iop.org/0022-3700/7/i=1/a=002.

[184] S. L. Guberman, "The doubly excited autoionizing states of H_2", The Journal of Chemical Physics **78**, 1404 (1983), http://dx.doi.org/10.1063/1.444882.

[185] M. Glass-Maujean, "Photodissociation of doubly excited states of H_2: Emission of Balmer lines", The Journal of Chemical Physics **89**, 2839 (1988), http://dx.doi.org/10.1063/1.454987.

[186] F. Martín, "Ionization and dissociation using B-splines: photoionization of the hydrogen molecule", Journal of Physics B: Atomic, Molecular and Optical Physics **32**, R197 (1999), http://stacks.iop.org/0953-4075/32/i=16/a=201.

[187] A. Palacios, J. L. Sanz-Vicario, and F. Martín, "Theoretical methods for attosecond electron and nuclear dynamics: applications to the H_2 molecule", Journal of Physics B: Atomic, Molecular and Optical Physics **48**, 242001 (2015), http://stacks.iop.org/0953-4075/48/i=24/a=242001.

[188] L. Wolniewicz, T. Orlikowski, and G. Staszewska, "$^1\Sigma_u$ and $^1\Pi_u$ states of the hydrogen molecule: Nonadiabatic couplings and vibrational levels", Journal of Molecular Spectroscopy **238**, 118 (2006), http://www.sciencedirect.com/science/article/pii/S0022285206001391.

[189] M. Raoult and C. Jungen, "Calculation of vibrational preionization in H_2 by multichannel quantum defect theory: Total and partial cross sections and photoelectron angular distributions", The Journal of Chemical Physics **74**, 3388 (1981), http://dx.doi.org/10.1063/1.441492.

[190] M. Glass-Maujean, J. Breton, and P. M. Guyon, "Accidental predissociation of the $4p\pi^1\Pi_u{}^+$ state of H_2", Physical Review Letters **40**, 181 (1978), https://link.aps.org/doi/10.1103/PhysRevLett.40.181.

[191] W. Cao, G. Laurent, I. Ben-Itzhak, and C. L. Cocke, "Identification of a previously unobserved dissociative ionization pathway in time-resolved photospectroscopy of the deuterium molecule", Physical Review Letters **114**, 113001 (2015), https://link.aps.org/doi/10.1103/PhysRevLett.114.113001.

[192] H. Gao, C. Jungen, and C. H. Greene, "Predissociation of H_2 in the $3p\pi D\ ^1\Pi_u^+$ state", Physical Review A: Atomic, Molecular, and Optical Physics **47**, 4877 (1993), https://link.aps.org/doi/10.1103/PhysRevA.47.4877.

[193] R. S. Freund, J. A. Schiavone, and D. F. Brader, "Dissociative excitation of H_2: Spectral line shapes and electron impact cross sections of the Balmer lines", The Journal of Chemical Physics **64**, 1122 (1976), http://dx.doi.org/10.1063/1.432299.

[194] P. M. Dehmer and W. A. Chupka, "On the mechanism for vibrational autoionization in H_2", The Journal of Chemical Physics **66**, 1972 (1977), http://dx.doi.org/10.1063/1.434154.

[195] I. Sánchez and F. Martín, "The doubly excited states of the H_2 molecule", The Journal of Chemical Physics **106**, 7720 (1997), http://dx.doi.org/10.1063/1.473773.

[196] I. Sánchez and F. Martín, "Doubly excited autoionizing states of H_2 above the second ionization threshold: the Q_2 resonance series", The Journal of Chemical Physics **110**, 6702 (1999), http://dx.doi.org/10.1063/1.478576.

[197] J. Itamar Borges and C. E. Bielschowsky, "Doubly excited states of molecular hydrogen: theoretical absorption and photodissociation cross sections", Journal of Physics B: Atomic, Molecular and Optical Physics **33**, 1713 (2000), http://stacks.iop.org/0953-4075/33/i=9/a=303.

[198] I. Sánchez and F. Martín, "Origin of unidentified structures in resonant dissociative photoionization of H_2", Phys. Rev. Lett. **79**, 1654 (1997), https://link.aps.org/doi/10.1103/PhysRevLett.79.1654.

[199] N. Kouchi, M. Ukai, and Y. Hatano, "Dissociation dynamics of superexcited molecular hydrogen", Journal of Physics B: Atomic, Molecular and Optical Physics **30**, 2319 (1997), http://stacks.iop.org/0953-4075/30/i=10/a=008.

[200] M. Glass-Maujean, "Photodissociation of doubly excited states of H_2, HD, and D_2", The Journal of Chemical Physics **85**, 4830 (1986), http://dx.doi.org/10.1063/1.451717.

[201] M. Glass-Maujean, C. Jungen, G. Reichardt, A. Balzer, H. Schmoranzer, A. Ehresmann, I. Haar, and P. Reiss, "Competing decay-channel fluorescence, dissociation, and ionization in superexcited levels of H_2", Physical Review A: Atomic, Molecular, and Optical Physics **82**, 062511 (2010), https://link.aps.org/doi/10.1103/PhysRevA.82.062511.

[202] M. Glass-Maujean and H. Schmoranzer, "Dissociation dynamics of doubly excited states of molecular hydrogen", Journal of Physics B: Atomic, Molecular and Optical Physics **38**, 1093 (2005), http://stacks.iop.org/0953-4075/38/i=8/a=002.

[203] F. Martín, J. Fernández, T. Havermeier, L. Foucar, T. Weber, K. Kreidi, M. Schöffler, L. Schmidt, T. Jahnke, O. Jagutzki, et al., "Single photon-induced symmetry breaking of H_2 dissociation", Science **315**, 629 (2007), http://science.sciencemag.org/content/315/5812/629.abstract.

[204] J. L. Sanz-Vicario, H. Bachau, and F. Martín, "Time-dependent theoretical description of molecular autoionization produced by femtosecond xuv laser pulses", Phys. Rev. A: At., Mol., Opt. Phys. **73**, 033410 (2006), https://link.aps.org/doi/10.1103/PhysRevA.73.033410.

[205] J. L. Sanz-Vicario, J. F. Pérez-Torres, F. Morales, E. Plessiat, and F. Martín, "Probing H_2 autoionizing states with femto- and attosecond laser pulses", Journal of Physics: Conference Series **194**, 012013 (2009), http://stacks.iop.org/1742-6596/194/i=1/a=012013.

[206] J. D. Bozek, J. E. Furst, T. J. Gay, H. Gould, A. L. D. Kilcoyne, J. R. Machacek, F. Martínand K W McLaughlin, and J. L. Sanz-Vicario, "Production of excited atomic hydrogen and deuterium from H_2 and D_2 photodissociation", Journal of Physics B: Atomic, Molecular and Optical Physics **39**, 4871 (2006), http://stacks.iop.org/0953-4075/39/i=23/a=006.

[207] A. Azarm, D. Song, K. Liu, S. Hosseini, Y. Teranishi, S. H. Lin, A. Xia, F. Kong, and S. L. Chin, "Neutral dissociation of hydrogen molecules in a strong laser field through superexcited states", Journal of Physics B: Atomic, Molecular and Optical Physics **44**, 085601 (2011), http://stacks.iop.org/0953-4075/44/i=8/a=085601.

[208] B. Manschwetus, T. Nubbemeyer, K. Gorling, G. Steinmeyer, U. Eichmann, H. Rottke, and W. Sandner, "Strong laser field fragmentation of H_2: Coulomb explosion without double ionization", Phys. Rev. Lett. **102**, 113002 (2009), http://link.aps.org/doi/10.1103/PhysRevLett.102.113002.

[209] J. McKenna, S. Zeng, J. J. Hua, A. M. Sayler, M. Zohrabi, N. G. Johnson, B. Gaire, K. D. Carnes, B. D. Esry, and I. Ben-Itzhak, "Frustrated tunneling ionization during laser-induced D_2 fragmentation: Detection of excited metastable D^* atoms", Phys. Rev. A: At., Mol., Opt. Phys. **84**, 043425 (2011), http://link.aps.org/doi/10.1103/PhysRevA.84.043425.

[210] T. F. Gallagher, *Rydberg Atoms* (Cambridge University Press, 1994), ISBN 9780511524530, http://dx.doi.org/10.1017/CBO9780511524530.

[211] H. Hagstrum, "Theory of Auger ejection of electrons from metals by ions", Physical Review **96**, 336 (1954), http://link.aps.org/doi/10.1103/PhysRev.96.336.

[212] P. J. K. Langendam and M. J. V. der Wiel, "The microchannel plate as detector for VUV photons and metastable atoms in the 1-0.1 Pa pressure region", Journal of Physics E: Scientific Instruments **10**, 870 (1977), http://stacks.iop.org/0022-3735/10/i=9/a=005.

[213] H. Hotop, *Experimental Methods in the Physical Sciences: Atomic, Molecular, and Optical Physics: Atoms and Molecules Vol. 29B* (Academic Press, 1996), https://www.elsevier.com/books/atomic-molecular-and-optical-physics-atoms-and-molecules/dunning/978-0-12-475976-3.

[214] W. Vassen, C. Cohen-Tannoudji, M. Leduc, D. Boiron, C. Westbrook, A. Truscott, K. Baldwin, G. Birkl, P. Cancio, and M. Trippenbach, "Cold and trapped metastable noble gases", Rev. Mod. Phys. **84**, 175 (2012), http://link.aps.org/doi/10.1103/RevModPhys.84.175.

[215] M. J. Rakovic and S.-I. Chu, "Ionization of hydrogen atoms by static and circularly polarized fields: Classical adiabatic theory", Journal of Physics B: Atomic, Molecular and Optical Physics **31**, 1989 (1998), http://stacks.iop.org/0953-4075/31/i=9/a=014.

[216] W. C. Wiley and I. H. McLaren, "Time-of-flight mass spectrometer with improved resolution", Review of Scientific Instruments **26**, 1150 (1955), http://dx.doi.org/10.1063/1.1715212.

[217] "Precision eforming", www.precisioneforming.com.

[218] M. Lundqvist, P. Baltzer, D. Edvardsson, L. Karlsson, and B. Wannberg, "Novel time of flight instrument for Doppler free kinetic energy release spectroscopy", Phys. Rev. Lett. **75**, 1058 (1995), https://link.aps.org/doi/10.1103/PhysRevLett.75.1058.

[219] M. Lundqvist, D. Edvardsson, P. Baltzer, M. Larsson, and B. Wannberg, "Observation of predissociation and tunnelling processes in O_2^{2+} a study using doppler free kinetic energy release spectroscopy and *ab initio* CI calculations", Journal of Physics B: Atomic, Molecular and Optical Physics **29**, 499 (1996), http://stacks.iop.org/0953-4075/29/i=3/a=016.

[220] M. Lundqvist, D. Edvardsson, P. Baltzer, and B. Wannberg, "Doppler-free kinetic energy release spectrum of N_2^{2+}", Journal of Physics B: Atomic, Molecular and Optical Physics **29**, 1489 (1996), http://stacks.iop.org/0953-4075/29/i=8/a=013.

[221] D. Edvardsson, M. Lundqvist, P. Baltzer, B. Wannberg, and S. Lunell, "Doppler-free kinetic energy release spectrum of NO^{2+} and *ab initio* CI calculations", Chemical Physics Letters **256**, 341 (1996), https://doi.org/10.1016/0009-2614(96)00485-X.

[222] S. Khan, Ph.D. thesis, Kansas State University (2012).

[223] W. Gordon, "Zur berechnung der matrizen beim wasserstoffatom", Annalen der Physik **394**, 1031 (1929), http://dx.doi.org/10.1002/andp.19293940807.

Appendix A

CCD imaging of the laser focus

To determine the peak intensity of the laser pulse, the spatial profile of the laser beam is directly measured on a CCD camera. This is possible because the focusing element, a 90° off-axis parabolic mirror, is located outside of the vacuum chamber. To measure the profile, a piece of glass placed just in front of the beamline entrance window reflects the laser beam onto a CCD camera. The parabolic mirror is translated along the laser propagation direction, which allows us to measure the profile of the focused beam. Images are captured at various positions on either side of the focus, and through analysis of these images we obtain the peak intensity distribution, $I_0(z)$, where z is the beam propagation direction, and $z = 0$ defines the position of the focus.

To analyze the CCD images, a Gaussian spatio-temporal profile is assumed. The intensity of a Gaussian beam (i.e. Gaussian in both time and space) is given by,

$$I(r,t;z) = I_0 e^{-\frac{2r^2}{\omega(z)^2} - 4\ln 2 \frac{t^2}{\tau^2}}, \tag{A.1}$$

where I_0 is the peak intensity, $\omega(z)$ is the beam waist defined as the $1/e^2$ radius of the intensity profile, and τ is the FWHM of the pulse envelope [47]. Eq. A.1 can be written equivalently in cartesian coordinates as

$$I(x,y,t;z) = I_0 e^{-2(\frac{x^2}{\omega_x(z)^2} - \frac{y^2}{\omega_y(z)^2}) - 4\ln 2 \frac{t^2}{\tau^2}}. \tag{A.2}$$

Integrating the intensity over time and space yields the pulse energy, ϵ. That is,

$$\epsilon = I_0 \int_{-\infty}^{\infty} e^{-2\frac{x^2}{\omega_x(z)^2}} dx \int_{-\infty}^{\infty} e^{-2\frac{y^2}{\omega_y(z)^2}} dy \int_0^{\infty} e^{-4\ln 2 t^2 \tau^2} dt. \tag{A.3}$$

$$= I_0 \times \omega_x(z)\sqrt{\pi/2} \times \omega_y(z)\sqrt{\pi/2} \times \tau\sqrt{\frac{\pi}{4\ln 2}}. \tag{A.4}$$

Rearranging, the peak intensity is then given by

$$I_0(z) = 2\sqrt{\frac{4\ln 2}{\pi}} \frac{\epsilon}{\pi\omega_x(z)\omega_y(z)\tau} \tag{A.5}$$

$$\approx 1.878 \frac{\epsilon}{\pi\omega_x(z)\omega_y(z)\tau}. \tag{A.6}$$

The pulse energy is determined from the average power and laser repetition rate, given by

$$\epsilon = \frac{P_{avg.}}{R}, \tag{A.7}$$

where R is the repetition rate. Plugging Eq. A.7 in to Eq. A.6, we obtain

$$I_0(z) = 1.878 \frac{P_{avg.}}{\pi\omega_x(z)\omega_y(z)R\tau} \tag{A.8}$$

Note that the factor of 1.878 is due to the Gaussian temporal profile that is assumed and is not accurate for different envelopes.

So, to determine $I_0(z)$ from the measured CCD images, the waist parameters, $\omega_x(z)$ and $\omega_y(z)$, must be found. Instead of fitting a 2D Gaussian function to the image of the laser spot, we fit 1D Gaussians to the projections in each direction. For example, the projection along the x-axis is equivalent to integrating Eq. A.2 over time and the y-direction,

$$I(x;z) = I_0 e^{-2\frac{x^2}{\omega_x(z)^2}} \int_{-\infty}^{\infty} e^{-2\frac{y^2}{\omega_y(z)^2}} dy \int_0^{\infty} e^{-4\ln 2 t^2 \tau^2} dt \tag{A.9}$$

$$= e^{-2\frac{x^2}{\omega_x(z)^2}} \times Constant, \tag{A.10}$$

```
18
19      % Define image directory (terminating \ is important!)
20 -    folder = 'C:\Users\Ben\Documents\MATLAB\CCD\April20-2016\';
21      % Define the size of the grid in pixels (not too tight)
22 -    xr = 80;
23 -    yr = 80;
24
```

Figure A.1: Screenshot of the CCD analysis code, *ccd_analysis_r2015b.m*, input lines where the user must specify the image directory and grid size.

By fitting a 1D Gaussian to the projection, the waist is found.

In the past, fitting of Gaussian functions to the image projections was performed manually and was very time-consuming. Recently, we developed a Matlab code that automates the image analysis. As described below, the Matlab program reads the images, creates the projections, fits Gaussians, and writes out a file containing the z position in mm and the area defined as $\pi\omega_x\omega_y$ in units of cm^2.

To use this code, the CCD images must be saved as bitmap images in the format "#.bmp", where # is the z-position (e.g. "12.5.bmp"). It is important to avoid saturating the CCD and thereby clipping the high intensities. It is also important to align the camera such that the beam spot is not near any stray reflections which may cause issues with the Gaussian fitting routine. And finally, this code requires Matlab's Curve Fitting toolbox, which is available on machines with Matlab R2105b or newer installed.

The Matlab code, entitled *ccd_analysis_r2015b.m*, is located in the CCD image directory, *S:\BenItzhak\IBI-group\CCD Scan*, or alternatively in my directory of Matlab codes (see Appendix G). The inputs to the code are shown in Fig. A.1. The path of the directory containing the CCD images must be defined. Note that the output file will also be saved in the same directory. The size of the grid in pixels over which the projections are performed is also defined. Too small a grid and the spots will be clipped; too large a grid and other stray reflections in the image may confuse the fitting routine. A default box size of 80×80 pixels works in most cases.

After entering the above information, run the code. A window will open displaying the first image in the directory, as shown in Fig. A.2(a). Click on the center of the spot selected for analysis; this graphically selects the center of the grid. Then, the code will loop through

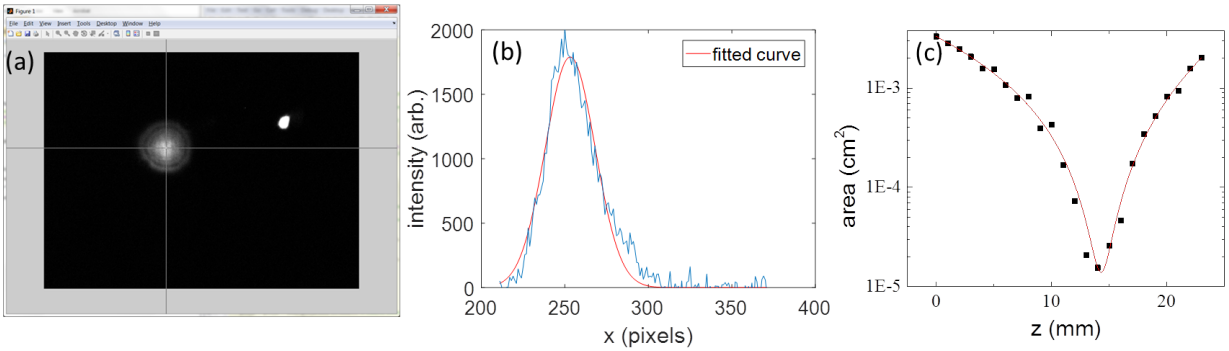

Figure A.2: (a) The center of the laser spot is selected graphically. (b) Example Gaussian fit to a 1D projection of the laser spot. (c) Plot of the calculated area as a function of position, z, with a 5^{th}-order polynomial fit shown in red.

all of the images, project them onto the x and y axes, and fit Gaussian functions. An example of the quality of the fit is shown in Fig. A.2(b). From the ω_x and ω_y parameters found by the fitting routing, the area $\pi\omega_x\omega_y$ is calculated and saved in the output file *ccd_area.out*, which is stored in the image directory. The first column contains the z-position in mm and the second column has the area in cm^2. This data can be loaded in Origin to perform fitting.

An example plot of the calculated areas is shown in Fig. A.2(c) with the 5^{th}-order polynomial fit that is used to define $I_0(z)$ as a function by substituting the polynomial fit for the area into Eq. A.8. Note that the plot is shown with a logarithmic y-axis scale. On a linear scale, a fit that looks good by eye may be off by more than an order of magnitude for the smallest areas near the focus. So, it is important to use a log scale to see any failures of the fit more clearly. For most focal profiles a 3^{rd}- or 5^{th}-order polynomial provides a good fit. In some cases when both of these functions fail, using linear interpolation between the data points may be the best solution.

Finally, since it may be useful in the future to upgrade the analysis to something more robust than the Gaussian beam profile we employ here while preserving the automation of the analysis, the Matlab code with labels describing the functions of each part of the code is shown in Fig. A.3.

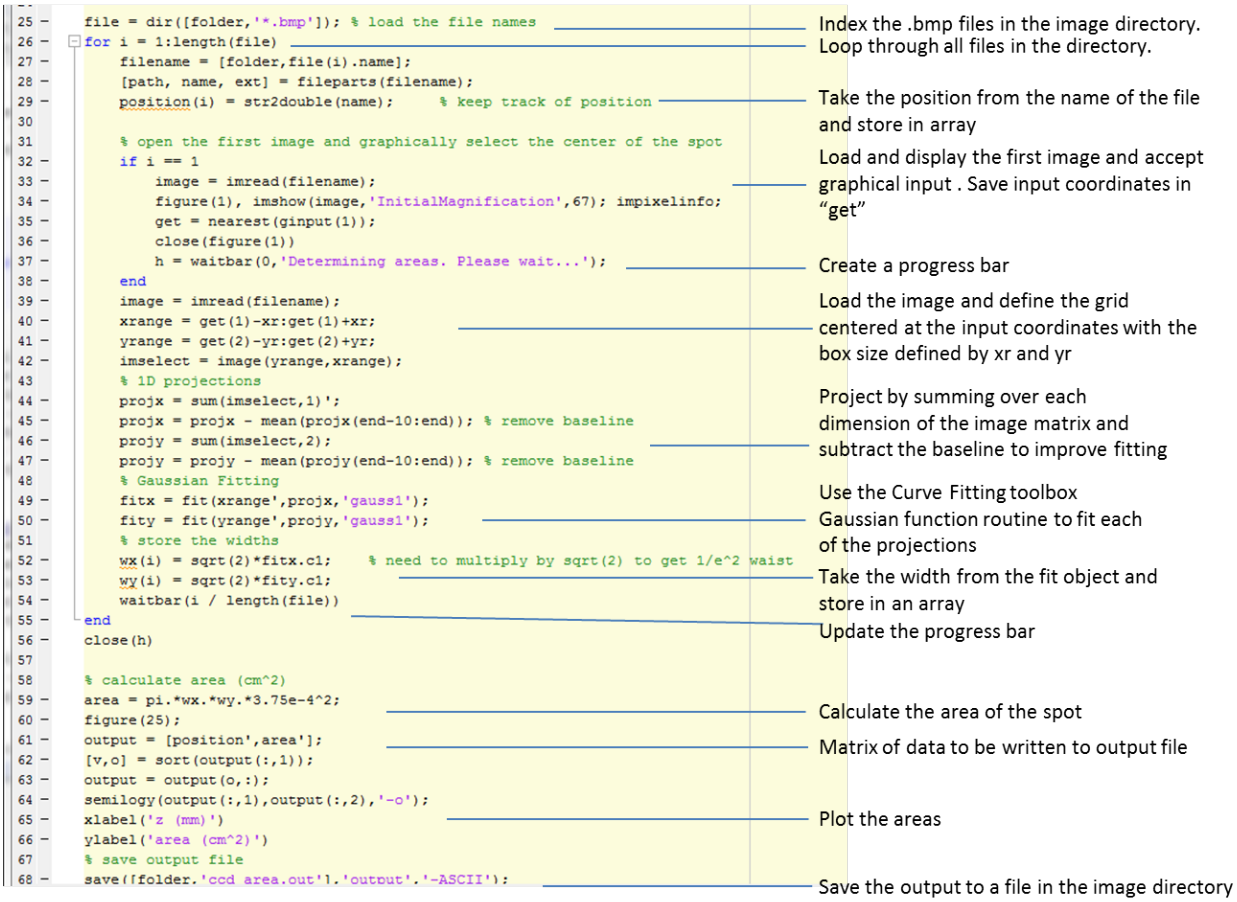

Figure A.3: Descriptions of each element of the CCD analysis Matlab code.

Appendix B

Shot-to-shot tagging of the laser pulse energy

Shot-to-shot tagging of the laser pulse energy is a useful diagnostic tool that is easily implemented in our experimental setup. By splitting off a small fraction of the laser beam and focusing it onto a large-area photodiode, the amplitude of the resulting photodiode signal is directly related to the pulse energy. As shown in Fig. B.1(a), we incorporate this in our setup by splitting off a small fraction of the beam using a piece of glass followed by ND filters and a lens which focuses this portion of the beam onto the photodiode.

The Thorlabs DET100A photodiode we use has a diameter of 10 mm and responds to wavelengths from 350 to 1100 nm. The photodiode is positioned at a distance of about $f/2$ from the lens, where the beam size is only slightly smaller than the photodiode. Using the largest beam that fits on the photodiode reduces the risk of damage. However, it is important to note that the photodiode response may not be uniform across the surface.

It is important that the photodiode is operated in a range where it responds linearly to the pulse energy. While we did not test the saturation limit, we did find that the photodiode responds linearly for ∼few nJ incident pulse energy, as shown in Fig. B.1(b). We found that a ND4.0 filter after the beamsplitter sufficiently reduces the power, but it is recommended that an additional ND wheel is used during setup, gradually reducing the filtering of the wheel

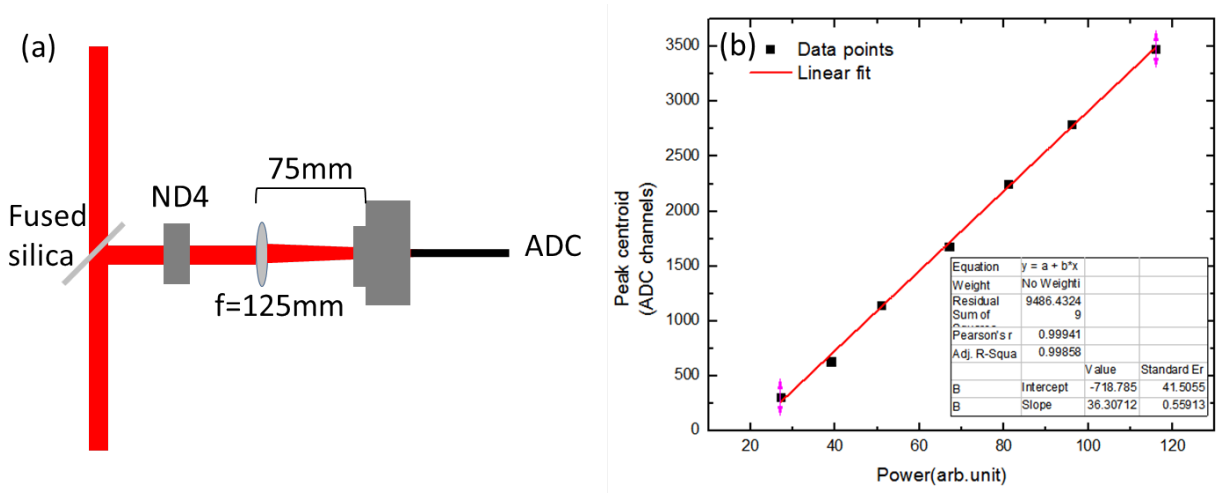

Figure B.1: (a)Setup of the photodiode used for tagging the laser pulse energy. (b) Linear dependence of the ADC channel on the laser power.

until a signal appears. The ND wheel should then be removed, as it does not uniformly attenuate the beam.

The photodiode signal is fed directly into the C.A.E.N V785 ADC, which responds to signal amplitudes from 15 mV to 4 V with a resolution of about 1 mV. The photodiode signal rise time is about 50 ns for wavelengths around 800 nm, equal to the minimum rise time for input to the ADC. For shorter wavelengths (second harmonic for example) the rise time will be below the minimum for the ADC and the signals will need to be stretched. We found that an Ortec 527 amplifier stretches the photodiode signal to a width greater than 50 ns while responding linearly to the pulse energy.

Appendix C

Electronics - ion beam experiments

The detector electronics used in the molecular ion beam studies presented in Chap. 3 have been described previously in the dissertations of Max Sayler [20] and Nora Kling [53]. The purpose of this appendix is to provide an updated electronics diagram, shown in Fig. C.1. Note that the TDC is a C.A.E.N model V1290N; the ADC is a C.A.E.N. model V785N; and, the Scaler is a C.A.E.N. model V560N.

As mentioned above, more complete descriptions can be found in Refs. [20, 53]. In short, timing signals from the front and back of the chevron MCP stack are amplified and inverted using Ortec VT120B preamplifiers. Position information is obtained using a hex delay line detector, which consists of three pairs of wires wrapped at 60° angles. One wire in each pair is biased at a slightly lower voltage, and the difference between the signals from each pair is amplified (indicated by the DLD amplifier in Fig. C.1) to suppress noise. The amplified time and position signals are then converted into standard NIM signals using constant fraction discriminators (CFD) before being fed into a time-to-digital converter (TDC). Replica NIM signals from the CFDs are also fed into a Scaler for monitoring signal rates. Unused outputs of the electronics are terminated with 50 Ω resistors.

A photodiode exposed to a small fraction of the laser beam provides a timing reference. This signal is also converted to a standard NIM signal and provides the TDC trigger (TDC COM) and a reference signal (TDC0). The photodiode rate is also monitored using the

Scaler.

A replica photodiode signal triggers the generation of veto signals used to block the output of the CFDs during specified time ranges where signals due to background ions occur at high rates. Another photodiode signal replica is used to generate a gate pulse that triggers a high voltage pulser, and the output voltage pulse of this unit operates the chopper (see Sec. 2.2.3). A final photodiode signal replica provides the gate pulse that triggers the analog-to-digital converter (ADC).

The signal of a second photodiode, used to measure and tag the shot-to-shot pulse energy, is fed into the ADC (see Appendix B). The analog voltage output from a current meter that monitors the ion beam current is converted into pulses with a frequency linearly proportional to the voltage using a voltage-to-frequency converter (VFC), and these pulses are fed into the Scaler. Similarly, the voltage output from the power meter is also converted to pulses using a VFC and is then fed into the Scaler.

The timing signals picked off the MCPs are decoupled from the high voltage applied to the detector by a decoupling box, which in principle uses a high-pass filter to decouple the signals from the DC high voltage. Recently, we have upgraded the decoupling boxes to the design shown in Fig. C.2. This design includes a low pass filter on the high voltage input to reduce noise from the power supply, and an adjustable load resistor (potentiometer) is used for impedance matching to reduce signal noise. In addition, a spark gap provides surge protection to the electronics downstream.

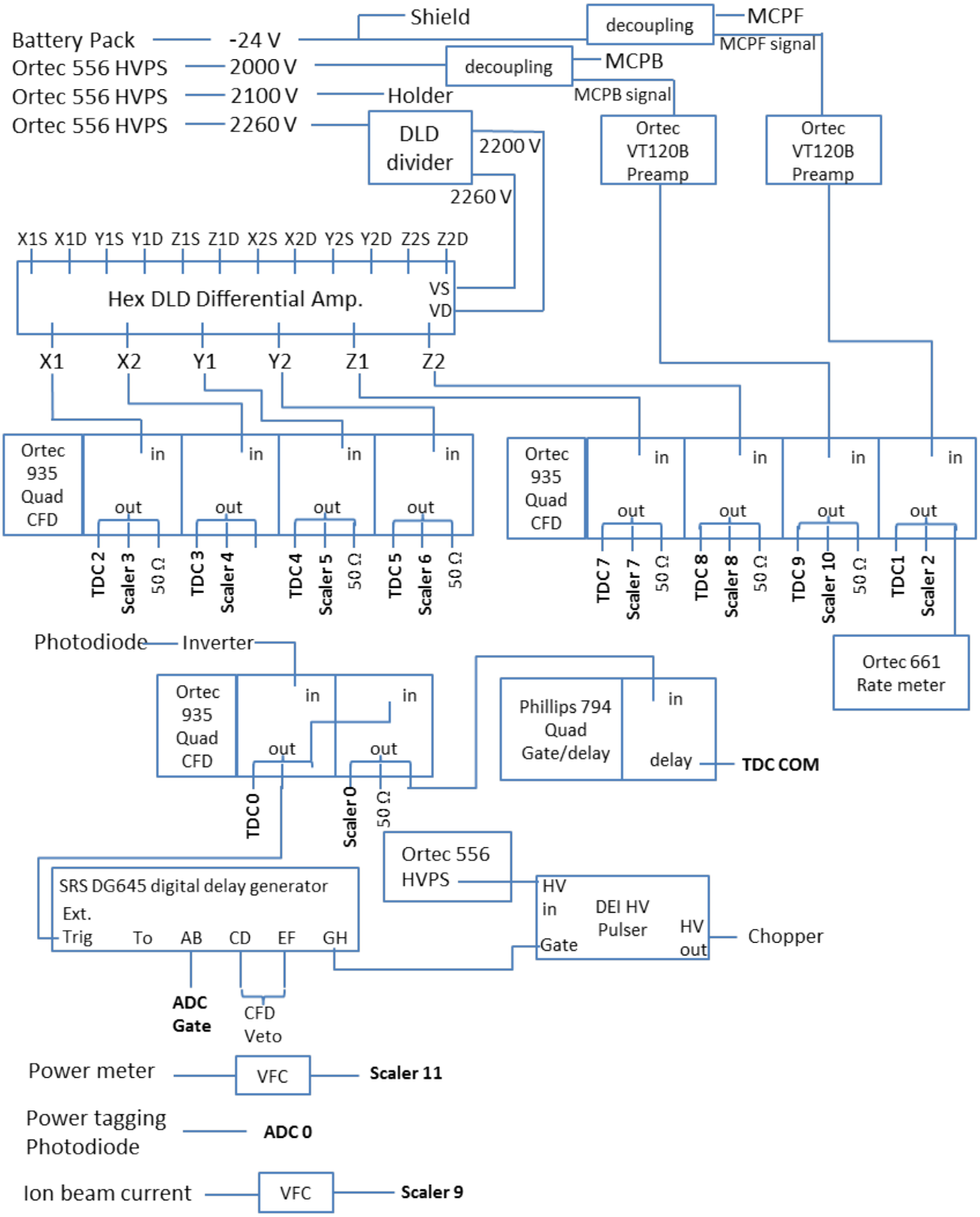

Figure C.1: Electronics for molecular ion beam studies.

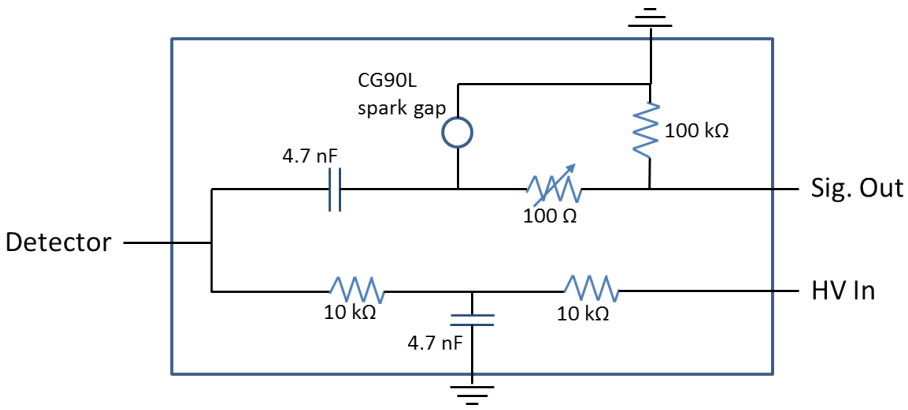

Figure C.2: Schematic of the decoupling box used to pick signals from the MCP detector.

Appendix D

Ion Sources

This appendix provides general operating instructions for the duoplasmatron and sputter sources, as well as source parameters for different beams and tips on troubleshooting. The information regarding the duoplasmatron is presented in Sec. D.1, followed by instructions for switching between the duoplasmatron and sputter sources in Sec. D.2. Guidelines for operating the sputter source are presented in Sec. D.3.

D.1 Duoplasmatron

D.1.1 Startup

1. If the filament is new, follow the conditioning procedure. If the filament has been open to air, follow the conditioning procedure for a shorter amount of time (30-60 min.). After outgassing, close the source bypass valve.

2. Plug in the water pump. Look in the reservoir and make sure water is flowing. If the water level is below the coil, add distilled water.

3. Reset the drop-out relay between the water cooling system and the source power supplies.

4. Make sure the switch in the power supply enclosure is set to Duoplasmatron.

5. Turn on the light switch.
6. Set the gas line pressure to 10-20 psi. Open the source needle valve 2.5-3 turns.
7. Press the red Arc start button.
8. Increase the voltage on the arc supply unit to 150 V.
9. Increase the magnet voltage until the current reaches 0.5 A (40V).
10. Slowly increase the filament current to 24-28 A. At this point an arc should start. Be patient; it may take 10-15 minutes. If it is not starting, try pressing and holding the red arc reset button for a few seconds. Adjust the source pressure and magnet over a wide range. If the arc current begins to slowly creep up, it is a sign an arc may be about to catch.
11. Set the extraction voltage.
12. Set Einzel 1 to 80% of the extraction voltage.

D.1.2 Shutdown

1. Lower the Einzel and extraction voltages and power off.
2. Slowly decrease the filament current.
3. Lower the arc and magnet supplies to 0 V.
4. Close the needle valve (not too tight!).
5. Turn off the light switch.
6. Wait at least 15 minutes before unplugging the water pump to allow the source to cool.

D.1.3 Switch between positive and negative operation

A minimum time of about 6 hours is needed to switch modes and pump.

- Make sure all source power supplies are off. Make sure water pump is off. Open the cage, and ground the source using the grounding stick.
- Isolate turbo pumps (close solenoid valves) and power down. Close the downstream gate valve just before the inflection magnet. Allow turbos to spin down and vent the beamline.
- Open the bypass valve.
- Disconnect filament cables, magnet cables, and intermediate electrode and ground cables.
- Disconnect water hoses B, C, D, and Out. Very little water should spill.
- Disconnect gas hose and needle valve control rod.
- Remove the source by unscrewing the 6 "E" screws on the clamp ring. Be careful not to jostle the source and shake the coating off the filament.
- Use a pin wrench (or two allen keys) to unscrew the anode insert cup. Remove the copper seal and the anode aperture. Note: the aperture can be tricky to get out. Just jiggle with your fingers until it falls out.
- Replace with the appropriate aperture (0.015" for positive, 0.025" for negative, or the 0.01" aperture specifically for hydrogen, i.e. H^+, H_2^+, H_3^+), and reassemble the anode.
- Loosen the four alignment screws and remove the 6 "S" screws to separate the source body from the anode.
- Remove the three intermediate electrode screws. Remove the intermediate electrode and replace. Use the crescent-shaped electrode for negative operation and the centered

electrode for positive operation. Note: when inserting the electrode for negative beams, make sure the crescent shape lines up with the alignment screws.

- Loosely reattach the source body and anode with the 6 "S" screws.
- Align the intermediate electrode with the anode aperture using the 4 adjustment screws. Note: For negative operation offset the electrode by 1 mm. Note: Removing the filament assembly may make alignment easier (remove 4 screws on filament base plate).
- Tighten the "S" screws and alignment screws.
- Reattach the source to the beamline with the 6 "E" screws.
- Reconnect all cables and water hoses.
- Start pumping by opening the solenoid valves. Start the turbo pumps when the pressure is lower than 50 mTorr.

D.1.4 Filament conditioning

Conditioning (i.e. outgassing) of the filament needs to be performed for new filaments, or anytime the filament is exposed to air. In the latter case the conditioning time is much shorter (especially if the source was only open for a short time). Allowing the filament to outgas slowly can greatly increase its lifetime.

1. Ground the source and make sure the bypass valve is open.
2. Turn on the water pump. Reset the drop-out relay. Turn on the light switch, and press the Arc start button.
3. Slowly increase the filament current a few Amps. Watch the pressure gauge. As the filament heats up the pressure will increase. Try not to exceed 50mTorr. Wait for the pressure to return to the base value before increasing more.

4. For a new filament, reaching 20 A may only take 30–45 minutes. At 20–25 A, outgassing can take a long time. It may take more than an hour. Above 25 A outgassing is typically faster again.

5. Continue increasing the current to 30 A. After the pressure returns to its base value the source is ready to use.

6. Close the bypass valve, remove the grounding stick, and close the cage.

D.1.5 Filament replacement/recoating

1. Ground the source and open the bypass valve. Close the downstream gate valve before the inflection magnet. Isolate the turbo pumps and power off. Vent the beamline.

2. Disconnect the filament cables.

3. Unscrew the 4 filament base plate screws and carefully remove the filament assembly.

If the mesh is mostly intact, recoat it. If the filament mesh is no longer intact, replace it:
Filament Replacement

1. Remove the center support pin.

2. Unclamp the filament and remove.

3. Get a $2.5 \times 10\,\text{cm}$ sheet of platinum gauze mesh.

4. Scroll each long edge (wind around a wire).

5. Flatten 1/4 in. at each end with pliers.

6. Clamp onto the copper rods. Ensure good contact by checking the resistance ($< 0.5\,\Omega$).

7. Coat the filament.

Filament Coating

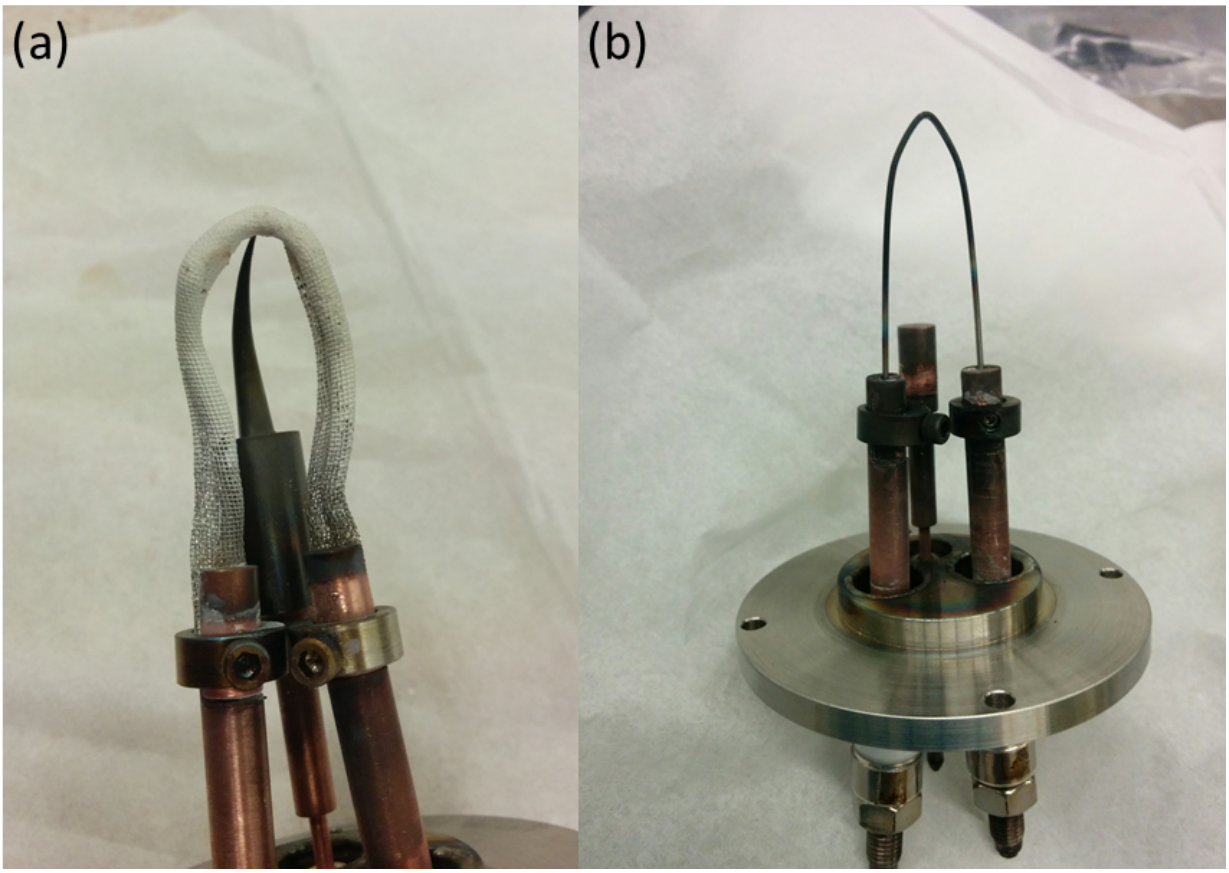

Figure D.1: Duoplasmatron filaments: (a) oxide-coated platinum mesh (b) thoriated tungsten.

1. Remove the center support pin.

2. If the supports or filament are very dirty, clean them with acetone.

3. Mix the coating solution (Transene cathode coating T-33C-118 stored in the hazardous chemicals cabinet) by shaking vigorously (really vigorously!) until all solids are mixed in. Note: It helps to first pour some liquid out of the container before shaking.

4. Pour some of the coating in a small beaker.

5. Dip the filament in the coating to apply a thin layer. Do not get any coating less than 1/4 in. from the copper rods.

6. Dry the coating with a heat gun. When dry it will turn solid white. If it turns brown the gun is too hot.

7. Apply and dry another coat.

8. Reattach the center support pin, gently pushing into the mesh.

9. Make sure the mesh is centered and the clamps are not touching one another. Gently bend them if needed.

10. Return to the source. Check that the resistance between the filament feedthroughs is $< 0.5\,\Omega$ and the resistance between the filament and source body is infinite (see the section on troubleshooting if these conditions are not met).

11. Pump down to at least 10^{-6} Torr range before conditioning the filament.

The filament assembly should resemble the picture in Fig. D.1(a).

Many target gases seem to react with the oxide coating of the mesh filament, such as hydrocarbons and fluorine-containing molecules. In these cases, a tungsten filament provides better performance.

Tungsten filament

1. Use a thoriated tungsten (2%) welding electrode, 1 mm diameter.

2. Heat the middle of the electrode with a torch until red hot. We have used the small propane torch in the welding shop.

3. Carefully bend until U-shaped.

4. Snip ends so the filament is about the same size as the mesh filament.

5. It will fit in the grooves of the filament holder. The support pin is not needed.

6. Condition at 40 A. It won't outgas very much.

7. Run at 40–45 A. Expect a lifetime of 100 hours.

D.1.6 Troubleshooting

Starting an arc

- Check the filament current. If it is zero, the filament is either broken or not making good contact with the feedthrough clamps.

- If there is arc current when the red "arc reset" button is pressed, but none otherwise, the filament may be shorting to the source body. Check the resistance between the filament and the wall of the source (with the filament cables removed), it should be infinite. If the resistance is not infinite, the filament needs to be repositioned.

- Check the filament current potentiometer setting. Typically, the potentiometer should be set at 35–40% to achieve 25 A filament current. If lower, the copper feedthrough posts may be touching each other and shorting the current flow through the filament.

If the above conditions are all normal, try varying the source magnet over a wide range (between 0 and 1 A). Also, scan the source pressure over a wide range. This is most easily done by adjusting the driving pressure from the gas bottle instead of the source needle valve. Be patient. Sometimes it takes a while for the pressure to stabilize. If all else fails, try recoating or replacing the filament.

In negative ion operation, the extraction supply may draw excessive current and limit the voltage. We think this is due to a high current electron beam escaping the source, and therefore drawing a large current from the source ground, i.e. the extraction supply. The offset intermediate electrode used in negative operation is supposed to block the main electron beam from leaving the source, and it may need to be repositioned if this problem arises.

D.1.7 Ion beams

General ion beam tuning tips

- Use the arc reset switch. While depressed, this drops the resistance between the intermediate electrode and source ground. If the source is unstable, try pressing and holding the arc reset for a few seconds.
- Ion current can be quite sensitive to the source magnet settings. Allow the source pressure to stabilize before carefully adjusting the magnet.
- Ion beams are typically insensitive to the filament current. Once an arc is struck there is no need to adjust the filament current.
- The best way to reproduce a good ion beam is to find the same arc conditions – that is, the same arc voltage and current settings. Simply applying the same gas load, magnet, and arc current is often not sufficient. Pay close attention to the arc voltage (the voltage drop required to draw the specified arc current). For example, for hydrogen beams, the arc supply is set to 100 V for 1 A. For Ar_2^+, 50 V for 1 A produces a good beam.

D.2 Switching between sources

Since the duoplasmatron and sputter sources share several power supples and connect to the source einzel, switching the source is fairly simple. Note that it takes about one day

H_2^+	Run the source at lower pressure (a few 10s of mTorr on the source pressure gauge). Maybe even mix hydrogen with a buffer gas (Ar). At higher concentrations of H_2, the dominant beam is H_3^+.
H_3^+	Run pure hydrogen. Source ion gauge around 275 mTorr.
HeH^+	Gas mixture 1/3 He + 2/3 H_2
Ar_2^+	Run at lowest pressure possible to maintain an arc (typically around 20–30 mTorr). The source magnet may be near 0 A. I had luck with 5 psi driving pressure and the leak valve open 3 turns.
Reactive gases	Make a dilute (1–2%) mixture with Ar.

Table D.1: Table of gas mixtures for various beams

to swap sources and pump down to good (10^{-8} Torr) vacuum. The following instructions are for switching from the duoplasmatron to the sputter source; follow the instructions in reverse for switching from sputter source to duoplasmatron.

- Ensure that all power supplies are shut off, the water pump is unplugged, and the source is grounded. Open the source bypass valve. Close the gate valve just before the inflection magnet. Isolate and power off the turbo pumps, and vent the source. It is easier to work with the cage removed, but it is possible to swap the source inside the cage.

- Disconnect all cables, the gas line and control rod, and the water in/out hoses.

- Remove the nuts/bolts connecting the extraction gap to the source einzel, and remove the source and extraction gap as one piece. This can be done by one person by bracing the source with their body while removing the screws.

- Mount the sputter source. Make sure the Cs reservoir is positioned on the bottom. Threading the small nuts is not easy. Use tweezers and a small spatula to hold the nut up to the screw. Carefully pull the tweezers away while still holding the back of the nut flush against the screw with the spatula. Use your fingers to spin the nut. Don't get too frustrated when this doesn't work.

- Load the Cs reservoir and a cathode (see instructions in Sec. D.3).
- Start pumping. Reconnect the water lines. Note that in/out are interchangeable. Connect the cathode cable, heater cables, and thermocouple. The ionizer uses the same cables as the duoplasmatron filament. Connect the extraction gap cable. Hang the remaining cables inside the cage, as they will still be at high voltage.
- Flip the switch from Duoplasmatron to Sputter source in power supply enclosure.

D.3 Sputter Source

D.4 Startup and shutdown

Startup

1. Turn on the water pump and make sure water is flowing. Refill with distilled water if the water level is below the coil.
2. Reset the drop-out relay between the water cooling system and the source power supplies.
3. Make sure the switch in the power supply enclosure is set to Sputter source.
4. Turn on the light switch.
5. Press the arc reset button.
6. Slowly increase the ionizer current to 21 A. As it warms up, the current will drop, so adjust accordingly. It should reach about 80% full scale on the variac. We try not to exceed 23 A.
7. Increase the reservoir heater to 0.7 A and the tube heater to 0.6 A. Monitor the thermocouple temperature, adjust the heaters to set the temperature to about 190 C. Running at high temperatures much above 200 C will reduce the lifetime of the Cs charge.

8. Increase the cathode voltage to 4–6 kV. Set the extraction supply so that the sum of the cathode and extraction voltages matches the desired beam energy.

9. Wait. Once the heaters warm up, it may take an hour for the source to stabilize.

10. Watch the cathode current. A few mA are needed for normal operation. We aim for a current between 2 and 5 mA. If the current is low, try increasing the temperature and/or ionizer current slightly, or see the troubleshooting section for possible issues.

11. Carefully adjust the cathode position to optimize the beam current.

Shutdown

1. Turn off the extraction and cathode supplies.

2. Turn off the heaters.

3. Wait until the reservoir temperature is less than 100 C to turn off the ionizer.

4. Allow the source 30 minutes to cool down before stopping the water pump.

D.5 Loading the Cs reservoir

Under normal conditions, the Cs reservoir filled with a 1 g load should last for about 10 days of operation.

1. Prepare all the tools, which can be found in a bag labeled "Cs tools": Allen keys for opening the reservoir, needle-nose pliers, tweezers, a file, a small beaker, some small wire, and a new copper seal. Also, gather some Kimwipes.

2. Place a foil layer in the bottom of the glove box and set all tools inside. Start the flow of Ar into the glove box and partially close the door.

3. Get a 1 gram Cs ampoule and place inside the heater in the glove box. Switch the heater on.

4. Leave the door cracked open with Ar flowing for about 20 minutes.

5. Ensure that all power supplies are shut off, the water pump is unplugged, and the source is grounded. Close the gate valve just before the inflection magnet. Isolate and power off the turbo pumps, and vent the source with Ar.

6. Disconnect the thermocouple and heater cables from the reservoir. Remove the two screws connecting the Cs vapor tube to the source, and unscrew the tube from the source.

7. Place the cap on the end of the tube and take the reservoir to the glove box. Close the door, leaving one latch open to allow the continued flow of Ar.

8. Set the reservoir in the vice clamp inside the glove box and remove the 6 screws from the reservoir.

9. Remove the old copper seal and use tweezers and a Kimwipe to clean the flanges.

10. Run the small wire through the tube to clean out any buildup.

11. Carefully break open the Cs ampoule and pour into the reservoir. Try to avoid dropping any pieces of glass into the reservoir, but do not try to remove any that fall in.

12. Place the broken ampoule in the small beaker.

13. Using a new copper seal, reseal the reservoir. Be careful to not break the screws when tightening.

14. Make sure the cap is on the end of the tube. Quickly take the reservoir back to the source and reinstall. Stop the flow of Ar in the beamline, remove the cap, screw into the source, and replace the two screws. Start pumping immediately.

15. Take the beaker with the broken ampule to the sink in the fume hood. Use a pipette to carefully drop water into the beaker to neutralize the remaining Cs. Now it is safe to dispose of the glass.

16. Stop the flow of Ar to the glove box. Remove and clean tools.

D.6 Loading and replacing the cathode

Under normal conditions, cathodes last for a few 10's of hours operation. Prepare one cathode per day of beamtime to start with. Note that the source does not need to be shut down completely to replace the cathode (see instructions).

Cathode replacement

1. Turn off the cathode and extraction high voltage supplies. The ionizer and heater may be left on as long as the water is flowing.

2. Open the cage and ground the source. Close the beamline gate valve.

3. Connect Ar to the cathode vent valve, running at 2–3 psi. Do not use nitrogen, as it reacts with the ionizer.

4. Remove the banana cable connector, and unscrew the cathode from the control screw completely, until the control rod disengages. Pull out the cathode until the end is visible in the clear plastic section. Loosen the cathode seal carefully if it is too tight.

5. Close the cathode gate valve. Open the vent and loosen the seal and pull out the cathode.

6. Unscrew the cathode (careful, it may be warm) and replace with a new one. Screw on tightly with pliers, as good contact between the cathode and copper heat sink is critical.

7. Reinsert the cathode and close the seal by hand. Close the vent. Attach roughing line to the vent. Pump the line down. Open the vent and pump the cathode airlock for a few minutes. Close the vent and detach the roughing line.

8. Slowly open the gate valve. Slide the cathode in and screw in with the control rod. Reconnect the banana cable.

To load cathodes,

1. Gather new cathodes, the tamping tool, and cathode material. From the Tandem cabinet next to the fume hood, gather the lead brick, cathode holder plate, hammer, scooper, and if needed the mortar and pestle.

2. Working in the fume hood, place the cathode holder plate on the lead brick, and place the new cathode in the holder slot.

3. The cathode material must be a fine powder. If not, use the mortar and pestle to crush.

4. Fill the cathode with the powder and press down with the tamping tool.

5. Continue to fill as much as possible and tamp down.

6. When full, use the hammer and tamping tool to compact the powder as much as possible – this is essential for long cathode lifetimes. Note that the cathodes may get stuck in the holder slot. Use the hammer to tap them loose periodically.

D.7 Source parameters and troubleshooting

To produce a beam from the sputter source, a few mA cathode current is required. Typically, we aim for a cathode current between 2 and 5 mA at 5 kV cathode voltage. This is achieved with Cs temp of about 195–200 C and ionizer current of 21 A. If sufficient cathode current is produced, the source is working and the beam current is optimized by simply adjusting the position of the cathode. However, there are many issues that impede the performance of the source, as outlined below.

- If the ionizer has been exposed to air, it needs to be outgassed. Slowly increase the ionizer current to 21 A while monitoring the source pressure. If the ionizer is outgassing while the source is running it may quickly kill the Cs charge and the cathode.

- If the cathode current is low, and there are no suspected problems with the Cs reservoir, the ionizer may need to be cleaned. Break vacuum, remove the ionizer and wipe gently. A mild abrasive may be used if it's very dirty.

- If the Cs was exposed to air, it may form a crust. The crust will eventually burn off, and it may be necessary to briefly increase the temperature to around 250 C.

- When the source is first started, especially with a new cathode, it may be unstable. Allow an hour or so for it to settle down.

- The Cs vapor tube may be clogged, preventing the cesium from entering the source. It is best to clean the vapor tube every time the reservoir is refilled.

- If the cathode cannot be inserted all the way, the insert aperture is blocked. Sputtered cathode material over time blocks the cathode insert aperture, as shown in Fig. D.2, and it needs to be drilled out. Open the source, remove the insert and drill out with a 25/64" drill bit. It is recommended to do this every time the Cs reservoir is refilled.

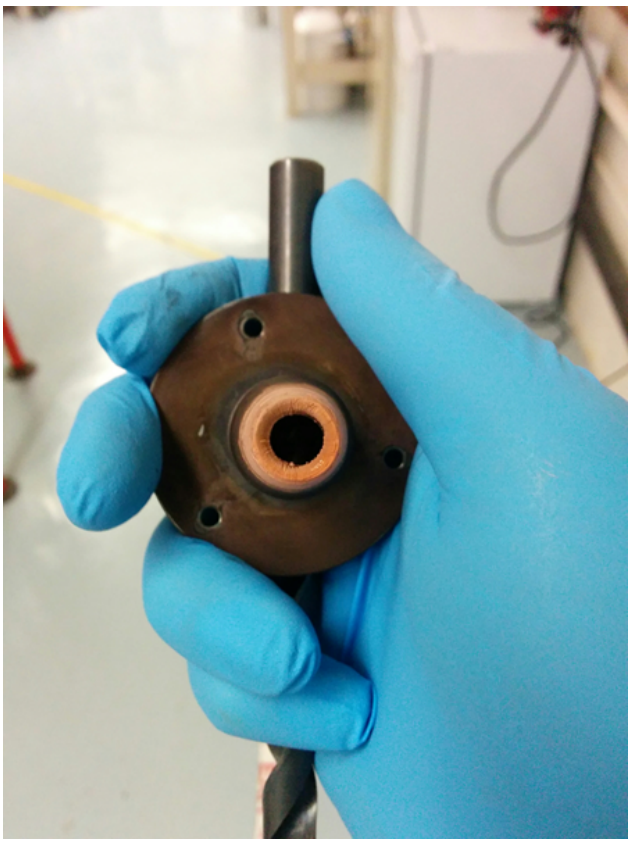

Figure D.2: Sputter source cathode insert aperture that has been blocked by sputtered copper from the cathode.

Appendix E

Experimental details - D* experiments

This appendix comprises additional details regarding the setup used to conduct the experiments on D* formation from D_2 described in Chap. 5. The detector electronics are given in Sec. E.1. The field ionization voltages used in the D* state-selective measurements and the theoretical model these values are based on are presented in Sec. E.2. Notes on controlling the LabView software used to control the state-selective measurements are given in Sec. E.3.

E.1 Electronics

The electronics used in the experiments presented in Chap. 5 process only the timing signals from each of the two detectors, making the setup much simpler than the electronics used in ion beam measurements (see Appendix C). The time signals are picked off the back of the MCP stack of each detector, decoupled from the high voltage using a HV decoupling box (see Appendix C), amplified, and then sent to a constant fraction discriminator (CFD) unit, as illustrated in Fig. E.1. The NIM output signals from the CFD are fed into the time-to-digital converter (TDC) and a Scaler that records the signal rate.

A small portion of the laser beam is split off and directed onto a fast photodiode, which

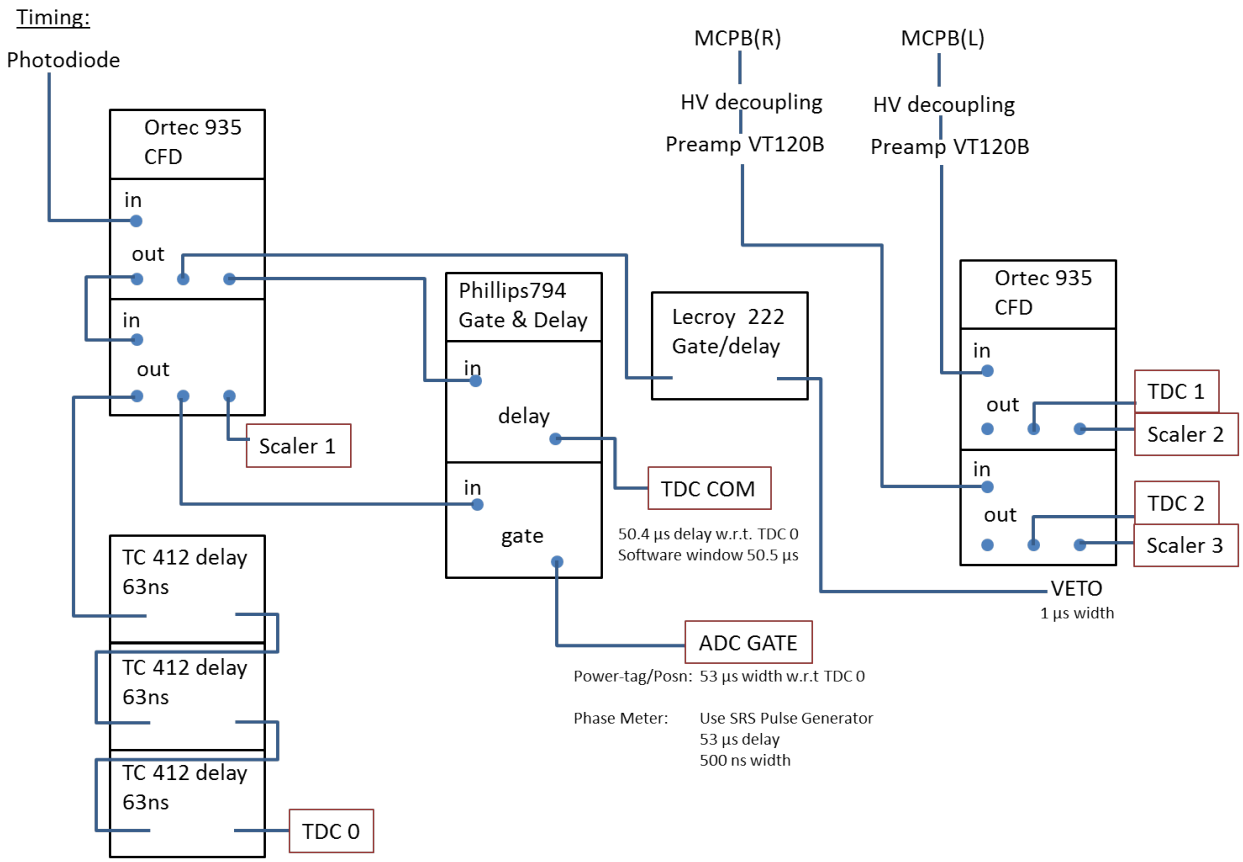

Figure E.1: Electronics schematic for experiments presented in Chapter 5.

provides the TDC trigger (COM) and reference (TDC0) signals. The photodiode signal is also fed into a Scaler for monitoring the rate, and another duplicate photodiode signal is used to generate a gate signal which triggers the analog-to-digital converter (ADC).

Note that the reference photodiode signal (TDC0) is delayed using a TC412 passive delay unit, and that a duplicate photodiode signal is used to generate a VETO signal that blocks the CFD output. The timing of these signals is illustrated in the bottom portion of Fig. E.2. The use of the CFD veto and the choice to delay the TDC0 signal are due to a high rate of fast particles (possibly energetic electrons) hitting the detector with TOFs less than 1 μs, with the highest rate of signals at times below 100 ns. While these particles do not seem to saturate the MCPs, they do inhibit the data acquisition. The VETO signal blocks these signals from being output from the CFD. However, the intrinsic delay in generating the veto signal is about 80 ns with respect to the TDC0 photodiode signal, leaving the high rate of

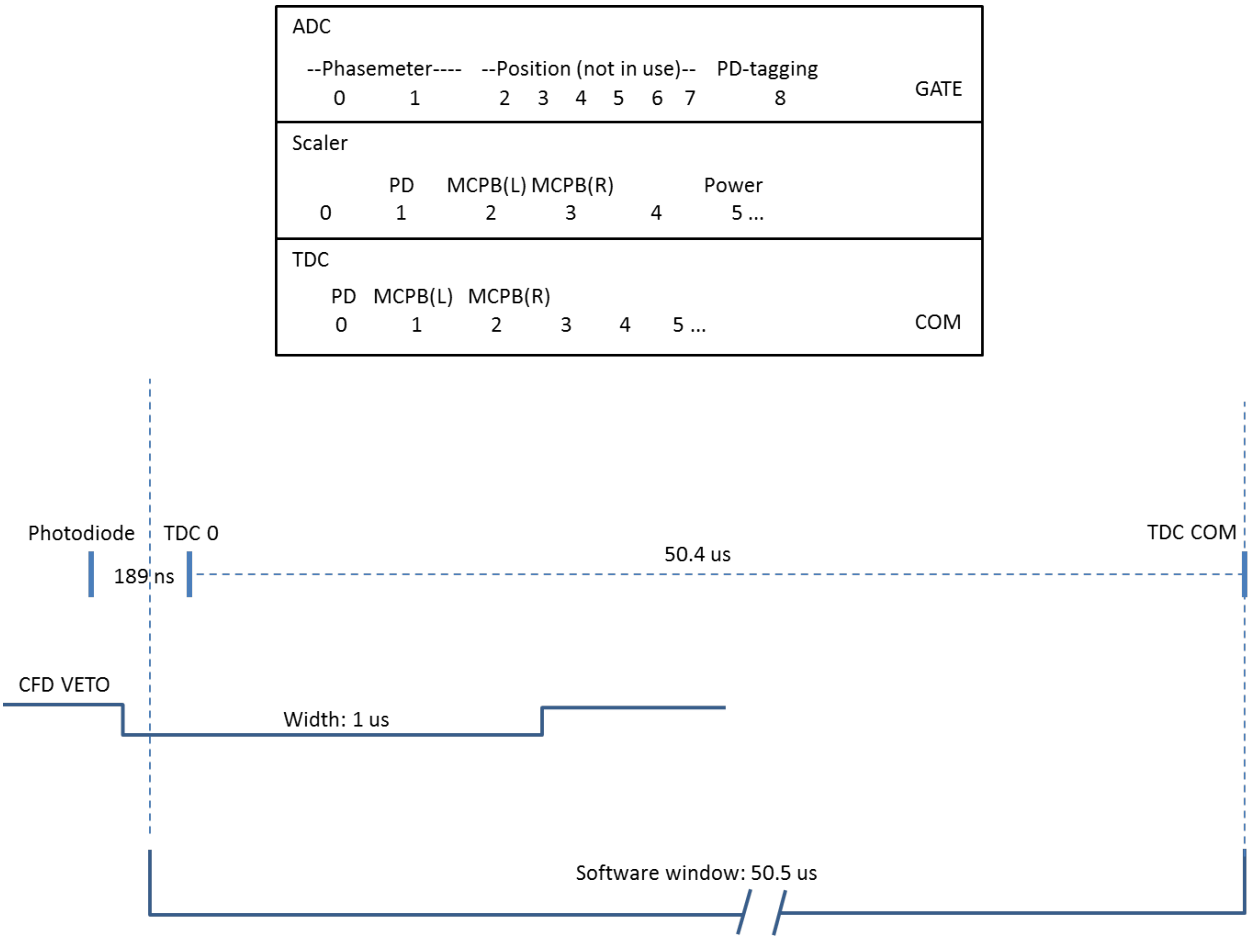

Figure E.2: (Top) TDC, ADC, and Scaler wire connections. (Bottom) Timing of the photodiode signal replicas that generate the TDC COM, TDC0, and CFD Veto signals.)

hits within that 80-ns gap unblocked. To solve this problem, the TDC0 signal is passively delayed by 189 ns so that it comes after the VETO signal begins. This introduces a 186 ns offset of the time-of-flight signals which is accounted for in analysis. A passive delay unit is used to delay TDC0 so as to not add timing jitter that reduces our time resolution.

The data acquisition time window, set in software, defines the search window with respect to the TDC COM. It is set precisely so that the window begins before the TDC0 signal, but after the start of the veto signal.

The ADC may also be used to record position signals from the detectors, however we did not use the position capability of these backgammon anode detectors in any experiment. A small fraction of the laser beam is split and focused onto a large area photodiode, from which the amplitude of the signal is used to monitor the laser pulse energy (see Appendix B

for details), and that signal is recorded by the ADC. For CEP studies, the output of the CEP meter electronics are also fed into the ADC.

A layout of the TDC, ADC, and Scaler inputs is shown in the top of Fig. E.2. Note that the TDC is a C.A.E.N model V1290N; the ADC is a C.A.E.N. model V785N; and, the Scaler is a C.A.E.N. model V560N.

E.2 Field ionization voltages

The voltages used for field ionization of Rydberg D* fragments in the state-selective studies of D* formation presented in Chap. 5 are based on a model by Rakovic and Chu [215]. They used a classical model to calculate the field ionization of hydrogen in a static field, which yielded the ionization probability shown as an inset in Fig. E.3. In this figure, P is the ionization probability, f is electric field strength in atomic units, and n is the principle quantum number. From these calculations, they define the threshold for field ionization as

$$f = 1/5.783n^4, \tag{E.1}$$

where f is the field strength for which 50% of the atoms in state n are ionized. Note that this is not a hard threshold. As illustrated in Fig. E.3, the threshold field for a given state, shown roughly by the yellow cells, does not imply that all higher states and no lower states are ionized. In fact, the ionization probability of surrounding states can also be near 50%. Even given the limitations of this model, it still is a useful tool for our state-selective studies.

The voltages that were applied to the meshes in our measurements are given in Table E.1. Note that the maximum voltage drop we were able to apply was about 2800 V between the meshes separated by 2 mm . Above this voltage, dielectric breakdown (likely across the ceramic insulators) occurs. This limits the low end of our resolvable n-state range to $n = 16$. At the high end, voltages below ∼45 V are not sufficient to repel high energy ions from reaching the detector, and we see the detector rate increase rapidly with lower mesh voltage. So, we cap the upper end of the n-state range at $n = 43$.

n	E (V/cm)	M2 (V)
15	17564.3	3512.9
16	13568.0	2713.6
17	10646.3	2129.3
18	8470.4	1694.1
19	6823.1	1364.6
20	5557.5	1111.5
21	4572.1	914.4
22	3795.8	759.2
23	3177.5	635.5
24	2680.1	536.0
25	2276.3	455.3
26	1945.8	389.2
27	1673.2	334.6
28	1446.7	289.3
29	1257.2	251.4
30	1097.8	219.6
31	962.8	192.6
32	848.0	169.6
33	749.8	150.0
34	665.4	133.1
35	592.5	118.5
36	529.4	105.9
37	474.4	94.9
38	426.4	85.3
39	384.4	76.9
40	347.3	69.5
41	314.7	62.9
42	285.8	57.2
43	260.1	52.0
44	237.2	47.4

Table E.1: Table of voltages applied to the mesh M2 with M1 always set to 0 V to provide the threshold field for ionization, E, of each n-state.

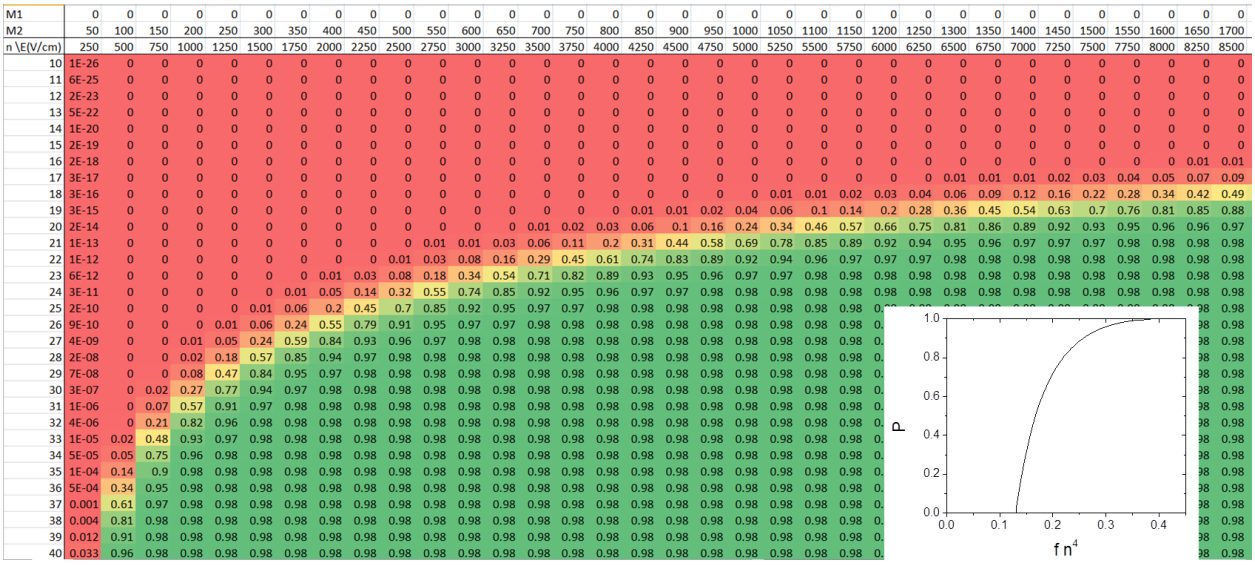

Figure E.3: Chart of n-state ionization probability for a range of electric field strengths. Inset: Plot of the ionization probability from Ref. [215].

E.3 Labview

The field ionization voltages described in the previous section were applied using an ISEG power supply, which allows external control through a CAN bus interface. This allowed us to use LabView to automate the control of the mesh voltage and the data acquisition in SpecTcl.

The CAN bus interface is controlled by computer via a PCAN PCI card. This card uses old drivers and only runs under Windows XP. The card and LabView code are installed on the computer "Wigner".

To control the program,

1. Connect the serial ribbon cable between the PCI card and the back of the ISEG power supply.

2. On Wigner, navigate to *F:\ItzikISEGVoltage* and open *ItzikISEGVoltage.vi*. Do not run this code, it only helps LabView find the necessary drivers.

3. Open *ISEGVScan_bb_v3.vi* on the Desktop and press Run.

4. Input the voltage, step, and time parameters.

5. Turn off the ISEG power supply.

6. Switch to Manual Control.

7. Unplug the unit from the rack and plug back in.

8. Switch to DAQ control.

9. Switch HV to On.

10. Start the measurement in LabView by pressing *Go*.

Failure to follow these steps will result in the power supply's refusal to "listen" to the input from LabView. The power supply changes voltage slowly, especially if the step is large. So, the default pause time is set to 20 s. The voltage is communicated to SpecTcl, where it is set as the *posno* parameter, i.e. the same parameter used for the step number in pump-probe scans.

The SpecTcl code labeled $FTI\_CEP\_BB\_pp$ located in $\backslash ibgroup \backslash FTI \backslash$ has a modified output file, $tofpm.out$, into which the values $ker1l \quad ker1r \quad posno \quad adc1$ are written. $ker1l$ and $ker1r$ are the calculated KER of the first hit on each respective detector, *posno* is the voltage applied to M2, and $adc1$ is the photodiode signal tagging the pulse energy. This data can then be sorted further in Matlab using the n-state code $df\_nsort.m$ described in Appendix G.

Appendix F

SD-FROG

Our home-built SD-FROG is based on the version developed by Sabih Khan [222] and uses several of the same elements. This FROG is designed to characterize second harmonic pulses of around 400 nm wavelength. With this wavelength in mind, all of the mirrors in the setup are aluminum. As shown in Fig. F.1, the laser beam is split in to the two arms of the FROG by a "D"-shaped mirror. The temporal delay between the two arms is controlled by a Thorlabs pizeo actuator that moves a linear translation stage. The beams from each arm are focused by a $f = 50$ cm mirror onto the nonlinear medium, a 111-μm thick quartz crystal, where the pulses are overlapped spatially and temporally. Note that the long focal length is necessary so that the beams intersect at a very shallow angle to improve the phase-matching conditions. One of the self-diffraction (SD) signal beams that exits the crystal is reflected into a spectrometer which is sensitive to wavelengths between 195 and 640 nm.

Two irises near the entrance of the FROG can be used to coarsely align the FROG, but additional tweaks to the alignment of the arms are often needed to overlap the beams in the quartz crystal. To aid in overlapping the beams in the crystal, a camera with 10× microscope objective can be placed just in front of the crystal to directly view the spots of the two beams. The temporal overlap is found by manually scanning the translation stage until the self-diffraction signal is observed (new diffracted beams appearing to the outsides of the main beams, as shown in Fig. F.1). In scanning the delay, one common mistake is using

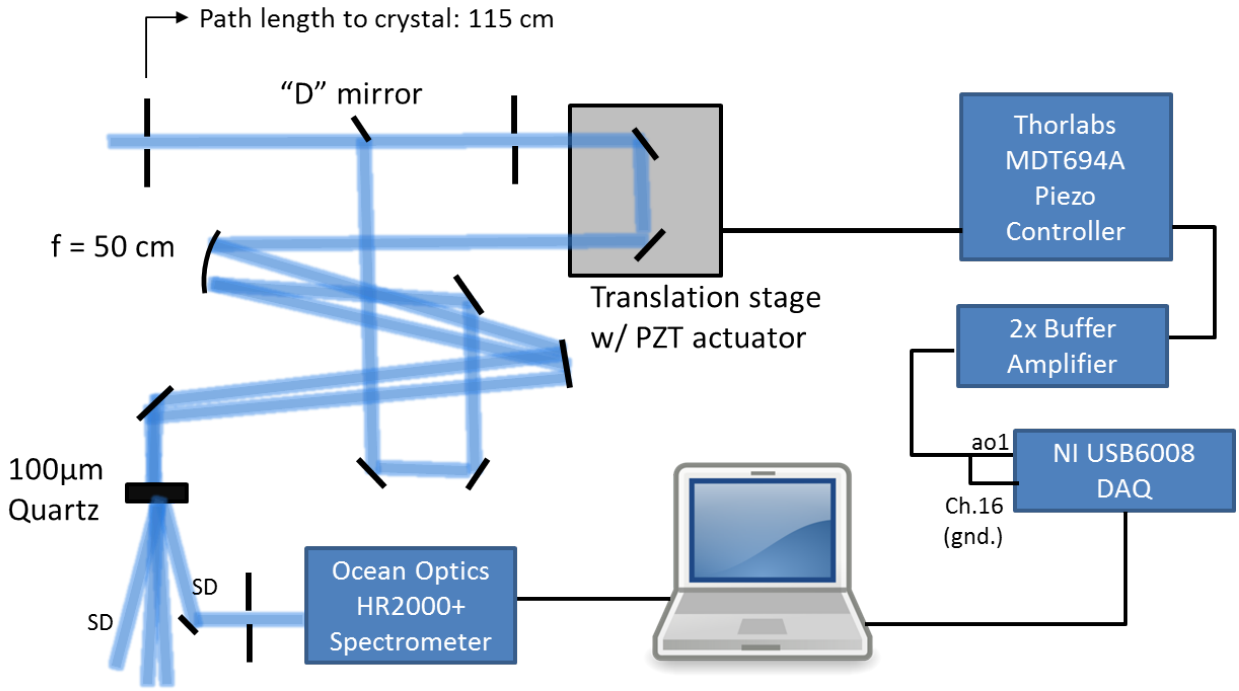

Figure F.1: SD-FROG schematic diagram.

insufficient power to generate a SD signal, making it impossible to find the temporal overlap. Self-diffraction is not an efficient process because it is not phase-matched, so a relatively high power is needed to see a signal. We have found that nearly 100μJ pulse energy at 400 nm is needed to observe a signal, but note also that this high power is near the damage threshold of the crystal.

The FROG is controlled by LabView software entitled "SDFROG_scan.exe" stored on the Desktop of our lab laptop. The source code can also be found in *S:\BenItzhak\FROG\SDFROG-Raju_2015*. This code generates the spectrogram by stepping the piezo stage and recording the spectrum for each delay step. The scan range of the pizeo stage is 0–100 V corresponding to a delay range of 270 fs (2.7 fs/V). A 0–10 V voltage is used to externally control the pizeo controller. The LabView code communicates with a National Instruments DAQ card that outputs a 0–5 V signal. This voltage is then amplified by a factor of two to provide the 0–10 V required to control the piezo stage. In some instances the LabView code fails to communicate with the DAQ card. This problem is often solved by changing settings in the NI_MAX software. Open NI_MAX, right click DAQ card in the

device list, create a new task, select Generate Signals–analog output–voltage–a01, and name the task "voltageout". Then, restart LabView.

To record a scan, manually set the piezo voltage to the middle of the scan range (typically 50 V). Then, manually adjust the translation stage to optimize the SD signal. This will ensure that the spectrogram is centered on the scan and reduce the likelihood of clipping either edge. Then, reset the controller to 0 V. Enter the start voltage, end voltage, and step parameters in the software, and the scan is ready to begin.

There are several options in the LabView code to improve the quality of the recorded spectrogram. Two averaging options are available: spectrum averaging, which averages any number of spectra at a given delay point, and delay averaging, which repeats the scan any number of times. We typically choose 5–10 spectra averages and 3–10 delay averages. A background spectrum can also be recorded and subtracted to reduce the amount of stray light entering the spectrometer. Before recording a background spectrum, manually scan the delay away from overlap so that there is no SD signal. Note that oversubtracting (i.e. negative values in the spectrogram) can cause some issues with the analysis. Often times it is sufficient to block the stray light so that the background intensity is below ∼200 counts.

With all the averaging implemented, recording the spectrogram can take a long time (often more than 30 minutes). So, first perform a coarse scan of only 10 steps with little or no averaging. This allows checking of the background levels, clipping of the spectrogram, and saturation of the spectrometer. Note that the spectrometer's maximum signal is 160000 counts. We typically aim for a peak signal of 10000 counts or less.

The recorded spectrogram is saved in a format that can be analyzed using the FROG software by Femtosoft Technologies ("XFrog3.exe" found in the FROG directory on the S: drive). Load the file and input the data parameters: number of delay points, number of wavelength points (2048 for the full spectrum), delay increment (2.7 fs/V), wavelength increment (0.2192 nm per pixel), and wavelength of first pixel (195 nm). Set order to "Delay", and Read In as "Constant wavelength". Then, use the options under the "Noise Subtraction" tab to clean the spectrogram, then click "Grid Data" and run the analysis to reconstruct the pulse.

Note that the FROG analysis software assumes the delay increment is uniform over the entire scan; however, in reality the voltage steps are not exactly linear. A Matlab code was written to interpolate the recorded spectrogram and generate a new one with uniform delay steps. The code, "FROG_interpolation.m" can be found in the FROG directory on the S: drive. In addition to interpolation, this code can also be used to truncate the spectrum in case stray light at other wavelengths is being recorded. To run the code, enter the voltage and spectrum parameters and load the recorded spectrogram. The program will save a new spectrogram as well as a file containing the relevant parameters for input into the analysis software ("FROG_info.txt").

Finally, while this SD-FROG was designed for 400-nm pulses, it also works for third harmonic 266 nm pulses. In this case, higher-order diffraction signals appear at around 600-nm and truncating of the spectrum is necessary. This FROG can also be easily converted to the transient grating FROG (TG-FROG) geometry by splitting the input beam into four beams using a mask (or two hex keys) and blocking one of the four beams. The 800-nm pulses can also be characterized using this FROG by converting it to a second-harmonic FROG. Simply replace the quartz crystal with the appropriate second harmonic BBO crystal.

Appendix G

Matlab codes

This appendix is an index of the "J:\Ben\Matlab Codes" directory, which contains several useful Matlab codes developed during my work in the group. This list is followed by more detailed descriptions of the functions, inputs, and outputs of each of these codes in Sec. G.2.

G.1 Index

- **Anions** see Sec. G.2.1 for details
  - **anion_analysis.m** Generates plots and performs cuts in φ, KER, and $\cos\theta$
  - **f2_stretch.m** Solves the classical equation of motion on a potential surface
  - **f2_morse.m** Tabulates the Morse potentials for F_2^- from Ref. [110]
  - **matrix_elements.m** Calculates bound–continuum transition matrix elements for a given transition between two potential curves
  - **vib_pop.m** Uses the matrix elements and measured KER to determine the vibrational population of F_2^-, as described in Sec. 3.3.3
  - **functions/** Directory containing various functions used for plotting
- **CCD** see Appendix A for details
  - **ccd_analysis.m** Gaussian fitting of focal spot images

- **intensity.m** Calculate peak intensity of a Gaussian beam

- **CEP analysis** see Sec. G.2.2 for details
  - **bb_DFLoad.m** Load the data
  - **bb_saturation.m** Removed bad points due to saturation of the phase meter
  - **bb_rebinphase_subsets.m** Sort the data into subsets and rebin to recover the CEP
  - **bb_asym_subsets.m** Generate the yield and asymmetry plots and perform FFT analysis
  - **bb_state_selective_testing_offset.m** Generation of state-selective asymmetry, yield, and FFT analysis of the data shown in Sec. 5.4

- **H_rates** see Sec. G.2.3 for details
  - **rates.m** Function used in rates_all.m to calculate decay rates
  - **rate_eqs.m** Function used in timeprop_ode.m to calculate decay rates
  - **rates_all.m** Calculate and store decay rates for a specified range of (n, l) states
  - **init_generator.m** Generate an initial (n, l) population
  - **init_generator_rev.m** Generate a final (n, l) population based on the measured n-state distribution
  - **timeprop.m** Solve rate equations using the Euler method for a given initial population produced by init_generator.m
  - **timeprop_ode.m** Solve rate equations using one of Matlab's built-in ODE solvers
  - **timeprop_rev.m** Solve the inverse rate equations (propagation backward in time) for a final distribution produced by init_generator_rev.m

- **n-state** see Sec. G.2.4 for details
  - **dfnsort.m** Load and analyze state-selective data, generate maps of the yield as a function of n-state and KER

- **FI.txt** Table of field ionization voltages needed for dfnsort.m

- **Pump-probe** see Sec. G.2.5 for details
  - **pumpprobe.m** General pump-probe analysis including ion beam normalization and background subtraction using the functions listed below, generates plots, and evaluates ionization enhancement using the methods described in Chap. 4
  - **functions/**
    - **bb_import.m** Import momentum output file from SpecTcl
    - **bb_truncate.m** Truncate incomplete scans or scans that did not end properly
    - **bb_ionbeam.m** Use the ion beam current to normalize the yield
    - **bb_step.m** Sort the data into bins corresponding to each delay step
    - **bb_randoms.m**, **bb_randoms2.m** Subtract random coincidences
    - **bb_enhancement.m** Evaluate ionization enhancement

- **Scripts_linux** see Sec. G.2.6 for details
  - **checkload.sh** displays the uptime information for most of the Linux data analysis machines
  - **rblink.sh** creates soft links to ring buffer .evt files in the working directory
  - **ecrlink.sh** creates soft links to old-format .evt files in the working directory

G.2 Code descriptions

G.2.1 Anions

The following codes were used in the analysis of the data presented in Chap. 3.

bb_anions.m is used primarily for making cuts in KER, $\cos\theta$, and ϕ and generating figures. Several examples of the plotting and cutting functions are shown in the code, and

some general instructions are listed here. The momentum file output from SpecTcl is loaded using the **bb_import.m** function, which stores the data in structures, e.g. "data.A.ker" contains the list KER values for channel A. The data is binned and plotted using any of the several plotting functions in the **functions** directory. Each plotting function can bin multiple data sets at the same time. The plotting functions have three inputs: a normalization flag (0 or 1) to turn on normalization by the peaks of each data set, a filename input to save output files, and the input data. The file names should be entered as a string in the form "'file1.out','file2.out'". So, for example, to generate a few non-normalized 1D KER plots, enter "kerplot(0,'file1.out','file2.out', data1.A.ker, data2.A.ker)". To make a cut in ϕ, use **phicut.m** with the arguments *data*, ϕ_{min}, and ϕ_{max}, where ϕ_{min} and ϕ_{max} define the range of ϕ to cut out. Similarly, making cuts in other variables such as KER and $\cos\theta$ can be done using the function **dice.m**.

f2_stretch.m solves the 1D equation of motion on a given Morse potential. Enter the masses and initial internuclear distance R as well as the Morse potential parameters. A Matlab ODE solver then solves the equations of motion and plots the internuclear distance as a function of time.

f2_morse.m tabulates the F_2^- Morse potentials from Ref. [110]. The Morse parameters are entered into the function **morseplot.m** that tabulates the values in atomic units, and the tabulated potentials are saved as .dat files. Options to convert to eV and angstroms can be toggled in the function file.

matrix_elements.m uses the phase amplitude method of *lap*2.*exe* from Ref. [112] to calculate bound and continuum wave functions and then calculates the transition matrix elements for any bound–continuum transition. For a given initial state, all of the bound state wave functions are calculated, then the continuum wave functions of a final electronic state with energy corresponding to the absorption of a photon are calculated. These wave functions and a supplied dipole moment $D(R)$ are used to calculate the transition matrix elements. Enter the tabulated initial potential at the top of the script as well as the reduced mass. There is an option to enter a value or range of values of J to include rotation. However, the code works best for $J = 0$ and more testing is needed to appropriately include rotation.

Under the label "step 2", enter the tabulated potential of the final state, reduced mass, and photon energy as well as the dipole moment if available (set equal to 1 if unknown). The resulting matrix elements are saved to the *Dm* variable, and an output file containing the inital vibrational levels, KERs, and matrix elements can be saved at the bottom of the file.

vib_pop.m uses the transition matrix elements produced by **matrix_elements.m** and a KER spectrum to calculate the vibrational population of the ion beam as described in Sec. 3.3.3. The output file from **matrix_elements.m** containing the KER and dipole matrix element associated with each vibrational level is plugged in to the equation for the KER as a function of the vibrational population (eq. 3.5) when the function **popfit.m** is called. Matlab's nonlinear regression model "nlinfit" is then used to fit the measured KER spectrum. The population is extracted from the fit parameters and the KER of each vibrational level is plotted by the function **pvker.m**.

G.2.2 CEP analysis

This CEP analysis code is written in a series of scripts that are run sequentially. It is often useful to save the output of each script to a .mat file for faster loading in the future. These codes were used to analyze the CEP-dependent production of D* fragments from D_2 presented in Sec. 5.4.

The "tofpm.out" output file from the SpecTcl CEP code (FTI_CEP_BB in the FTI directory) contains the KER on each detector and the two phase meter ADC signals. A second file, "PM.out", is a random sample of phase meter signals used to create a reference phase potato (the sampling rate can is set in the SpecTcl parameter file). To load these files to Matlab, run **bb_DFLoad.m**. The reference phase values are saved to the "Phase" variable while the KER and associated phase values are saved to the "data_read1" variable. Loading the files is often the slowest part of this analysis, so it is very useful to save these variables to a .mat file which loads much faster.

For "bad" laser pulses that do not generate useable phase meter signals, output is still recorded and appears as "saturation" at the edge of the phase potato spectrum. The "sat-

uration" must be removed before rebinning the CEP. The saturation is removed from both the reference and data values in **bb_saturation.m**. This means some data is thrown out, but it is typically less than 1%. The updated reference phase and data are stored in the "phaseRef" and "data_read" variables, respectively.

Next, the phase meter values are converted to CEP. The centroid of the reference phase potato is found automatically by and is given by the average value of each of the two signals. The angle θ is then defined as arctan of the two values. The θ values are then binned, and the total yield in each bin is used as a normalization factor to convert to bins in CEP, φ. This ensures that the CEP is uniformly distributed as expected from a free-running laser. Then, each value of θ is converted to φ by linear interpolation using the φ bins. The values of φ corresponding to each data point are calculated next, and the respective data from each detector is stored in the arrays "data_left" and "data_right", which contain the KER and CEP.

Note that before the phase is rebinned, the data and reference arrays can be split into subsets, which are later used for Fourier analysis of the CEP-dependent asymmetry and yield (see Sec. 5.4). The phase rebinning is performed for each subset, as fluctuations in the measurement may mean a single rebinning procedure doesn't work equally well for each subset and may introduce artifacts. Again, it is useful to save the "data_left" and "data_right" variables to a .mat file so that the analysis up to this point does not ever need to be repeated.

Finally, **bb_asym_subsets.m** generates CEP-dependent asymmetry and yield plots and performs Fourier analysis of the results. The "data_left" and "data_right" arrays are binned in 2D with respect to KER and CEP. The asymmetry is defined as the normalized difference between the and the yield as the sum of the two. The binned spectra are saved to the variables "asym_total" and "yield_total" and can be exported for plotting in Origin.

The Fourier analysis is done using Matlab's fft function, and the results are written to the variables "ftasym" and "ftyield". These are 2D binned spectra with the yield mapped as a function of KER and $\Delta\omega$ which can also be exported for plotting in Origin.

For the state-selective studies of CEP effects presented in Sec. 5.4, the binned asymmetry and yield spectra for different field ionization settings are subtracted to obtain the

maps for different subsets of n-states. The subtraction was performed by running the code **bb_state_selective_testing_offset.m**. The "asym_total" and "yield_total" arrays for each of the relevant measurements were saved for loading into this code. Then, the code calculates the difference between all combinations of these arrays, and generates plots of each resulting asymmetry or yield spectrum that corresponds to a specific range of n-states. Then, the Fourier analysis of each map is performed using the same routine as in **bb_asym_subsets.m**. The asymmetry and yield spectra are saved to output files, with filenames corresponding to the range of states included in the subset (e.g. "yield_30-40.out").

G.2.3 H_rates

rates_all.m is a script that calculates all of the spontaneous emission rates for a specified range n-states of hydrogen. An array of all possible transitions $(n, l) \rightarrow (n' < n, l \pm 1)$ is then generated and the transition rates are calculated using the function **rates.m** using the analytic solution from Ref. [223]. The table of rates is saved to a .txt file.

The calculated rates are then used in **time_prop.m** to simulate the time evolution of an initial hydrogen (n, l) population. An initial population can be generated using the script **init_generator.m**, which provides a few different model populations. An array containing the initial n and l values and the fraction of the initial population is written out to the file "init.txt". The rate equations for spontaneous emission, eq. 5 in Sec. 5.4, are then solved using the Euler method for a specified time range and time step. Note that the Euler method is only accurate if the step size is sufficiently small, in this case smaller than the shortest lifetime. Steps of 1 ns were found to provide results that agree well with other methods, and even though the large number of steps is computationally expensive, this method was just as fast or even faster than other methods. For each time step, the n-state population is stored in a cell array "npop".

Alternatively, the reverse time evolution can be simulated, i.e. beginning with a final population and propagating backwards to recover the initial population. **time_prop_rev.** solves the the rate equations for this scenario using the exact same methods as **time_prop.m**.

A final population based on a measured n-state population can be generated using the code, **init_generator_rev.m**.

As a way to test the stability of the Euler method solution, another version of the simulation was written that utilizes more sophisticated ODE solvers. The rates and initial population that are loaded into **time_prop_ode.m** are input into any of Matlab's built-in ODE solvers, such as "ode45", a Runga-Kutta method. In this case the rate equations are written in the function **rateqs.m**, which is called in the solver.

G.2.4 n-state

dfnsort.m was written to analyze the output from SpecTcl for the D* state-selective measurements presented in Chap. 5. The SpecTcl code ("FTI_CEP_BB_pp" in the FTI directory) for sorting the D* n-state measurements is a modified pump-probe code that writes the KER on each detector and the field ionization voltage to an output file. This file is loaded in to **dfnsort.m** along with **FI.txt**, which is used to convert the voltage to a value of n.

Optionally, the power-tagging photodiode signal (see Appendix B) can be added as another column to the SpecTcl output. Then **dfnsort.m** allows filtering of the data based on the photodiode signal. Uncomment and enter the centroid and tolerance parameters to apply the filtering.

Recall that to obtain the yield and spectra of a given n-state, two measurements are subtracted from one another, one measuring $n = 2$–n and the other $n = 2$–$n-1$ (see Sec. 5.3 for details). The Matlab code sorts and groups the data corresponding to each field ionization voltage. Typically, the n-state scans are performed on one detector while the other is held at constant voltage for normalization purposes. A normalization factor for each step of the scan is calculated based on the yield on the second detector. Then, the KER spectrum for each step of the scan is generated and adjacent steps are subtracted to obtain the state-selective KER spectra. This information is binned in 2D to plot the yield as a function of n-state and KER.

G.2.5 Pump-probe

The following codes were used to perform the analysis of the data presented in Chap. 4. To use, the momentum output file from the pump-probe SpecTcl code is needed, and to normalize by the ion beam current, a saved ion beam scaler spectrum is also needed.

The code **pumpprobe.m** performs the general analysis by calling several functions located in the **functions** subdirectory. Enter the parameters corresponding to the total time per delay step (summing over all loops), as well as the delay steps and number of loops. Enter the path to the momentum file to load the data. **bb_import.m** stores the data in structures, e.g. "data.A.ker" contains the list of KER for the A channel. Since loading data is often slow, it can be useful to save these structures to a .mat file for faster loading in the future.

In some cases, there is some malfunction in the scan and only parts of it are useable. Use **bb_trunc.m** to truncate the scan at a given step number.

To normalize by the ion beam current, enter the path of the ion beam scaler spectrum. **bb_ionbeam.m** will remove zeroes from the end of the spectrum and find the end of each step. It then integrates over each step and creates a normalization vector. Sometimes, the step-finding routine doesn't work very well, and its accuracy can be seen in the generated plot that shows the ion beam scaler spectrum with the found steps superimposed.

Next, the KER–step spectra for each channel are binned. Then, **bb_step.m** is used to convert the step numbers to actual time delay and sum over the number of loops in the scan.

Random coincidences can be subtracted using the method presented in Sec. 4.4.1. Specify the part of the KER–delay map that clearly contains random coincidences. Running **bb_randoms.m** replicates and randomly permutates the bins containing random coincidences to generate a spectrum spanning the full delay range, which can then be subtracted from the data. Alternatively, the subtraction can be done using the statistical method presented in Sec. 4.4.1 using **bb_randoms2.m**

Finally, using the method presented in Sec. 4.4.2, the enhancement of the ionization of the dissociating wave packet is evaluated in **bb_enhancement.m**

The binned data at any point in this code can be saved or exported to Origin for plotting. The binned spectra are added to the data structures with obvious naming, e.g. "data.C.kerstep" is the binned KER–step map for the C channel.

G.2.6 Scripts_linux

The scripts in this directory are not the actual versions that are run on the Linux machines. The actual versions are located on the J: drive in "J:\ibgroup\scripts", or form the Linux system in "∼/ibgroup/scripts". This directory has been added to the $PATH environment on most of the Linux machines, and therefore these scripts can be executed from any directory simply by entering the filename. To add this directory to the $PATH environment on another Linux machine, edit "∼/.bashrc" by adding the line "export PATH = $PATH ∼/ibgroup/scripts".

To run **checkload.sh**, enter "checkload.sh" in a console window. This displays uptime information using the Linux "uptime" command. For more detailed information, use the option "-w" (i.e "checkload.sh -w"). This displays the users logged in to each machine as well as their processes, using the Linux "w" command. To add another machine to the list, use the template provided in the file and follow the commented instructions.

The scripts **rblink.sh** and **ecrlink.sh** create symbolic links to .evt files stored in the stage area. **rblink.sh** is meant for the newer ring buffer files while **ecrlink.sh** works for the older .evt files. Creating symbolic links to .evt files within the working analysis directory makes the .evt files more accessible while saving space that would be used by copying .evt files to the working directory. In the console, navigate to the working directory. Symbolic links for all the files in a run series can be created by entering the first three digits of the run series, for example "rblink.sh run-192", which would create links for all files starting with "run-192". Alternatively, create links to all segments of a single run by entering the full run number.